

The interaction of veins and foliations in metaturbidites of the Lower Ugab Domain, NW Namibia

Dissertation zur Erlangung des Grades
“Doktor der Naturwissenschaften”

am Fachbereich Geowissenschaften
der Johannes Gutenberg-Universität Mainz

Xavier Maeder

geboren in Pompaples (Schweiz)

Mainz, Mai 2007

*Das Schönste, was wir erleben
können, ist das Geheimnisvolle*

Albert Einstein, Mein Weltbild

Abstract

The junction between two related Neoproterozoic – Cambrian Mobile belts, the Kaoko and Damara Belts lies in the Lower Ugab Valley in NW Namibia. The area consists of siliciclastic and carbonates metaturbitites of Neoproterozoic age which are characterized by spectacular quartz and calcite veins, which show a complex but systematic deformation pattern regular over an area of more than 3000 km². These syntectonic veins are important markers of deformation since they carry information on polyphase structural evolution, shear sense and the fluid composition during deformation. This thesis presents a detailed structural study on the regional deformation and on the veins in the Lower Ugab domain which adds new data to our understanding of the structural evolution at the junction of the mobile belts. This structural study has been completed by finite element numerical modelling of boudin neck rotation for a better understanding of the formation of asymmetric boudins in the area. A parameter sensitivity analysis allowed to determine the influence of the condition of the flow, the relative viscosity of the veins and the wall rock, the initial geometry of the boudin and the total finite strain on the shape of the reworked boudins. Finally a new type of foliation which occurs at proximity to syntectonic syenite intrusions, named flame foliation (S2f) has been investigated.

The lower Ugab Domain is affected by three phases of deformation related to two main tectonic events D1-D2 and D3. D1 marks an event of sinistral transpressional E-W shortening. D1 forms kilometre scale N-S trending upright to west vergent folds accompanied by the main regional S1 slaty cleavage in axial planar position. The less conspicuous D2 phase of deformation developed coaxial open folds, mostly in the flat limb of D1 folds, and with an S2 crenulation cleavage that everywhere overprints S1 at a high angle. Both D1 and D2 occurred at regional metamorphic peak conditions in greenschist facies in the biotite zone (Goscombe et al. 2004). D3 produced E-W to NE-SW trending minor folds and foliations and is associated to a late N-S shortening event. A minor D3 N-S sinistral shearing component is evidenced in the NW part of the area where D3 asymmetric fold trains trend NE-SW. The metaturbitites are intruded by a series of plutons composed of syenite and biotite granite. Hornblende syenite intruded during late D1-syn D2 in the early Cambrian and biotite granite intruded pre-syn D3 at about the same time, indicating that D2 and D3 were close in age.

Three main types of syntectonic veins are distinguished in the metaturbitites. V_{bed} veins are striped bedding veins of quartz showing pre D1 top to the west bedding-parallel slip. V_A and V_B are two contemporary sets of composite quartz and calcite veins occurring pre-early D1. V_A are lensoid veins that lie approximately orthogonal to D1 folds axes and which formed by N-S extension during D1. They are strongly deformed due to mainly D1 shearing which produced a characteristic asymmetric shape of the boudins and flanking fold alongside the veins, defining a sinistral sense of shear in outcrop. V_B veins lie at a small angle to the S1 slaty cleavage, slightly oblique to D1 fold axes. They show a present constant orientation in both limbs of D1 folds dipping towards the ESE. In the steep limbs and wherever the tip of the veins penetrated a few centimetres from metapelite into the adjacent sandstone, hook-shaped folds developed, interpreted as an effect of reorientation by flexural slip during tightening of D1 folds. V_A and V_B veins are generally restricted to the more pelitic layers in the siliciclastic formations, which is unusual for boudinage and crack

formation which elsewhere usually occurs in more competent sandstone layers. The preference for metapelite may be explained by fluid overpressure. Quartz and calcite isotopic compositions indicate a mainly local origin of vein filling. The contemporaneous formation of two sets of veins, V_A and V_B , roughly orthogonal to each other, is explained by local inversion of stress axes σ_2 and σ_3 which were probably very similar in magnitude during vein formation.

Numerical simulation of deformation of boudins in coaxial and non-coaxial flow show that the flow conditions and the relative competence of the veins and the wall rock can be constrained according to the shape of the resulting reworked boudins. Bone-shaped boudins occur in pure shear flow with shortening perpendicular to the layers where the boudin necks are stronger than the wall rock. They can also form by rotation of tension gashes in coaxial or non-coaxial flow in simple shear, transpressional or slightly transtensional flows. Asymmetric boudins occur where the boudin necks are stronger than the wall rock and the flow is composed of a significant simple shear component. Domino boudins form where the veins are less competent than the wall rock which allows slip to occur between the boudins. A comparison between the simulation results and the asymmetric boudins observed in the Lower Ugab Domain show that the quartz rich boudin necks were stronger than the quartz and mica rich host metapelite during the deformation of the boudin in the greenschist facies.

Flame foliation defines penetrative anastomosing biotite rich selvages that form at a high angle to S_1 late-post D_1 . The orientation of the biotite perpendicular to the foliation and parallel to S_1 suggests that flame foliation formed in extension rather than in compression like the classical foliations. The flame foliation developed in proximity to the contemporaneous syenite intrusions, which suggests that it formed due to devolatilization reactions and fluid overpressure in the metapelite as a kind of synmetamorphic alteration rim along microfractures. Flame foliation is the preferentially nucleation site for the development of S_2 crenulation cleavage, which explains its orientation at a high angle to S_1 throughout the area.

Zusammenfassung

Das Arbeitsgebiet befindet sich im Lower Ugab Valley in NW-Namibia, das den Schnittpunkt der neoproterozoisch-kambrischen Mobilien Gürtel des Kaoko und des Damara Belts bildet. Das Gebiet besteht aus siliziklastischen und karbonatischen Metaturbiditen neoproterotoischen Alters, welche durch eindrucksvolle Quarz- und Kalzitadern charakterisiert sind. Diese Adern weisen über eine Fläche von 3000 km² ein zwar komplexes, doch gleichförmiges Deformationsmuster auf. Die vorliegende Arbeit besteht aus einer detaillierten strukturgeologischen Studie der regionalen Deformation sowie der Mineraladern des Lower Ugab Gebietes, die neue Einsichten in die strukturelle Entwicklung des Mobilien Gürtels vermittelt.

Um ein besseres Verständnis der Entwicklung asymmetrischer Boudins, wie sie im Arbeitsgebiet auftreten zu erlangen, wurden, ergänzend zur strukturgeologischen Untersuchung, Finit-Element-Modellierungen von boudin necks durchgeführt. Eine Parameter-Sensitivity-Analyse erlaubte es, den Einfluss der Art der Fließbewegung, der relativen Viskosität von Adern zum Nebengestein, der initialen Geometrie des Boudins sowie des Betrages der finiten Verformung auf die entstandene Form des aufgearbeiteten Boudins zu bestimmen. Abschließend wurde ein neuer Foliationstyp, die Flammfoliation (S2f), untersucht, der im untersuchten Gebiet nahe syntektonischer Syenitintrusionen auftritt.

Der Lower Ugab Bereich wurde durch drei Deformationsphasen geprägt, die mit zwei tektonischen Hauptereignissen, D1-D2 und D3, in Verbindung gebracht werden können. Das D1-Ereignis besteht aus sinistral-transpressionaler Einengung, wodurch senkrechte bis W-vergente Falten im Kilometermaßstab sowie die regional vorherrschende Achsparallele S1-Schieferung entstanden. Die D2-Phase ist im Vergleich weniger stark ausgeprägt. Auf sie geht die Bildung koaxialer offener Falten zurück, die zumeist im flachen Schenkel von D1-Falten auftreten, sowie einer S2 Krenulationsschieferung, die S1 in großem Winkel überprägt. Sowohl D1 als auch D2 fanden während des Höhepunkts der regionalen Metamorphose statt, innerhalb der Grünschieferfazies und der Biotitzone (Goscombe et al., 2004). Während einer späten N-S orientierten Einengung (D3) entstanden E-W bis NE-SW orientierte kleinere Falten und Foliation. Eine mit D3 zusammenhängende, relativ gering ausgeprägte sinistrale Scherkomponente kann im NW-Abschnitt des Arbeitsgebietes durch NE-SW orientierte asymmetrische Faltenzüge aufgezeigt werden. Die Metaturbidite werden durch eine Serie von Plutonen intrudiert, die aus Syenit und biotithaltigem Granit bestehen. Die große zeitliche Nähe von D1-D2 und D3 wird durch nahezu gleichaltrige Intrusionen von Hornblende-Syenit während der Spätphase von D1 bis D2 im frühen Kambrium und biotitreichen Graniten aus prä-syn D3 belegt.

Innerhalb der Metaturbidite können drei Hauptarten syntektonischer Adern unterschieden werden: V_{bed} sind 'striped bedding quartz-veins' die durch top-to-the-W, schichtparalleles Gleiten entstanden sind. V_A und V_B sind zwei zeitgleich entstandene Scharen von Quarz- und Kalzitadern, die vor und während des frühen D1 entstanden sind. V_A sind linsenförmige Adern, die etwa im rechten Winkel zu D1-Faltenachsen orientiert sind und durch N-S Extension während D1 entstanden. Sie sind, hauptsächlich durch sinistrale Scherung während D1, stark deformiert, worauf die charakteristische asymmetrische Form der Boudins und Flanking Folds entlang der Adern hinweisen. V_B Adern stehen in kleinem Winkel zur S1-Schieferung, leicht geneigt zu D1-Faltenachsen. Das Einfallen ist ESE, mit identischer Orientierung in beiden Schenkeln der D1-Falten. In steilen Faltenachsen bzw. wenn die Spitzen der Adern aus dem Metapellit heraus benachbarte

Sandsteinlagen penetrieren, entwickeln sich hakenförmige Adern, deren Form durch Reorientierung durch Biegegleitfaltung während der Einengung von D1-Falten erklärt werden kann. Adern vom Typ V_A und V_B treten ausschließlich in pelitischen Lagen innerhalb der siliziklastischen Formationen auf, was untypisch für Boudinage und Kluftbildung ist, die in der Regel eher in den kompetenteren Sandstein-Lagen zu erwarten ist. Das bevorzugte Auftreten in Metapelliten kann durch Fluid-Überdruck erklärt werden. Die Beschaffenheit der Isotope sowohl von Quarz als auch von Kalzit der Aderminerale weisen auf eine lokale Herkunft hin. Die zeitgleiche Bildung zweier Adern-Scharen, V_A und V_B , in einem etwa rechten Winkel zueinander, kann durch eine lokale Inversion der Stressachsen σ_2 und σ_3 erklärt werden, die während der Bildung vermutlich etwa gleichgroß waren.

Numerische Simulationen der Deformation von Boudins in koaxialem sowie nicht-koaxialem Fluss zeigen, dass sowohl die Fließbedingungen als auch der relative Kompetenzkontrast der Adern zum Nebengestein anhand der Form der wiederaufbereiteten Boudins abgeschätzt werden können.

Knochenförmige Boudins entstehen, wenn Fluß unter dem Regime reiner Scherung in Kombination mit einer Einengung im rechten Winkel zu den betroffenen Lagen auftritt und der boudin neck härter ist als das Nebengestein. Sie können sich zudem durch Rotation von tension gashes in Koaxialem or Nicht-Koaxialem Fluss während einfacher Scherung, Transpression oder Transtension bilden. Asymmetrische Boudins können auftreten, wenn die boudin necks härter sind als das Nebengestein und der Fluss durch einfache Scherung dominiert wird. Domino Boudins entstehen, wenn Mineraladern eine geringere Kompetenz als das Nebengestein aufweisen, so das Boudins gegeneinander gleiten können. Ein Vergleich der Simulationen mit asymmetrischen Boudins des Lower Ugab Gebietes zeigt, dass die Quarzreichen boudin necks während der Deformation der Boudins innerhalb der Grünschieferfazies härter waren als das Quarz- und Glimmerreiche metapellitische Wirtsgestein.

Flammfoliation wird durch anastomisierende, biotitreiche Lagen in großem Winkel zu S1 gebildet, die spät-post D1 entstanden sind. Biotitkristalle sind im rechten Winkel zur Foliation und parallel zu S1 orientiert, was die Annahme nahelegt, dass sich Flammfoliation unter dem Einfluss von Extension bildet, ganz im Gegensatz zur klassischen Foliation, deren Entwicklung durch Kompression bestimmt wird.

Flammfoliation tritt in der Nähe zeitgleich intrudierter Syenite auf, wodurch die Folgerung nahegelegt wird, dass sie sich durch Entgasungsreaktionen und Fluidüberdruck in den Metapelliten als eine Art synmetamorpher Alterationsrand entlang Mikrobrüchen entwickelten. Flammfoliation ist die bevorzugte Nukleierungsstätte für die Entwicklung von S2 Krenulationsschieferung, wodurch sich auch die zu S1 in großem Winkel stehende Orientierung über das gesamte Arbeitsgebiet erklärt.

Table of Content

| | |
|--|-----------|
| Abstract | i |
| Zusammenfassung | iii |
| Content | v |
| | |
| Chapter 1 – Introduction | 1 |
| | |
| Chapter 2 – Geology and structural evolution of the Lower Ugab Domain | 3 |
| 2.1 <i>Geological setting</i> | 3 |
| 2.1.1 Kaoko belt | 3 |
| 2.1.2 Damara belt (s.s) | 5 |
| 2.1.3 Temporal tectonic evolution of the Damara belt | 6 |
| 2.1.4 Geology of the Lower Ugab Domain | 7 |
| 2.1.4.1 <i>Physiography and geomorphological development</i> | 7 |
| 2.1.4.2 <i>The Zerrissenne Turbidite System</i> | 7 |
| 2.1.4.3 <i>Syntectonic syenite intrusions</i> | 9 |
| 2.1.4.4 <i>Metamorphism</i> | 10 |
| 2.2 <i>Deformation in the Lower Ugab Domain</i> | 10 |
| 2.2.1 Introduction | 10 |
| 2.2.2 First deformation phase, D1 | 11 |
| 2.2.3 Second deformation phase, D2 | 19 |
| 2.2.4 Asymmetric folds in the flat limb of D1 folds | 20 |
| 2.2.5 Third phase of Deformation, D3 | 21 |
| 2.2.6 Relative age of intrusions and deformation | 24 |
| 2.2.6.1 <i>Doros and Voetspoor intrusions</i> | 24 |
| 2.2.6.2 <i>Bandombaaai pluton</i> | 24 |
| 2.2.6.3 <i>Brandberg West and De Rust plutons</i> | 24 |
| 2.3 <i>Discussion on the regional deformation</i> | 27 |
| 2.3.1 Significance of D1-D2 | 27 |
| 2.3.2 Significance of D1 cleavage fanning | 30 |
| 2.3.2 Significance of D3 | 31 |
| | |
| Chapter 3 – Syntectonic veins in the Lower Ugab Domain | 32 |
| 3.1 <i>Introduction</i> | 32 |
| 3.2 <i>Syntectonic veins</i> | 32 |
| 3.2.1 V_b veins parallel to the bedding | 32 |
| 3.2.2 V_A veins at a high angle to D1 fold axes | 34 |
| 3.2.2.1 <i>Texture and composition</i> | 39 |
| 3.2.2.2 <i>Deformation</i> | 40 |
| 3.2.2.3 <i>Spacing of V_A veins</i> | 46 |
| 3.2.2.4 <i>Flanking folds along V_A veins</i> | 46 |
| 3.2.3 V_B veins at a small angle S_1 | 49 |
| 3.2.3.1 <i>Texture and composition</i> | 52 |
| 3.2.3.2 <i>Deformation</i> | 53 |

| | |
|--|------------|
| 3.2.4 Veins network in the marble | 55 |
| 3.2.5 Veins associated with N-type flanking folds..... | 60 |
| 3.3 <i>Stable isotope analysis</i> | 62 |
| 3.3.1 Introduction..... | 62 |
| 3.3.2 Stable isotope thermometry method..... | 62 |
| 3.3.3 Analytical technique..... | 63 |
| 3.3.4 Results | 63 |
| 3.3.4.1 <i>Isotopic compositions</i> | 63 |
| 3.3.4.2 <i>Thermometry</i> | 64 |
| 3.4 <i>Fluid inclusion study</i> | 66 |
| 3.4.1 Introduction..... | 66 |
| 3.4.2 Analytical technique..... | 66 |
| 3.4.3 Sample description | 66 |
| 3.4.4 Results | 68 |
| 3.4.4.1 <i>Fluid inclusion descriptions</i> | 68 |
| 3.4.4.2 <i>Fluid composition</i> | 69 |
| 3.4.4.3 <i>Microthermometry</i> | 69 |
| 3.5 <i>Discussion on the formation of the syntectonic veins</i> | 72 |
| 3.6 <i>Discussion on the deformation of the syntectonic veins</i> | 76 |
| 3.6.1 Effect of D1 deformation | 76 |
| 3.6.2 Effect of D2 deformation | 76 |
| 3.6.3 Effect of D3 deformation | 76 |
| Chapter 4 – Modelling of boudin neck rotation | 78 |
| 4.1 <i>Introduction</i> | 78 |
| 4.2 <i>Asymmetric boudins of the Lower Ugab Domain</i> | 79 |
| 4.3 <i>Bone shape boudins in the Lower Ugab Domain</i> | 83 |
| 4.4 <i>Numerical technique</i> | 84 |
| 4.4.1 Mesh generation and boundary conditions..... | 85 |
| 4.5 <i>Parameter sensitivity analysis</i> | 88 |
| 4.5.1 Effect of the total finite strain in simple shear flow | 89 |
| 4.5.2 Effect of the kinematic vorticity number..... | 90 |
| 4.5.2.1 <i>Transtensional regime</i> | 90 |
| 4.5.2.2 <i>Transpressional regime</i> | 93 |
| 4.5.3 Effect of the competency contrast between the layers | 96 |
| 4.5.4 Effect of the competency contrast of the veins | 96 |
| 4.5.5 Effect of the initial aspect ratio of the boudins | 101 |
| 4.5.6 Effect of the thickness of the veins | 101 |
| 4.5.7 Effect of the stress exponent | 101 |
| 4.6 <i>Discussion on the parameter sensitivity analyses</i> | 105 |
| 4.7 <i>Comparison between the simulations and the natural structures</i> | 113 |
| Chapter 5 – Flame foliation | 117 |
| 5.1 <i>Introduction</i> | 117 |

| | |
|---|------------|
| 5.2 Geological setting..... | 117 |
| 5.3 Flame foliation | 119 |
| 5.4 Occurrence of flame foliation | 121 |
| 5.5 Development mechanism of flame foliation | 122 |
| 5.6 Significance of flame foliation | 123 |
| Chapter 6 – Conclusion | 126 |
| 5.1 Structural evolution of the Lower Ugab Domain | 126 |
| 5.2 Syntectonic veins of the Lower Ugab Domain | 127 |
| 5.3 Modelling of boudin neck rotation | 128 |
| 5.4 Flame foliation | 129 |
| 5.5 Further perspectives | 129 |
| Appendices | 130 |
| References | 153 |
| Acknowledgments | 159 |
| Lebenslauf | 160 |

Chapter 1

Introduction: aims of the study

This thesis results from a study focussed on the interpretation of small-scale structures in the Lower Ugab Domain, north-west Namibia. The aim was to determine what information could be gained from small-scale structures in metapelite and psammite associated with veins. Such structures are common in metapelites throughout the world, but few areas allow a continuous analysis over a large area with perfect outcrop. The Lower Ugab Domain in Namibia is an area of 3000 km² of nearly perfect outcrop and ideal to study the development of small-scale structures in metapelite.

Several subjects were studied in the 2004 and 2005 field seasons and lab works. The development of secondary foliations in metapelite; their relation with folds; the effect of non-coaxial flow on folding; the development and deformation of syntectonic veins in metapelites and the development of asymmetric reworked boudins.

The thesis is structured in four main Chapters (Chapters 2, 3, 4 and 5). This first Chapter is a general introduction. The second Chapter is concerned with the deformation and the structural evolution of the Lower Ugab Domain. The third Chapter is about the development of different sets of syntectonic veins in the metasediment of the Lower Ugab Domain. Finite element numerical modelling of boudin neck rotation have been performed for a better understanding of the flanking structures which form along the syntectonic veins in the area and forms the third part of the present study (Chapter 4). Finally I focussed on a special foliation structure which occurs at proximity to the syntectonic granite intrusions of the area (Flame foliation, Maeder et al., 2007, Chapter 5). The foliation is interpreted to form perpendicular to the extension direction.

Chapter 5 has been published in the *Journal of Structural Geology*, the other Chapters are in preparation to be published in the *Journal of Structural Geology* or *Tectonophysics*.

Chapter 2 discusses structural evolution of the Lower Ugab Domain. The Lower Ugab Domain at the junction of the two related Damara and Kaoko belt is well situated to reveal the tectonic evolution at the transition between the two belts. Several structural investigations have performed in the area (Coward, 1981, 1983; Miller et al., 1983, Miller and Grote, 1988; Freyer in Hoffman et al., 1994, Passchier et al., 2002; 2007; Goscombe et al.; 2003a; 2004). Although the chronology of the main deformation events and the main kinematic of the area were already investigated, some important questions still remained to be answered, mainly concerning the relationship of foliations and veins. The present study confirms the different findings of the previous studies and adds some new detailed observations which allow a better constrained of the tectonic evolution of the area. D1-D2 transpressional phase of deformation have been investigated in the present study to constrain the timing of the sinistral shearing which occurs overall the

area. The relations between the deformation in the metasediments and the different syntectonic syenite intrusions of the area have been also investigated. The formation of large scale cleavage fanning which occur in the east of the area near the syenite intrusions is discussed in some detail

Chapter 3 discusses syntectonic veins in the Lower Ugab Domain. The metasediments of the Lower Ugab Domain are especially rich in different sets of quartz and calcite veins. The investigation of the formation and the deformation of the different sets of veins allows a better understanding of the tectonic evolution of the area. Several aspects of the veins have been investigated. A detailed structural study of the different sets of veins was performed. Isotopic geochemistry has been applied to quartz and calcite in the veins and to the respective host rocks to constrain the source of vein materials. An attempt has been made to do stable isotope thermometry with the couple quartz-calcite in the veins to constrain the temperature of the formation of the veins. A preliminary fluid inclusion study on four veins in the area was carried out to investigate the nature of the fluids and the temperature of formation of the veins.

Chapter 4 describes modelling of boudin neck rotation. Asymmetric shape boudin structures occur all over the area. The shape of the boudins is marked by buckling of the bedding into an asymmetric flanking fold at the tips of the boudin neck veins. Deformation of the boudin by rotation of the veins in coaxial and non coaxial flow was modelled by finite element analysis. I performed a parameter sensitivity analysis to compare the influence of the different parameters of flow and the initial geometry of the boudins on the resulting shape of the deformed boudins. The different parameters investigated are the relative viscosity of the boudinaged layer and the veins, the amount of deformation, the nature of the flow and the kinematic vorticity number, the initial aspect ration of the boudin and the thickness of the veins. The parameter sensitivity analysis constrains the initial condition of the flow and the viscosities of the layers and the veins to form such asymmetric shape boudins in nature. We performed the same parameter sensitivity analyses on the rotation of tension gashes in coaxial and non-coaxial flow which can lead to the formation of bone shape boudins.

Chapter 5 describes Flame foliation. Flame foliation is a new foliation type, which forms in the metapelite of the Lower Ugab Domain in proximity to the syenite intrusions of the area. This foliation is unique in that it is interpreted to form perpendicular to the instantaneous *extension* direction and approximately parallel to the YZ plane of finite strain, while foliations usually form parallel to the XY plane of finite strain, perpendicular to the main *compression* direction. The content of this Chapter have been published in the Journal of Structural Geology as:

Maeder, X, Passchier, C.W., Trouw, R.A.J., 2007. Flame foliation: Evidence for a schistosity formed normal to the extension direction. Journal of Structural Geology 29, 378-384.

Chapter 2

Geology and structural evolution of the Lower Ugab Domain

2.1 Geological setting

The Panafrican Damara Orogen in Namibia has a triple junction geometry, related to the convergence of the Congo Craton in the north, the Kalahari Craton in south and the Rio de la Plata Craton in Brazil and reflects part of the West Gondwana suture (Porada, 1989; Fig. 2.1). It consists of three branches, the north-north-west coastal arm, named Kaoko belt, the south trending southern arm, named Gariep belt and the east-northeast trending inland arm, named Damara belt (Kröner, 1977, Martin & Porada, 1977a and b; Miller, 1983). The Lower Ugab Domain lies at the junction of the Kaoko and Damara belts in north-west Namibia and is considered to be the southern zone of the Kaoko belt (Miller, 1983; Miller and Grote, 1988; Hoffman et al., 1994; Fig. 2.1), separated from the main part of the belt by the Etendeka Plateau, composed mainly of basalts of Cretaceous age (Fig. 2.3). The area has been also named the Ugab Zone (Goscombe et al., 2003a, b).

2.1.1 Kaoko belt

The Kaoko belt presents the core of a transpressional orogen between the Congo and the Rio de la Plata Cratons (Fig. 2.1). The basement of the belt consists of lenses of Proterozoic to Archean rocks with ages significantly different from the age of the adjacent part of the Congo Craton (Seth et al., 1998), which favour the collision scenario for the formation of the belt (Stanistreet and Charlesworth, 2001). The belt has been subdivided structurally into three parallel north-northwest trending zones, with increasing metamorphic grade from the east to the west. The Eastern zone comprises sub-greenschist facies shelf carbonates that have been folded upright due to a dominant late stage of east-west shortening (Goscombe et al. 2003ab; 2005b). The eastern zone is delimited in the west by the brittle shallowly west-dipping Sesfontein Thrust. The Central zone consists of the Damara Sequence of deep basin and slope facies, strongly deformed during sinistral transpression and cumulating in large-scale east-vergent nappes towards the foreland margin. It contains cores of Archean and Paleoproterozoic basement. Metamorphic conditions range from lower greenschist facies in the east to upper amphibolite facies in the west. The western margin of the Central Zone is delineated by the Puros Mylonite zone which consists of a crustal-scale transcurent sinistral shear zone of upper-amphibolite mylonite to ultramylonite. The shear zone runs through the entire length of the Kaoko belt from Angola to the south of the Etendeka plateau, exposed as the Ogden mylonites (Fig. 2.3). The Western Kaoko zone comprised the Orogen core and the outboard Coastal Terrane (Goscombe et al., 2005b). The core of the orogen is composed of amphibolite to granulite-grade

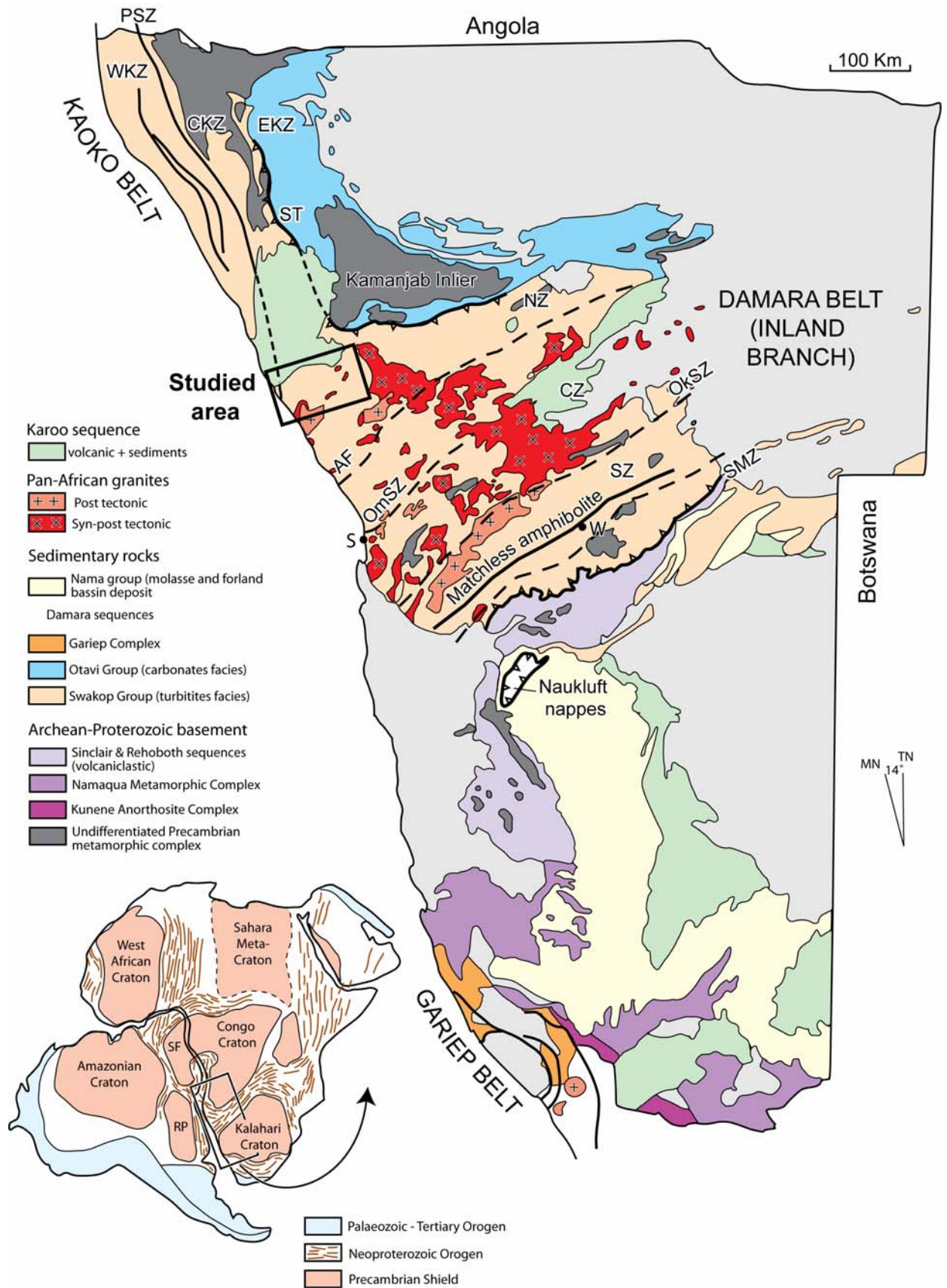


Fig. 2.1. Geologic map of the Damara Orogen showing the main geological units, the major faults and the emplacement of the plutonic rocks (Modified from Gray and al., 2006). PSZ: Puros shear zone; WKZ: Western Kaoko Zone; CKZ: Central Kaoko Zone; EKZ: Eastern Kaoko Zone; ST: Sesfontein Thrust; NZ: Northern Zone; CZ: Central Zone; SZ: southern Zone; AF: Autseib fault; OmSZ: Omaruru shear zone; OkSZ: Okahandja Shear Zone; SMZ: Southern Margin Zone; W: Wondhoek; S: Swakopmund; SF: Sao Fransisco craton; RP: Rio de la Plata Craton

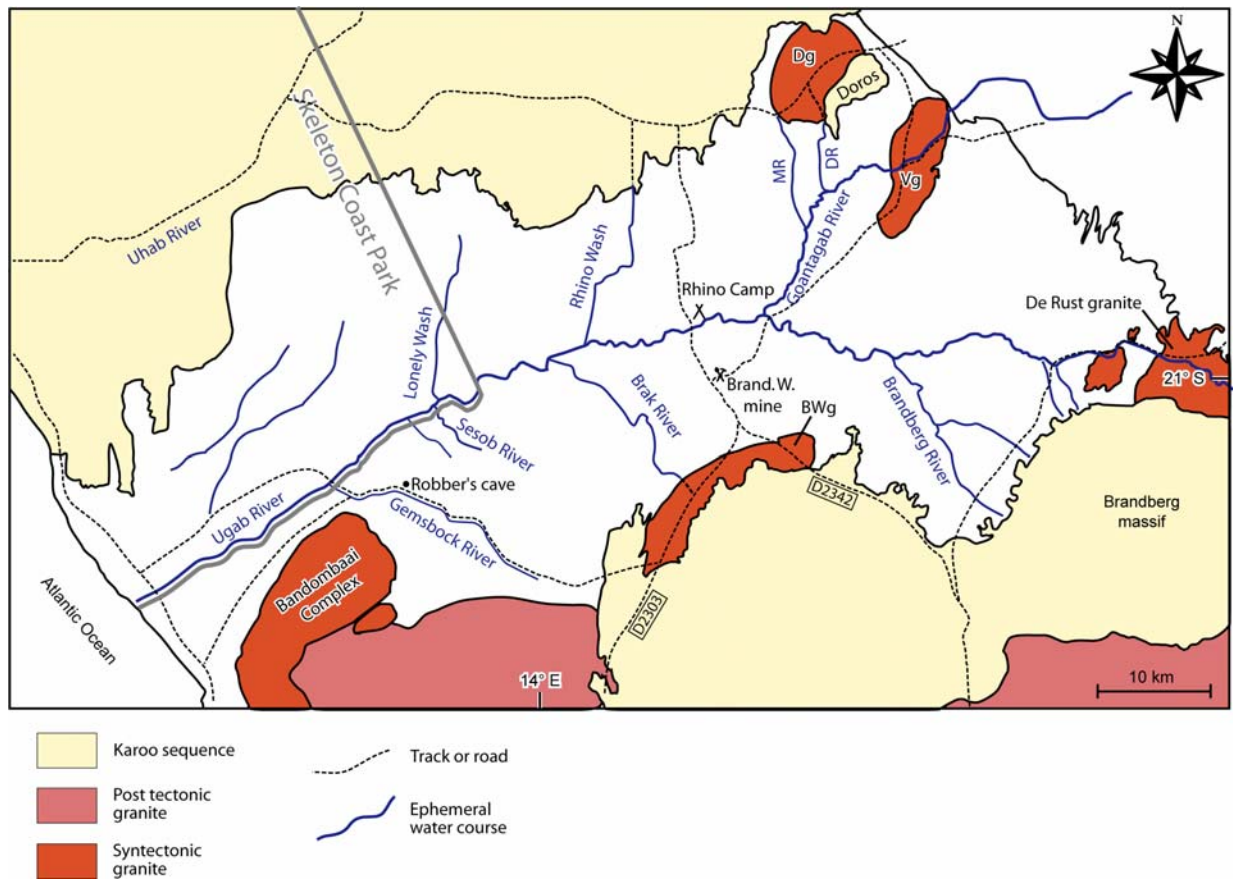


Fig. 2.2. Map of the Lower Ugab River showing major drainage lines, tracks, roads and localities discussed in the text. Dg: Doros granite; Vg: Voetspoor granite; BWg: Brandberg West granite; MR: 28 Mile River; DR: Doros

metasediment intruded by numerous granites. Deformation is characterized by deep crustal scale sinistral shear zones and formation of upright isoclinal folds, vertical to shallowly west-dipping at the coast (Goscombe et al., 2003a, b). The Coastal Terrane has a distinct lithostratigraphy composed of metagraywacke and metapsammite with a high proportion of intermediate and granitic meta-intrusive, and an earlier high-grade metamorphic cycle up to upper-amphibolite-grade that is otherwise absent from the rest of the Kaoko belt (Goscombe et al., 2005b).

2.1.2 Damara belt (s.s.)

The Damara belt (s.s.) is a continent-continent collision zone between the Kalahari and the Congo Cratons, associated with subduction towards the north under the Congo Craton. (Miller, 1983; Kukla and Stanistreet, 1991; Prave, 1996). The belt consists mainly of 1.2 – 2.0 Ga-old basement gneisses, Pan-African igneous rocks and Damara Neoproterozoic metasedimentary sequences. The Damaran sediments result from an initial stage of continental rifting between the two cratons which lasted from ~ 1000 Ma to ~ 750 Ma ago (Porada, 1989). The rifting induced crustal thinning and marine transgression. The Matchless amphibolite exposed in the Khomas Trough in the south of the belt is thought to preserve the remains of this ocean floor spreading estimated at ~ 780-760 Ma (Porada, 1989).

The Damara belt shows an asymmetric geometry with doubly vergent structures. Folds and thrust structures in the north verge to the north and to the southeast in the centre and the south of the belt (Coward, 1981; 1983). The Damara belt has been subdivided into northern, central and southern tectono-stratigraphic zones. The northern and central parts of the belt are characterised by a vast amount of granitic rocks of ages from 560 to 460 Ma old, cropping out over an area of approximately 75000 km² (Jung et al., in press). In the Central zone, the metamorphism increases from the east to the west where garnet-cordierite- K-feldspar migmatitic granulites are found, indicating conditions of 720–850 °C and 4–6 kbar and a high average thermal gradient (30–50 °C/km) (Goscombe et al., 2004b). The Damara belt joins the Zambezi belts in the east in Zambia and Zimbabwe (Martin and Porada, 1977a and b).

2.1.3 Temporal tectonic evolution of the Damara belt

The temporal tectonic evolution of the Damara Orogen has been summarized by Gray et al. (2006; submitted). Calc-alkaline magmatism between 625 and 580 Ma in the Ararcai, Riberia belt and Dom Feliciano Belt (Basei et al., 2000) are evidence for the start of the subduction-related closure in the northern part of Adamastor ocean between the Rio de la Plata and the Congo Cratons. Similar magmatism from 655 to 615 Ma related to the same event has been shown in the Coastal Terranes of the Kaoko belt (Goscombe et al., 2005b). Collision in the Brasiliano Orogen started at ~640 Ma with nappe-implacement on the São Francisco Craton (Gray et al., submitted) and as arc-continent collision in the Riberia belt that occurred at ~ 600 Ma in the Ribeira belt and the Kaoko Belt (Heilbron et al., 2004; Goscombe et al. 2005b). Peak metamorphism of the early thermal phase in the Kaoko belt occurred at ~ 580-570 Ma and the peak of the deformation of the transpressional phase at 570-550 Ma (Goscombe et al., 2003a, 2005b). During that time (580-570Ma), subduction-related metamorphism took place in the south of the Adamastor Ocean, indicated by the Marmora Terrane in the Gariep Belt (Frimmel and Frank, 1998). In the Damara belt (s.s.), mafic magmatism at 560-530 Ma suggests subduction-related in the Khomas ocean between the Kalahari and Congo Craton. Closure of the south Adamastor Ocean occurred at ~ 550-540 Ma (Frimmel and Frank, 1998). The peak of deformation and metamorphism in the Southern Zone of the Kaoko belt linked to Damara belt (s.s.) collisional deformation took place between 530-505 Ma (Goscombe et al. 2005b). In the centre of the Damara belt and through the Lufilian Arc into the Zambezi Belt, the peak of the deformation and metamorphism occurred at 530-520 Ma (Jung and Mezger, 2003; Singletary et al. 2003; John et al. 2003; 2004). The chronology sketched above shows that the Damara belt formed in two major episodes. The first episode is the closure of the Adamastor Ocean and the oblique collision which caused the formation of the Kaoko belt between ca. 590 and 530 Ma. The second episode is the closure of the Khomas Ocean between the Congo Craton and the Kalahri Craton which created the inland branch of the Damara belt with a peak of deformation between ca. 530 and 505 Ma.

2.1.4 Geology of the Lower Ugab Domain

2.1.4.1 Physiography and geomorphological development

The studied area lies in the catchment area of the ephemeral Ugab River in NW Namibia, west from the Brandberg Massif to the mouth of river, at the south limit of the Skelton Coast Park (Fig. 2.2). The river transects the Lower Ugab metaturbidites, forming an incised east-west canyon which gives a natural cross section through the area. A regular pattern of kilometre-scale tight folds in the metasediments forms north-south trending ridges alternating with gravel plains that are easily visible on satellite images. Spectacular hectometric folds hinges and folds interference pattern of Ramsay Type 2 C (Ramsay, 1967) can be seen in the landscape and on satellite images. The synclines form majority the ridge and the anticlines the valley, particularly in the marbles (Hoffman, 1994). The ridges form ranges of hills with a maximum height of 748m in the southwest. The area is delimited in the north and the south by the Etendeka Plateau which forms flat topped hills, capped by Etendeka volcanics (Etendeka means “land of the flat topped hills”). The Brandberg Massif marks the southeast limit of the area and consists of a perfectly circular Cretaceous granite intrusion, forming the highest mountain in Namibia, culminating at 2573m. The metasediments of the Lower Ugab domain have been covered by Karoo sediments and volcanics during the Carboniferous, which comprise mostly fluvial and shallow marine and lacustrine deposits. The unconformity of Permo-Carboniferous glacial sediments at the base of the Karoo sequence shows that the area was exposed at that time (Miller et al., 1983). A major period of volcanism occurred during the Cretaceous due to the continental break-up, rapidly followed by erosion which exhumed the pre-Karoo surface. The Lower Ugab metaturbidites had therefore a long period of exposure and stability since the Tertiary, which produced to a deep weathering surface, obscuring the structures in some places.

2.1.4.2 The Zerrissenne Turbidite System

The sediments that composed the Lower Ugab Domain are a succession of Neoproterozoic siliciclastic and interbedded carbonate metaturbidites, known as the Zerrissenne turbidite system (Miller et al., 1983; Swart, 1992, 1994) and which crops out between the Ogden Rocks in the west and the Goantegab Domain in the northeast (Fig. 2.3). The succession has minimum thickness of 1.6 km without the base and the top being exposed (Swart, 1992; Miller et al., 1983). It is subdivided into five formations, in stratigraphic order from the base to the top:

- 1) Zebraputz Formation (>350m of metasandstone and metapelite)
- 2) Brandberg-West Formation (15-20m of turbiditic marble, calcsilicate and metapelite)
- 3) Brak River Formation (500m of metasandstone and metapelite with rare dropstones)
- 4) Gembok River Formation (200m of turbiditic marble, calcsilicate and metapelite)
- 5) Amis River Formation (>500m of metasandstone and metapelite with rare marble).

The sediments are interpreted as deepwater deposits with a depositional age between ca. 750 and 580 Ma and a source area in the Congo Craton (Miller et al. 1983, Passchier et al. 2002). A number of large isolated clasts, which are interpreted as glacially-derived dropstones, are found in the Brak River formation. This formation has therefore been correlated with the Chuos Formation of Sturtian

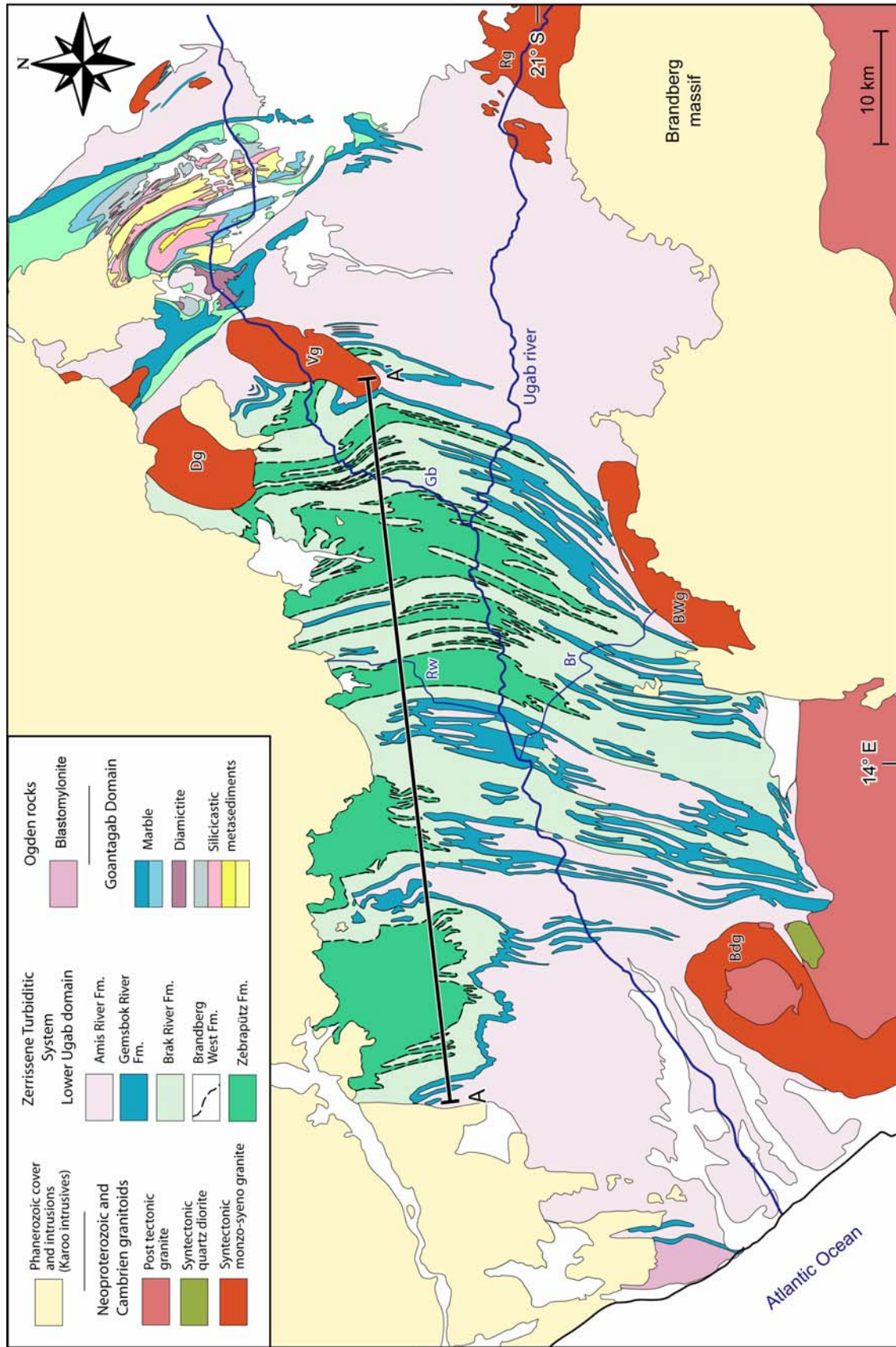


Fig. 2.3. Geological map of the Lower Ugab Domain (modified from Miller and Grote, 1988; geology of the Goantagab after Passchier, unpublished report). Dg: Doros granite; Vg: Voetspoor granite; Rg: De Rust granite; BWg: Brandberg West granite; Bdg: Bandombaa

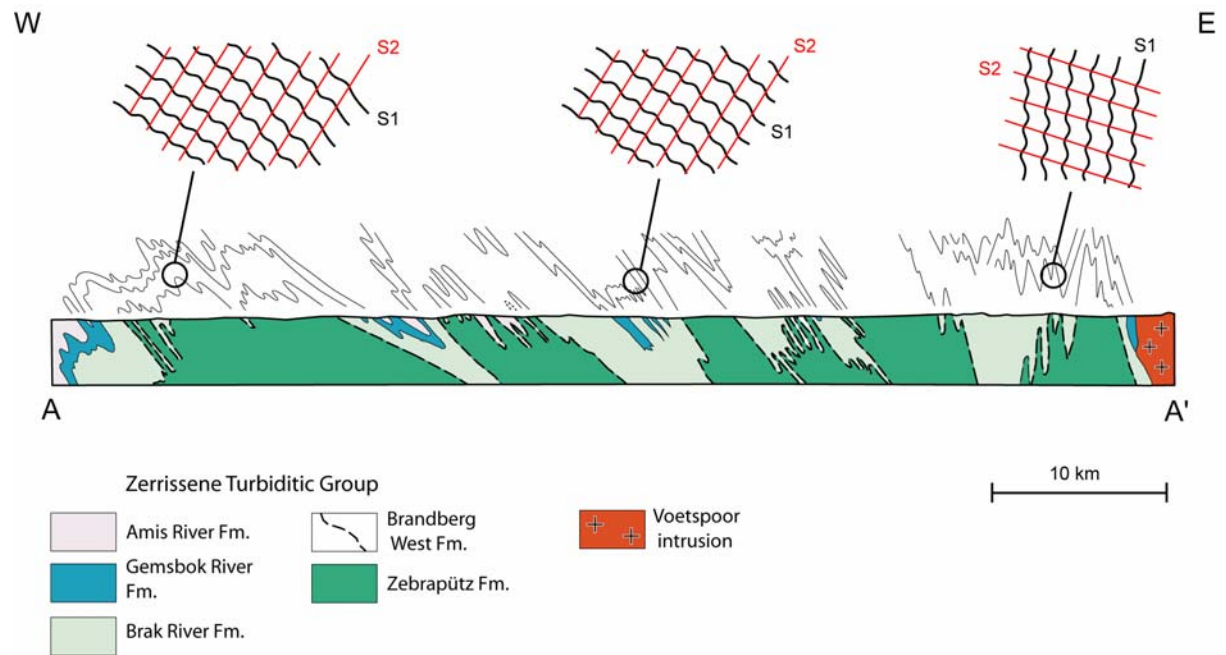


Fig. 2.4. Cross section through the metasediments of the Lower Ugab Domain (modified from Miller and Grote, 1988). D1 form regular chevron shaped west vergent folds. D1 folds become upright and East vergent near the Voetspoor granite showing a cleavage fanning structure over several kilometres. S2 is always at a high angle to S1, and dips towards the west in the western and central part of the area and to the east near the Voetspoor granite.

age of the Otavi group which shows the same characteristic and forms an important chronostratigraphic horizon in other parts of the Damara Orogen (Miller et al., 1983). Regional scale mapping suggests that the Brandberg West and Gembok River marbles correspond to cap carbonates (Passchier et al., 2007), which represent the end of the Sturtian and Marinoan glaciations, now dated at ca. 710 and 635 Ma (Kendall et al., 2004).

2.1.4.3 Syntectonic syenite intrusions

Several syenite and granite plutons intruded the metasediments of the Lower Ugab Domain (Fig. 2.3). The Doros and the Voetspoor Plutons in the northeastern part of the area have been subject to a specific structural study by Passchier et al. (2007). Both are nested Plutons, composed of hornblende syenite and biotite granite. The hornblende syenite forms 60-70% of each pluton with a range in composition of quartz-syenite to gabbroic (Passchier et al. 2007). The biotite granite forms the southwest rim of both plutons. The minimum age for the hornblende syenite in the Voetspoor granite was obtained at 530 ± 2 Ma by Pb-Pb single zircon evaporation (Seth et al., 2000) and at 541 ± 6 Ma by conventional U-Pb dating of sphene (Jung et al., 2005). Recent U-Pb shrimp datation give an age for the hornblende syenite of the Voetspoor intrusion at 533 ± 6 Ma (Passchier, unpublished report). The biotite granite in the Voetspoor intrusion has been dated to 513 ± 1 Ma by zircon evaporation (Passchier et al. 2007). More recently the biotite granite from Doros Plutons has been dated at 530 ± 5 Ma by U-Pb shrimp analysis (Passchier, unpublished report). Syenite whole rock Rb-Sr age was obtained at 573 ± 33 Ma for the Doros pluton (Kröner, 1982) and more recently at 528 ± 5 Ma by U-Pb shrimp analysis (Passchier et al., unpublished report). The recent datations seem to indicate that the syenite hornblende were contemporaneous in both plutons and intruded at ca. 530

Ma. The biotite granite seems to have about the same age, dated at ca. 530 Ma. Structural study of field relationships and thin section show that the hornblende syenite intrusions formed during late D1-D2 regional deformations phases and that the biotite granite intruded pre to syn-D3 (Passchier et al. 2007). Since the biotite granite is dated at about the same age than the syenite at ca. 530 Ma, D2 and D3 must have been relatively close in age. The geochemistry and the O-isotope signature of the Voetspoor syenite intrusion suggest involvement of a subduction zone component (Jung et al., 2005). The source of the syenite have been interpreted as an association of mantle rocks and subducted upper crustal material, most likely altered basaltic rocks from subducted oceanic crust (Jung et al. 2005).

The Bandombaai Complex (Fig. 2.1) in the western part of the area is composed of metaluminous hornblende- and sphene-bearing quartz diorite with an U-Pb age of 540 ± 3 Ma (Van de Flierdt et al., 2003). It is intruded by younger allanite-bearing granodiorites and granites, and a peraluminous garnet- and muscovite-bearing leucogranite. Isotope geochemistry indicates heterogeneous mafic lower crust for the source of the quartz diorite, most probably crustal garnet- amphibolite-bearing basalt (Van de Flierdt et al., 2003). The source of the granodiorites and granites has been interpreted as partial melting of meta-igneous (intermediate) lower crustal rocks. The leucogranite is interpreted as the result of melting of heterogeneous felsic lower crustal rocks (Van de Flierdt et al., 2003).

No data have been yet published on the Neoproterozoic granites at the Brandberg West and at De Rust (Fig. 2.3).

2.1.4.4 Metamorphism

Regional metamorphism in the Lower Ugab Domain is of middle to upper greenschist facies, indicated by the presence of biotite in almost all rock types, which formed and recrystallized in two first deformation phases. Actinolite can be found in calcsilicates and impure marble. Garnets are rare and can only be found locally, probably due to the relatively low pressure and the unsuitable rock composition. Estimates of 540-570°C and 2.5-3.2 kbar have been made for the peak of metamorphism in the area (Goscombe et al., 2004b). A slight gradient of metamorphism condition seems to occur from the north to the south over the Lower Ugab Domain since biotite is more abundant in the southern part of the area (Goscombe et al., 2004b). This agrees with the fact that metamorphism grade increases southwards towards the core of the Damara orogen where upper amphibolite facies are recorded (Goscombe et al., 2004b). The regional metamorphism is overprinted by contact metamorphism in a typical 5 km wide margin around the intrusive bodies. It produces dark spots in the metapelites composed of biotite and biotite muscovite chlorite aggregates pseudomorphing original cordierite and/or andalusite (Goscombe et al., 2004b).

2.2 Deformation in the Lower Ugab Domain

2.2.1 Introduction

Descriptions of deformation in the Lower Ugab Domain have been published by Coward (1981, 1983), Miller et al. (1983), Miller and Grote (1988), Passchier et al. (2002) and Goscombe et al. (2003a, 2004b) and by Freyer in a geological excursion guide: Hoffman et al. (1994). The present detailed study confirms

their findings and adds new observations. Three phases of deformation have been recognised in the area, labelled D1, D2 and D3.

2.2.2 First deformation phase, D1

Spectacular kilometric and very regular north-south to northeast-southwest trending folds that dominate the structure of the Lower Ugab Domain are generated during the main and first phase of deformation D1 (Passchier et al., 2002; Figs. 2.4, 2.5, 2.6, 2.8). The folds have a wavelength of 50-500m depending of their tightness. They show en chevron geometry with subhorizontal fold axis. The tightness of the folds varies with interlimb angle from 20 to 90°, mostly around 25-35°. D1 folds are asymmetric and west vergent at regional scale, defined by 20–80° eastward dip of axial planes (Passchier et al., 2002, Fig. 2.7). Close to the Voetspoor granite and the De Rust granite, on the west side of the both intrusions, the folds become upright and east vergent towards the granites over a distance of several kilometers (Figs. 2.4, 2.5). This can be observed in the Goantagab Valley at the west of the Voetspoor intrusion or in the Ugab Valley west of the De Rust granite. D1 folds form thus part of large cleavage fans (Figs. 2.4; 2.5). The fanning of D1 structures occurs locally, e.g. close to the granite. South of the Goantagab Valley and the Voetspoor intrusion D1 structures keep their west vergence in the east-west section (Fig. 2.5).

The formation of D1 folds is accompanied by the development of the regional main penetrative slaty to spaced cleavage in an axial planar position. The cleavage is essentially marked in the siliciclastic formation by alignment of biotite, white mica and chlorite. The cleavage is weakly developed or absent in the metasandstone and the marble. Locally in pelitic layers in the hinges of some D1 folds in the central and eastern part of the area, a pre-S1 biotite foliation can be observed in microlithons (Fig. 2.9). No folds or large scale structures associated to a pre-D1 deformation have been recognized. The formation of this Pre-S1 schistosity is therefore interpreted to form locally in the hinge of D1 folds early during the formation of the folds. It is also possible that the origin of pre-S1 schistosity is due to the compaction of the sediments when the series were still unfolded.

The sedimentary layers are boudinaged on the both limbs of D1 folds. Roughly east-west oriented boudin necks (V_A veins, Chapter 3), quartz strain fringes around pyrite crystals and deformed intraclasts indicate a principal extension direction of the bulk finite strain ellipsoid approximately north-south and subhorizontal, parallel to the D1 fold axes (Passchier et al., 2002). Boudinage seems to be pre-syn D1 since the boudin necks are deformed and displaced by D1 (cf. Chapter 3). In the steep limbs of D1 folds, asymmetric folds, delta and sigma clasts, shear bands, flanking folds along the boudin necks and displaced veinlets (V_A veins, Chapter 3) testify a strong sinistral shearing over all the area (Fig. 2.10). The axes of the asymmetric folds and the flanking folds attest a subvertical rotation axis and a steep north-northeast– south-southeast trending flow plane. Locally a subvertical stretching lineation can be observed in steep limbs of D1 folds (Passchier et al., 2002). The regional sinistral shearing seems to be mainly due to D1 since S2 is observed to cut the asymmetric folds and the flanking folds without being affected (Fig. 3.12). D1 is therefore a transpressional

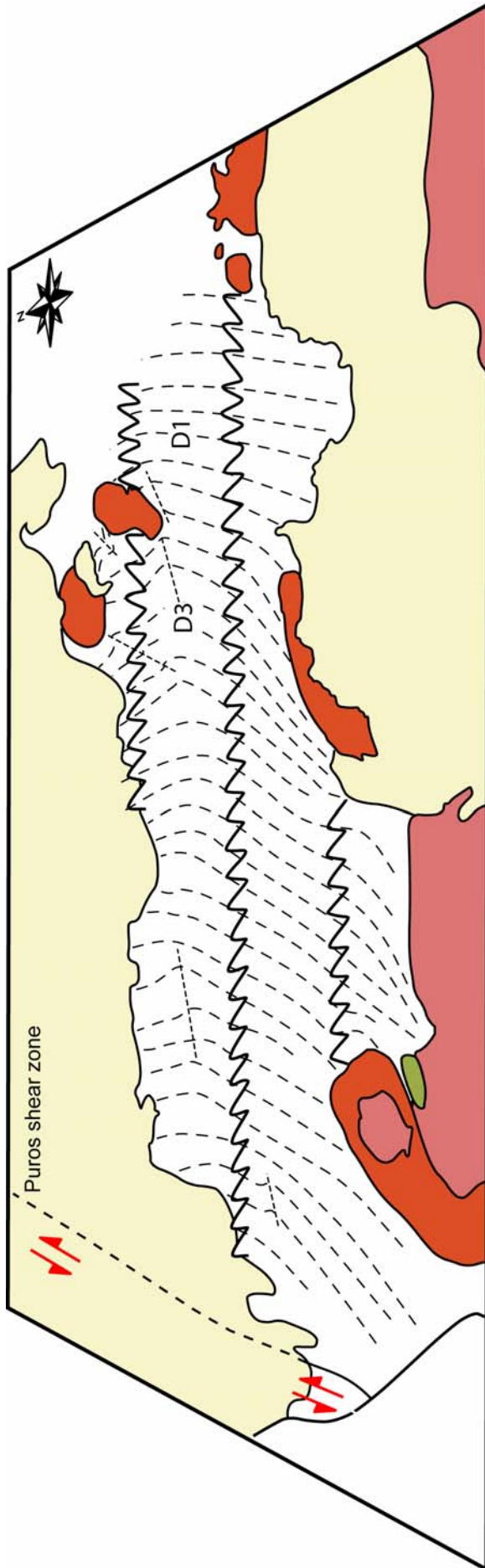


Fig.2.5. Diagram illustrating the structure of the Lower Ugab Domain. D1 developed very regular west vergent chevron folds all over the area except in proximity to the Voetspoor and the De Rust granite where the folds become upright and east vergent.

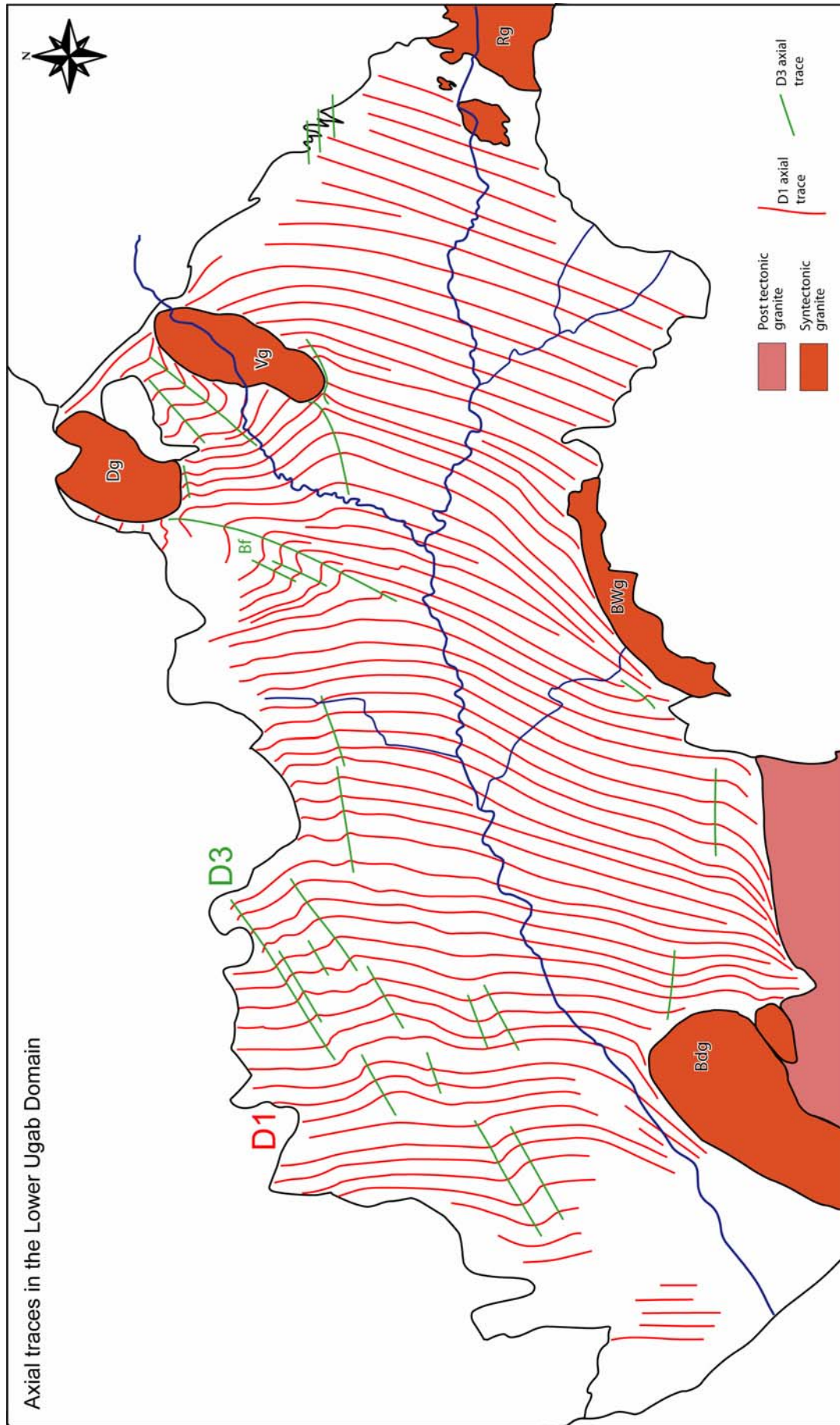
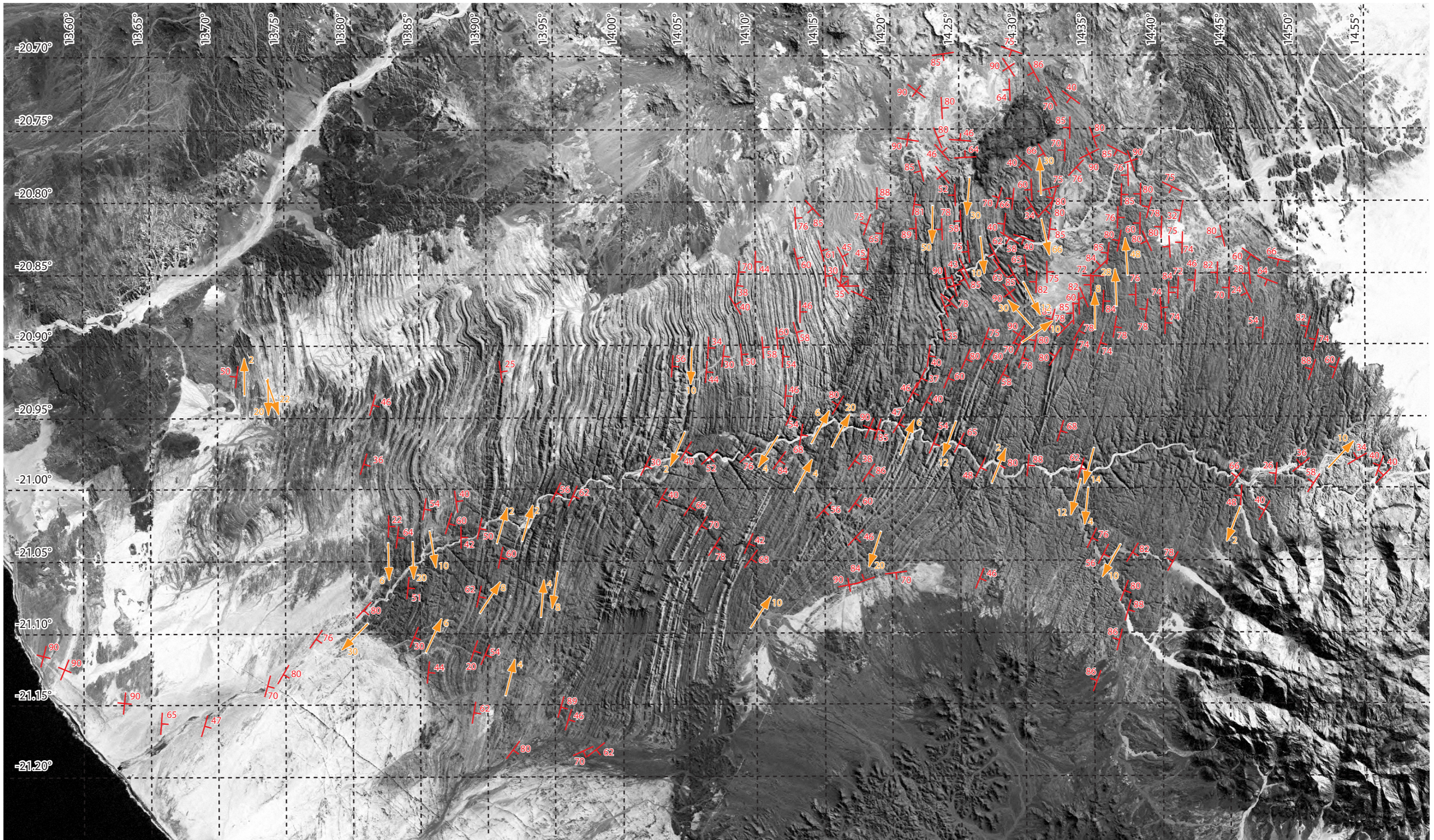


Fig. 2.6. Axial traces of the major D1 folds of the Lower Ugab Domain. D1 folds are plurikilometric regular N-S to NE-SW trending folds all over the area. D1 axial traces wrap around the Bandombaai and Brandberg West granites. D3 form E-W to NE-SW trending folds. Dg: Doros granite; Vg: Voetspoor granite; Rg: De Rust granite; Bdg: Bandberg West granite; BWg: Bandberg West granite; Bf: Bushman fold train.

D1





-  D1 fold axis with plunge
-  D1 foliation with dip

Fig. 2.7. Structural map of D1 in the Lower Ugab Domain

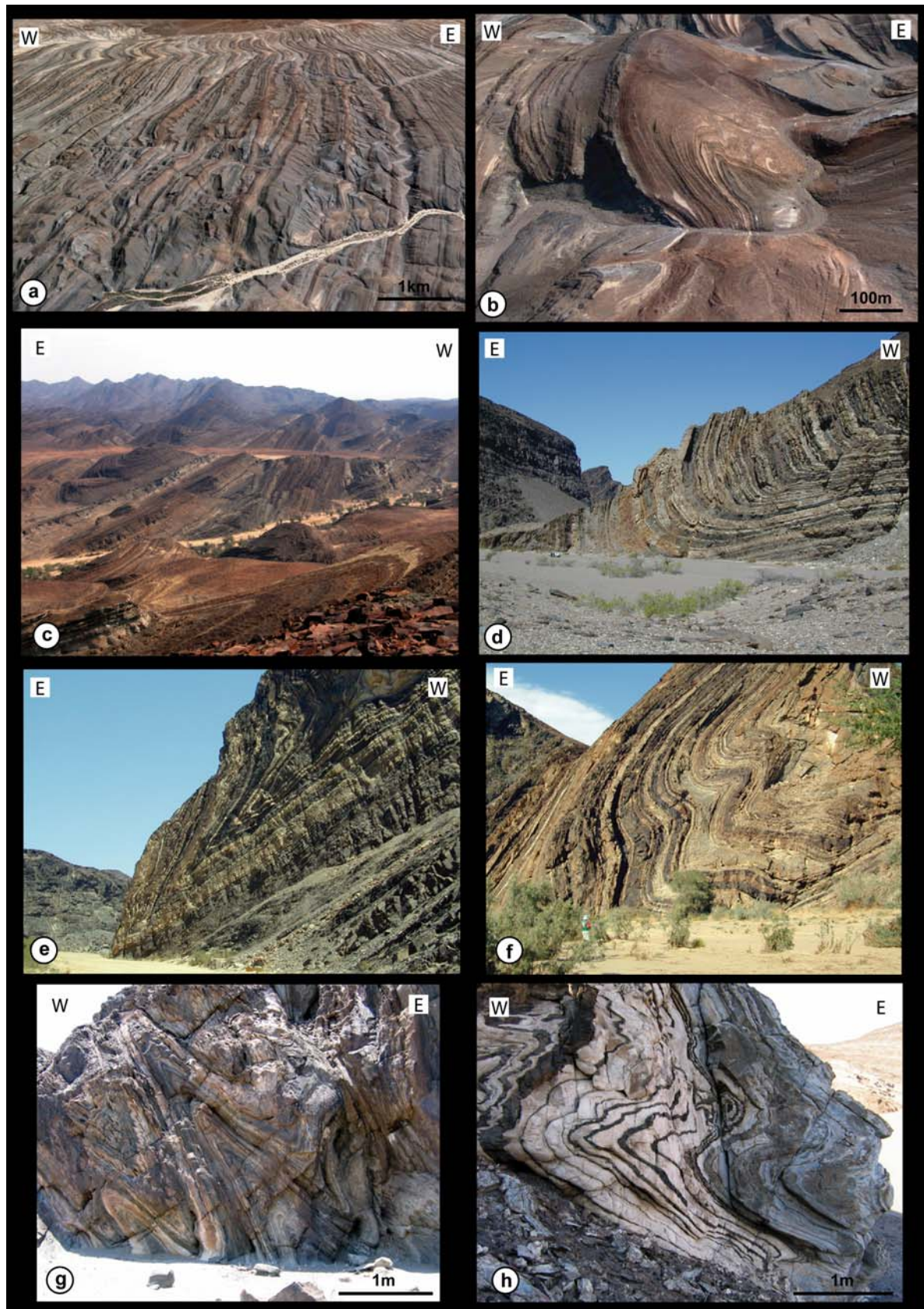


Fig. 2.8. Examples of D1 folds in the Lower Ugab Valley. (a) 3D Satellite image of the Ugab River and the Rhino Wash (from Google Earth). (b) 3D Satellite image of D1 anticlinal hinge in the Lower Gemsbock formation (from Google Earth, location: $-20^{\circ}55'18.31''/14^{\circ}02'34.59''$). (c) D1 folds series south of the Ugab (photographer location: $-20^{\circ}57'54.36''/14^{\circ}02'15.73''$). (d) D1 fold hinge in the Rhino Wash ($-20^{\circ}57'38.12''/14^{\circ}02'34.04''$). (e), (f) D1 synclinal hinges in the Lower Gemsbock formation in the Ugab River (respective locations: $-21^{\circ}00'30.14''/13^{\circ}56'18.93''$; $-20^{\circ}57'45.43''/14^{\circ}12'38.03''$). (g), (h): D1 in Lower Gemsbock formation (respective locations: $-21.07303^{\circ}/13.93875^{\circ}$; $-21.06972^{\circ}/13.90188^{\circ}$).

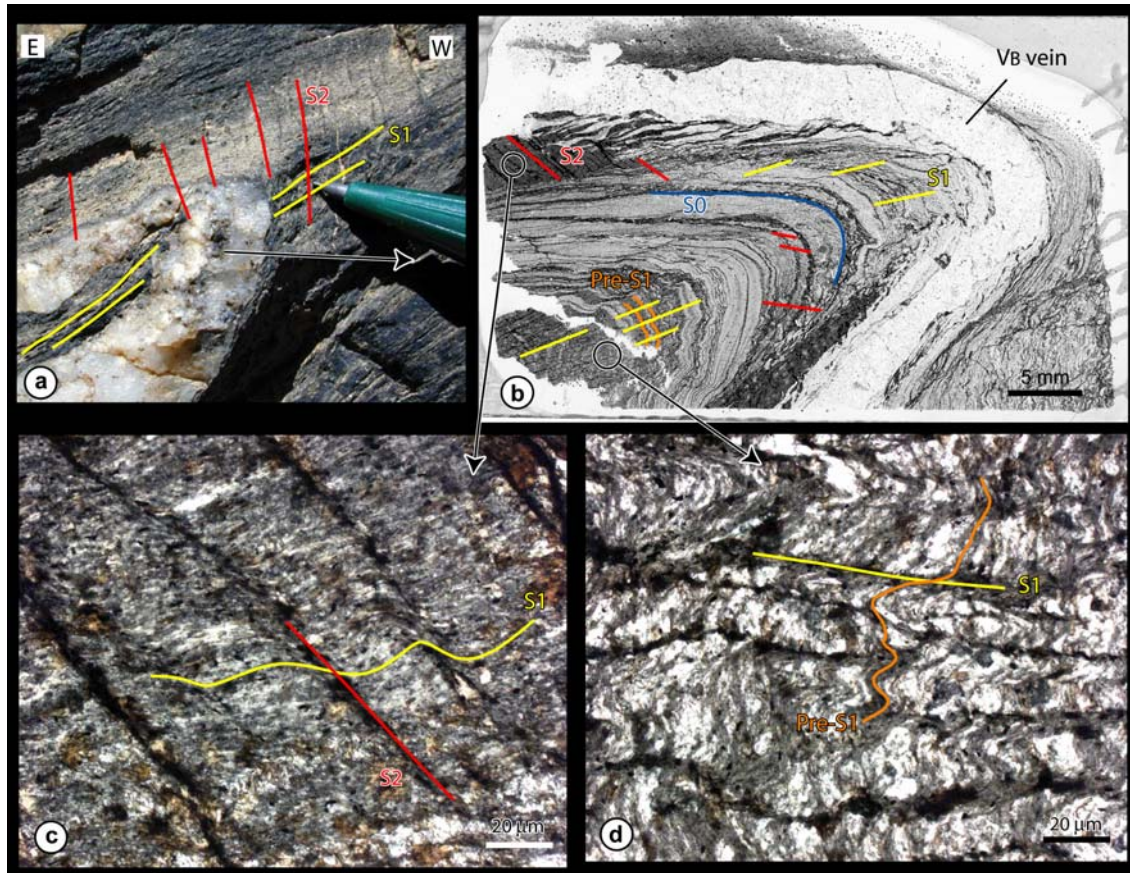


Fig. 2.9. (a) Quartz vein (V_B vein, Chapter3) folded by $D1$. $S1$ is the axial surface and $S2$ creulation cleavage is oblique to the fold. (location: $-20.97504^\circ/14.04987^\circ$). (b) Thin section of the fold shown in (a). In the hinge a pre- $S1$ schistosity can be observed in microlithons. (c) Detail of the thin section illustrating $S1$ and $S2$ creulation cleavage oblique to the fold. (d) Detail of the thin section showing the Pre- $S1$ microlithons.

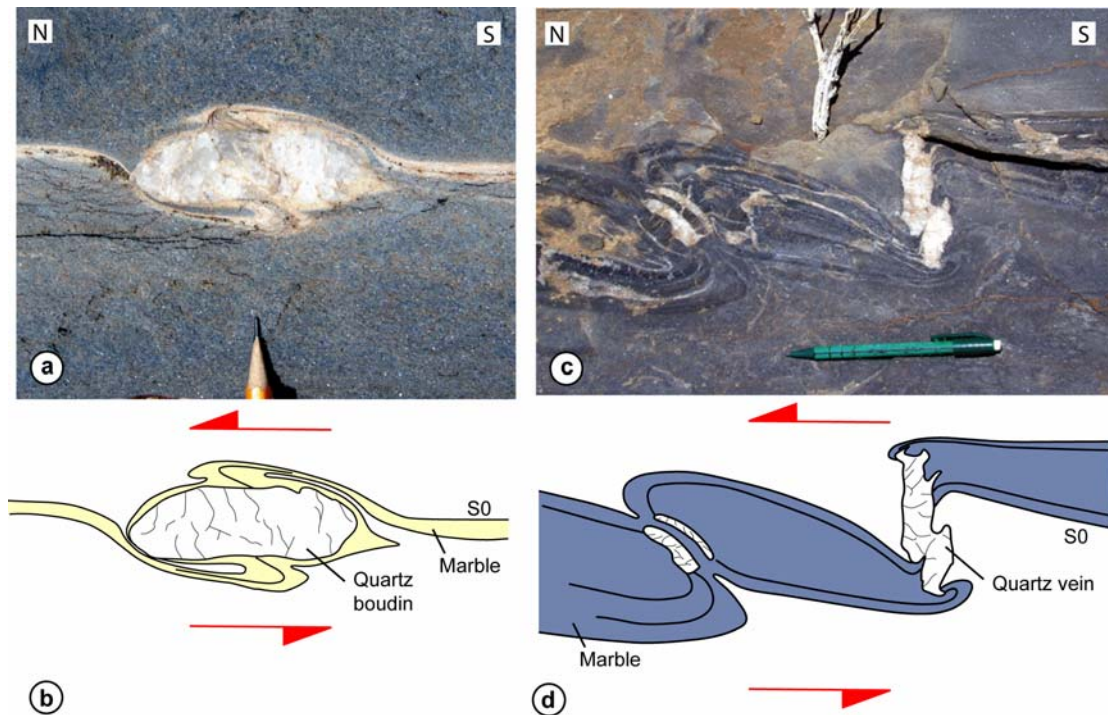


Fig. 2.10. (a) (b) Photograph and drawing of a quartz boudin in marble. The flanking folds around the boudin indicate a sinistral sense of rotation (red arrows) (location: $-21.07178^\circ/13.93661^\circ$). (c) (d) Picture and respective drawing of asymmetric flanking folds in upper Gemsbock marble. The flanking folds around the quartz boudin veins also indicate a sinistral sense of rotation of the veins (location: $-20.86527^\circ/14.35565^\circ$).

phase of deformation, with a strong component of north-south sinistral shearing which accompanies east-west shortening.

In the contact margin of the granite, biotite rich selvages at high angle to S1 developed in the pelitic layers (S2f). They form an anastomosing disjunctive cleavage which was named “flame foliation” (Maeder et al., 2007, Chapter 5; Fig. 2.11). Flame foliation is interpreted to form due to contact metamorphism devolatilization reactions and microfracturing in the pelite. Flame foliations formed at the end of D1 and before D2, since they cut S1 and are overprinted by S2 crenulation cleavage. They formed orthogonal to the direction of late D1 –extension orthogonal to S1 in the both limbs of D1 folds during their tightening (Maeder et al., 2007). Flame foliation is described in Chapter 5.

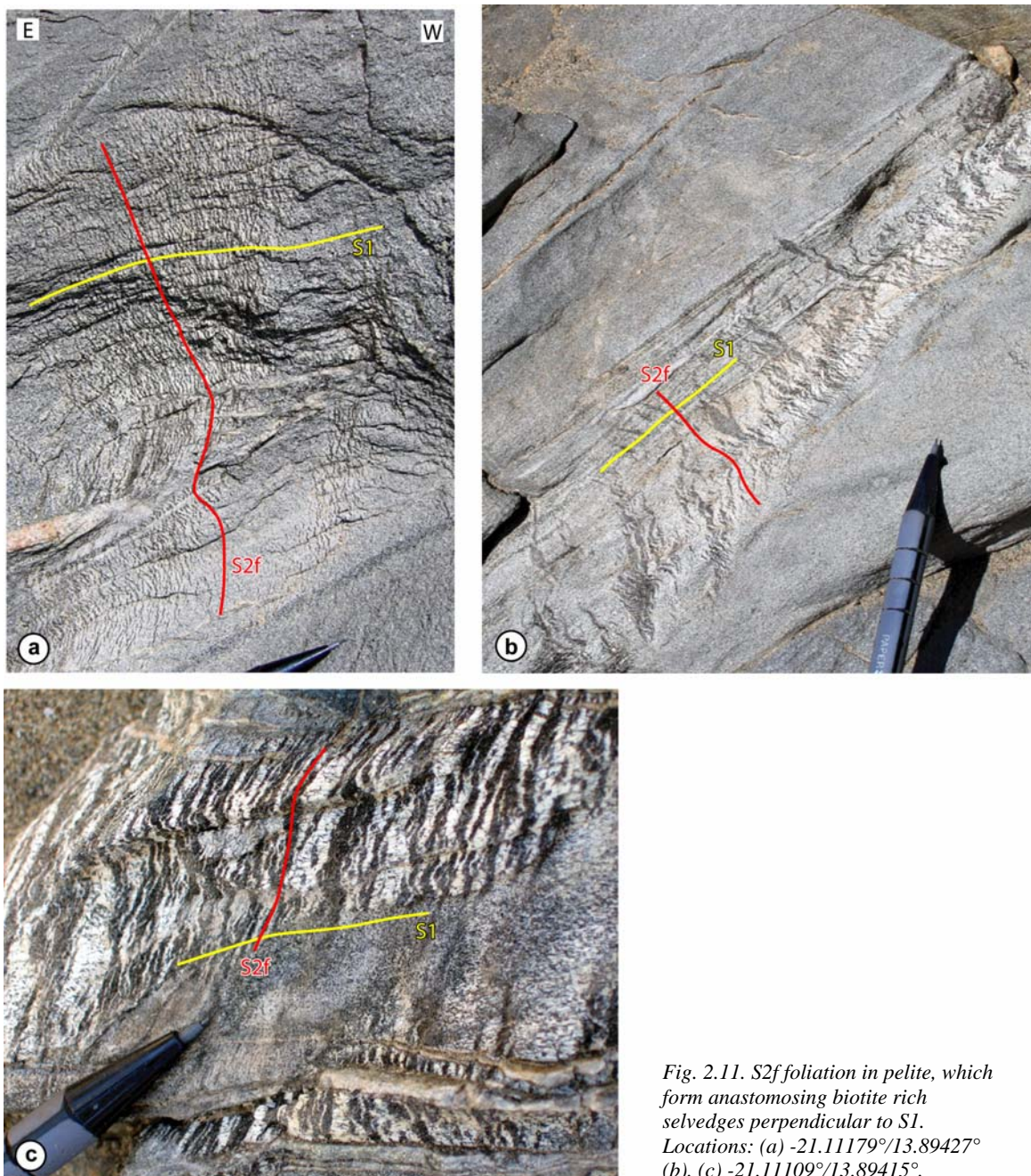


Fig. 2.11. S2f foliation in pelite, which form anastomosing biotite rich selvages perpendicular to S1. Locations: (a) -21.11179°/13.89427° (b), (c) -21.11109°/13.89415°.

D2

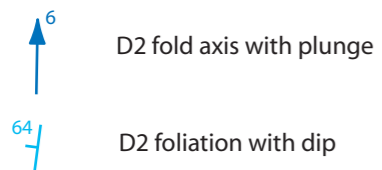
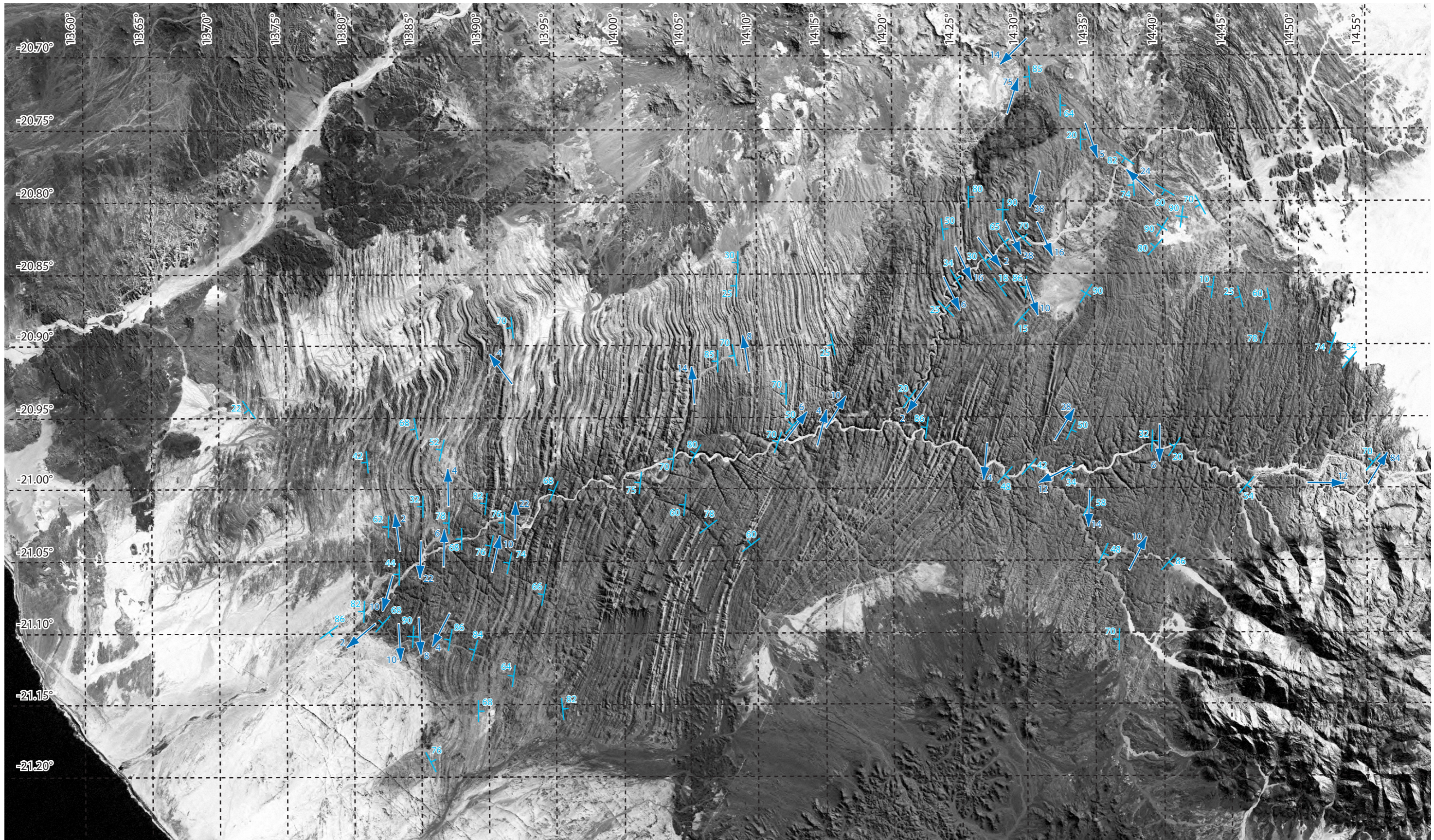


Fig. 2.12. Structural map of D2 in the Lower Ugab Domain

2.2.3 Second deformation phase, D2

D2 deformation is less prominent than D1 in the Ugab domain and develops some open folds preferentially in the flat limb of D1 folds. D2 folds have normally subhorizontal north-south oriented axes, subparallel to D1 fold axes (Fig. 2.12). D2 produced also an S2 crenulation cleavage in approximate axial planar orientation and which developed preferentially in the pelitic layers (Fig. 2.13). The flame foliation in the pelite is commonly the nucleation site for the formation of the S2 crenulation cleavage (Maeder et al, 2007). S2 overprints and developed therefore subparallel to S2f. S2 is invariably at a high angle to S1; where S1 is vertical, D2 axial planes are horizontal and vice-versa (Passchier et al., 2002; Fig. 4). This is an effect of the link between D1 and S2f (Chapter 5). S2 follows therefore the cleavage fanning which occur to the west of the Voetspoor and De Rust granites. S2 crenulation cleavage is associated with crystallisation or recrystallization of biotite in the pelitic layers. Both D1 and D2 show therefore the same metamorphic condition in the biotite zone of the greenschist facies. The formation at similar metamorphic conditions and the two coaxial deformations indicate that D1 and D2 are related phases of one continuous tectonic event. D2 intensity progressively increases from west to east of the studied area. In the western and central part only minor open folds developed, generally of micro to mesoscale. In the eastern part of the area D2 can form plurimetric folds. In the Goantagab area to the east of the Lower Ugab Domain, D2 is the dominate deformation feature (Passchier et al., 2002) and form tight folds and a dominant foliation.

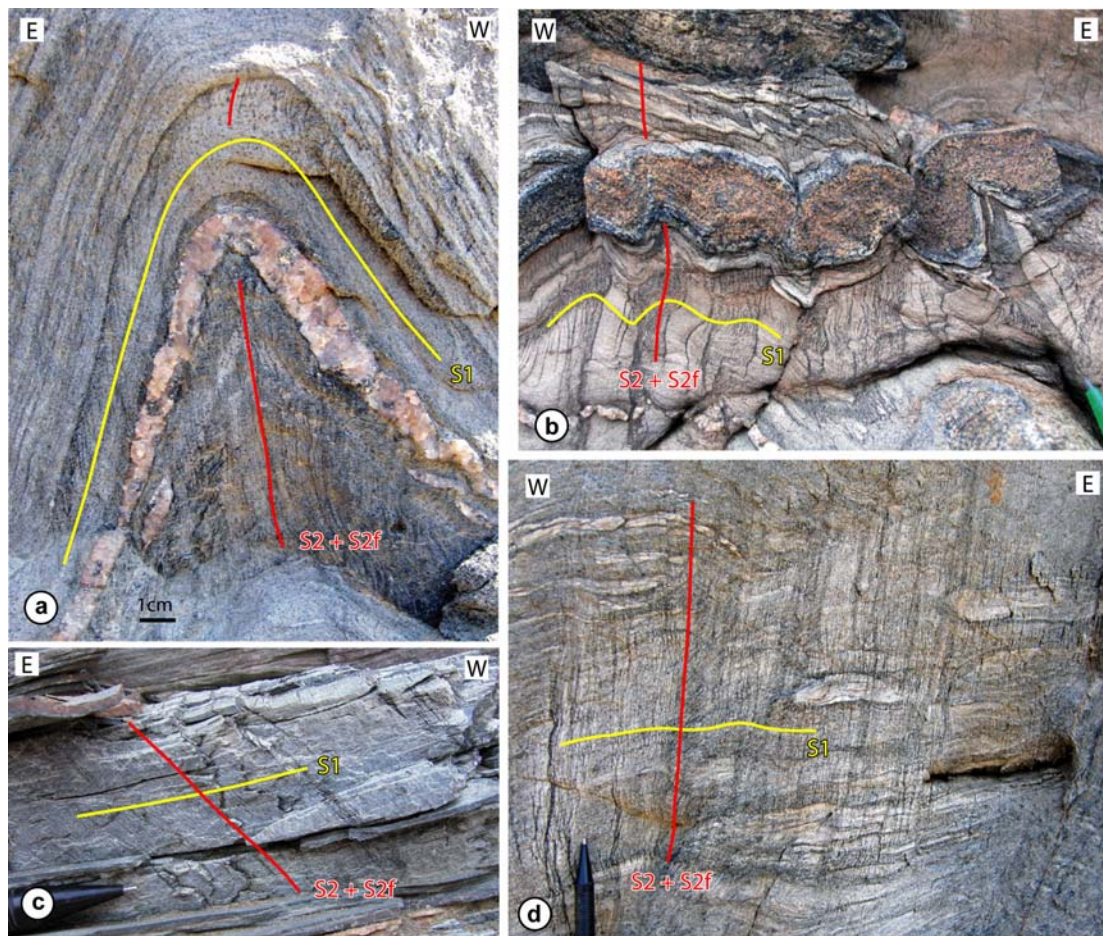


Fig. 2.13. (a) Example of D2 fold in the pelite. S2 crenulation cleavage is axial planar to the fold and overprints the parallel S2f. (location: $-21.09782^{\circ}/13.85852^{\circ}$) (b) granite dropstone in pelite deformed by D2. S2 crenulation overprints S2f biotite rich selvages. (location $-21.09736^{\circ}/13.86308^{\circ}$) (c), (d) Illustrations of S2 cleavage in pelite (respective locations: $-20.97727^{\circ}/13.86400^{\circ}$; $-21.10094^{\circ}/13.86668^{\circ}$).

2.2.4 Asymmetric folds in the flat limb of D1 folds

West of the Voetspoor granite in the Goantagab Valley, metric asymmetric folds are observed in the marble of the Brandberg Formation and the Gemsbock River Formation in flat limbs of D1 folds (Figs. 2.14, 2.15). They could be taken at first sight for parasitic folds of large D1 folds, but their asymmetry shows the opposite sense to normal parasitic folds (Fig. 2.14). The asymmetric folds displace quartz veinlets and deform already boudinaged layers. They refold minor D1 structures attesting that they postdate D1. However their exact relation with regional D2 and D3 is unclear because of lack of markers. The fold axes plunge gently towards the NW ($\sim 310^\circ$ on average) and the axial surface is gently dipping towards the SW-WSW ($\sim 250^\circ$ on average). The folds are therefore northeast vergent. They are clearly oblique to the D1-D2 and D3 folds axes and therefore belong to a distinctive deformation episode. The type of folding attests very ductile conditions during the formation of the folds, and they most probably formed therefore before D3 which occurs at lower metamorphic conditions. The folds may be linked to movement in the flat limbs of D1 folds during reorientation of the major D1 structures during the sinistral shearing. Their location near the Voetspoor intrusion may also indicate that they are linked to the granite intrusive event or the effect of the rigid pluton on deformation in the wall rock.

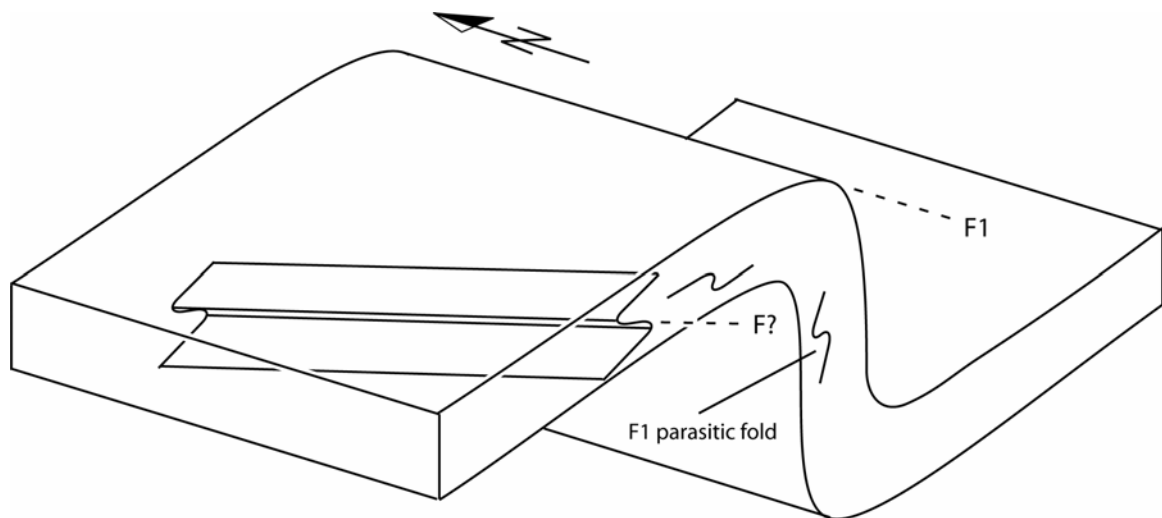


Fig. 2.14. Diagram illustrating the disposition of asymmetric folds which occur in the flat limb of some D1 folds to the west of the Voetspoor granite. The asymmetry of the folds shows the opposite geometry to D1 parasitic folds. The fold axis is also oblique to F1, slightly plunging towards the NW.

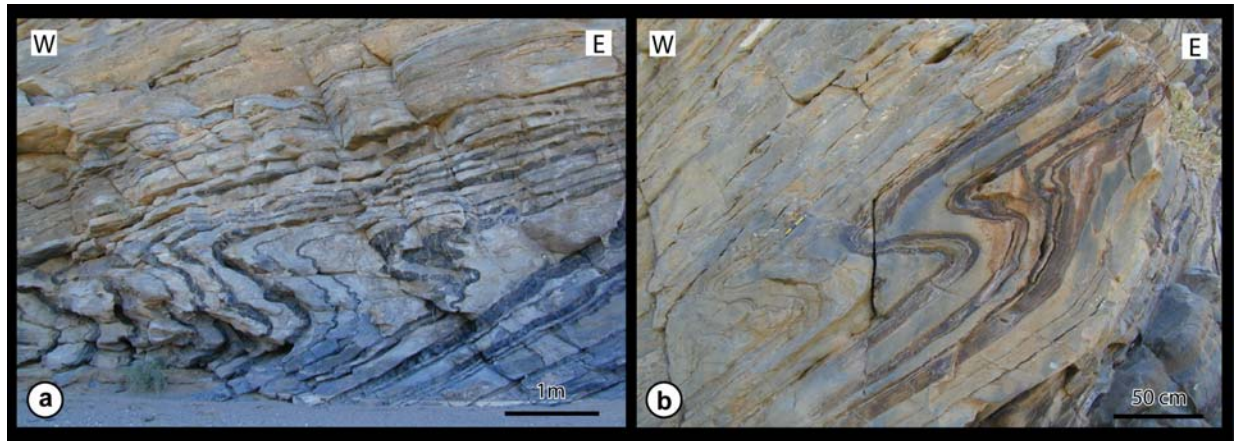


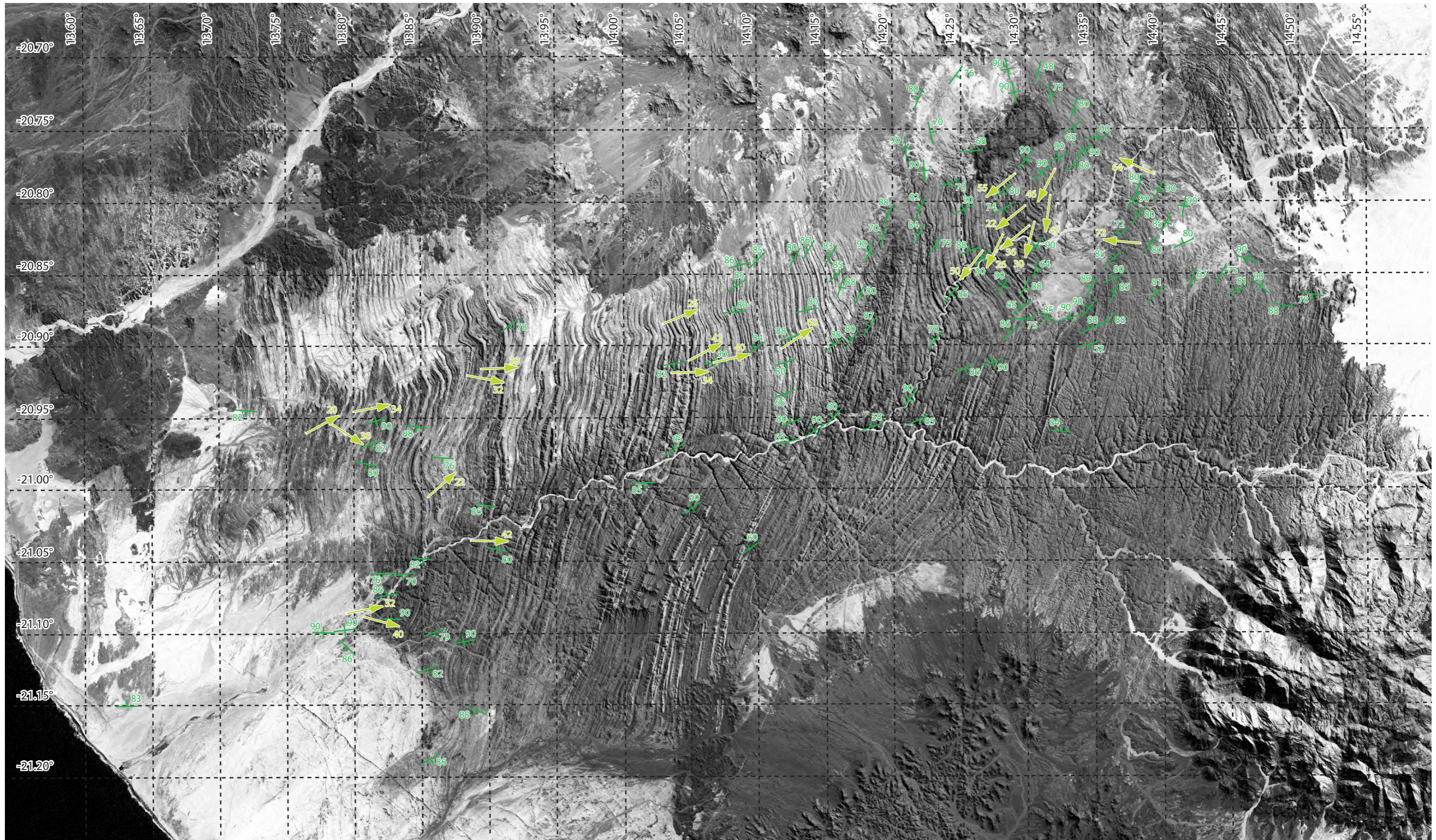
Fig. 2.15. (a), (b) Examples of asymmetric folds of “wrong” vergence in the flat limb of the D1 folds in the marble in the Goantagab River (respective locations: $-20.82785^{\circ}/14.28212^{\circ}$; $-20.83971^{\circ}/14.26495^{\circ}$).

2.2.5 Third phase of deformation, D3

D1 and D2 are overprinted by micro- to map-scale open folds with west-southwest- east-northeast trending axes and steep axial planes (Passchier et al., 2002; Figs. 2.16; 2.17). It caused the Type 2 C folds interference pattern on km-scale (Ramsay, 1967) that can be seen on satellite images (Fig. 2.4a). D3 developed a spaced crenulation cleavage preferentially in the pelitic layers (Fig. 2.17). Generally no new growth of biotite is seen in S3, which means that the deformation occurs at a lower grade than D1-D2 in the subbiotite zone.

The effects of D3 are strongest in the northern part of the area. Few map scale D3 fold trains can be seen in the south of the Ugab, while in the north of the area several symmetric and asymmetric fold trains can be observed (Fig. 2.5). The largest asymmetric fold train is the “Bushman fold train” with southwest-northeast trending axes which wraps around the west side of the Doros intrusion (Passchier et al., 2002; Fig. 2.5). The asymmetric shape of the folds indicates a sinistral component of shearing. S3 and D3 axial planes also warp around the southern part of the Voetspoor intrusion, which could also suggest a sinistral rotation of the pluton during D3 (Passchier et al., 2007). Locally, rare clockwise cleavage-transected D3 folds (Johnson, 1991) and brittle en-echelon subvertical tension gashes in the hinges of several D3 folds also attest to a sinistral shearing component during D3 (Passchier et al. 2002). However, the regional component of sinistral shearing is mainly due D1-D2 which developed shear zones in the steep limb of D1 folds over all the area. The weak sinistral shearing component associated with D3 is only local since asymmetric D3 folds and the rare shear indicators only appear in the north-eastern part of the area near the Voetspoor and Doros granites. In the Western part of the area and along the southwest rim of the Goantagab domain, D3 folds are symmetric and more east-west oriented. D3 is therefore associated with a regional north-south shortening which can create east-west trending structures in pure shear, or sinistral shear in some northeast-southwest trending folds trains.

D3





-  D3 fold axis with plunge
-  D3 foliation with dip

Fig. 2.16. Structural map of D3 in the Lower Ugab Domain

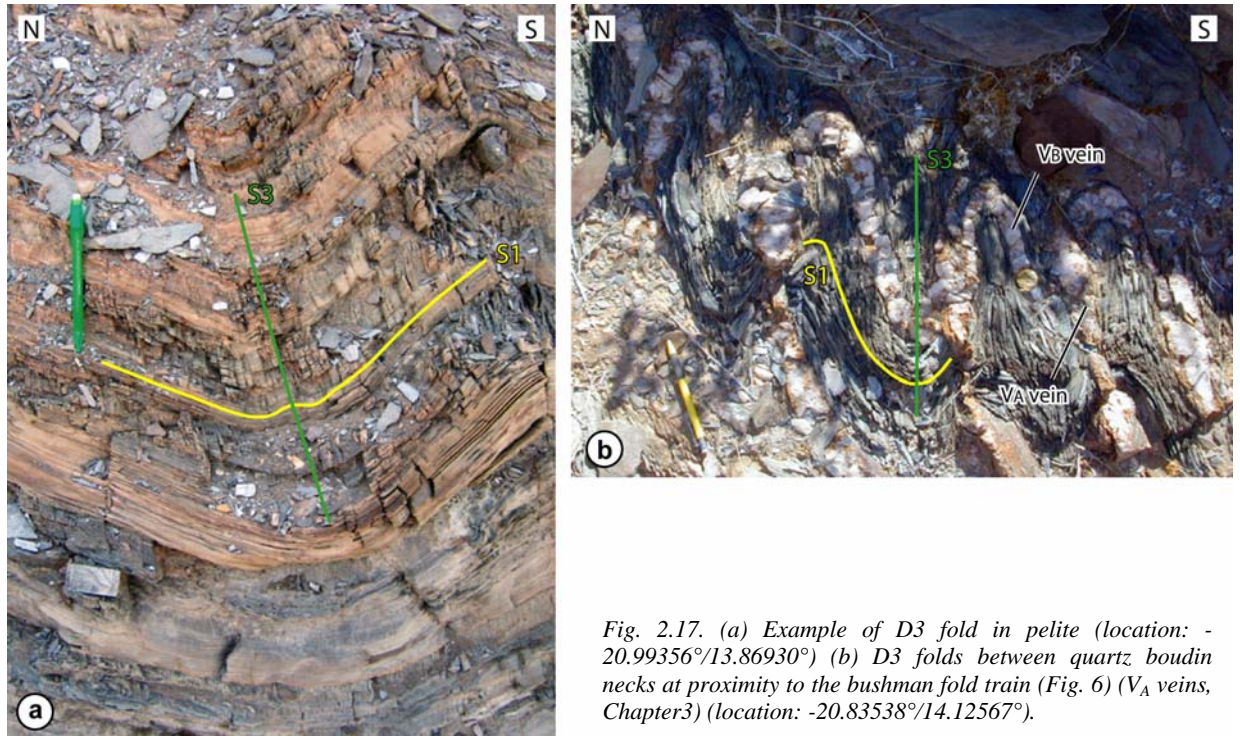


Fig. 2.17. (a) Example of D3 fold in pelite (location: -20.99356°/13.86930°) (b) D3 folds between quartz boudin necks at proximity to the bushman fold train (Fig. 6) (V_A veins, Chapter3) (location: -20.83538°/14.12567°).



Fig. 2.18. Granitic vein in a metasediment panel in the Doros intrusion showing D1 deformation (boudinage + folding) (location: -20.72630°/14.28848°).

2.2.6 Relative age of intrusions and deformation.

2.2.6.1 Doros and Voetspoor intrusions

The relation between the Doros and Voetspoor intrusions and the regional deformation has been described by Passchier et al. (2007). The hornblende syenite generally cuts D1 structures (Fig. 2.6). In the south of the Voetspoor granite, the syenite cuts a D1 fold which has an unusual open geometry, indicating that the intrusion took place before tightening of the fold caused by late D1 and D2 deformation (Passchier et al., 2007). In the rocks panels that lie inside of the Doros intrusion, some fine grained granitic veins are folded and deformed by D1 (Fig. 2.18). In some places, contact metamorphism andalusite porphyroblasts in the metasediments preserved deviation patterns of S1 that indicate porphyroblasts growth late syn-D1 (Passchier et al., 2007). These observations indicate that the hornblende syenite in the Doros and the Voetspoor intrusion intruded during late D1 to early D2. Biotite granite associated dykes are seen to cut D3 structures without being deformed and in some other places to be folded by D3. S3 is seen to bend around the plutons (Passchier et al., 2007). These observations indicate that the biotite granite of the two plutons intruded during D3.

2.2.6.2 Bandombaai pluton

In the northern rim of the biotite-bearing granodiorite and granites of the Bandombaai Complex, panels of sediments with hook shaped veins (V_B veins, Chapter 3) surrounded by the granite indicates that the granite postdates the formation and the reorientation of the veins in the metasediments. Some metasediments panels with strongly flattened clasts parallel to S1 are also cut by the granite, indicating that it intruded after the flattening of the elements in the metasediment related to D1 (Fig. 2.19c). The granitic dykes are also seen to cut D1 folds. Some dykes at a small angle to bedding show boudinage patterns with an extension direction parallel to the bedding (Fig. 2.19b). On the map, we can observe that D1 axial traces bend around the Bandombaai granite (Fig. 2.6). The contact between the granite and the metasediments is sharp. The contact of the granite is frequently parallel to the bedding (Fig. 2.19a). In some places the dykes are affected by D2 deformation (Fig. 2.19c, d). Some dykes cut also D2 folds without being affected (Fig. 2.19e, f). All granitic veins are folded by D3. The contact metamorphism porphyroblasts overprint S2f and S2. All these observations indicate that the biotite-bearing granodiorite and granite of the Bandombaai Complex intruded late D1 to syn-post D2, similar to observations by Passchier et al. (2007) in the north-east of the area. Cross cutting relations show that the leucogranite in the center of the Bandombaai Complex postdates the biotite-bearing granodiorite (Van de Flierdt et al., 2003), but its location far from the contact with the metasediments does not allow a relative dating with respect to the deformation.

2.2.6.3 Brandberg West and De Rust plutons

Granitic dykes related to the Brandberg West intrusion cut D1 structures. Some dykes at a small angle to bedding show boudinage in a direction subparallel to the layer associated with D1-D2 deformation. Granitic veins cut syntectonic quartz veins (V_A veins and V_B veins, Chapter 3). At the outcrop near the junction

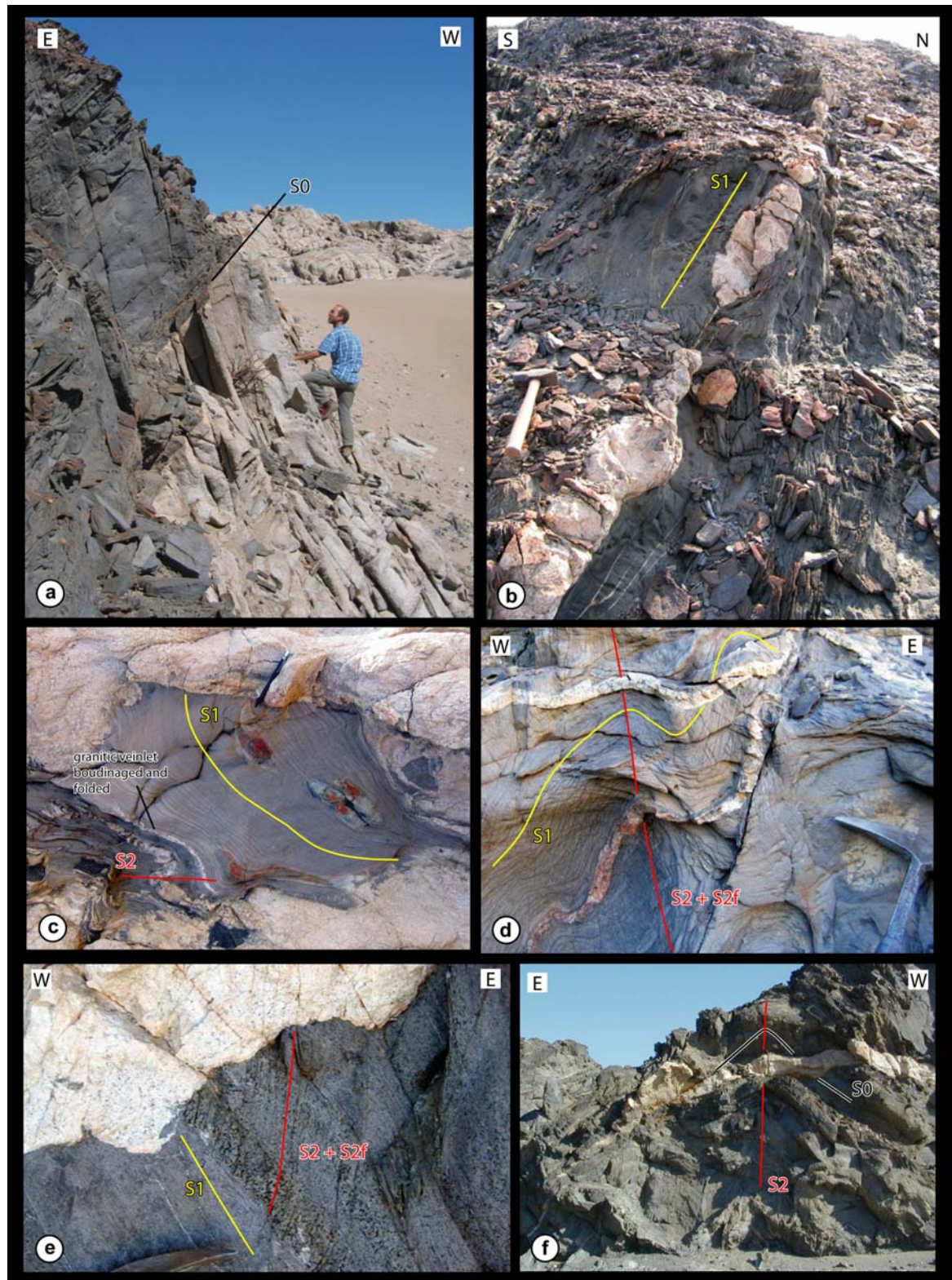


Fig. 2.19. (a) Contact between the Bandombaai biotite-bearing granite and metasediment of the Amis River Formation. The granite intrudes here parallel to bedding. (location $-21.10844^{\circ}/13.83174^{\circ}$). (b) Granitic vein slightly oblique to S1. Boudinage of the vein is due to D1-D2 (location: $-21.10251^{\circ}/13.80140^{\circ}$) (c) small sediment panel surrounded by the granite. The granite cuts S1 and the tip of an already flattened element parallel to S1 in the metasediment. Small associated granitic veinlets show boudinage parallel to S1 which is interpreted to mean they were partly deformed during late D1. The veinlets show D2 deformation (location: $-21.10251^{\circ}/13.80140^{\circ}$). (d) Two granite-associated veinlets in the metasediment close to the contact. The vein at the bottom of the picture is strongly folded by D2 and the upper one shows more open folding and is partly cutting the D2 fold (location: $-21.10187^{\circ}/13.84673^{\circ}$). (e) granitic dyke that cuts S2 crenulation cleavage (location: $-21.10844^{\circ}/13.83174^{\circ}$). (f) granitic dyke cutting D2 folds without being folded (location: $-21.1014^{\circ}/13.84722^{\circ}$).

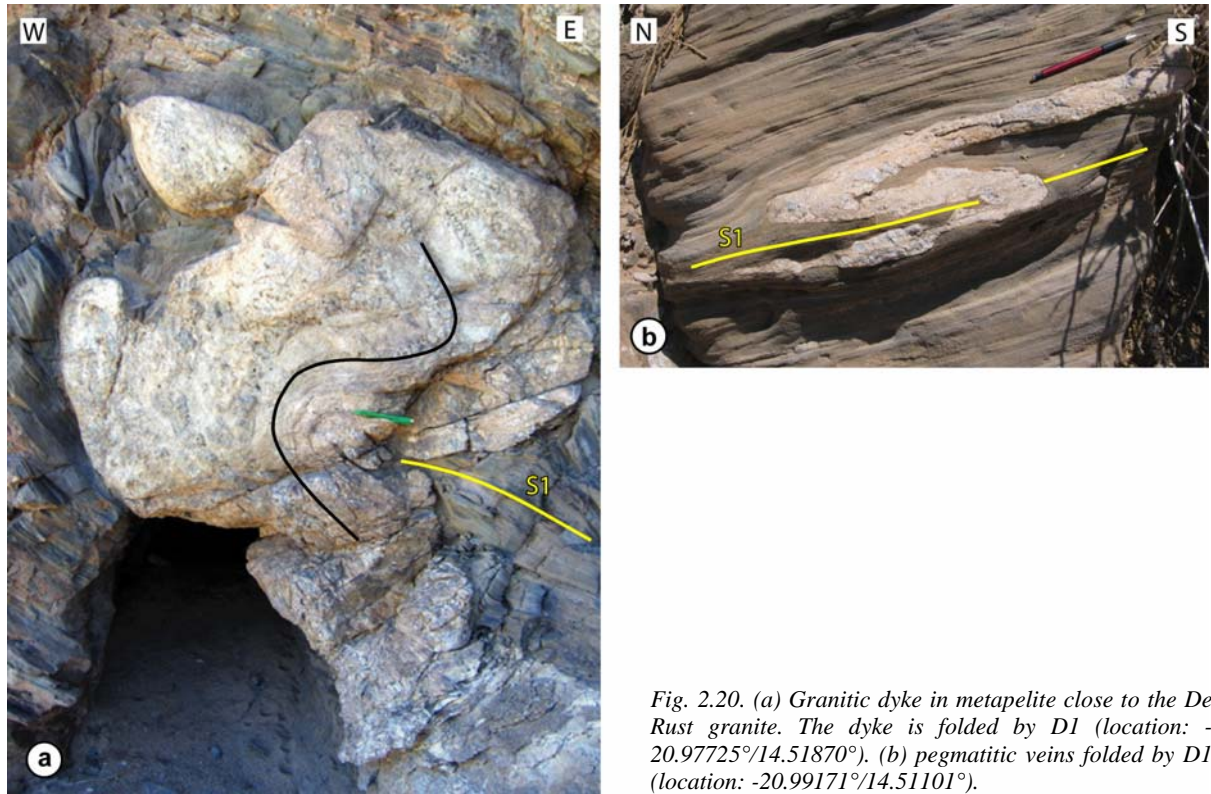


Fig. 2.20. (a) Granitic dyke in metapelite close to the De Rust granite. The dyke is folded by D1 (location: $-20.97725^{\circ}/14.51870^{\circ}$). (b) pegmatitic veins folded by D1 (location: $-20.99171^{\circ}/14.51101^{\circ}$).

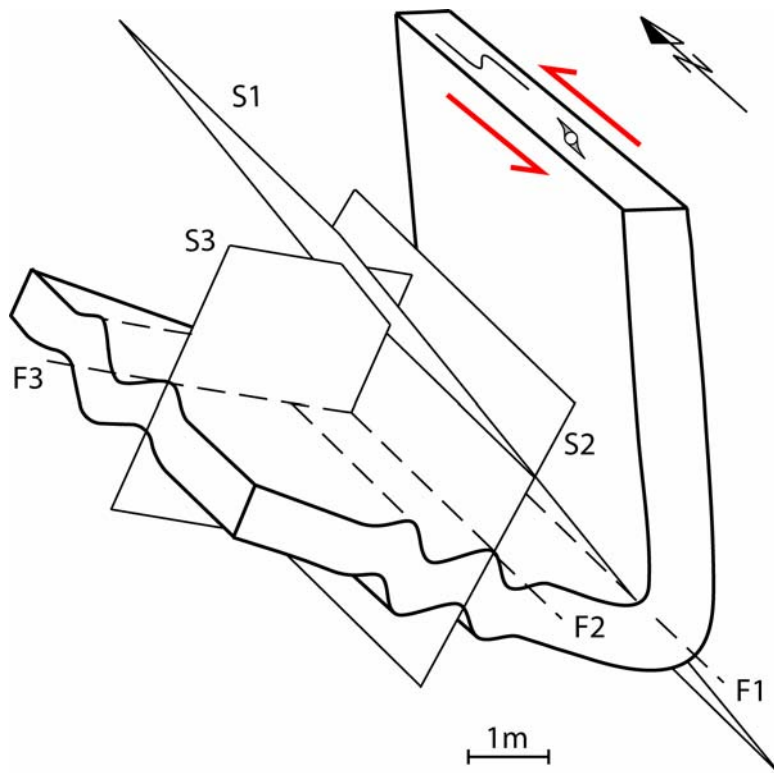


Fig. 2.21. Diagram illustrating the mean orientation of the three phases of deformation in the Lower Ugab Domain.

between the Brandberg West mine road (D2303) and the road to Uis (D2342) (outcrop location: -21.05577°/14.19982°) one granite vein cuts a D2 folds without being deformed. In the same outcrop some smaller granitic veins show sinistral displacement associated with D1-D2 deformation. There are therefore several generations of granite veins. That may be linked to two intrusive events as in the Voetspoor and the Doros granites. These observations around the Brandberg West granite indicate that it also intruded during late D1 to syn-post D2.

Dykes associated with the De Rust granite are strongly boudinaged and folded by D1 (Fig. 2.20). The granitic dykes in this area show clearly stronger deformation than those from the other syntectonic intrusions of the Lower Ugab Domain. No dating is available for the De Rust granite, but similar rock facies seems to indicate that it is associated with the same intrusive event as the other syenite intrusions of the region. The deformation may therefore be diachronous through the area. D1 may start earlier in the western part of the Lower Ugab domain than in the eastern part.

2.3 Discussion on the regional deformation

2.3.1 Significance of D1-D2

The three phases of deformation define two roughly perpendicular deformation orientations linked to two main tectonic events: D1-D2 and D3 (Fig. 2.21). The formation of boudin necks of rough east-west direction partly before the formation of D1 folds (V_A veins, Chapter 3) and the east-west oriented fibres in the striped bedding veins formed before D1 folding indicate dominant east-west northeast-southwest shortening during the early stages of the deformation. The development of the rough north-south trending D1 and D2 folds shows that an east-west component of shortening prevailed during all D1 and D2. Asymmetric folds, displaced and boudinaged veins, flanking folds along rotated boudin necks and delta and sigma clasts show that sinistral shearing occurred both in the flat and the steep limbs of the D1 folds, but preferentially in the steep limbs. The sinistral shearing component is mainly attributed to D1 since S2 cuts the asymmetric folds and the flanking folds without being affected. D1 is therefore interpreted as a transpressional phase of east-west shortening and sinistral shearing. D2 seems to have only minor sinistral shearing component and form therefore mostly a phase of east-west shortening. D1-D2 occurred at greenschist facies condition as attest crystallisation of biotite underlining S1 and S2 throughout the area.

The syntectonic syenite intrusions cut relatively open folds during late D1. This indicates that at the last stages of D1, the folds were still relatively open. The coaxial D2 east-west component of shortening tightened therefore the D1 folds to the present geometry. The west-vergence of the folds in the western and the central part of the area can also be due to D2. The origin of the west vergence is not well known. It may be due to relative westwards movement of an overlying nappe. The striped bedding veins which occur at the early stages of deformation when the layers were still unfolded indicate top to the west bedding parallel slip (Chapter 3, § 3.2.1). This indicates that the regional top to the West movement started early in D1 deformation and may have prevailed until late D2.

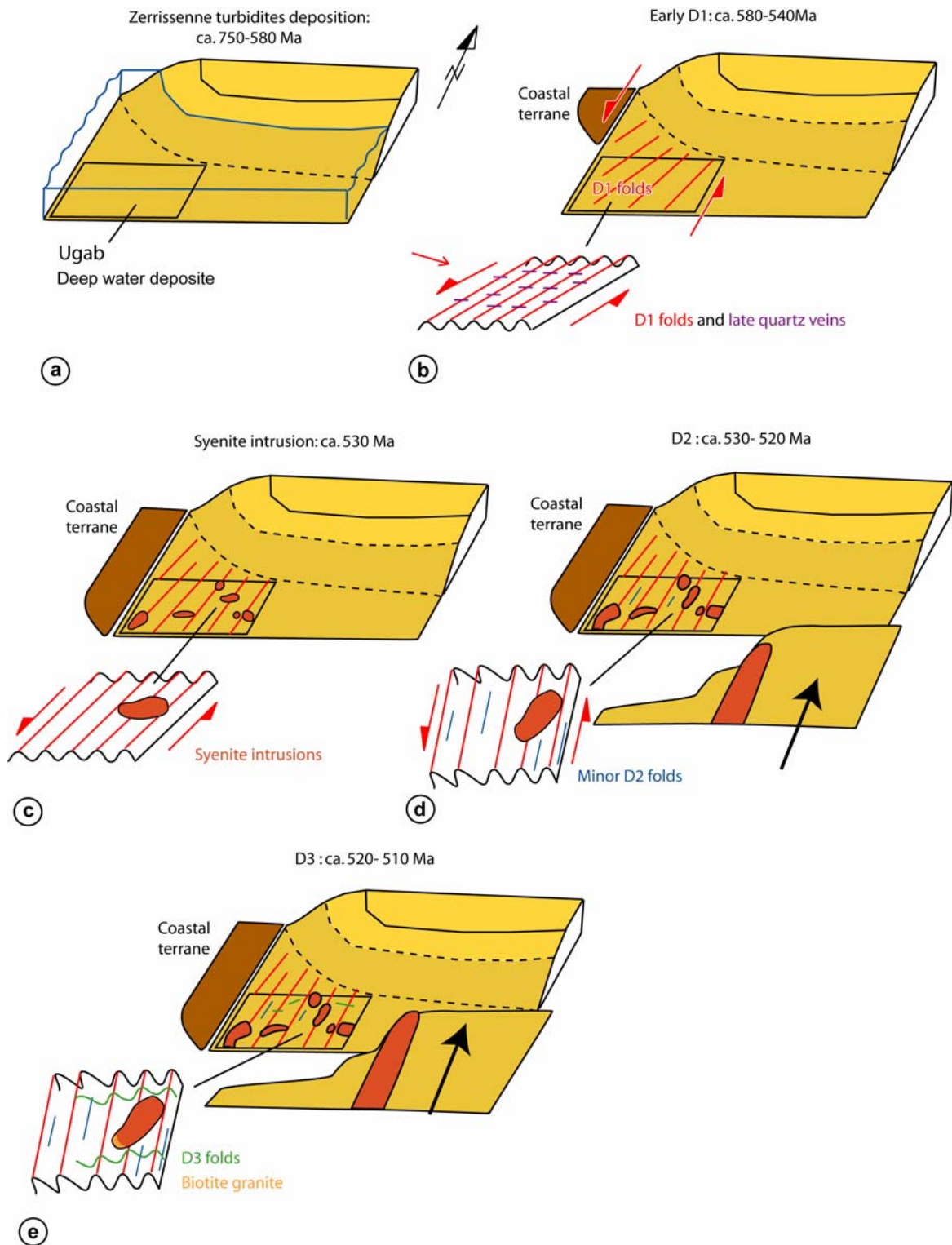


Fig. 2.22. Diagrams showing the tectonic evolution of the Ugab Zone during the formation of the Damara Orogen (a) Deposition of the Zerrissenne turbidites in deep water for the continental slope during the Neoproterozoic. (b) Formation of the D1 folds due to the oblique docking of the coastal terrane at ca. 580-540 Ma in the Ugab area. The folds trend NE-SE. Strong sinistral shearing occurs overall the area. Late quartz boudin veins form perpendicular to the folds axes due to extension parallel to the fold axes (V_A vein, Chapter 3). (c) Syenite and biotite granite intrusions during late D1-D2 at ca. 530 Ma. Progressive reorientation of D1 structure due to regional sinistral shearing (d) Rotation of the plutons and reorientation of the structures due to regional sinistral shearing and formation of the D2 minor coaxial folds at 530-520 Ma. Advance of granitic intrusion in the east of the area (e) Intrusion of the biotite granite and formation of D3 folds due to the docking of the Kalahari Craton from the south at ca. 520-510 Ma (figure adapted from Passchier, unpublished field report)

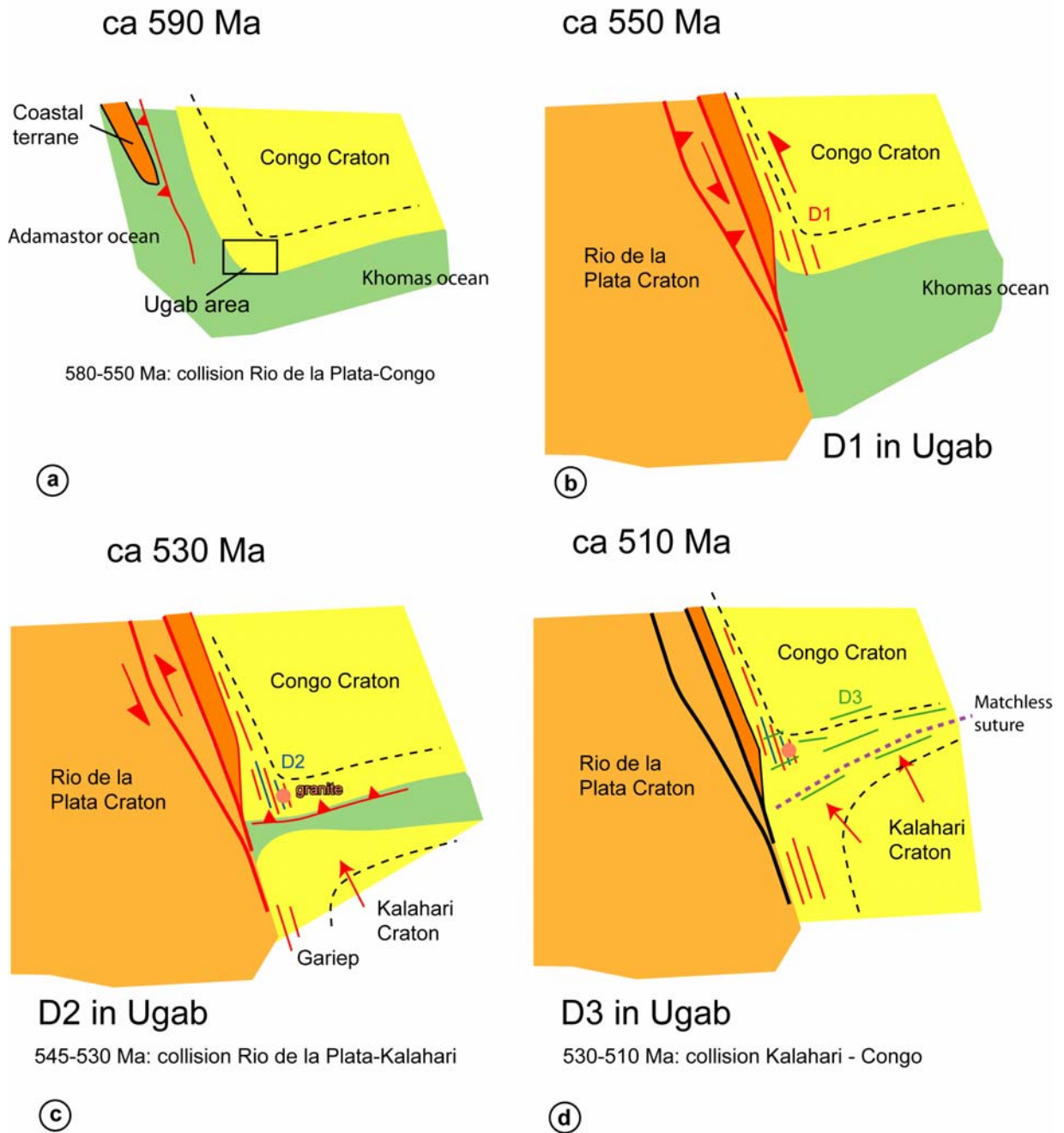


Fig. 2.23. Diagrams showing the tectonic evolution of the Damara Orogen (a) Oblique convergence of the Coastal Terrane towards the Congo and subduction of the Adamastor Ocean under the Coastal Terrane. (b) docking of the Coastal Terrane and the Rio de la Plata Craton causing the early main transpressional N-S trending deformation in the Kaoko belt and the Ugab Zone. (c) Collision between the Rio de la Plata and Kalahari Cratons and formation of the Gariep Belt. Subduction of the Khomas Ocean under the Congo Craton and formation of the syenite intrusions in the Damara belt and the Ugab Zone. Formation of D2 in the Ugab Zone. (d) Collision between the Kalahari and the Congo Cratons and formation of D3 folds in the Ugab Zone (figure adapted from Passchier, unpublished field report).

The early sinistral transpressional deformation with east–west shortening component and north-south sinistral shearing deformation is well established in the tectonic evolution of the Kaoko belt, and marks the main deformation episode from the western to the eastern zone of the Belt, although with distinct deformation style (Goscombe and al., 2003a). The deformation of the Ogden rocks mylonitic shear zone which mark the western border of the studied area, aligned with the great Puros shear Zone to the north of the Etendeka covering, shows the same subvertical sinistral transpressional deformation which predates D3. In the Ogden rocks deformation is stronger and forms at metamorphic conditions in the amphibolite facies, exceeding deformation conditions in the rest of the Ugab area. This early regional transpressional phase has been interpreted as the result of oblique convergence and collision between the Rio de la Plata craton and the Congo craton and docking of the Coastal Terranes between 580 to 530 Ma (Goscombe et al., 2003a, 2005a, 2005b; Konopásek et al., 2005; Goscombe and Gray, 2007; Gray et al. 2006, sub.). These authors suggested that the collision started from the north of the Kaoko Belt at about 580 Ma and progressively developed towards the south to reach the Gariiep belt at around 545 Ma (Gray et al., submitted). D1 in the Lower Ugab Zone probably started therefore before 545 Ma. The D1-D2 event prevailed until at least until 530 Ma which marks the late D1- early D2 syenite intrusive event in the Lower Ugab Domain (Seth et al., 2000; Passchier et al, 2007). Granitic veins from Doros pluton intruded in the Amis River Formation and folded by D2 have been dated at 533 ± 6 Ma by U-Pb shrimp analysis which give a maximum age for D2 (Passchier, unpublished report). Evolution of the deformation in the Lower Ugab Domain and the Damara Orogen are summarised in Figs. 2.22 and 2.23.

2.3.2 Significance of D1 cleavage fanning

Cleavage fanning structures in folded sediment series are described in several geological settings, for instance in the Mosel area in the Rhenohercynian Zone of the Variscan orogenic belt in central Europe (Biermann, 1987), in the Pelvoux massif in the Western Alps (Tricart et al., 1977), and the Lachlan Fold Belt in the south-east of Australia (Gray and Willman, 1991). In these studies, cleavage fanning is always associated with a thrust-related tectonic context with listric reverse faults. Divergent cleavage fanning occurs typically in the upper part of a thrust, at the top of a ramp where the thrust mass flattens again (Biermann, 1987). Cleavage fanning therefore depends on the topography of the basement under the thrust faults. No thrust faults however have been identified in the Lower Ugab Domain and therefore such a tectonic context is unlikely here. All around the Voetspoor pluton and on the south side of the Doros pluton D1 folds axes plunge subvertically, while they are subhorizontal on a regional scale (Passchier et al., 2007). The change from subhorizontal to subvertical occurs over a distance of a few hundred metres. The sense of deflection and several shear sense indicators show a relative downward motion of the plutons with respect to the wall rock. The downwards motion of the plutons have been interpreted as being the result of relative sinking of the floor of the pluton during intrusion (Passchier et al., 2007). It is therefore possible that cleavage fanning in the Lower Ugab Domain is associated with downwards displacement of the intrusions. D1 structures may have been reoriented towards the intrusion to fill the space created by the sinking pluton. At the west side of both plutons, the folds could then have progressively rotated towards an east vergence, following the movement of the pluton. Since east-west regional component of shortening prevail during D2,

a compression of the sediments around the planar intrusions occurred and could have also rotated the structures towards an east vergence at the west of the plutons. This effect can be also strengthened by the sinking of the pluton at the same time.

2.3.3 Significance of D3

D3 is entirely distinct from D1-D2 deformation in orientation and kinematics. The folds axes are east-northeast- west-southwest oriented, attesting a north-northwest –south-southeast compression component direction. A small component of sinistral shearing may prevail during D3, mainly in the north-eastern part near the Doros and the Voetspoor intrusions, but remain local and relatively weak. The metamorphic conditions are lower than during D1-D2 in the subgreenschist facies. The late north-south shortening is well established in the Kaoko and Damara branches (“shortening phase”, Goscombe et al., 2003a), and is associated with the north-south convergence between the Congo and Kalahari Cratons (Coward, 1981, 1983; Miller, 1983). The north-south shortening is minor in the rest of the Kaoko belt but forms the main deformation direction in the Inland branch of the Damara orogen (Coward, 1981, 1983; Miller, 1983).

The age of D3 in the Lower Ugab Domain is given by the pre-syn-D3 biotite granite of the Doros intrusion estimated at 530 ± 5 Ma by U-Pd Shrimp analysis (Passchier, unpublished report). This coincides with the estimations of the peak of deformation and metamorphism of the Damara belt (s.s.) collisional event in the southern zone of the Kaoko Belt between 530-505 Ma (M3, Goscombe et al. 2005b).

Chapter 3

Syntectonic veins in the metaturbidites of the Lower Ugab Domain

3.1 Introduction

Folding of metasediments usually induces abundant syntectonic fractures and veins (Bergbauer and Pollard, 2004; Guiton et al., 2003; Bellahsen et al., 2006). The metaturbidites of the Lower Ugab Domain are particularly rich in composite quartz and calcite veins, which show a complex but systematic deformation pattern over the area. These syntectonic veins are important markers of regional deformation since they carry information on polyphase structural evolution, shear sense and the fluid composition during deformation. A detailed structural study on the veins in the Lower Ugab domain contributes new data to the understanding of the regional evolution at the junction of the Kaoko and Damara mobile belts.

Three main types of syntectonic veins, labelled V_{bed} , V_A and V_B , are recognised in the metaturbidites of the Lower Ugab Domain. V_{bed} veins are 1-5 cm thick internally laminated quartz veins that lie parallel to bedding. V_A veins are 1cm -1m thick quartz-calcite veins of roughly E-W trend approximately orthogonal or at a high angle to the D1 fold axes. V_B veins are 5mm-30 cm thick quartz-calcite veins at a small angle to S1 and approximately perpendicular to V_A veins.

3.2 Syntectonic veins

3.2.1 V_{bed} veins parallel to the bedding.

Throughout the siliciclastic metasediments of the Lower Ugab Domain, laminated veins occur parallel to bedding (V_{bed} veins). Their thickness is generally between 1 and 5cm and in extreme cases up to 10cm. These veins consist of partially recrystallized elongate quartz and calcite crystals at a small angle to the vein edges and to bedding (Fig. 3.1). They are typical “striped bedding veins” of Koehn and Passchier (2000) and are interpreted to be a result of bedding parallel slip. V_{bed} veins are strongly deformed by the D1 phase of deformation and they are therefore interpreted to form earlier, representing the first recorded event of deformation in the rocks. V_{bed} veins are preferentially found in the steep limb of asymmetric D1 folds. The reason is probably that the flattening in the flat limb during D1 and D2 usually destroyed the structure.

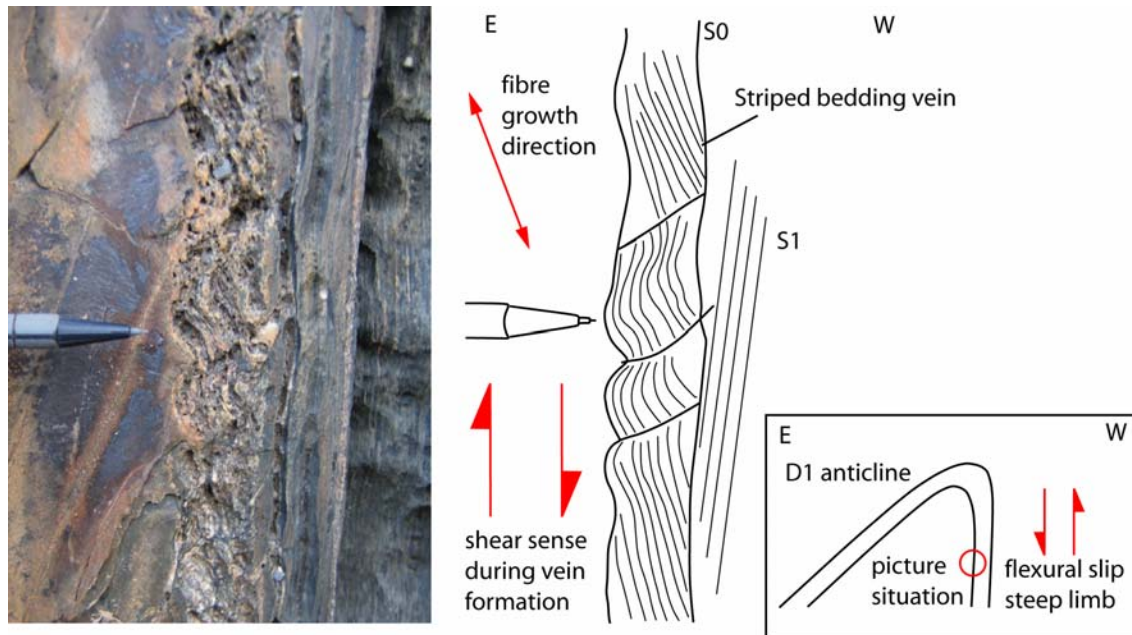


Fig. 3.1. Striped bedding vein in sandstone (location: $-20.97640^{\circ}/14.09268^{\circ}$). Quartz fibres grow slightly oblique to the vein edge indicating the shearing sense during the formation of the veins. This shear sense is opposite to flexural slip in the steep limb of D1 folds.

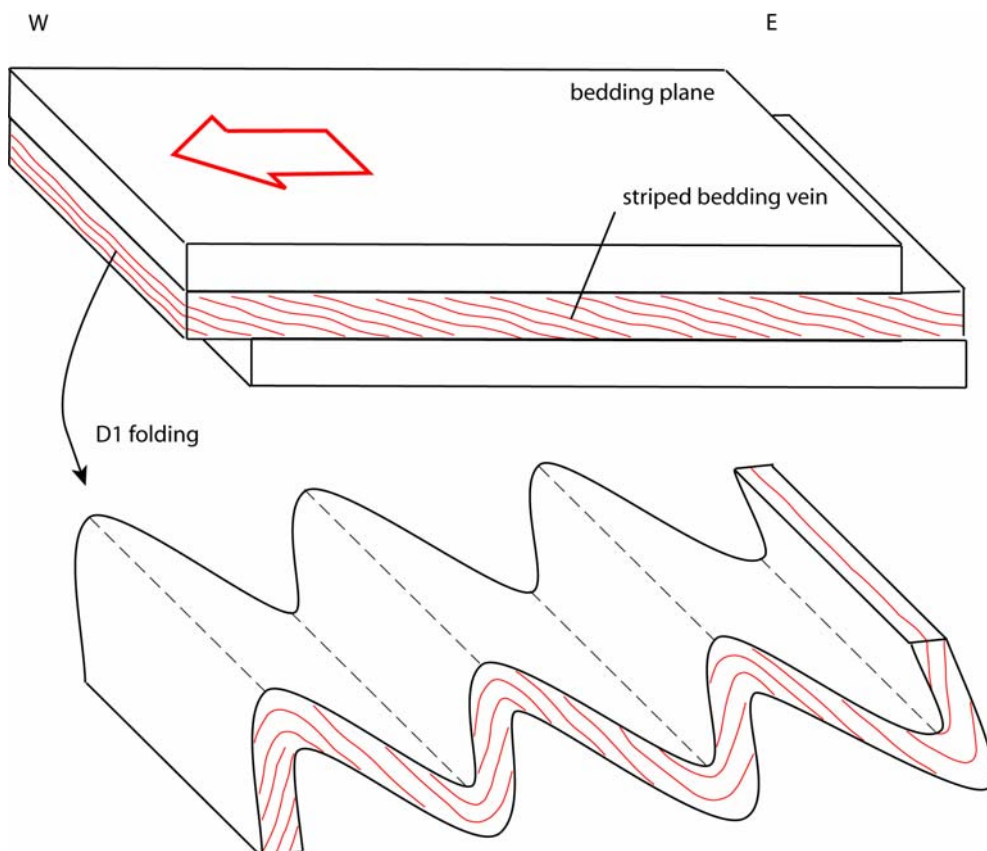


Fig. 3.2. The striped bedding veins are folded by D1. By unfolding the beds, the fibres indicate an initial top to the west sense of shear in the Lower Ugab region.

Vergence of crystal orientation in the veins with respect to bedding, i.e. the relative quartz crystal orientation, does not change from the long limb to the short limb of D1 folds (Fig. 3.2). In flexural slip, one would expect the vergence to be opposite in opposite limbs (Jessell et al., 1994). In the short limb, however, the internal structure gives a shear sense opposite to what can be expected from flexural slip (Fig. 3.1). If bedding is back-rotated to horizontal, the orientation of the elongate quartz crystals in the vein structure indicates top to the west movement (Fig. 3.2; Koehn and Passchier, 2000). Shear fracture boudinage in the veins is frequent, indicating the same sense of shearing as the elongate crystals (Fig. 3.1). Chlorite locally crystallizes in the boudin necks.

3.2.2 V_A veins at a high angle to D1 fold axes

In all formations of the Zerrissene turbidite system of the Lower Ugab Domain, composite lensoid quartz and carbonate veins (V_A veins) occur at a high angle to the bedding and roughly perpendicular to D1 fold axes (Fig.3.3). Examples of V_A veins in the pelite and in the marble are given in Figs. 3.4 and 3.5. Both in the pelite and in the marble, they are generally restricted to one layer and show a regular spacing within the layer, which is characteristic for boudinage structure with the veins forming the boudin necks. V_A veins can be followed in some of the marble and pelitic layers over several tens of metres (Fig. 3.4i) and occasionally develop domino-type boudinage corresponding to the regional sinistral shear sense (Fig 3.3; Goscombe and Passchier, 2003). In some localities, particularly in marble layers, V_A veins developed only at the top or at the bottom of the layers (Figs. 3.4g, h, i; 3.6). The explanation for the localisation of the veins at the limit of the beds is that fractures in a boudinage context preferentially initiate from the bedding interface, where the stress concentrates (Bai and Pollard, 2000b). In the graded beds, the veins developed preferentially in the coarse-grained part which is more competent than the fine-grained part. The coarse-grained part is generally at the bottom of the bed in turbidites. The veins show often a triangle shape at the limit of the layer as tapered veins which are typical of graded beds (Price and Cosgrove, 1990, Fig. 3.6c). They are larger in the coarse grained part of the bed and become progressively thinner in the finer part of the bed.

In several places V_A veins grade into arrays of tension gashes indicating that a shear component can be present during their formation (Fig. 3.7). Two conjugated sets of tension gashes can be found, their disposition attests a subvertical main stress direction during the formation of the veins when the layers were unfolded.

In the carbonates sequences, V_A veins occur preferentially in marble layers rather than in interbedded pelitic layers, while in the siliciclastic formations, they occur always in the more pelitic layers.

Generally the fracture spacing in sedimentary rocks is roughly proportional to the thickness of the fractured layer (Narr and Suppe, 1991; Wu and Pollard, 1995; Ji and Saruwatari, 1998; Bai and Pollard, 2000a). This is not always the case in the Lower Ugab Valley, where in the same outcrop we can find different spacing in layers with similar thickness. V_A Veins in relatively thick layers can have a narrower spacing than in thin layers in the same localities, for example in the pelitic layers in the Rhino Wash (Fig. 3.8)

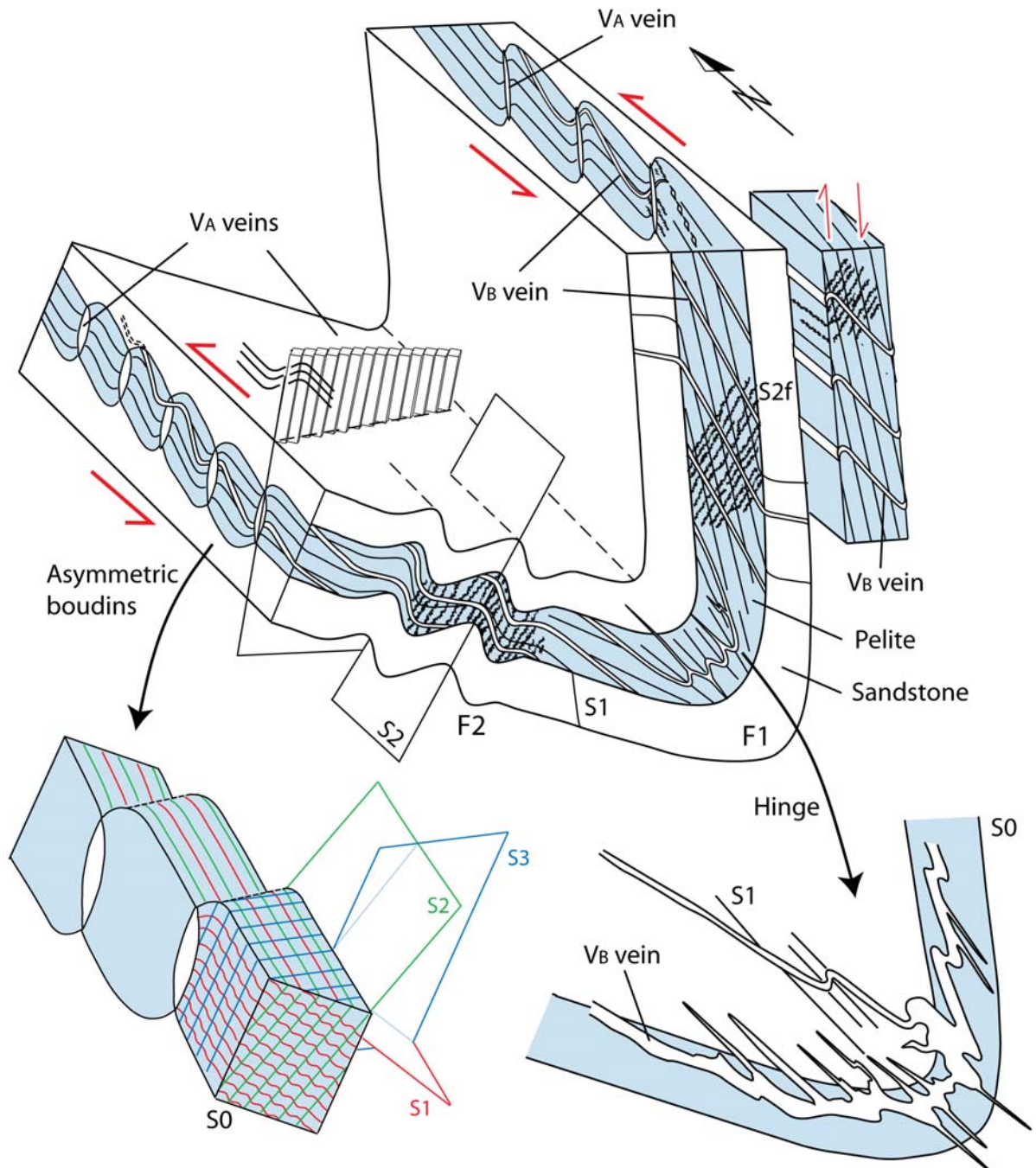


Fig. 3.3. Block diagram schematically illustrating a D1 folds in the siliciclastic formations of the Lower Ugab Domain. Two main types of syntectonic veins formed in the more pelitic beds, V_A and V_B veins. V_A veins formed roughly orthogonal to D1 fold axes. They are strongly sheared by a sinistral shearing in both limbs, which produces flanking folds alongside the veins and a characteristic asymmetric shape of the boudins. Note the formation of domino boudins in the veins in the flat limbs and the development of flanking folds due to rotation of the veins. Flanking folds developed along the V_A veins due to their rotation. V_B veins developed at a small angle to S1 and are slightly oblique to the D1 fold axis. Their orientation is similar in both limbs. Hook shaped folds locally formed at the tip of V_B veins at the boundary with adjacent sandstones layers in the steep limb. This is shown in the inset to the right of the fold. V_B veins and S1 are strongly refracted in the sandstones. V_B veins are folded in the hinge of D1 folds and new veins developed subparallel to the fold axial surface.

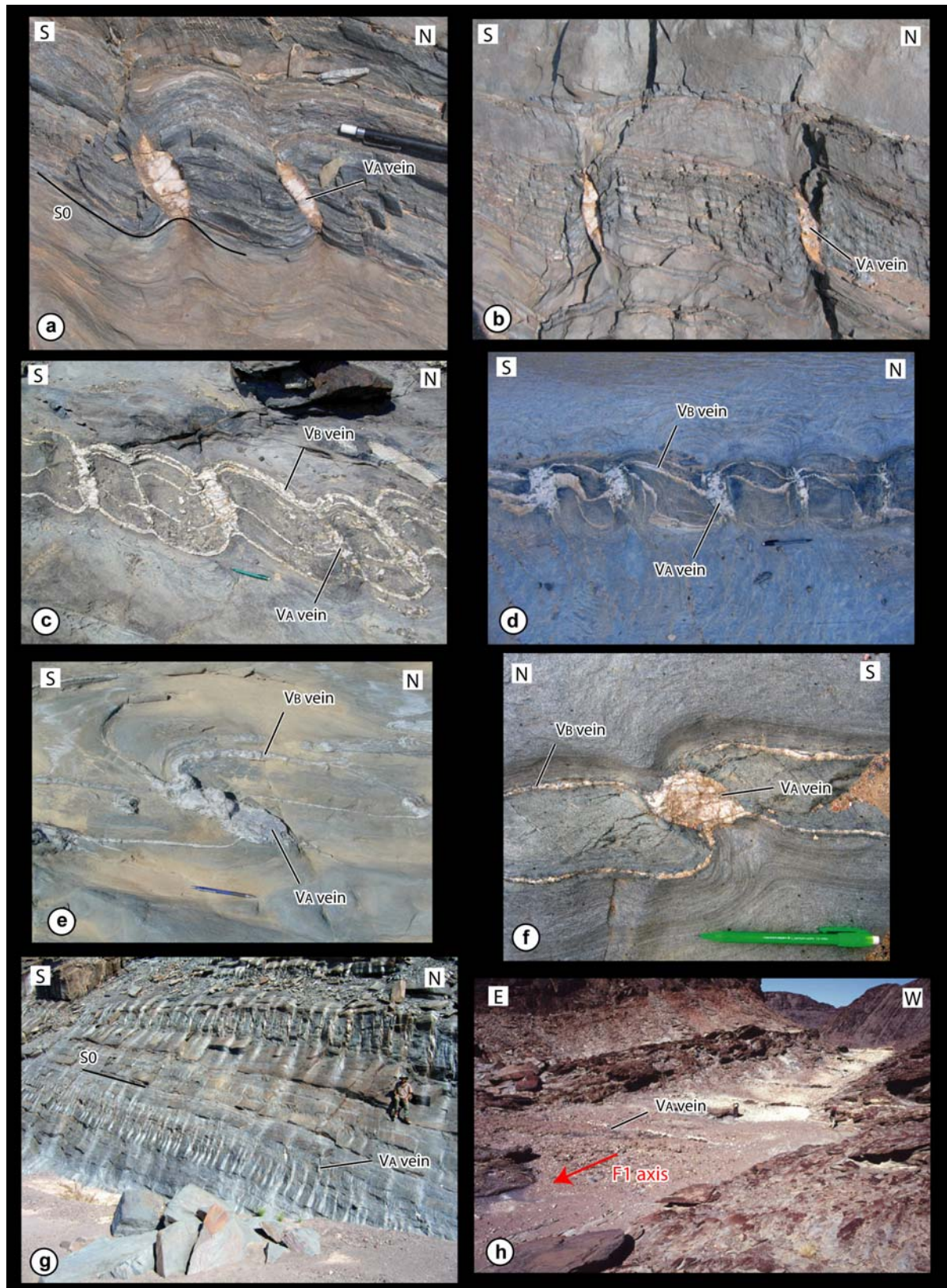


Fig. 3.4. Examples of V_A veins in pelite. Locations: (a) and (b) $-20.85563^\circ/14.08447^\circ$ (c) $-21.07974^\circ/13.81535^\circ$ (d) $-21.07346^\circ/13.81854^\circ$ (e) $-21.08946^\circ/13.80249^\circ$ (f) $-21.07094^\circ/13.80933^\circ$ (g) $-20.85563^\circ/14.08447^\circ$ (h) $-20.91687^\circ/14.054818^\circ$.

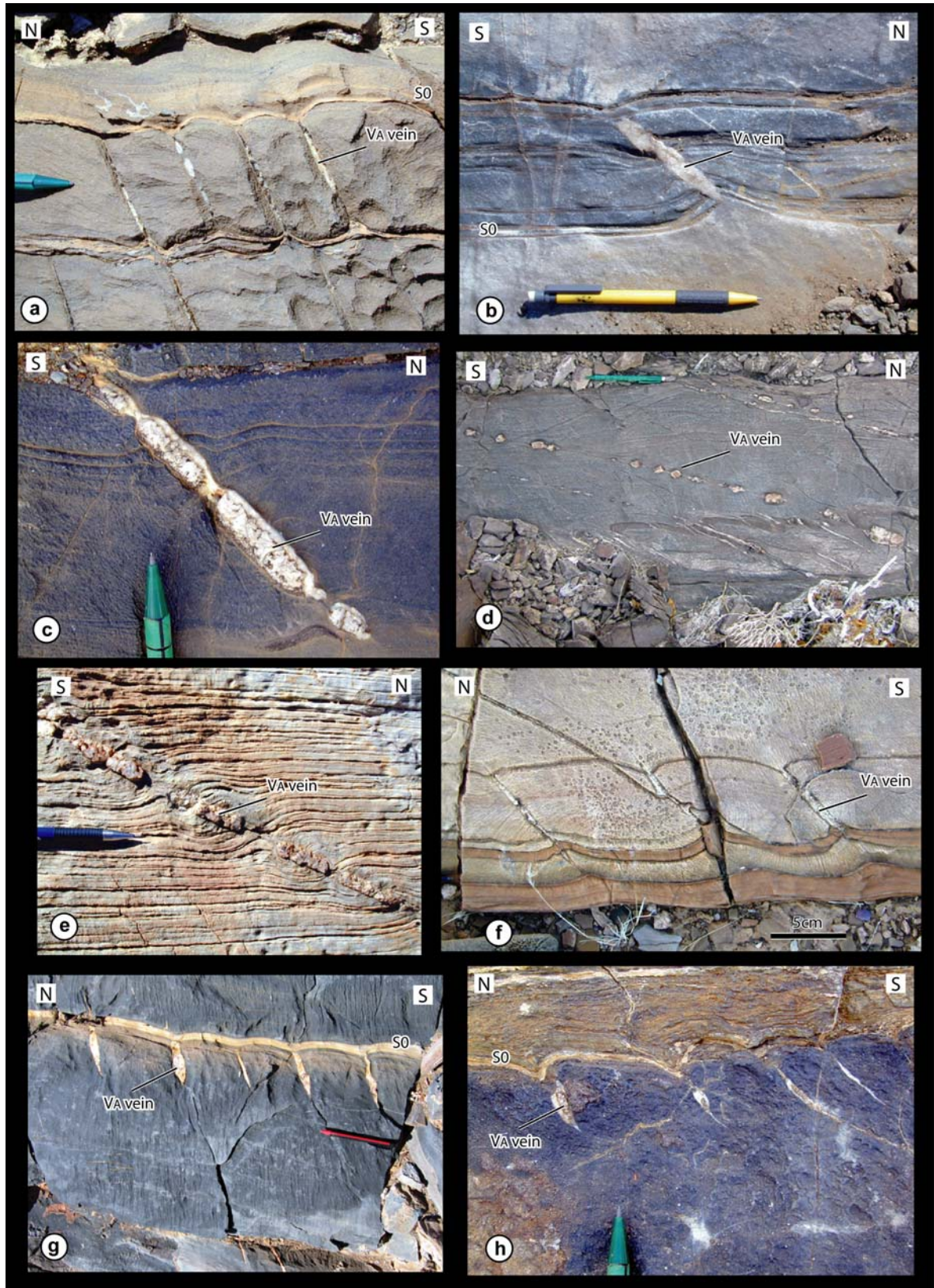


Fig. 3.5. Examples of V_A veins in marble. Locations: (a) $-20.87275^\circ/14.02060^\circ$ (b) $-20.90787^\circ/14.30331^\circ$ (c) $-20.91654^\circ/14.04847^\circ$ (d) $-20.78958^\circ/14.301187^\circ$ (e) $-21.02719^\circ/14.1675^\circ$ (f) $-20.88888^\circ/14.14615^\circ$ (g) $-20.84035^\circ/14.13567^\circ$ (h) $-20.91654^\circ/14.04847^\circ$.

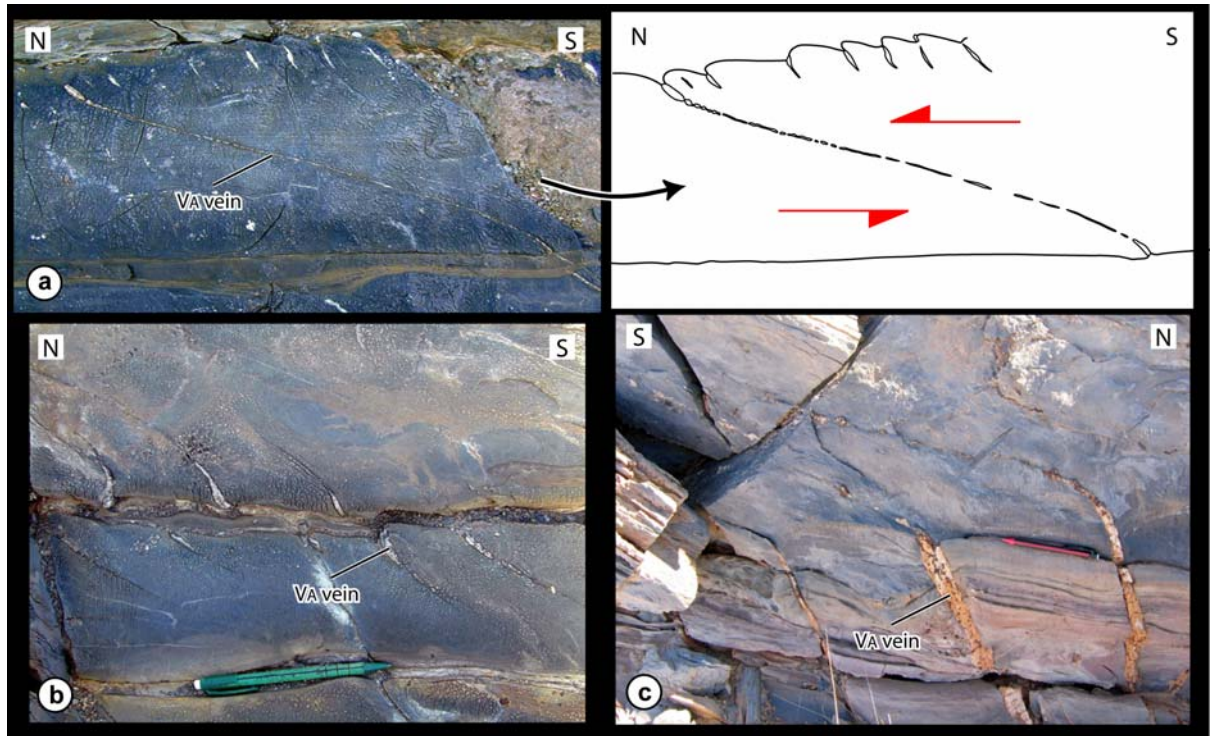


Fig. 3.6. V_A veins developing at the top or the bottom of marble layers. (a), (b) picture and drawing of a series of veinlets at the top of a marble layer. One vein crosses the entire layer and show progressive increase of deformation towards the centre of the bed due to grading in the turbidites (location: $-20.91654^{\circ}/14.04847^{\circ}$) (c) Veins formed at the top and the bottom of marble layers. They show a triangle shape at the contact with the bedding and progressive increase of shearing towards the centre of the layers (location: $-20.91654^{\circ}/14.04847^{\circ}$) (d) Strong refraction of V_A veins in the marble layer due to grading in the bed and the preferential concentration of the deformation in the finest part of the layers (location: $-20.84024^{\circ}/14.13434^{\circ}$).

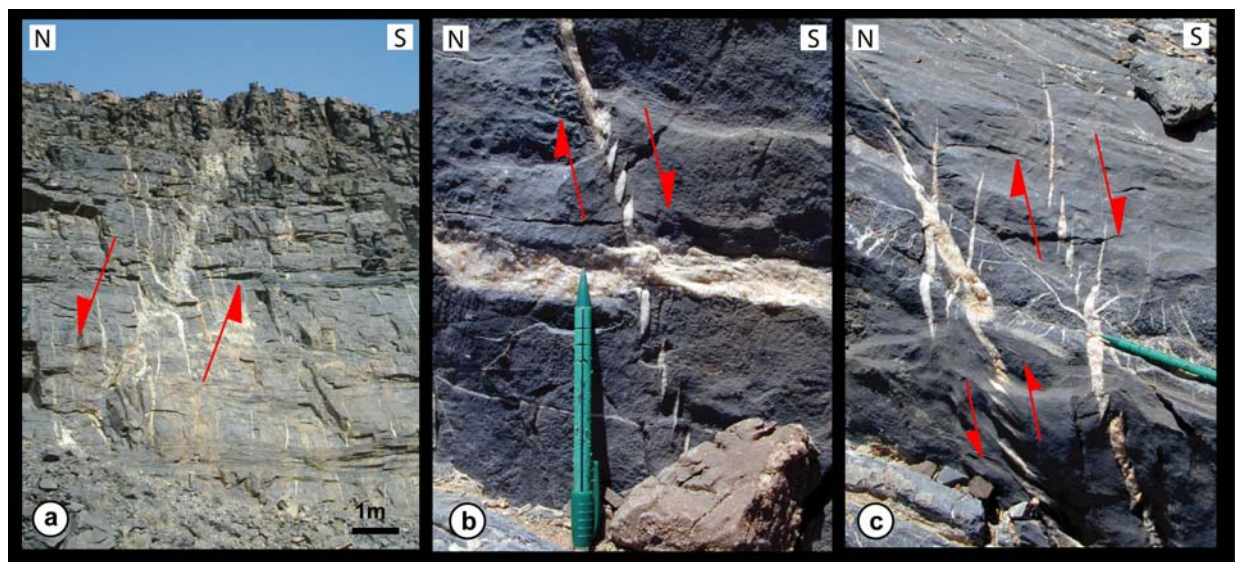


Fig. 3.7. Examples of V_A veins forming along shear fractures Locations: (a) $-21.01163^{\circ}/13.93915^{\circ}$ (b), (c) $-20.8561^{\circ}/14.36188^{\circ}$.

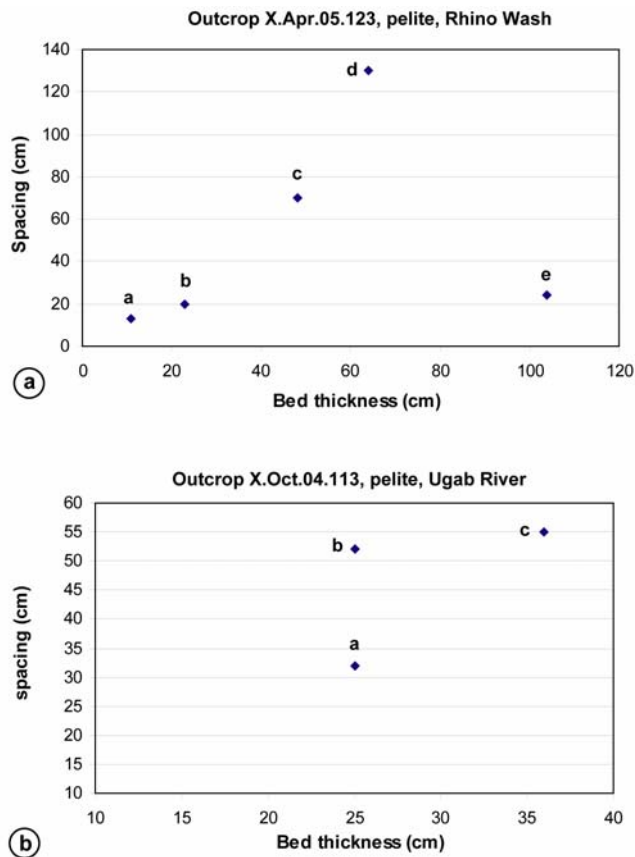


Fig. 3.8. Boudin neck spacing vs. bed thickness graphs. The boudin neck spacing is regular within each layer. The spacing values in the graphs are average values for each layer. The different boudinaged layers in each outcrop present the same lithology and therefore a similar rheology. (a) outcrop in Brak River Formation in the Rhino Wash (location: $-21.05577^{\circ}/14.19982^{\circ}$). The spacing increases with the bed thickness except for the largest layer (point e) who shows a relative small spacing (b) outcrop in Amis River Formation (location: $-21.07974^{\circ}/13.81535^{\circ}$). Two layers of similar thickness show two different spacing of the boudin necks (points a and b). The thicker layer (point c) show a similar spacing than the layer of the point b.

3.2.2.1 Texture and composition:

V_A veins are quartz and calcite composite veins. The modal composition of the veins in the marble is generally dominated by calcite, while the veins in the pelite are largely dominated by quartz. In the marble layers, the two component minerals are zonally arranged, so that the quartz forms the central zone and the calcite the two marginal zones of the vein (Fig. 3.9). Such a structure is common for composite veins, where generally the mineral forming the marginal zones is the same as that predominant in the host rock. The grains are crystallographically continuous with crystals in the vein walls (Ramsay and Huber, 1983). In contrast, the mineral forming the central part of the vein is either of minor volumetric importance in the host rock or only found in rock types outside the immediate environment of the composite vein. The marbles of the Lower Ugab domain generally contain a small modal percentage of quartz (generally around 1-2%) which can be the source of the quartz in the central zone of the veins. Another possible source is proximal sandstone beds. Composite quartz-calcite veins in the Leytron deformed marble, in the Morcles nappes of the helvetic Alps in Switzerland show the same zonation, with quartz forming the central zone and calcite the two marginal zones (Ramsey and Huber, 1983, Fig. 3.10). In the Leytron veins the central zone shows fibrous fabric of antitaxial fibres with a median line of included rock fragments and the marginal zone shows a syntaxial vein fibre fabric. No fibre fabric is present in V_A veins in the marble of the Ugab Valley,

but a centrally disposed median line composed of wall fragments and small calcite grains is developed in the zone of quartz. This suggests antitaxial growth of the quartz in the central zone, as the Leytron veins.

In the pelitic beds, V_A veins show less clear component zonation. Calcite is found as isolated blocky grains or zones in the quartz matrix (Fig. 3.11). It tends also to concentrate in the border of the veins. The veins in the pelites frequently contain chlorite, usually in a fan shape fabric, concentrated in centimetric zones in the large veins. In some rare cases V_A veins are composed of only chlorite. Albite is frequent in the veins as automorphic grains. Siderite can also be found. It occurs as idiomorphic millimetric to centimetric grains and can form pluricentimetric zones in meter scale veins. V_A veins show mostly blocky or elongate blocky texture. Only in rare cases, fibrous quartz, calcite and chlorite can be found (Fig. 3.12). The fibres or the elongated grains are always perpendicular to the border of the vein. A laminated texture parallel to the vein edge can be observed in some places. It shows crack seal filling indicating that the vein formed by successive opening events.

3.2.2.2 Deformation:

V_A veins are strongly deformed by all deformation phases. They lie oblique to bedding with variable orientations. Those with smallest angle between bedding and vein are most deformed and boudinaged. They also developed flanking folds along their sides (Passchier, 2001; Grasemann and Stüwe, 2001; Grasemann et al., 2003). Veins normal to the bedding are undeformed and lack flanking folds. When the tip of the veins penetrate the surrounding psammite layers, the veins developed a slight s-shape which indicates less rotations in the psammite layer than in the pelite host layer (Fig. 3.11). These observations indicate that the gradient in geometry of the veins and bedding can be interpreted as an effect of relative rotation of the veins and bedding. The veins would stretch in response to relative rotation with the bedding causing the boudinage of the veins. There are therefore two generations of boudinage in the area: first of the bedding to create the veins and then of the veins themselves. V_A veins boudins have a variable geometry, depending on the rheological contrast between the vein and the layers and the strain intensity (Brunt, 2003). Pinch-and-swell structure is the most common feature (Fig. 3.5c). The boudins show frequently rectangular or lensoid equidimensional shape, especially in marble layers where the competency contrast between the quartz veins and the surrounding rock is high (Fig. 3.5d, e; Brunt, 2003). Shear fracture and domino type boudins (Goscombe and Passchier, 2003) can be also observed in some pelitic layers. The reorientation of the veins and their boudinage can be very strong in some localities (Fig. 3.5d). Both quartz and calcite can precipitate in the boudins neck, but calcite seems to be more common.

The bedding surface close to the tips of V_A veins is deflected into asymmetric flanking folds (Passchier, 2001; Grasemann and Stüwe, 2001; Grasemann et al., 2003). This gives a characteristic asymmetric boudin shape to bedding aside the veins (Fig. 3.3; 3.4; 3.5). This structure has been modelled by finite element technique and the results are presented in the Chapter 4 of this thesis. At first sight, asymmetry of boudins associated with V_A veins seems to be due to D3, since D3 is axial planar to folds boudin. However S2 cut the flanking folds without being deformed (Fig. 3.13), indicating that they formed pre-D2. Asymmetric folds, sigma and delta clasts attest a strong component of regional north-south sinistral shearing during the

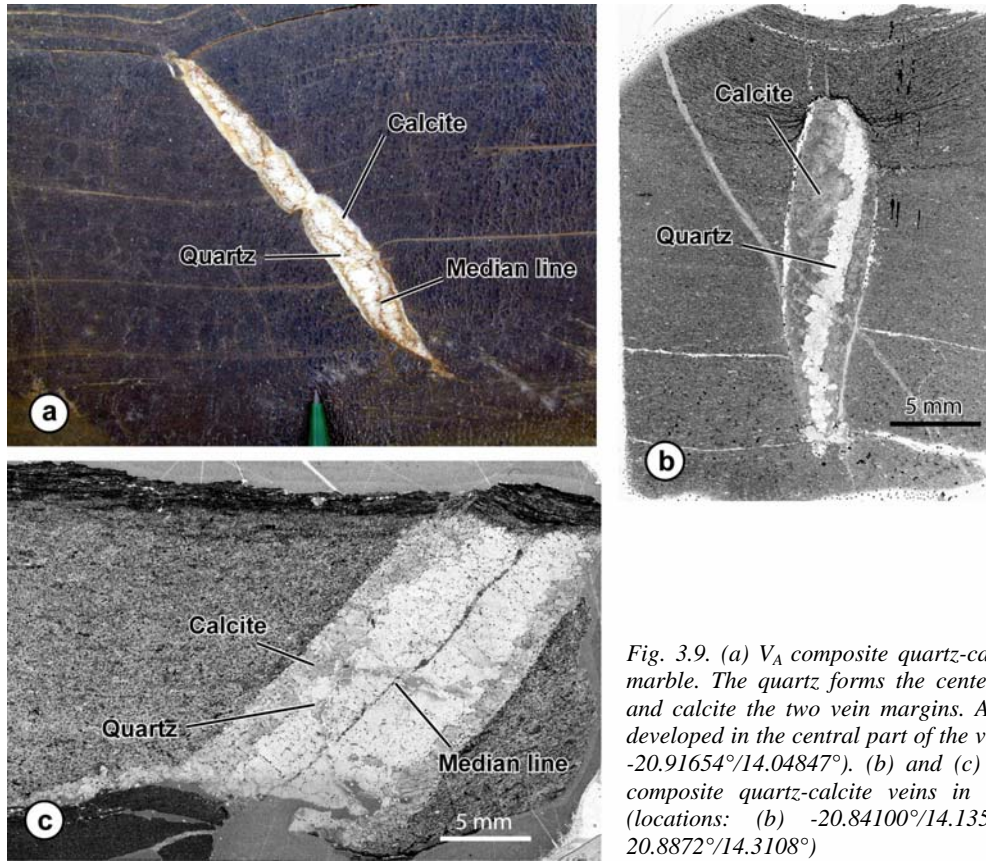


Fig. 3.9. (a) V_A composite quartz-calcite veins in marble. The quartz forms the center of the vein and calcite the two vein margins. A median line developed in the central part of the vein (location: $-20.91654^\circ/14.04847^\circ$). (b) and (c) Examples of composite quartz-calcite veins in thin sections (locations: (b) $-20.84100^\circ/14.13514^\circ$, (c) $-20.8872^\circ/14.3108^\circ$)

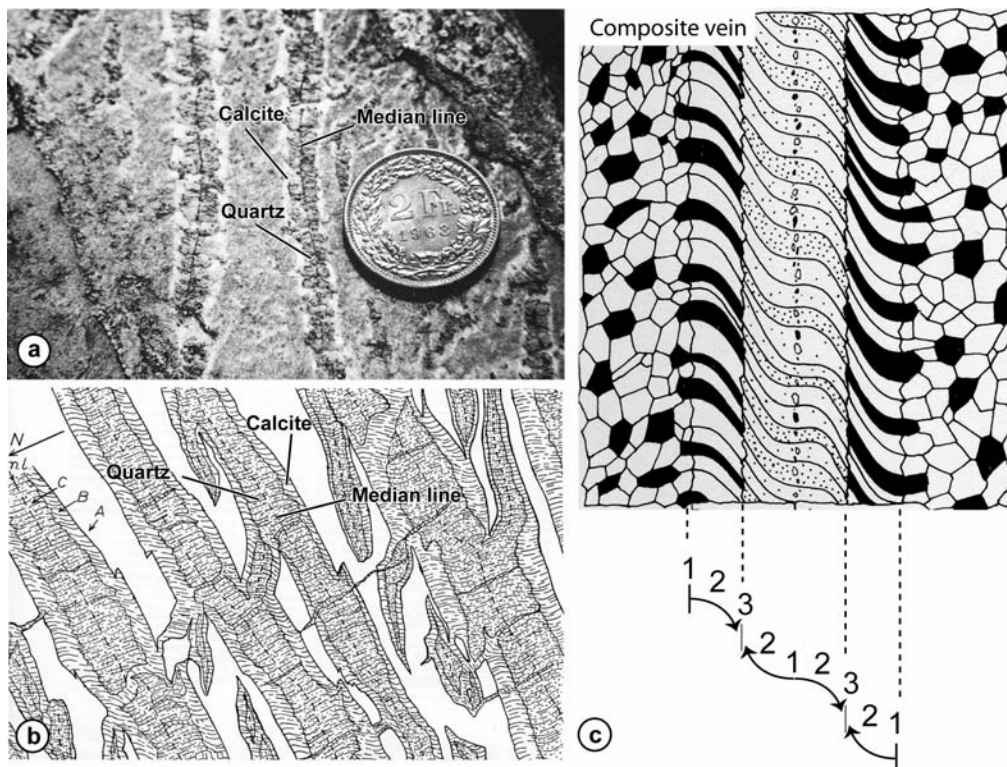


Fig. 3.10. (a) and (b) picture and drawing of composite quartz-calcite veins in the Leytron marble, in the Morcles nappes of the helvetic Alps in Switzerland (from Ramsay and Huber, 1983, Fig. 13.9 p. 241, Fig. 13.19 p.247). The veins show the same zonation as the composite veins in the Ugab Valley, with the quartz in the centre and the calcite in the rim. (b) Drawing of a composite vein, the centre zone form by antitaxial growth and the two border zones by syntaxial growth (from Ramsay and Huber, 1983, Fig. 13.25 p.252).

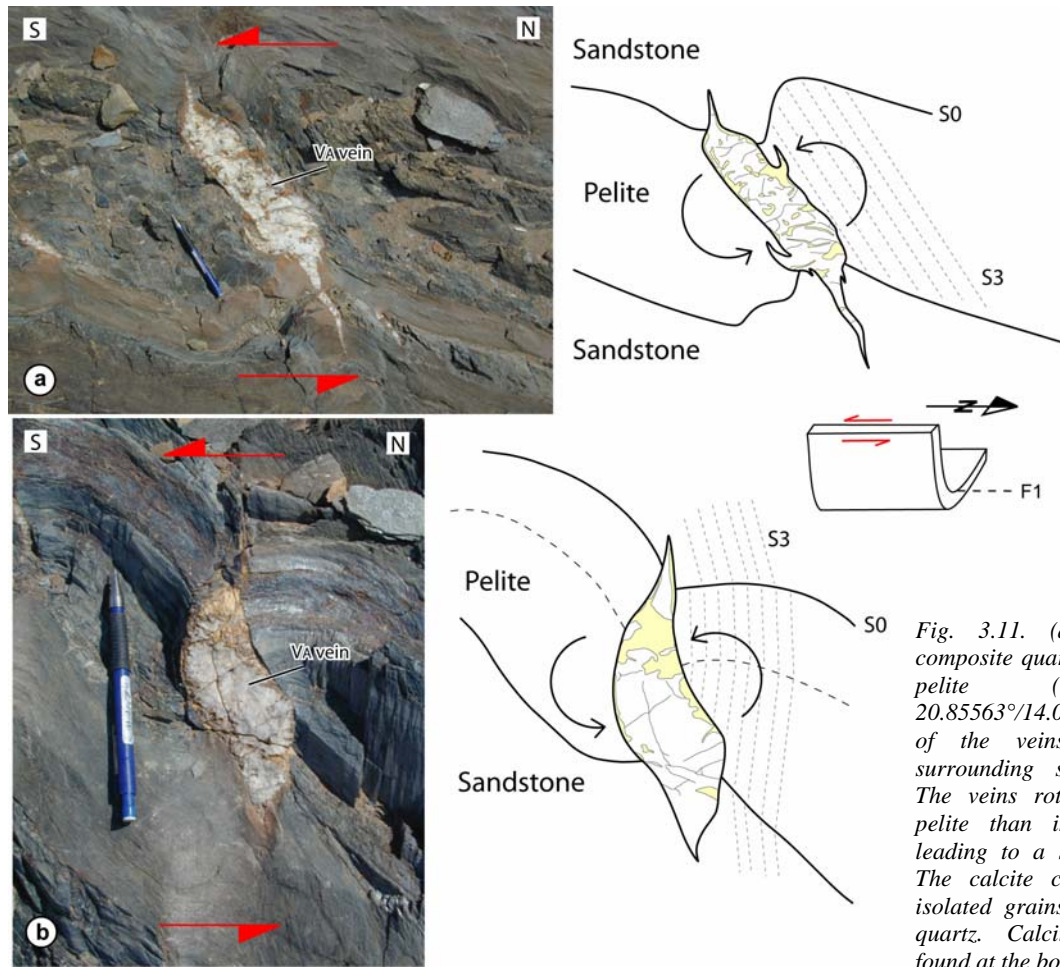


Fig. 3.11. (a) and (b) V_A composite quartz-calcite veins in pelite (location: $-20.85563^\circ/14.08447^\circ$). The tips of the veins penetrate the surrounding sandstone layers. The veins rotate more in the pelite than in the sandstone leading to a slight "s" shape. The calcite can be found as isolated grains or zones in the quartz. Calcite is frequently found at the border of veins.

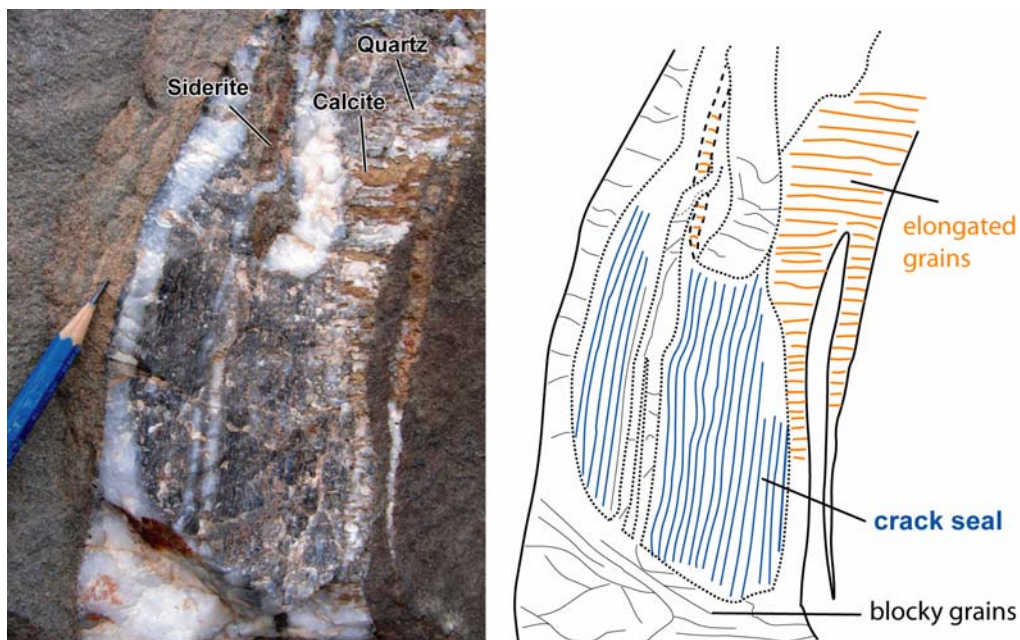


Fig. 3.12. V_A veins in pelite. Elongated grain texture marks the border of the vein, with an intercalation of calcite and quartz grains. The elongation of the grains indicates an opening perpendicular to the vein border. Laminated texture in the centre of the vein shows crack seal vein filling with several successive opening episodes. The blocky grain part of the vein cut the crack seal and elongated grained part of the vein showing that it forms later. (location: $-20.92358^\circ/14.050152^\circ$).

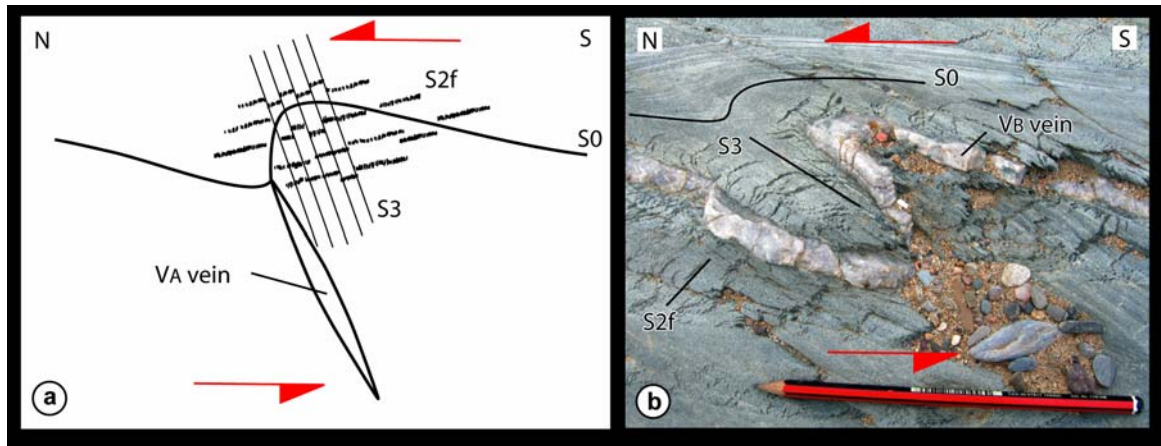
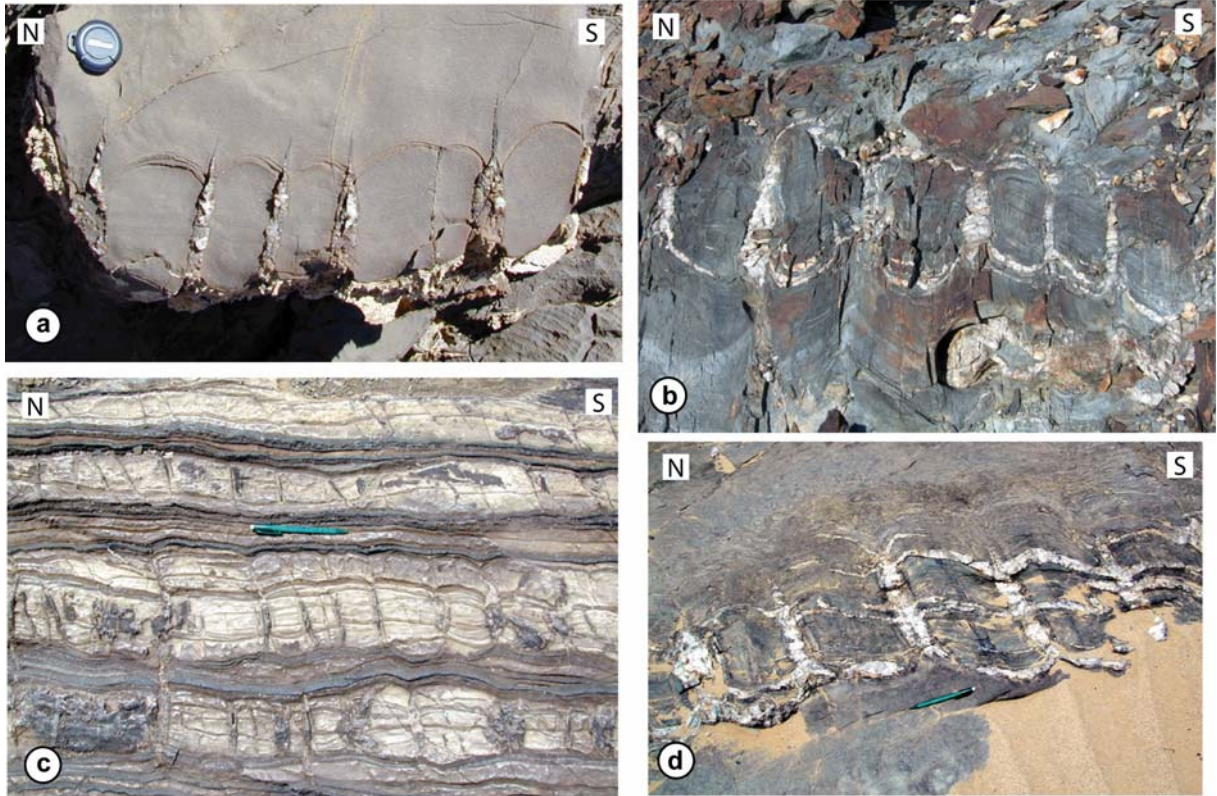


Fig. 3.13. (a) and (b) Drawing of an asymmetric buckling of bedding at the tip of V_A veins. S_3 is axial planar to the buckling folds. S_{2f} is not affected by and postdates the asymmetric folding, but it is overprinted by S_3 (b) asymmetric fold marked by the bedding and a V_A vein at the tip of V_A veins (sand covered in the photograph). S_{2f} cut the fold without being affected (location: $-21.083353^\circ/13.8084016^\circ$).

east-west shortening which marks the first phase of regional deformation D1 (Chapter 2). The asymmetric flanking folds marked by the bedding interface at the tip of the boudin veins are therefore interpreted to form due to the rotation of the veins with respect to bedding during D1 non-coaxial flow. The shape of the boudin is also influenced by D3 north-south shortening, which strengthened the buckling of S_0 by compression parallel to the layer. In outcrops S_3 is generally axial planar to the buckle folds and slightly oblique to the veins (Fig. 3.10; 3.12). Compression is marked in some localities by chocolate boudinage of V_A veins with both extensions parallel and perpendicular to the bed surface (Fig. 3.14). In less sheared areas where V_A veins are orthogonal to bedding, boudins present a shape of shortened boudins as described by Passchier (1991) and Goscombe et al. (2004a) with an extreme convex shape of the bedding between the boudin necks (Fig. 3.15). Such structures have been also observed in the high Ardennes in Belgium and named “Mullion boudin structures” (Urai et al., 2001; Kenis et al., 2000; 2002; 2004; 2005) or “narrow reworked boudin” (Vanbrabant and Dejonghe, 2006). The shortened boudins in the high-Ardennes Slate Belt in Belgium are interpreted to form by a first stage of extension parallel to the layers and formation of boudins, followed by a second stage of compression parallel to the layers causing the buckling of S_0 between the boudin necks (Vanbrabant and Dejonghe, 2006). Sintubin et al. (2000) and Kenis et al. (2002) argue that the vein in the Ardennes have form by hydraulic fracturing in an already compressional setting rather than layer-parallel extension by the process of boudinage. The asymmetric boudins in the Lower Ugab Domain are also polyphase structures. The boudins necks form pre-to early D1, since they are deformed and reoriented by D1. Their east-west orientation perpendicular to D1 fold axes fit with north-south extension parallel to the bedding and boudinage of the layers which occur during the first stages of the deformation. The boudins are then deformed by D1 transpressional sinistral deformation, causing the asymmetric flanking folds of the bedding interface. The boudins underwent also D2 of regional east-west shortening at a high angle to the layer (Chapter 2, Fig. 4.4) and D3 shortening parallel to the layer, which narrowed the boudins necks.

Lower Ugab Mullion boudins



High-Ardenne Slate Belt Mullion boudins (Urai et al., 2001)

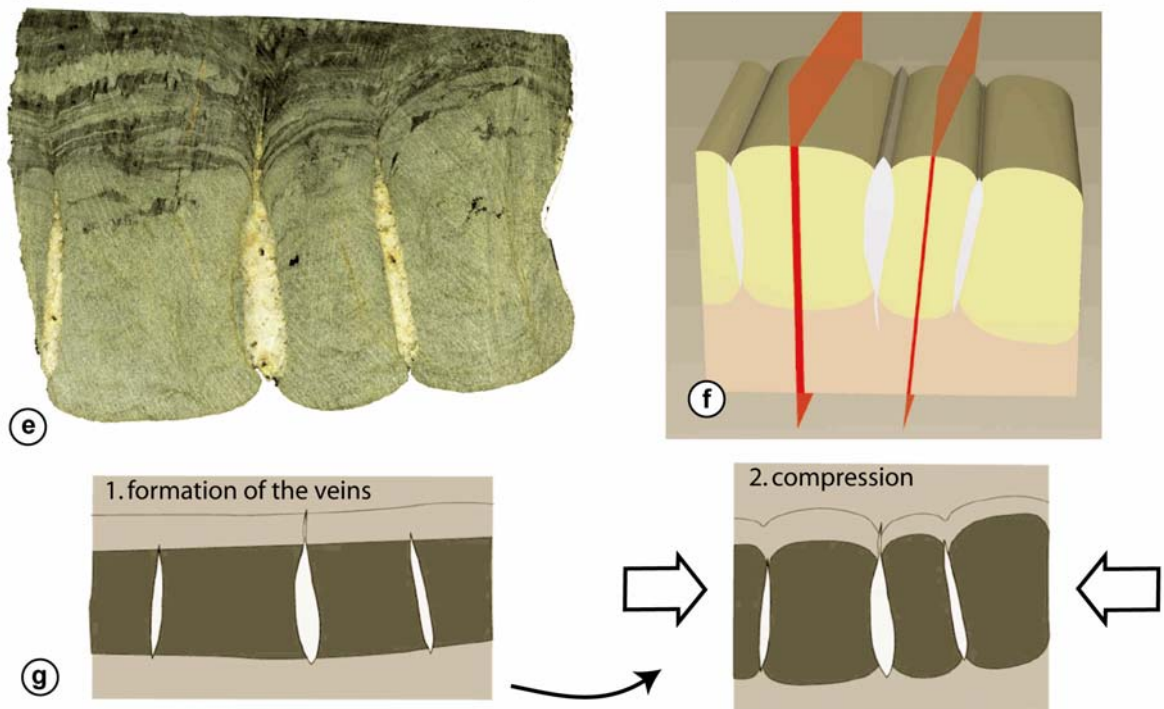


Fig. 3.14. (a)-(d) Examples of shortened boudin in the Lower Ugab Region. The bedding show an extreme convex surface between the boudin neck, indicating shortening parallel to the layer (locations: (a) $-20.86593^{\circ}/14.09651^{\circ}$ (b) $-21.09104^{\circ}/13.82326^{\circ}$ (c) $-20.86565^{\circ}/14.35929^{\circ}$ (d) $-21.07974^{\circ}/13.81535^{\circ}$) (e)-(g) Illustrations of shortened boudins in the High Ardennes Slate Belt (modified from Urai et al, 2001).

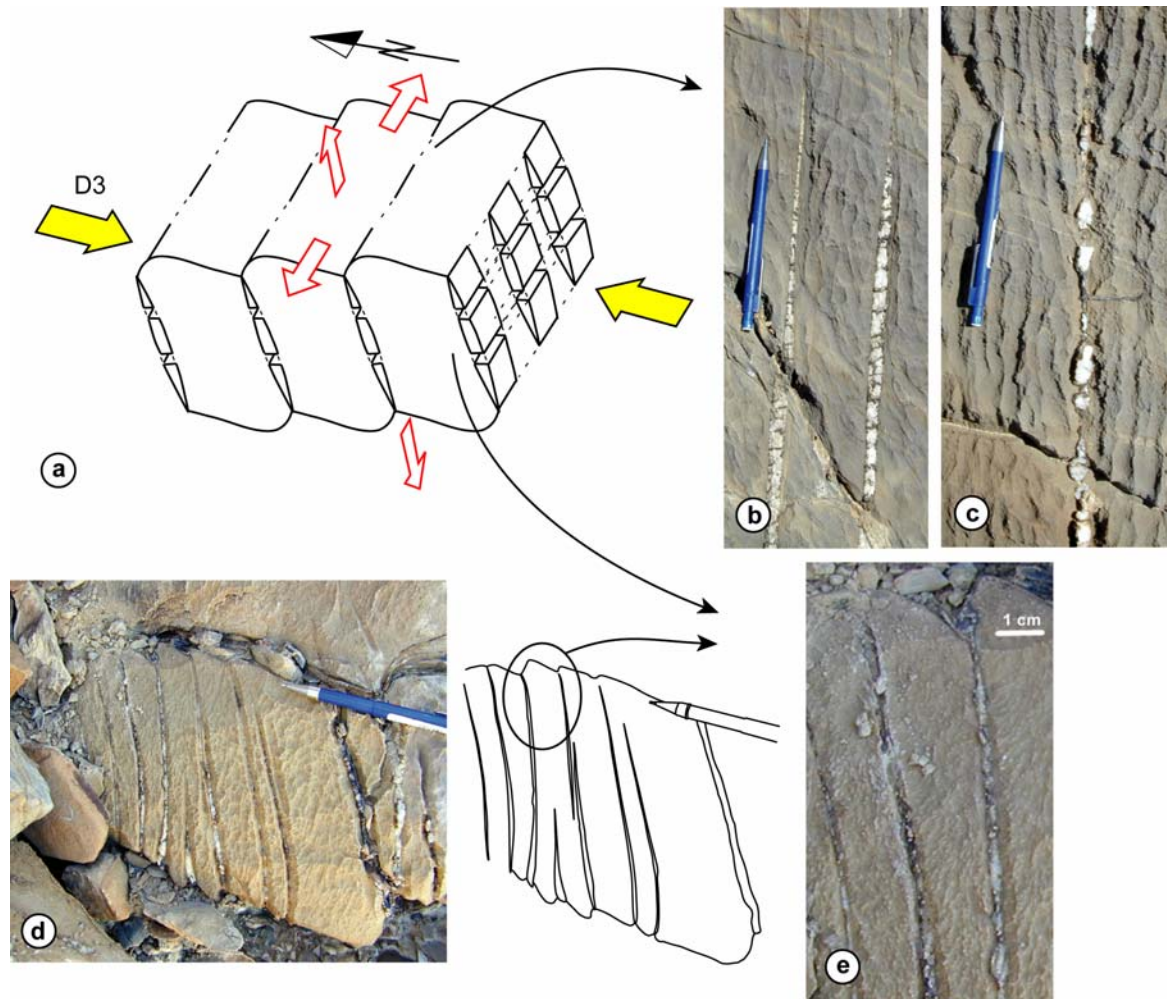


Fig. 3.15. (a) D3 north-south compression caused boudinage of V_A veins both orthogonal and parallel to the layer. (b) and (c) Illustration of boudinage of V_A veins on the bedding plane (d) and (e) illustrations of boudinage of V_A veins on a plan orthogonal to the bedding plane (location: $-20.86639^\circ/14.09544^\circ$).

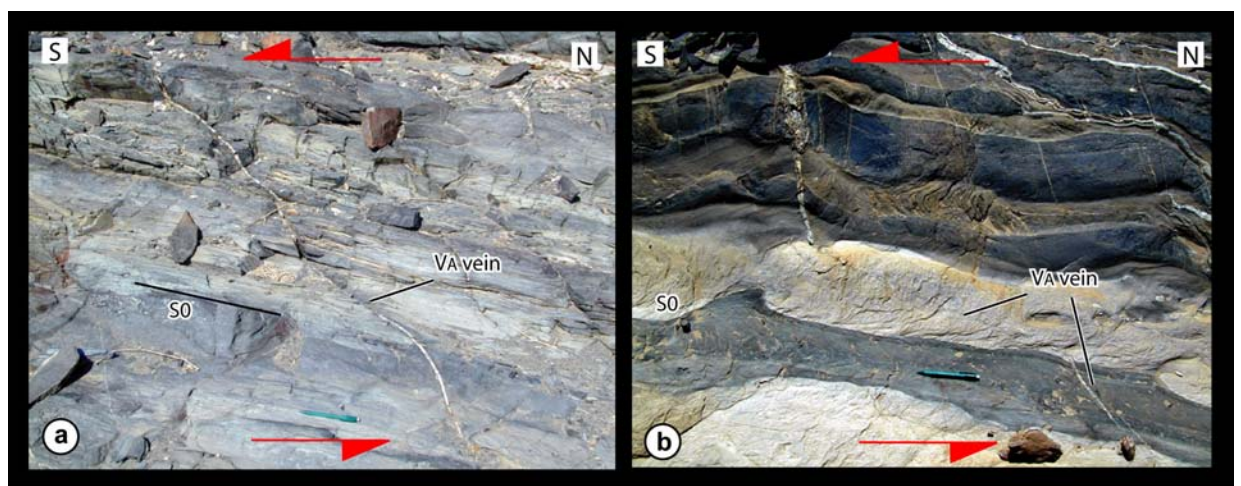


Fig. 3.16. (a) Example of V_A veins cutting through several pelitic and sandstone layers. The refraction of the veins is due to more intense deformation in the pelite layers (location: $-21.05392^\circ/13.82628^\circ$) (b) Example of V_A veins cutting through sandstone and marble layers. The vein is strongly boudinaged and more oblique to the bedding in the marble layer due to more intense deformation (location: $-21.04852^\circ/13.84794^\circ$).

In the north of the Voetspoor granite, the displacement and the reorientation of V_A veins in the kilometric “boomerang-shaped” D1-3 fold interference structures is attributed to D3, since the veins show opposite shear reorientation in the two limbs of the D3 folds which coincides with flexural slip during the tightening of the fold.

V_A veins developed both in the steep and flat limb of the D1 folds, but show more deformation and relative rotation in the steep limb. This can be explained if D1 sinistral non coaxial deformation is concentrated in the steeply dipping beds. The strain depends on the rock rheology. Where V_A veins developed at the top or at the bottom of the layers, they show a progressive deformation according to the grading in the beds. In the finest part of the beds, the veins show a smaller angle to the bedding, interpreted as a more relative rotation due to more shear strain (Fig. 3.5h, i; 3.6). When V_A veins cut through several layers, gradient of deformation can be observed from one layer to the other, with more deformation and reorientation in the softer (Fig. 3.16).

Strong undulose extinction with the formation of subgrains is observed in the quartz. Polycrystalline grains with irregular grain boundaries are also frequent. This implies low to medium grade deformation conditions of around 300–400°C. The calcite shows type III geometry of the e-twins which implies deformation over 200°C (Burkhard, 1993).

3.2.2.3 Spacing of V_A veins

The aspect ratios of the boudins (spacing/thickness) measured in the Lower Ugab area are between 0.5 and 5, frequently below 1. In some localities the aspect ration can reach the extreme value of 0.1 (Fig 3.14d). Bai and Pollard (2000b) argue for a critical spacing to layer thickness, defining a condition of “fracture saturation”, which is usually an aspect ratio between 0.8 and 1.2 in sedimentary rocks. They conclude that aspect ratio below 0.3 with very narrow spaced veins or joints must can not form only the local stress by requires another mechanism as hydraulic fracturing. D3 deformation reduced the spacing between the V_A veins, decreasing the aspect ratio of the boudins. The amount of D3 shortening is not easy to estimate in outcrops by the lack of markers. In the total area the maximum shortening is in order of ~10% as indicated by the shape of the large scale folds. The frequently observed aspect ratio in the order 0.5 or below could be explained by major D3 layer parallel compression. However the weak development of S3 and D3 folds makes this possibility unlikely. In those localities, where the aspect ratio is low, the veins must have been originally very narrow, probably indicating a formation by high fluid pressure and hydrofracturing.

3.2.2.4 Flanking folds along V_A veins

The formation of flanking along the sides of the veins can be explained by rotation of V_A veins in non-coaxial flow. The passive markers of the flanking folds are the bedding and the S1 main schistosity. All the three main types of flanking folds with antithetic, synthetic and no displacement slip (respectively a-type, s-type and n-type, Passchier, 2001) were recognised in the Lower Ugab Domain (Fig. 3.17). Flanking folds

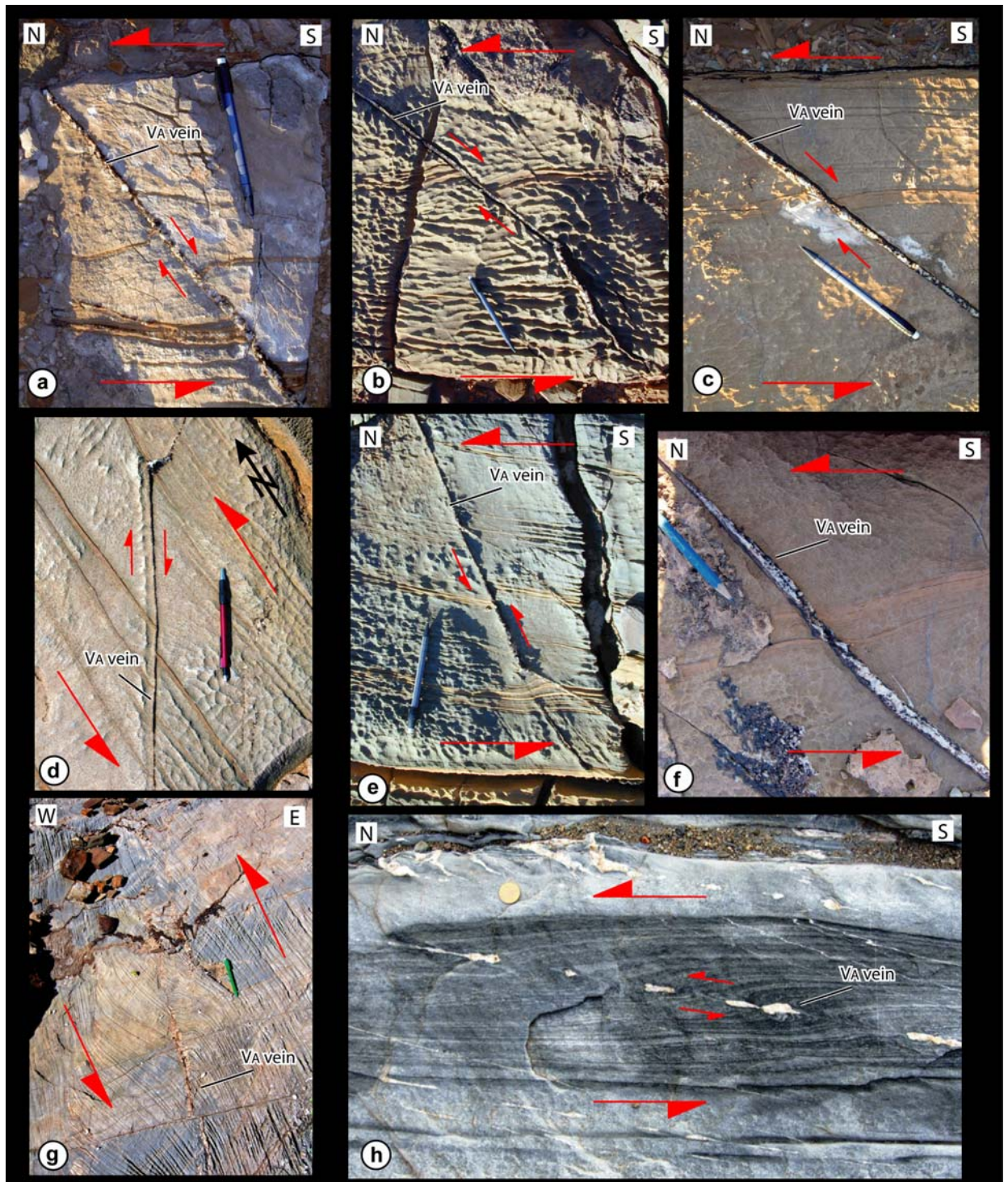


Fig. 3.17. (a), (b), (c) and (d). Examples of a-type flanking folds in the Lower Gemsbok formation with antithetic displacement of the bedding markers. (e) s-type flanking folds with synthetic displacement of the marker. (f) n-type flanking fold with antithetic drag. (g) and (h) Asymmetric flanking folds along boudinaged V_A veins in the marble. Large red arrows: bulk shear sense known from asymmetric folds, boudinaged veinlets and deltas and sigma clasts (not shown in the pictures). Small red arrows: slip direction on crossing element of the flanking fold structure. (Locations: (a), (b), (c), (e), (f) $-20.88888^\circ/14.14615^\circ$, (d) $-20.83780^\circ/14.12542^\circ$, (g) $-21.05302^\circ/14.19460^\circ$, (h) $-20.85701^\circ/14.35745^\circ$)

on oblique boudin train trace are also very common in the area and formed also by the sinistral rotation of the veins (Fig. 3.5e; 3.18; Passchier, 2001; Goscombe et al. 2004).

A-type flanking folds are very common, especially in the marble layers. Numerical simulations show that reverse drag a-type flanking folds develop in a transpressive regime when the cross cutting element (CE) originally cut the passive marker at high angle (Grasemann et al., 2003), which is supposed to be the case for the V_A veins in the Lower Ugab area. However in those simulations, the CE is a slip surface. The quartz veins in the Ugab are more competent than the pelite and the marble layers (cf. Chapter 4) and in principle should not behave as slip surfaces. According to analogue and numerical modelling, rigid objects that originally cut the passive marker at high angle lead to n-type flanking folds (Heesakkers, 2003; Grasemann and Stüwe, 2000). Some slip nevertheless occurred along the veins in the Lower Ugab region. Since V_A veins are composite veins with quartz in the centre and calcite forming the two margin zones, slip may have occurred along the calcite margin which probably had a slightly weaker competence than the host rock during the deformation. Slip may have also been helped by localisation of fluids at the vein boundary during the deformation. Another possibility is that slip occurred during the formation of the veins, before they were filled. However the deformation of quartz and calcite in the veins and the boudinage of the veins attest that the veins were filled during at least part of the rotation.

S-type flanking folds are less common than the a-type structure along the V_A veins of the Lower Ugab Domain. According to analogue and numerical modelling, they form when the CE is originally at a small angle to the passive marker, with an angle higher than 135° to the shear zone boundary (Grasemann et al., 2003; Exner et al., 2006). Numerical and analogue simulations show also that a-type flanking folds can develop into s-type flanking folds with increasing the shearing deformation and the rotation of the vein (Grasemann et al., 2003; Exner et al., 2006; Chapter 4). Since V_A veins originally formed at high angle to the bedding, s-type flanking folds may therefore have developed with the progressive deformation when the veins had sufficiently rotated to allow contractional displacement along the veins. However s-type and a-type can occur in the same outcrop along veins with a similar orientation. It seems thus that the orientation of the CE and the bulk flow are not the only parameters which control the type of flanking structures. The different veins may show different slip properties along their side, depending of the internal structure of the veins and maybe the different amount of fluids at their boundaries during the deformation. It is so possible that, from a vein which was originally at high angle to the bedding and along which no slip occurred during the first steps of the rotation, synthetic slip start to develop due to the diminution of the friction force at the boundaries of the vein caused by the new orientation of the vein or increase of fluids pressure.

Observation of n-type flanking structures along veins without reaction rims in the Lower Ugab area may therefore be explained in two ways: 1) no slip could occur along the veins which act as rigid objects, or 2) during the transition between an a-type into a s-type flanking structure, the passive marker passed through a stage where no slip between the markers is measured (Exner et al. 2006). N-type flanking folds, which develop along veins with reaction rims, are explained in paragraph 3.2.5.

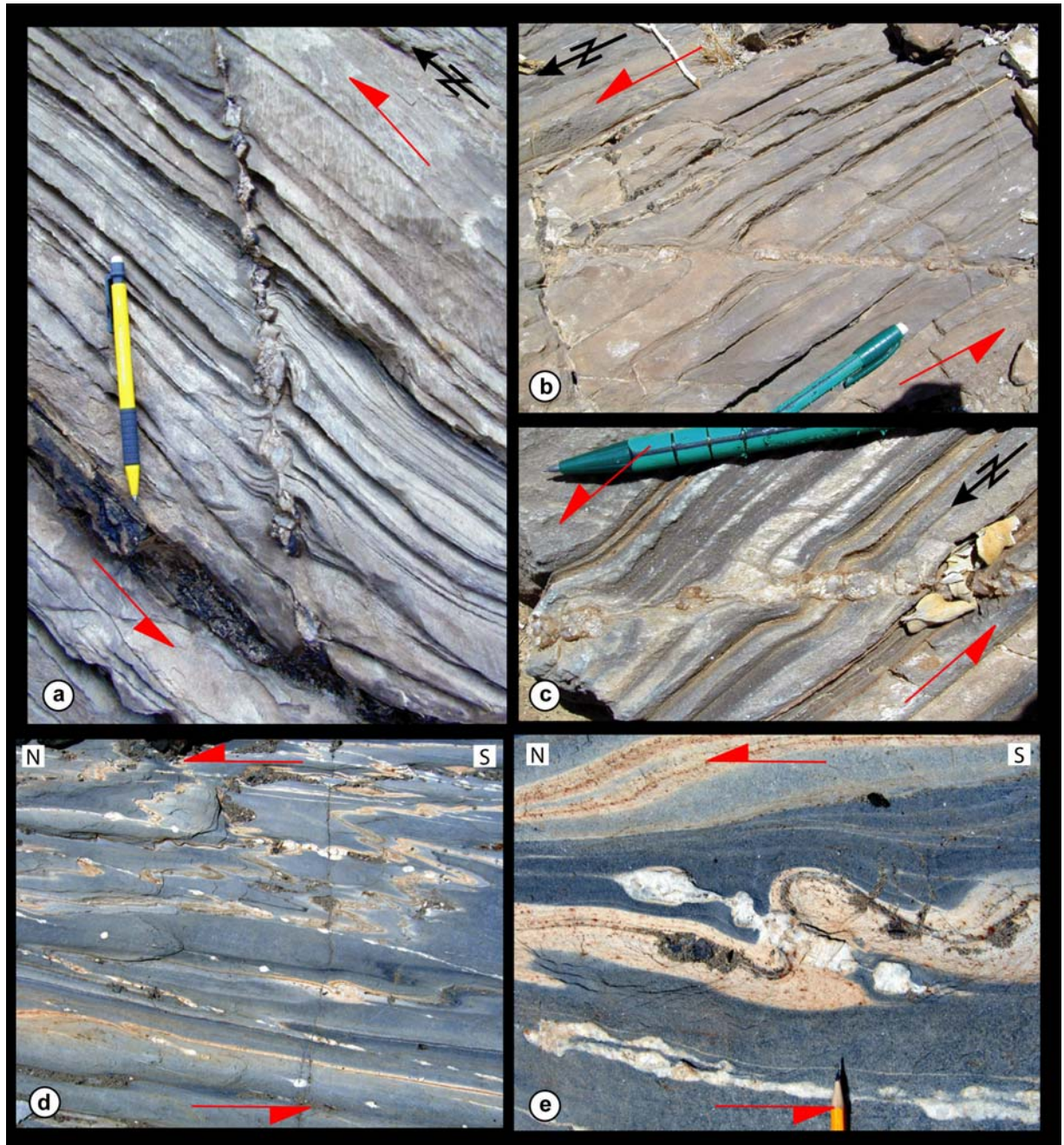


Fig. 3.18. Examples of boudin associated flanking folds in marble of the Lower Gemsbok Formation. Locations: (a), (b), (c) $-20.86123^{\circ}/14.35804^{\circ}$, (d), (e) $-21.07178^{\circ}/13.93661^{\circ}$.

3.2.3 V_B veins at a small angle to S_1

In the more pelitic layers of the siliciclastic metaturbidites of the Ugab Valley, composite quartz- calcite veins (V_B veins) are found at a small angle to S_1 , generally between 5 and 15° to S_1 (Fig. 3.19). Their thickness varies from 5mm up to 30 cm , most frequently around $1\text{-}3\text{ cm}$. V_B veins are slightly oblique to D_1

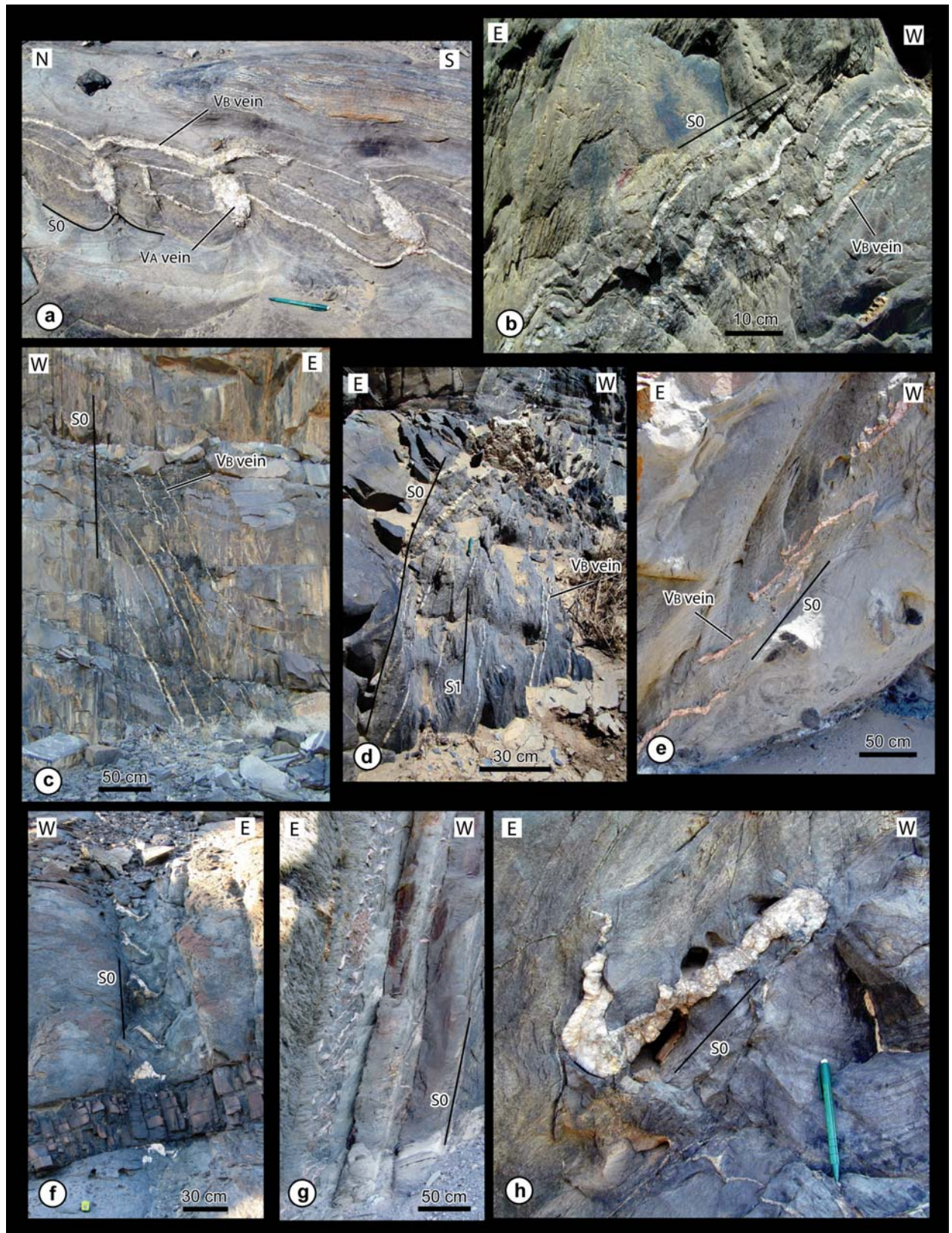


Fig. 3.19. (a) V_A and V_B veins in pelite. V_B veins developed at angle to S_0 and S_1 (location: $-21.07974^\circ/13.81535^\circ$). (b) V_B veins in the flat limb of a D_1 fold (location: $-21.09638^\circ/13.79722^\circ$) (c) and (d) V_B veins in the steep limbs of D_1 folds (respective locations: $-21.04225^\circ/14.09493^\circ$; $-20.96563^\circ/14.11145^\circ$) (e)-(h) V_B veins with hook folds in the steep limb of D_1 folds. The hook folds developed when the tips of the vein penetrated into the adjacent sandstone layers. (Locations: (e) - $21.10094^\circ/13.86668^\circ$, (f) $-21.05293^\circ/13.82630^\circ$, (g) $-20.98027^\circ/13.81002^\circ$, (h) $-21.10060^\circ/13.86818^\circ$).

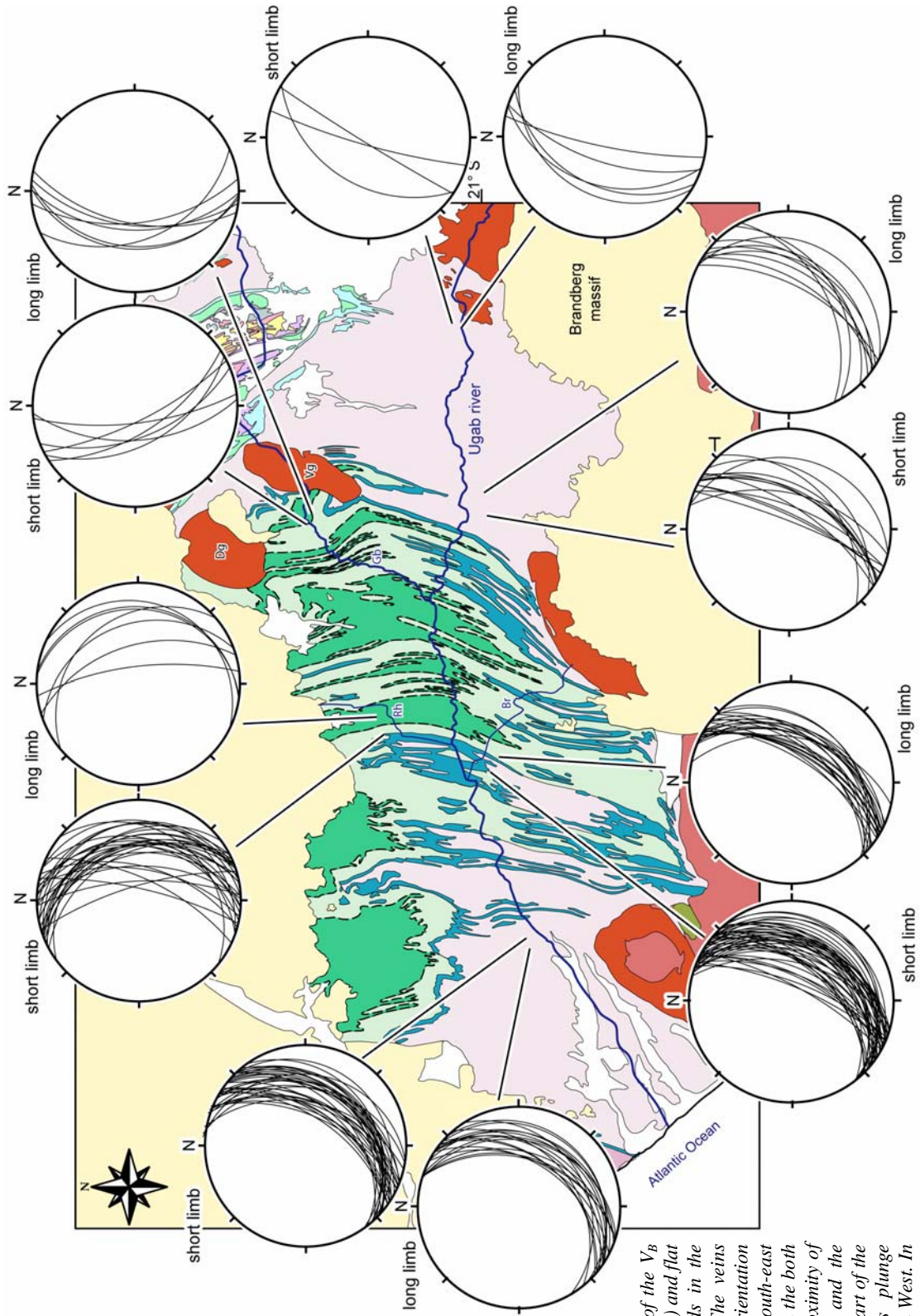


Fig. 3.20. Orientation of the V_B veins in the steep (short) and flat (long) limb of D1 folds in the Lower Ugab Valley. The veins show a constant orientation plunging towards the south-east all over the area and in the both limbs, except in the proximity of the Voetspoor granite and the granite in the eastern part of the area where the veins plunge towards the West-North West. In those areas, the D1 folds are east vergent.

fold axes. In some rare cases V_B type veins are found with symmetric orientation with respect to the folds axes, indicating an arrangement as conjugate veins. V_B veins are generally steeper than S_0 and S_1 in the flat limbs of D1 folds and less steep than S_0 and S_1 in the steep limbs, since they present about the same orientation in both limbs, dipping towards the east-south-east. They show a similar orientation all over the region of the Lower Ugab Domain except in areas where D1 folds are east vergent, such as at the west of the Voetspoor granite and at the west of the De Rust granite. This change in orientation is associated with fanning of the D1 structure (Chapter 2). In these two domains V_B veins are dipping towards the west-north-west (Fig. 3.20). The angle between V_B veins and the bedding in the flat limb is generally smaller than in the steep limb, so that the veins are frequently sub parallel to bedding in the flat limb. V_A and V_B veins are contemporaneous since conflicting crosscutting relations can be found in outcrops.

3.2.3.1 Texture and composition

V_B veins are composite quartz and calcite veins, largely dominated by the quartz. Albite, chlorite and biotite are also frequently present. The veins have a blocky texture. No mineral zonation is observed since calcite is generally randomly distributed in the veins. In some cases the calcite can form also the border of the veins. V_B veins underwent the same deformation as V_A veins and show the same texture as observed in V_A veins, with undulose extinction and formation of subgrains in the quartz. Polycrystalline grains with irregular grain boundaries are also present, implying deformation around 300-400°C. The calcite shows type III e-twins geometry as well (Burkhard, 1993).

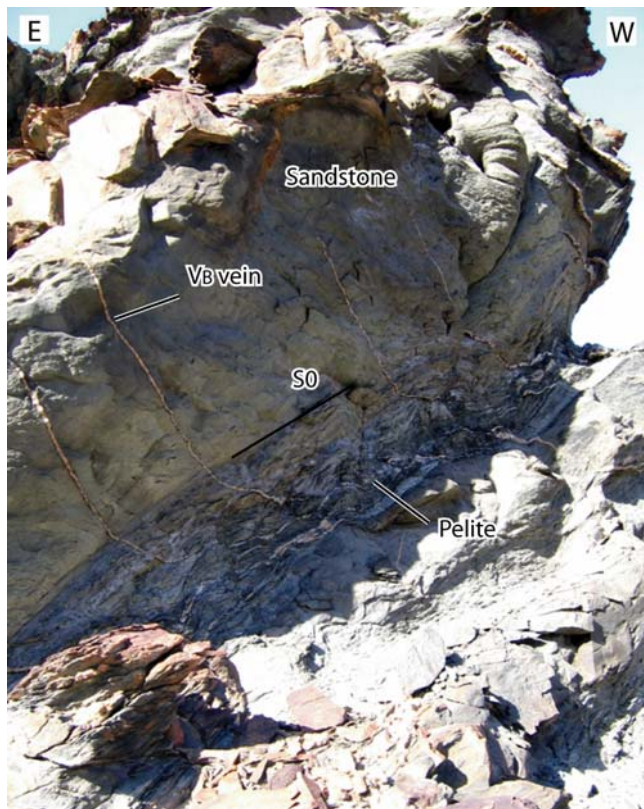


Fig. 3.21. Refraction of V_B veins between pelitic and sandstone layers. The vein is oriented at a high angle to bedding in the sandstone layer (location: $-21.05293^{\circ}/13.82630^{\circ}$).

3.2.3.2 Deformation

V_B veins are deformed by the three regional phases of deformation. They are strongly boudinaged in both north-south and horizontal-vertical directions. In the steep limbs they develop frequently domino boudins representing a sinistral sense of shearing with steep to subvertical boudin axes (Goscombe and Passchier, 2003).

Where V_B veins extend into adjacent sandstone layers, refraction can be observed, due to the difference in rheology (Fig. 3.21). The veins show more deformation in the pelitic layers, where pinch and swell boudinage or domino boudins are observed with extension parallel to the layers. In the steep limb of D1 folds, where the tip of the veins penetrates a few centimetres into the pelite-adjacent sandstones, hook-shaped folds develop at the limits of the pelite layer (Fig. 3.19e-h; Fig. 3.22; 3.23). The axes of the “hooks” have a north-south direction and are subhorizontal and therefore subparallel to D1 fold axes. The hooks appear to be syn-D1, as S1 is axial surface of the folds and S2 cut them without being affected. In some localities movements along the limit between the pelite and the sandstone layer is indicated by displacement of the veins. These displacements are in accordance with flexural slip in the limbs of D1 folds. The “hook folds” are therefore interpreted to form by reorientation of the veins due to flexural slip during the tightening of D1 folds. A pure shear component of east-west direction during D1 and D2 deformations may have also contributed to the formation of V_B veins hook folds by passive rotation of the veins. Reorientation of the veins occurs preferentially in the pelitic layers of weaker competence than the sandstone layers. The orientation of the veins at a high angle to the bedding in the sandstone layers may show the original orientation of the veins before deformation.

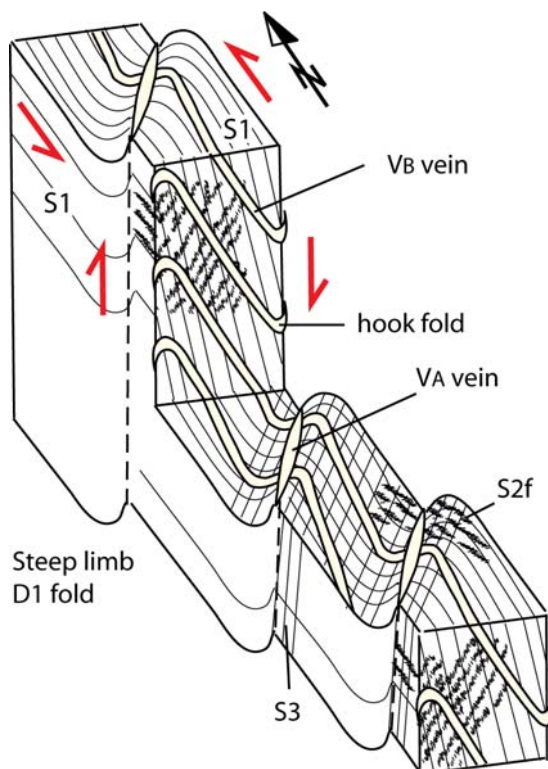


Fig. 3.22. Block diagram schematically illustrating the nature of V_B veins in steep limb of D1 fold with the formation of hook folds at the boundary of the pelitic layer.

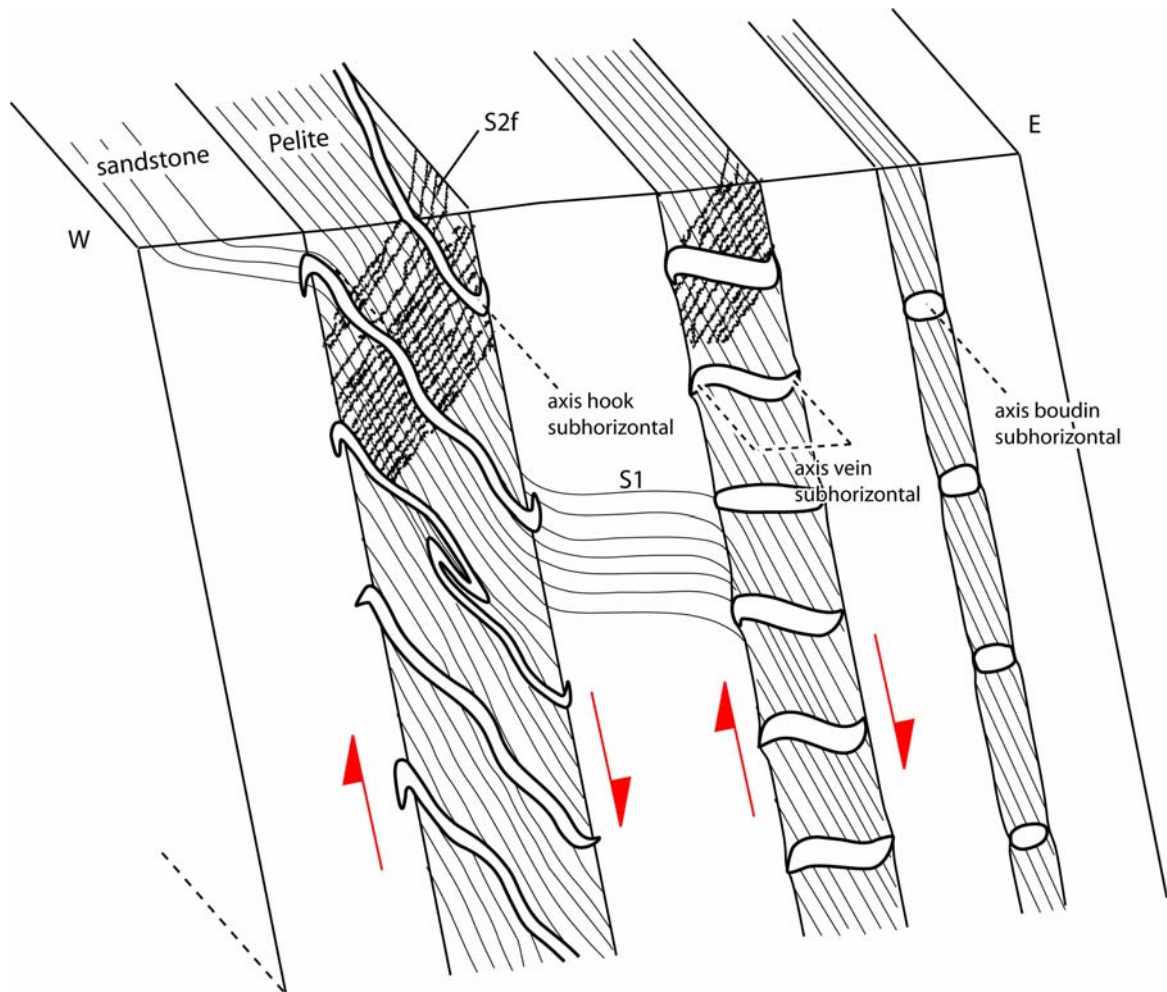


Fig. 3.23. Block diagram illustrating possible geometries of V_B veins in the steep limb of a D1 folds. The veins are folded by D1 deformation. S1 show a strong refraction between the pelite and the sandstone. Subhorizontal lensoid veins developed in the narrow layers probably due to boudinage of the layer. They show a sigmoid shape attesting a reorientation which corresponds to flexural slip (indicated by the red arrows).

In the hinge of the D1 folds, V_B vein are strongly folded. New veins subparallel to the fold axial surface frequently developed from the pre-existing V_B vein (Fig. 3.3). These new veins probably formed due to extension in the hinge. A puzzling feature is that some of those veins develop towards the centre of the folds, while extension and development of veins in hinges generally occur towards the outside of the fold. The inner arc of the folds is usually associated with pressure solution and loss of material (Twiss and Moores, 1992). An explanation for these veins could be that they formed due to slight unfolding during the last stage of the deformation due to flattening of the folds. The pressure solution planes in the inner arc may have then been reworked as fractures with material infilling.

Two hypotheses could be made for the present similar orientation of V_B veins in the both limbs of the D1 folds. 1) The veins could postdate the folding 2) the veins have been reoriented to their present orientation. The first hypothesis is unlikely as V_B veins show clear evidence of D1 deformation as demonstrated above. If some veins could postdate the folding, most of them formed before the folding or at the early stage of the

folding. The hook folds suggest a reorientation of the veins during D1 due to flexural slip. Some rare hook folds in the flat limb of D1 folds coincide with a reorientation by flexural slip.

In the steep limbs of the D1 folds, composite quartz and calcite lensoid veins are found with subhorizontal orientation (Fig. 3.23). Those veins formed generally in the smallest pelite layers. The shape of the veins and the regular spacing between the veins suggest that they developed as boudin neck during the boudinage of the layer. Some of the boudin neck can show sigmoid shape. Since S1 is axial surface of the sigmoid folds at the tip of the veins and S2 cut through the folds without being affected, the sigmoid shape is interpreted to result from the deformation of the veins during D1. The shape of the sigmoids is in agreement with a reorientation of the veins due to flexural slip. They may so form contemporaneously and in the same way than V_B veins. It is also possible that they form by layer boudinage during the folding due to the east-west oriented compression.

3.2.4 Veins network in the marble

The veins in the marble layers developed a different pattern from that in the pelite except for V_A veins. Many cross-cutting composite quartz and calcite veins of contemporaneous age occur in various orientations but with a regular disposition (Fig. 3.24; 3.25). Some veins developed at small angle to the bedding similar to the V_B veins in the pelite (V_{La} , Fig. 3.25). Two conjugated sets of veins less steep than V_A veins frequently develop in the steep limbs of the D1 folds (V_{Lb} and V_{Lc} , Fig. 3.24; 3.25). They are contemporaneous with V_A veins, since they show conflicting crosscutting relations. Similar conjugated veins occur in the flat limbs. Particularly in the flat limbs of D1 folds, where V_{Lb} or V_{Lc} cut V_A veins, asymmetric fold form at the intersection (Fig. 3.24d). The folds probably formed during the reorientation of the V_A veins during D1 transpressional sinistral shearing. The tightening of boudins during D3 north-south compression may have also reworked the structure. Where V_{Lb} or V_{Lc} are cut by V_A veins, flanking folds form at the intersection (Fig. 3.25). Triple intersection between V_{Lb} , V_{Lc} and V_A veins are frequently observed, where V_A veins is the bisector of the conjugate veins (Fig 3.24c).

Contemporaneous subhorizontal veins at a high angle to the bedding are also observed in the steep limbs of the D1 folds (V_{Ld} , Fig 3.24a, b). They are frequently gently plunging towards the west. Similar veins at a high angle to the bedding occur in the flat limbs. The veins have north-south intersection lines with the bedding and are most steeply west dipping. They show also asymmetric folds or flanking folds where they cut V_A veins. Outcrops with only V_A veins and perpendicular V_{Ld} veins present typical patterns of chocolate boudinage of the layer. All the veins in the marble frequently occur only at the surface of the bed, penetrating only a few centimetres into the layers.

The quartz and calcite in the veins is frequently disposed in a particular geometry. The quartz forms thin bands perpendicular to the vein, or defines an "X" shape (Fig. 3.24e, f, g). The spacing between the quartz bands is regular within the veins. Such a texture could result from boudinage of the vein with the quartz bands forming the boudin necks. A problem for boudinage as an explanation is that the disposition of the quartz bands are always perpendicular to the veins, and do not depend on the orientation of the vein, so that

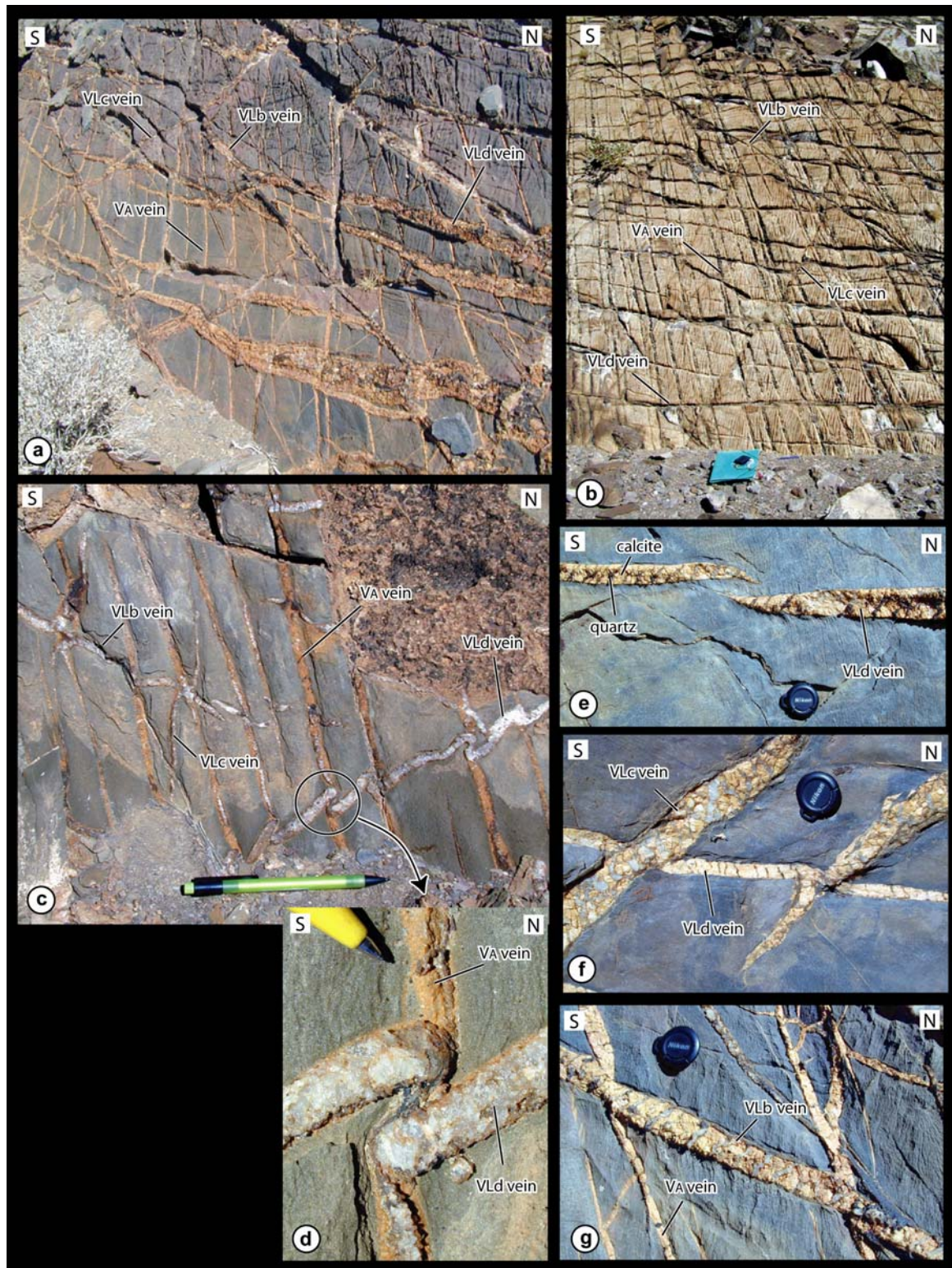


Fig. 3.24. Typical vein networks in marble layers of the Lower Ugab Domain. (a), (b) and (c) Vein network on the bedding surface. All vein set are contemporaneous since they show alternating crosscutting relations. (d) Detail of the intersection between V_A and V_{Ld} veins, which show the development of an asymmetric fold. (e) Detail of V_{Ld} veins. Quartz bands formed perpendicular to the veins. The tips of the veins show curvature when approaching each other. (f) and (g) Examples of V_A , V_{Lb} , V_{Lc} and V_{Ld} veins all showing the same texture of quartz bands at a high angle to the veins. Locations: (a) $-20.89349^\circ/14.12337^\circ$, (b) $-20.91554^\circ/14.04326^\circ$, (c)-(d) $-20.83268^\circ/14.17053^\circ$, (e)–(g) $-20.89279^\circ/14.12326^\circ$.

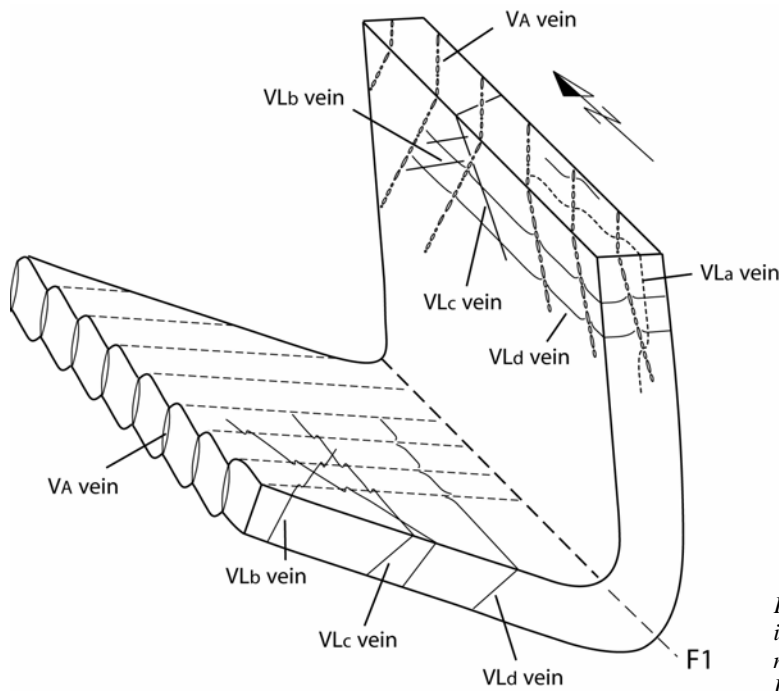


Fig. 3.25. Block diagram schematically illustrating the orientation of the vein network in marble layers of the Lower Ugab Domain in D1 folds.

the bands do not mark any preferred extension direction. However, the quartz bands could have formed during tightening of the D1 folds, when the layers were pressed together due to the east-west component of shortening during D1 and D2. If σ_2 and σ_3 were similar during compression perpendicular to bedding, extension could theoretically occur in several directions on the bedding plane. A primary origin for such a texture could be also possible. It could be an effect of preferential growth of quartz at specific sites. During the initiation of the vein, the quartz nuclei at the border of the veins may have been randomly distributed. During the development of the vein, it may be possible that only some of those nuclei could have grown as fibres or bands perpendicular to the vein wall in the direction of opening. The quartz bands could therefore result from an initial fibrous texture in the veins. Elsewhere, examples of fibrous quartz and calcite veins in limestone show similar distribution of quartz (Ramsay and Huber, 1983, Fig. 13.6 p. 239).

The intersection line between the different syntectonic veins in the marble show a west plunge in the Lower Ugab area, except at to east and north of the Voetspoor granite, where the intersection plunges towards the east (Fig. 3.26). The intersection may present the apparent direction of σ_1 during the formation of the veins. The variable orientation of the veins can be explained by small difference between σ_2 and σ_3 with possible local inversions. A first set of veins may form due to a fluid pressure pulse which shifts the Mohr circle to the tensile fracture field (Fig. 3.27b). The formation of a crack in the rock causes σ_3 to jump to a value of 0. σ_2 becomes the new σ_3 of maximum tensile stress (Fig. 3.27c). A second fluid pressure pulse may occur, causing the shifting of the new Mohr circle to the tensile fracture domain. A new set of veins will then form in a perpendicular orientation to the first set. The intersection line of the two sets of veins is parallel to σ_1 (Fig. 3.27d).



Fig. 3.26. Orientations of the intersection lineations between V_A , V_{Lb} , V_{Lc} and V_{Ld} veins in marble layers of the Lower Ugab Domain.

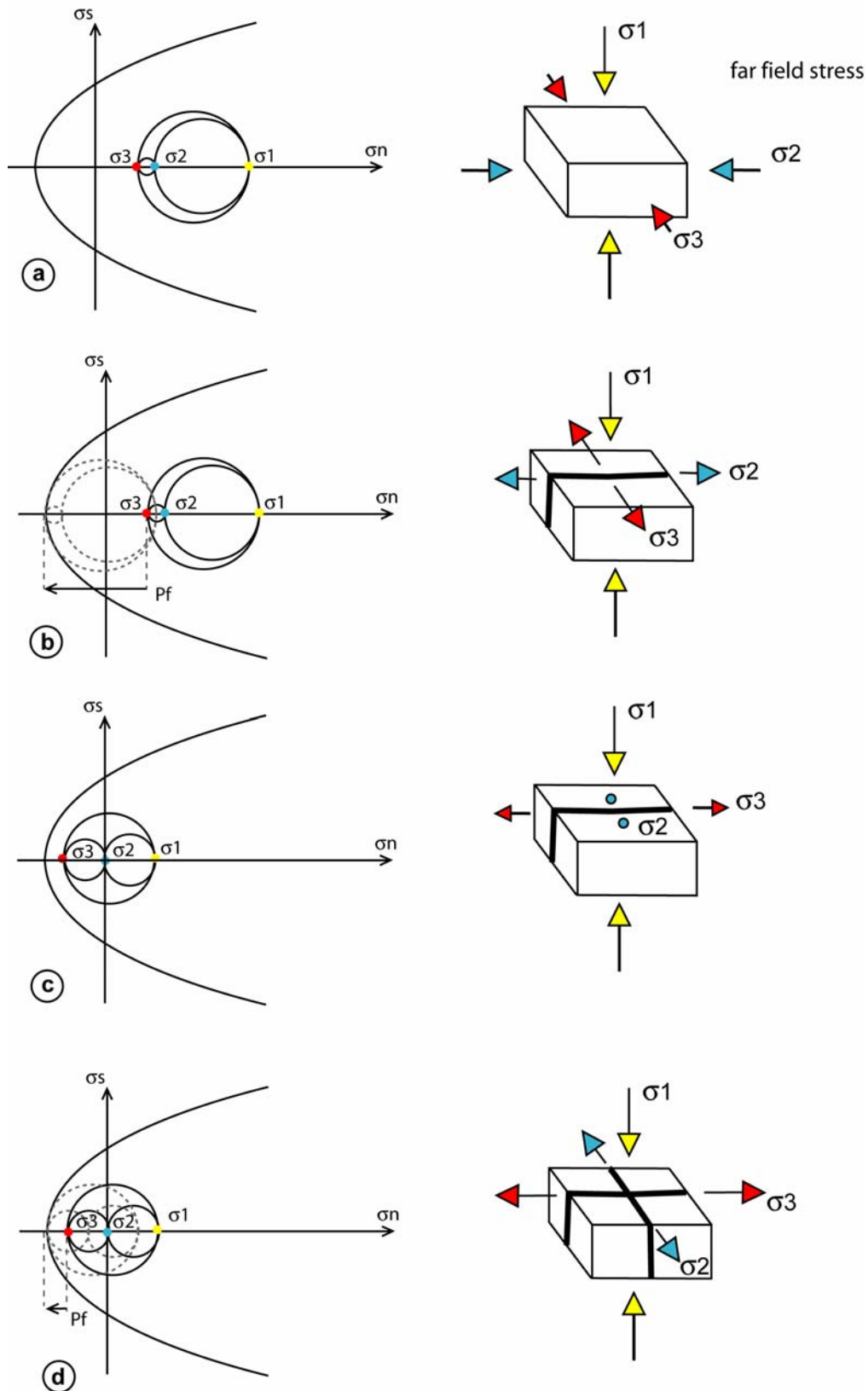


Fig. 3.27. (a) Mohr diagram and orientation the stress at the initial stage. (b) Increase of fluid pressure shifts the Mohr circle into the field of tensile fracture and a fracture forms with an opening direction parallel to σ_3 . (c) σ_3 locally jumps to a value of zero because of the formation of a crack in the rock. σ_2 becomes then the new σ_3 . (d) A second fluid pressure pulse occurs, which shifts again the Mohr circle into the domain of tensile fracture and a new fracture forms perpendicular to the first one, with opening direction parallel to the new σ_3 .

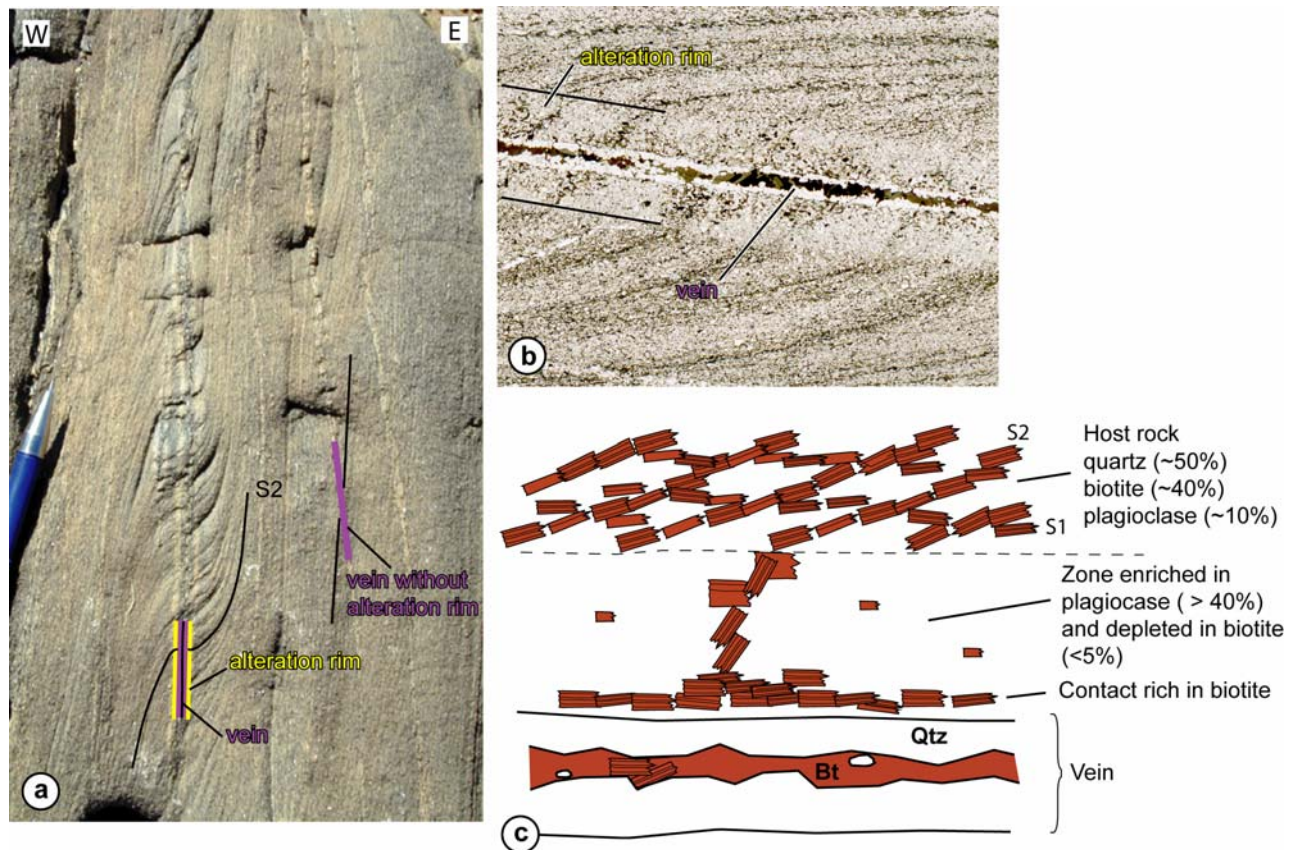


Fig. 3.28. (a) Veins in the Amis river formation near the Doros intrusion. N-type flanking folds developed along veins with alteration rims (location: $-20.72565^{\circ}/14.28931^{\circ}$). (b) Detail of a vein in thin section (same location). The schistosity in the alteration rim is at high angle to the vein. (d) Sketch of the veins and the alteration rims.

3.2.5 Veins associated with N-type flanking folds

N-type flanking folds have no slip of the passive marker along the crossing element (Passchier, 2001). Flanking folds of this type developed in the Amis River formation metasediments near the Doros granite in the NE of the field area (Fig. 3.28; Passchier, 2001; 2007). Here the sediments have been intruded by pegmatite veins during D1 deformation. The granitic veins lie at a small angle to the N-S trending steep S1 foliation. They are boudinaged and folded by further D1 and D2 deformation. Along some thin pegmatite veinlets the wall rock was altered. The pelite consists of quartz, oligoclase and biotite and a rim of 2-5 mm wide along the two edges of the veinlet is strongly enriched in plagioclase (andesine-oligoclase) and depleted in biotite. Along those veinlets S1 shows a deflection into N-type flanking folds which coincides with the plagioclase-rich rim. In the rim and close to the veins, the angle between the vein and S1 varies between 70° and 90° . In the host rock outside the rim, the angle between S1 and the vein varies between 10° and 20° . The flanking folds seem to have developed by a relative rotation of the vein with the attached rim sinistrally with respect to S1. Although folds with “sinistral sense” are dominant, dextrally rotated veins can also be found in the same outcrop (Fig. 3.28a), showing similar angle to S1 between 10° and 20° . The presence of both dextral and sinistral vein rotation means that the deformation was locally dominated by

pure shear (Heesakkers, 2003). The vein and the feldspar rim acted as a rheologically similar unit during the rotation in a more ductile matrix, which allowed preservation of a high angle between S1 and the veinlets. Proof for this is that where the feldspar rim is lacking, no flanking folds develop (Fig.3.28a). Measurements of the angle between S1 and the veins in the far field and in the rim suggest a minimal relative rotation of the vein and S1 of about 60°.

N-type flanking folds similar to those near the Doros pluton develop along quartz veins in the Zebraputz formation in the Ugab River near the Brandberg tin mine (Fig. 3.29). Along the edge of those veins the host rock is also altered. A rim up 5 cm wide develops on both sides of the veins consisting mainly of fibrous tourmaline with minor quartz and biotite, while the host rock consists of quartz, white mica and biotite. The tourmaline grew orthogonal to the veins, similar to what has been observed in metasediments of Cap-the-Creus in Spain, where a tourmaline rim develops along pegmatitic veins (Passchier, 2001; Druguet et al., 1997). The rocks are strongly affected by syn-D1 or D3 sinistral shearing. Adjacent to the tourmaline rim S1 is deflected into a flanking fold. S1 is orthogonal to the veins in the rim and forms an angle with the vein between 15° and 35° outside the rim. The veins and their alteration rim are strongly boudinaged, which coincides with extension during sinistral rotation of the veins. The veins with alteration rims were more

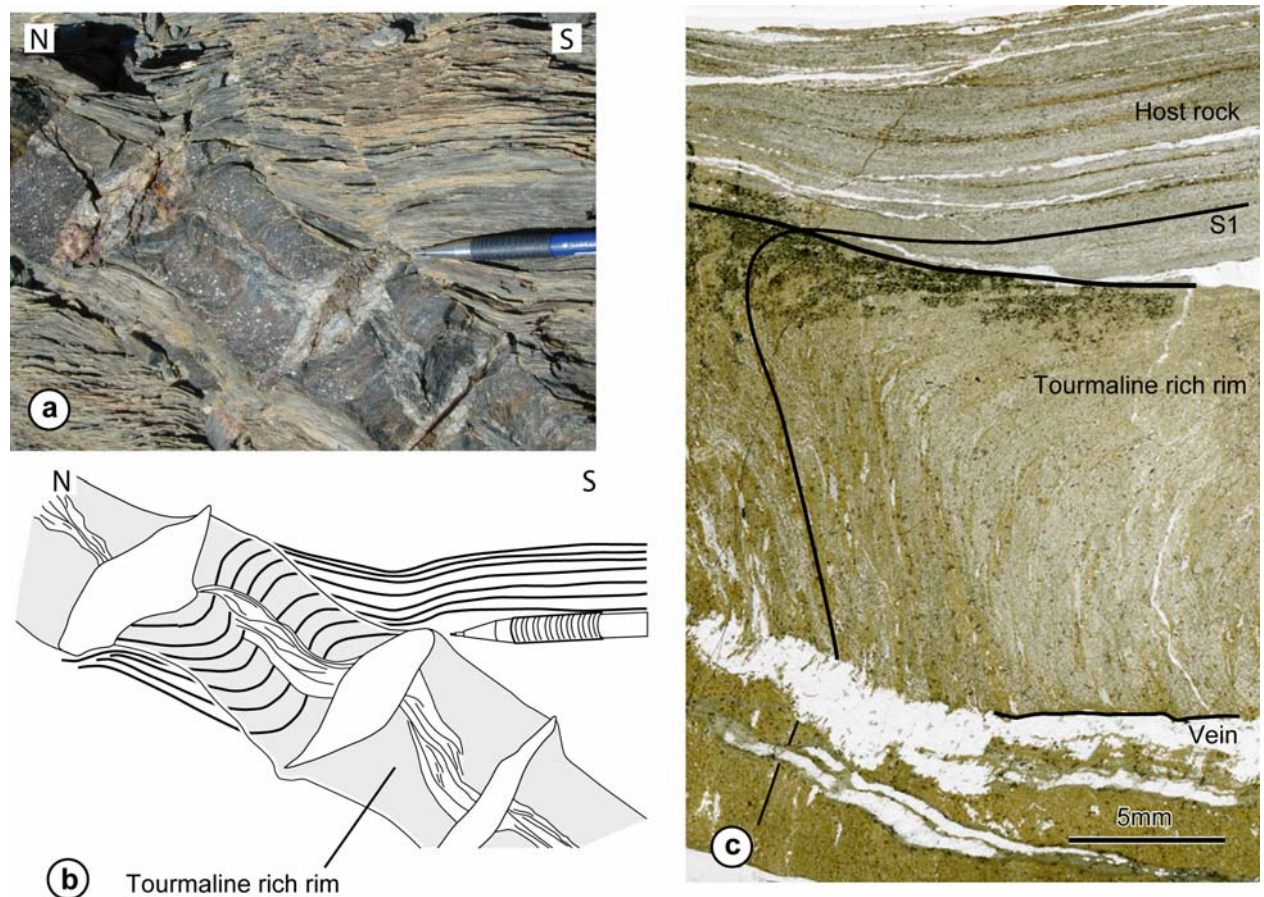


Fig. 3.29. (a) and (b) Quartz veins with tourmaline rims in the Amis river formation. N-type flanking folds developed due to rotation of the veins. The vein and the alteration rim have been boudinaged during their rotation (location: -20.95699°/14.18523°). (c) Thin section of the vein and the alteration rim. The main schistosity S1 is at a high angle to the vein in the alteration rim and at low angle to the vein in the wall rock. This can be attributed to relative rotation of the vein and the far-field foliation.

competent than the host rock during the rotation, which explains the boudinage during the rotation and the formation of flanking folds, where a high angle between S1 and the vein has been preserved in the rim. The proximity of the Brandberg tin mine and the presence of pseudomorphosed porphyroblast of cordierite and andalusite in the host rock suggest the presence of a granite not far below the outcrop level in this part of the area (Goscombe et al., 2004). The progressive enrichment in tourmaline towards the veins may have formed by metasomatism of the pelite by a boron rich fluid which may come from the underlying granite. The common inclusion of tourmaline in quartz grains in the veins suggest that the tourmaline was the first phase to crystallise during the crack opening. The boron rich fluid may have proceeded or be of same age as the quartz rich fluids. The angles between S1 in the far field and in the rim of the veins suggest a minimal relative rotation of the vein and S1 of about 60°. Observations on these two sets of N-type flanking folds in the Lower Ugab domain confirm that their formation is directly linked to an alteration border along the veins as suggest by Passchier (2001) and Druguet et al. (1997), acting as a competent bloc during the rotation of the vein and preserving the original angle between the vein and the external element (S1).

3.3 Stable isotope analyses

3.3.1 Introduction

Oxygen and Carbon isotopic ratios are commonly use to determine the origin of the calcite and quartz of syntectonic veins (Dietrich et al., 1983; Burkhard and Kerrich, 1988, Henry et al., 1996; Kenis et al., 2000). Isotopic compositions of quartz and calcite of the syntectonic veins of the Lower Ugab Domain and their respective host rocks have therefore been investigated. Oxygen isotope thermometry estimations have been made with the couple quartz-calcite in the veins in order to constrain the temperature conditions of the crystallization of the two phases and the formation of the vein.

3.3.2 Stable isotope thermometry method

The equilibrium between the oxygen isotope compositions of two phases depends on the temperature. The temperature is given by the following equation for two phases A and B:

$$1000 \ln \alpha_{A-B} = a_{AB} \cdot 10^6 / T^2 \cong \delta^{18}O_A - \delta^{18}O_B$$

Where: $\alpha_{A-B} = (1000 + \delta^{18}O_A) / (1000 + \delta^{18}O_B)$

And: $\delta^{18}O = [^{18}O / ^{16}O_{(\text{échantillon} - \text{standard})}] / [^{18}O / ^{16}O_{\text{standard}}]$

a_{AB} is the fractionating coefficient between the two phases A and B. The calibration of Sharp and Kirschner (1994) has been used, as it is based on natural data and seems to give the geologically most realistic temperatures.

3.3.3 Analytical technique

Attention has been paid to select only pure grains for the analyses, by careful hand picking. Sample batches of 1.7–2.0 mg were analysed by laser fluorination (Sharp, 1992) for oxygen at the stable isotope laboratory of the University of Lausanne. Analyses have been normalised relative to Standard Mean Ocean Water (SMOW) and corrected using an in-house standard (Qtz Lausanne-1: $\delta^{18}\text{O}_{\text{SMOW}} = 18.15\%$) and the international standards NBS-28 ($\delta^{18}\text{O}_{\text{SMOW}} = 9.6\%$). Calcite batches of 250–300 μg have been analyzed by Gas-Bench in the same laboratory for the carbon isotope. Analyses have been normalized relative to the Pee Dee Belemnite (PDB) and corrected using an in-house standard (CM: $\delta^{13}\text{C}_{\text{PDB}} = 2.05\%$). Both for oxygen and carbon, each run was bracketed by standard analyses at start and finish to allow corrections of constant and systematic errors. Each sample has been analysed twice on the same day to test for reproducibility.

3.3.4 Results

3.3.4.1 Isotopic compositions

Isotopic composition of the veins and the host rocks are presented in Fig 3.30. The veins in the Brandberg West formation have $\delta^{18}\text{O}$ in quartz between 17.6 and 18.3. In the Gemsbok River formation, the $\delta^{18}\text{O}$ quartz vein values show more variation and seem to be slightly higher, between 19.3 and 22.7. The $\delta^{18}\text{O}$ of calcite in the veins follows the same trend, with slightly lower isotopic composition in the Brandberg West formation (13.4 to 16.4) than in the Gemsbok River formation (18.4 to 21.4). In the Pelitic Brak River formation, the isotopic compositions of oxygen in quartz in the veins vary between 17.8 and 18.0. Veins analysed in the Amis River formation show lower $\delta^{18}\text{O}$ values for quartz, between 15.6 and 15.8.

In the Host rocks, the $\delta^{18}\text{O}$ quartz value in the Brack River formation is 17.9, similar to that in the veins. $\delta^{18}\text{O}$ of the calcite in the Gemsbok formation rocks varies between 18.6 and 21.4, which is also in the range of values for the veins. In the Brandberg formation, the $\delta^{18}\text{O}$ of the calcite in the rock varies from 15.8 to 18.9, also comparable to values in the veins.

Carbon isotopes of calcite in the different veins and the respective host rocks show also similar values. Isotopic compositions of the host rocks are therefore similar to those in the veins and show also the same differences between different formations. This indicates a local origin of the fluids and implies that fluids did not migrate through the rock over large distances. Values of the veins and host rocks of the same formation vary also slightly with geographic locality, which confirm the local origin of the fluids. No traces

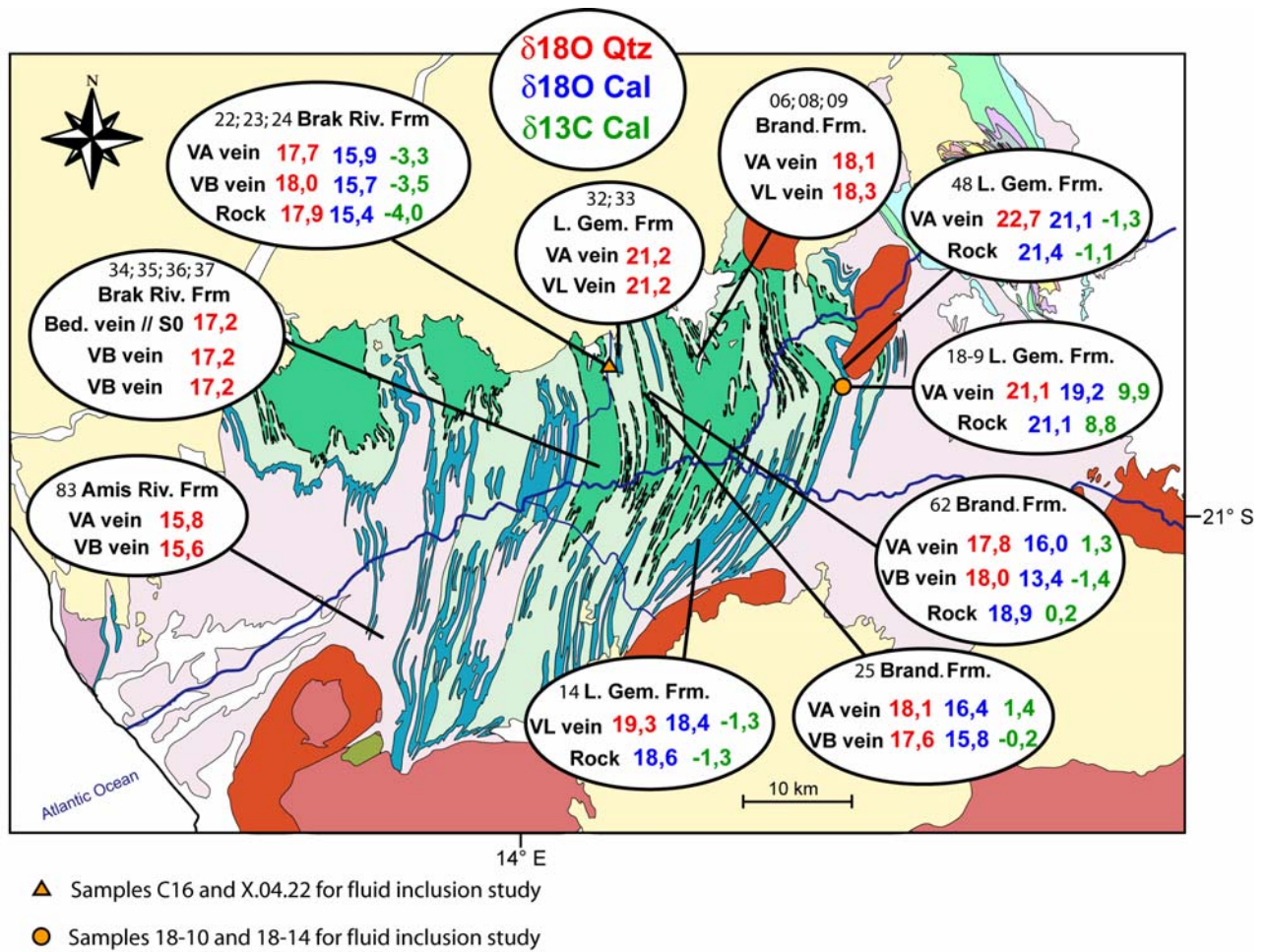


Fig. 3.30. Isotopic compositions of quartz and calcite of the veins and their respective host rock in the Lower Ugab Domain. Red: $\delta^{18}O$ quartz, blue: $\delta^{18}O$ calcite, green: $\delta^{13}C$ calcite.

of large scale fluid flow have been observed, as for example in large transecting vein networks. The veins are generally restricted to one layer. The different types of veins in the same localities show the same isotopic composition indicating a similar origin of the fluid and a formation at about the same time, which confirms the structural observations.

3.3.4.2 Thermometry

Among the different vein samples, only five show relative equilibrium between the oxygen isotopes of quartz and calcite, allowing a rough estimation of temperature (Fig.3.31). Calcite isotope analyses show less reproducibility than the analyses in the quartz. Calcite is known to be more subject to weathering which may have favoured low temperature reequilibrations. The five samples which show relative equilibrium are from the Pelitic Brak River formation (V_A samples n°22 and 23), the Lower Gemsbok formation (V_A samples n°18-9 and 48) and the Brandberg West formation (V_A sample n°62) (Fig. 3.30). These five samples give temperatures in a coherent range between 420 and 500°C with an average of 460°C (calibration of Sharp

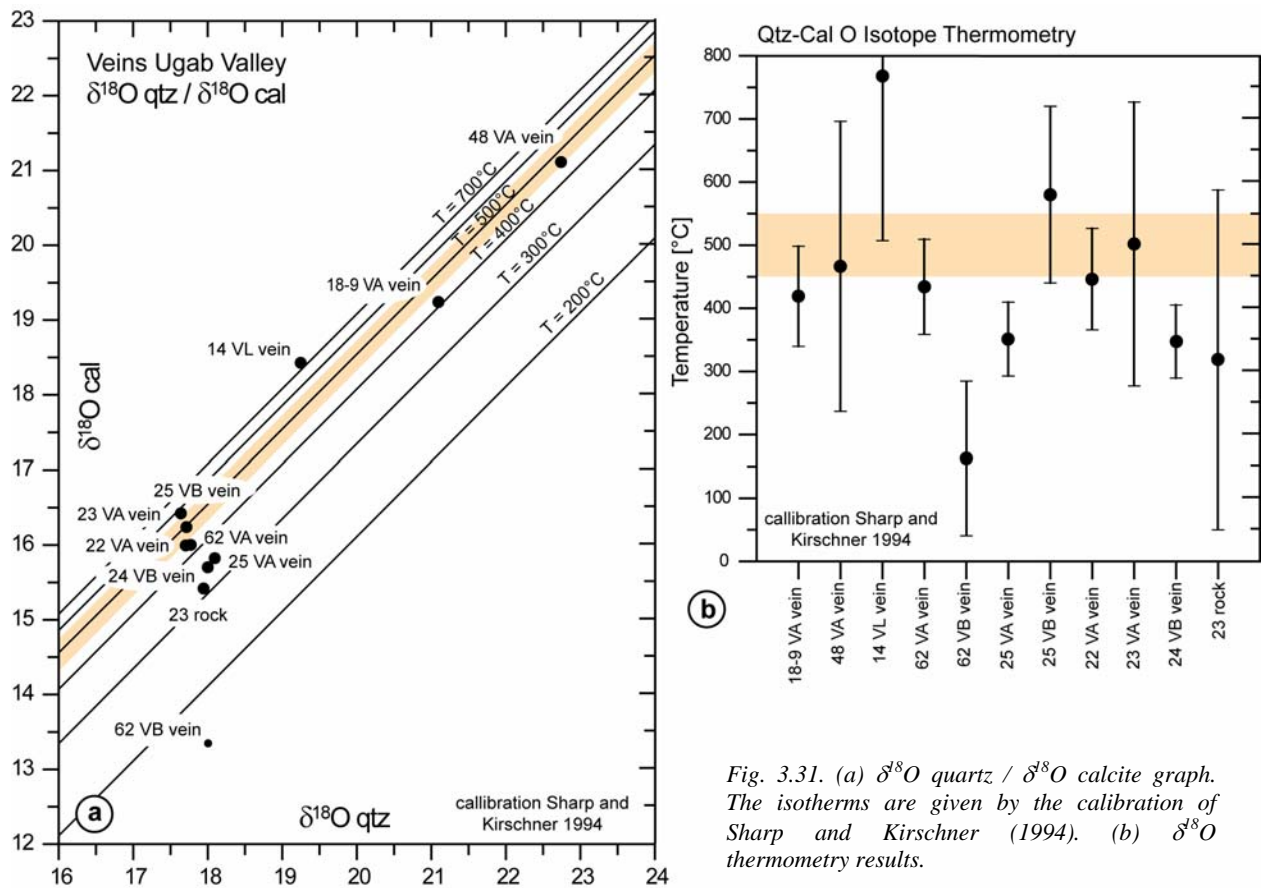


Fig. 3.31. (a) $\delta^{18}\text{O}$ quartz / $\delta^{18}\text{O}$ calcite graph. The isotherms are given by the calibration of Sharp and Kirschner (1994). (b) $\delta^{18}\text{O}$ thermometry results.

and Kirschner, 1994) (Fig. 3.31). The accuracy on the temperature is relatively low, especially for the samples n° 48 and 23, due to the bad reproducibility of the oxygen isotopic values of calcite, despite a relative fresh state of the grains. The repartition of calcite and quartz in the two types of veins in metapelite of the Brak River formation is random, with some isolated plurimillimetric calcite grains in quartz. In the three samples of veins in marble, calcite lies in the border of the veins and quartz in the centre. Both quartz and calcite show blocky grain texture, which may indicate a recrystallization from an original fibrous texture. Recrystallization may have influenced the isotopic composition of the grains, if it opened the system to new incoming fluids. Inheritance of the material in a closed system during the restructuring of the texture in the veins is also possible as shown for instance by the retromorphoses of aluminosilicate in veins of the Campo Tensia Unit in the Central Alps (Allaz et al. 2005). Since the veins in the Lower Ugab domain underwent three deformation phases, it is possible that they were subject to several stages of crystallization and recrystallization. The intensity and complexity of deformation is shown by crystallization of calcite in the boudin necks as can be observed in the field.

The calcite grains used for analyses of the veins have been carefully taken in the veins and not in boudin necks. Nevertheless, the possibility of recrystallization of the grains in multiple phases of deformation has to be taken in account. Because of this problem of possible resetting, the temperature obtained by oxygen isotope thermometry in the veins of the Lower Ugab Domain must be used with some care. The estimated range of temperature of the crystallization of the veins in the Ugab Valley coincides with the range of

temperature of the stability of biotite in greenschist facies. Structural observations indicate formation of the veins during the first stage of the D1 phase of deformation. The main S1 schistosity is marked by the alignment of biotite indicating that the rocks were in this range of temperature during the peak of the D1 deformation. Local relics of previous biotite schistosity in the hinge of D1 folds may indicate that metamorphic conditions during the first steps of regional deformation were already in greenschist facies.

3.4 Fluid inclusion study

3.4.1 Introduction

Most mineral growth take place by means of fluids and the study of fluid inclusions provides a way to reconstruct the composition, density and history of this now-missing fluid phase (Touret, 2001; Roedder, 1984). Fluid inclusions are common in quartz of the syntectonic veins of the Lower Ugab Domain. Microthermometry has been performed on four samples in order to constrain the conditions of vein formation. This number is insufficient for a complete control of fluid composition history, but serves as a pilot study.

3.4.2 Analytical technique

Rock sections of 150 μ m, polished in the both sides, were analysed using a Linkam THM 600/S/Geo heating-freezing stage coupled to a TMS 94 temperature controller with an error of $\pm 1^\circ\text{C}$ at the University of Giessen. The heating and cooling stage was calibrated using synthetic fluid inclusion calibration standard: CO₂ and H₂O from ©Bubbles Corporation. Raman microspectrometry has been performed at the University of Frankfurt am Main, using a Leica/Renishaw Raman microprobe with the softwares Renishaw WiRETM 2.0 and GRAMS in order to identify the gas and fluid phases in the fluid inclusions. An Argon laser (green laser: $\lambda = 514.5 \text{ nm}$) was used as excitation source.

3.4.3 Sample description

Fluid inclusions have been investigated for microthermometry in four V_A vein samples from two localities. Two samples are from the Lower Gemsbok Formation (samples 18-10 and 18-14, Fig. 3.30; coord. -20.8872° / 14.3108° in the marble) and two from the Brak River Formation (samples C16 and X.04.22, Fig. 3.30; coord. -20.8557° / 14.0845° in the pelite). The veins in the marble are composite quartz-calcite veins with a central zone composed of quartz and two marginal zones composed of calcite. The two veins have a

median line composed of small calcite grains. The veins in the pelite are also composite quartz-calcite veins. Calcite is found as isolated grains in the vein and at the margin. Fluid inclusions have been investigated only in the quartz, since they were too small in the calcite. Quartz in all veins shows a blocky texture. Deformation causes undulose extinction and rare subgrains. Attention has been paid to measure the fluid inclusions in the less deformed zones only.

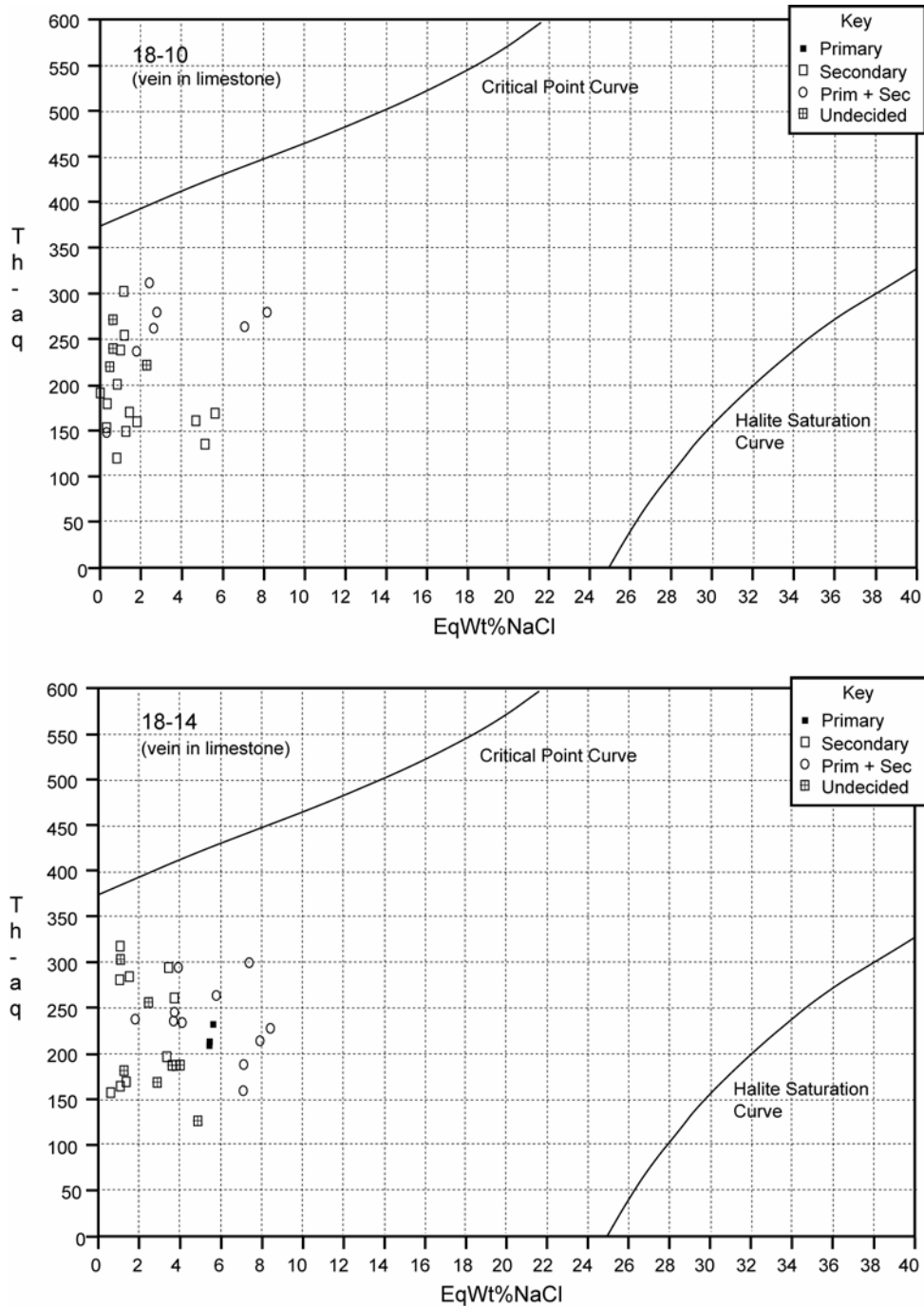


Fig. 3.32. Diagrams salinity / homogenisation temperature for the fluid inclusions of the samples 18-10 and 18-14.

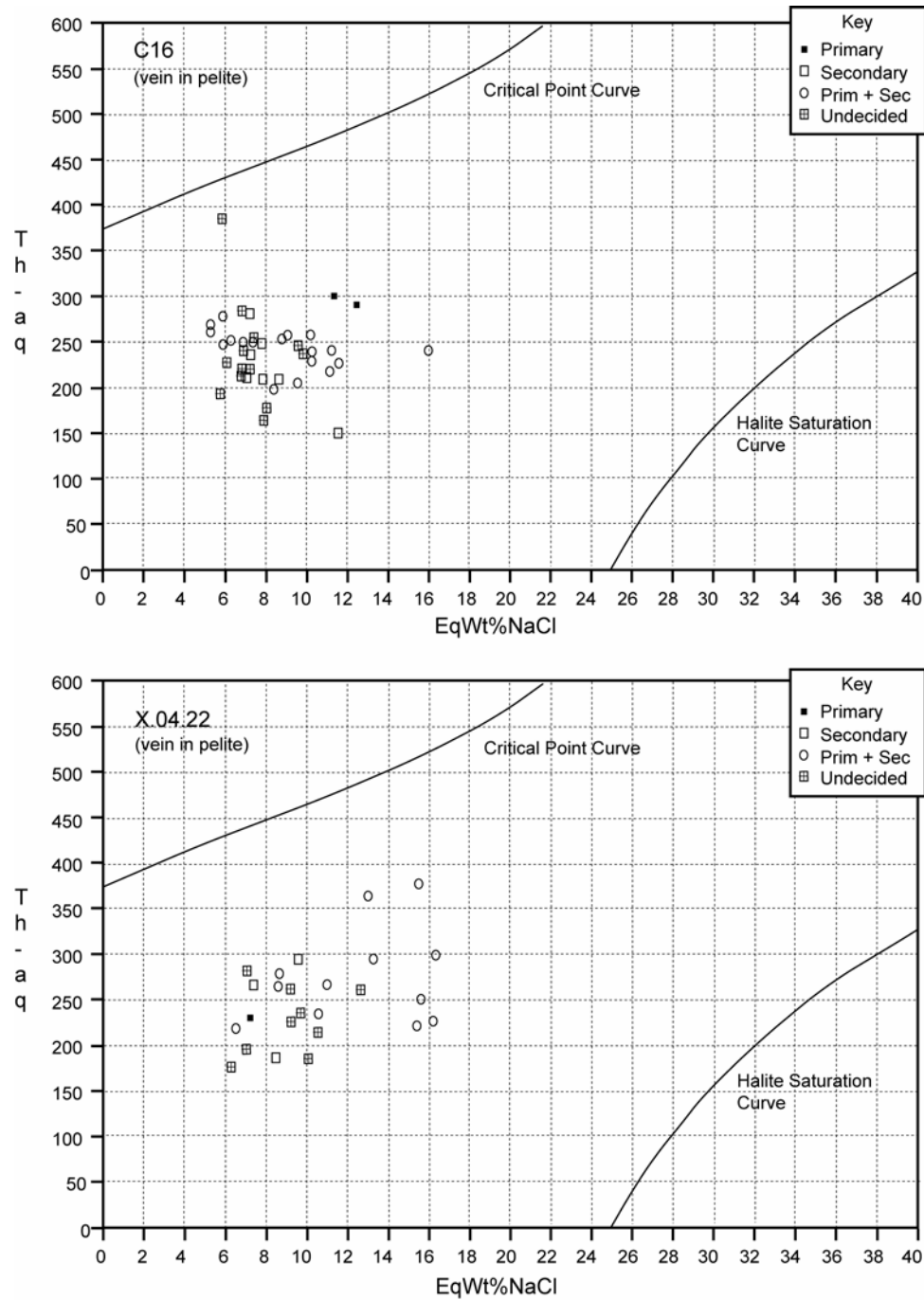


Fig. 3.33. Graphs salinity / homogenization temperature for the fluid inclusions of the samples C16 and X.04.22.

3.4.4 Results

3.4.4.1 Fluid inclusion descriptions

Different generations of fluid inclusions were recognized in the samples. Secondary fluid inclusions have been found in trails of variable orientation. Secondary fluid inclusions are generally smaller than primary

ones. Their size is in the order of 4 to 10 μm or smaller, with a round shapes. They show both an aqueous and a gaseous phase. Fluid inclusions interpreted to be primary are found in clusters or are isolated in the grain. They are of various size but show a main trend around 10-15 μm . They are frequently deformed and present irregular shapes. They show also mixed aqueous and gaseous phases.

3.4.4.2 Fluid composition

Raman microspectrometry indicated only water as a component for the fluid and gas phases. Both in the pelite and the marble, the nature of fluids during the formation of the veins and the deformation seems so to have had a relative simple composition of salt plus water, as no trace of CO_2 , CH_4 or N_2 has been detected. Heating-freezing stage measurements showed that both secondary and primary fluids inclusions in the marble contain in general less salt than the ones in the pelite, between 0 and 8% EqWt. NaCl in marble and between 4.5 and 16% in the pelites (Fig. 3.32; 3.33). The results show that the primary fluid inclusion contains generally more salt than the secondary ones. For the veins in the marbles, sample 18-10 shows a main composition trend for the fluid inclusions between 0 and 1 % EqWt. NaCl, presenting mostly secondary fluid inclusions (Fig. 3.34). In this sample, another population of secondary fluid inclusions has a composition between 4.0 and 6.0 % EqWt. NaCl, representing probably another fluid inclusion generation. Two primary fluid inclusions present composition of between 7.0 and 9.0 % EqWt. NaCl and are distinct from the other primary inclusions in the sample, which are mainly of composition around 2 – 3 % EqWt. NaCl. The sample 18.14 shows three main composition trends (Fig. 3.34). One is between 1.0 and 2.0 % EqWt. NaCl and comprises mostly secondary fluid inclusions. Another trend is between 3.0 and 4.0 % EqWt. NaCl and comprises primary and secondary fluid inclusions. The third trend presents composition between 7.0 and 8.0 % EqWt. NaCl and is formed by primary fluid inclusions. For the pelite, sample C16 present a main trend of around 6.2-7.2 % EqWt. NaCl, formed by both primary and secondary fluid inclusions. One population of primary fluid inclusions in this sample shows a more salt-rich composition between 10 and 16 % EqWt. NaCl (Fig. 3.33). Sample X.04.22 show the same trend with a population of primary fluid inclusions with more salt-rich composition around 13-16 % EqWt. NaCl and a main compositional trend between 6 and 10 % EqWt. NaCl with both secondary and primary fluid inclusions.

3.4.4.3 Microthermometry

Microthermometry measurements of fluid inclusions in the four samples shows a large range of homogenization temperature, between 120°C and 320°C in the marble and 150°C and 370°C in the metapelites (Fig. 3.35). The large spread of temperature makes interpretation difficult. However, several main trends can be distinguished. The primary fluid inclusion show generally higher temperature of homogenization than the secondary fluid inclusions. Both in the pelite and the limestone, large and irregular shaped primary fluid inclusions show high homogenization temperatures, mainly between 220 and 320°C. Some deformed primary fluid inclusion show lower homogenization temperatures between 150 and 200°C, which probably indicates reequilibration. Secondary fluid inclusions can show very different

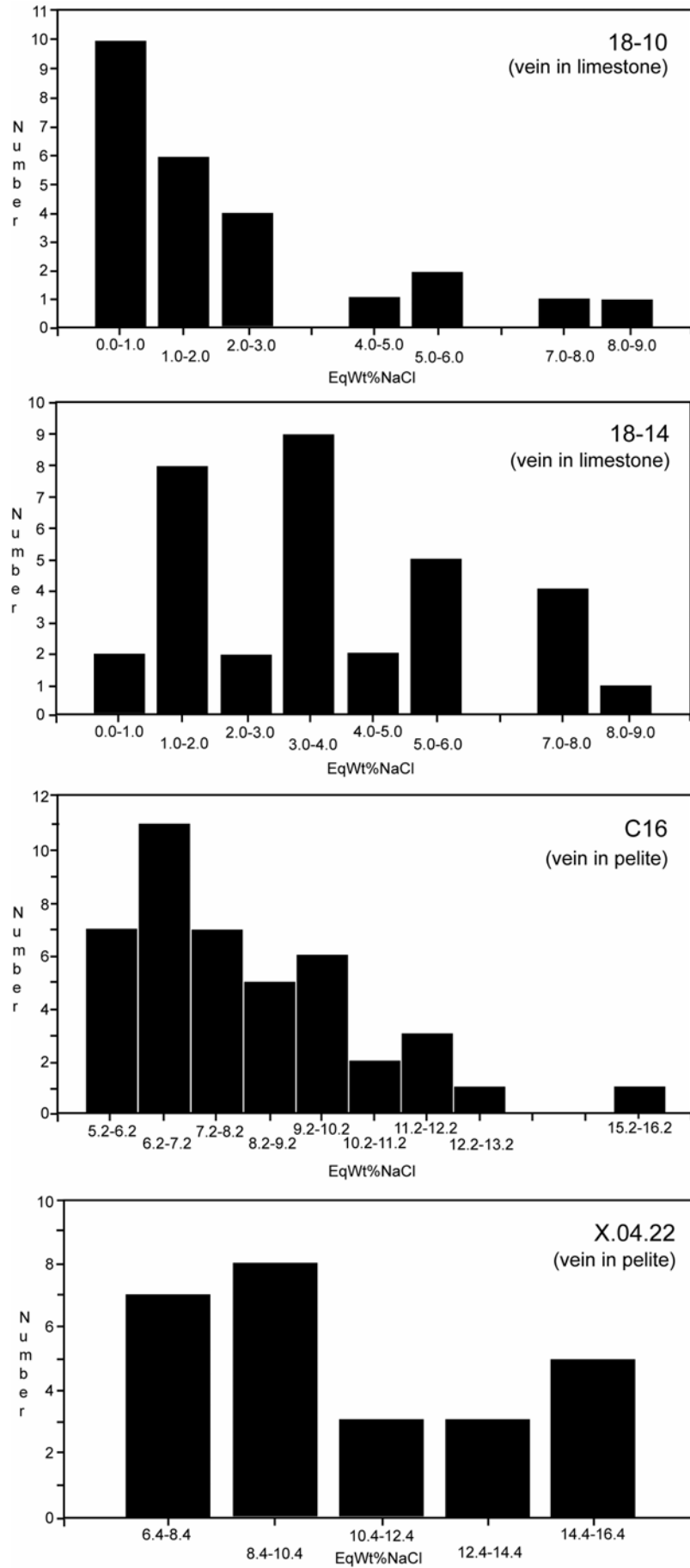


Fig. 3.34. Histograms showing distribution of the salinity of the fluid inclusions of the samples 18-10, 18-14, C16 and X.04.22.

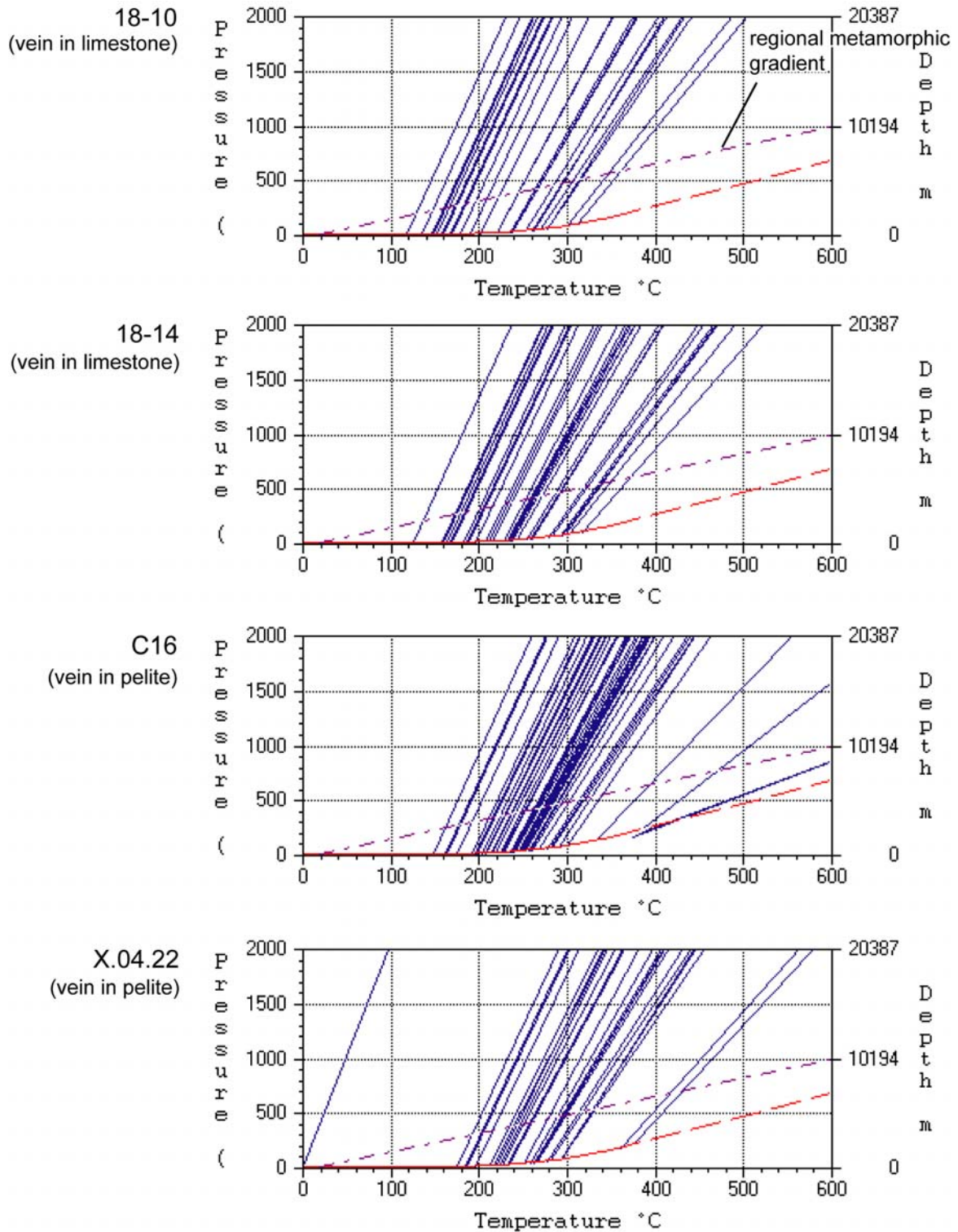


Fig. 3.35. Microthermometry results. The purple dash line is the regional pressure-temperature gradient (after Goscombe et al. 2004b).

homogenization temperatures between 120 and 300°C, probably due to the presence of several different generations of inclusions and late reequilibration. The homogenization temperature and the salt concentration of different fluid inclusions does not show any dependence on their position in the veins, and show the same trend in the border or center of the veins.

Regional peak metamorphic conditions in the Lower Ugab Valley have been estimated at 540-570°C and 2.5-3.2 kbar (Goscombe et al., 2003). This implicates relative low pressure and a high temperature gradient of about 60°C/km. This gives temperature estimates for the formation of the primary fluid inclusions in a range of about 240 to 370°C in the samples in the marble and of 240 to 440°C in the samples in the pelite. The large range of temperature and the deformed state of the primary fluid inclusions indicates probably late reequilibration which does not allow a precise constraint on the formation temperature of the veins. The maximum estimates which probably present the best preserved inclusions are in the range of temperature of greenschist facies conditions which correspond well to estimates from the stable isotope thermometry and structural constraints for the formation of the veins. The secondary fluids inclusions give temperature estimates for their formation from about 120 to 350°C according to the regional metamorphic gradient. The large range of temperature probably indicates several generations and late reequilibration.

3.5 Discussion on the formation of the syntectonic veins in the Lower Ugab Domain

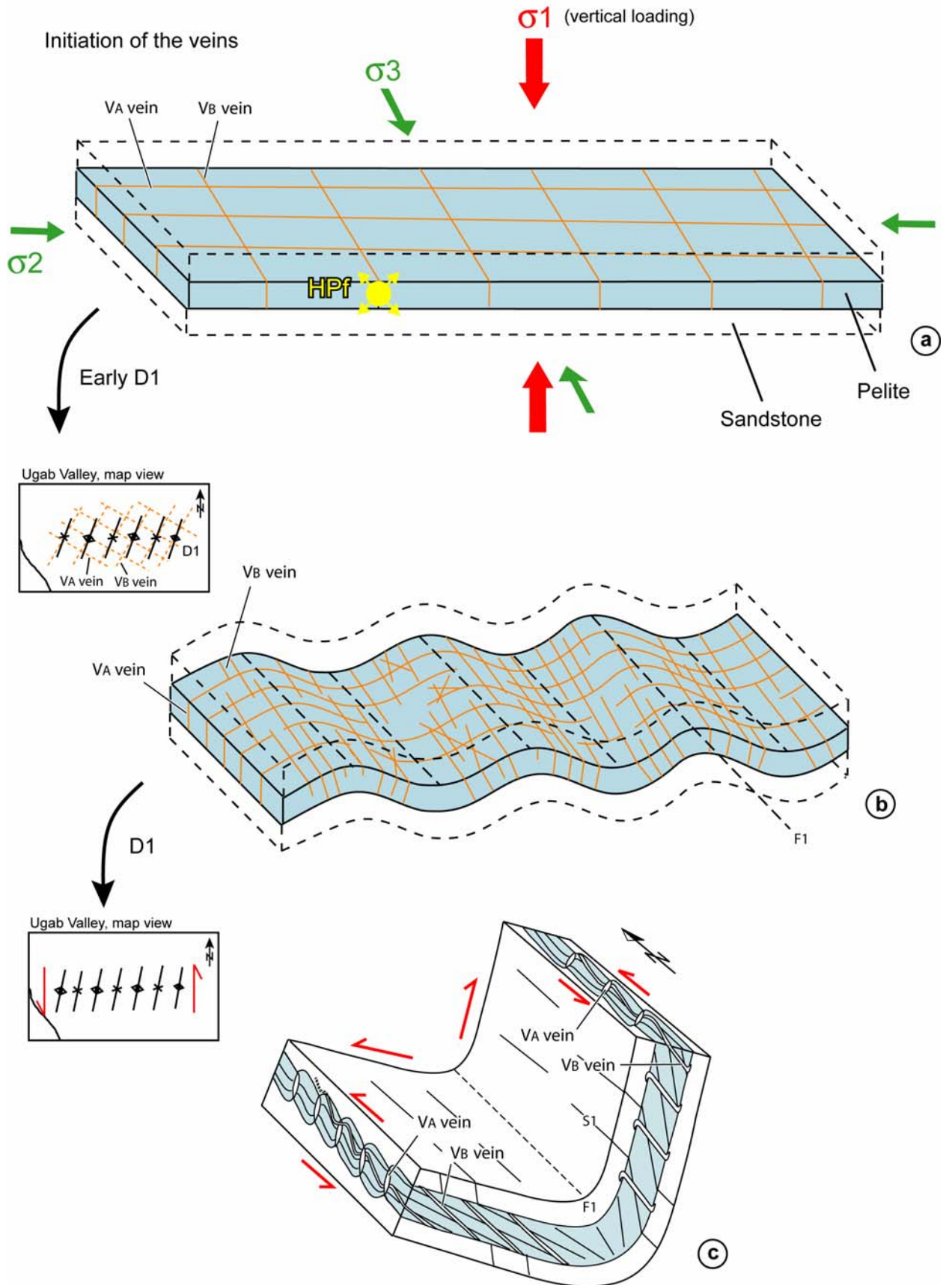
Disposition of fractures associated with folding described in the literature generally shows two main direction trends, disposed symmetrically to a fold. One set forms perpendicular to the fold axes and the other parallel to the fold axes. These sets are known respectively cross-strike joints and outer-arc extension joints (Van der Pluijm and Marschak, 2004; Twiss and Moores, 1992). Cross-strike joints form due to extension perpendicular to the compression direction which caused the folding. Outer-arc extension fractures form due to stretching in the outer-arc of folding layers. V_A veins are at high angle to the fold axis and may have formed as cross-strike joints due to extension parallel to the fold axis. V_B veins are not strictly parallel to D1 folds axes, but everywhere slightly oblique to the latter. They must therefore have formed in a different way from outer-arc extension joints. Bergbauer and Pollard (2004) have recently described orthogonal sets of joints at a high angle to bedding in folded sediments which are not symmetrically arranged to the fold hinge line. The joints are interpreted to initiate before the onset of folding. The formation of the folds then induced further propagation of the already existing joints, with formation of new joints of same strike than as the older ones. This model may be applied to the Lower Ugab Domain with formation of V_A and V_B veins as two sets of orthogonal veins at a high angle to the bedding when the metaturbitites were still unfolded (Fig. 3.36a). The D1 phase of folding may have initiated slightly oblique to V_B veins, maybe due to a slight regional reorientation of the main stress direction. Further propagation of veins in the same direction as V_A and V_B veins can then have occurred during the

deformation, as show by the presence of common veinlets of same orientation, which formed between V_A veins boudin necks.

Observation on the relative age of veins in grid a pattern suggests that they initiated at about the same time, or by alternating cracking episodes, occurring one after the other. No single set of veins can be shown to predate another, based on cross-cutting relation. Lithostatic pressure on horizontal non folded layers implies a vertical main stress direction σ_1 perpendicular to the bedding. Orthogonal sets of veins at high angle to the bedding can form by back-and-forth interchange of σ_2 and σ_3 (Van der Pluijm and Marschak, 2004; Rives et al., 1994; Twiss and Moores, 1992; Dunne and North, 1990, Fig. 3.27). This happens if σ_2 and σ_3 are relatively similar during the formation of veins. Such a similarity can therefore be postulated for veins in the Ugab Domain.

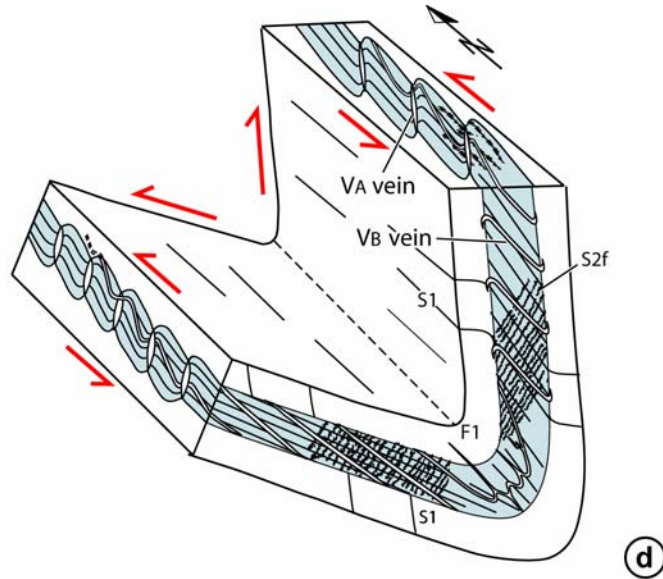
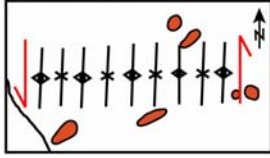
The formation of V_A and V_B veins mainly occurred in the apparent less competent layers of the siliciclastic formations and is unexpected for fracturing. Boudinage of the layers was, therefore, probably assisted by high fluid pressure. The large density of veins and the narrow spacing between veins, as well as the abundant development of vein networks in the marble beds are indications for hydrofracturing. Fluid pressure depends upon the porosity and the permeability of the beds and specifically on the presence of low-permeability capping layers. An alternation of fine grained sandstone and pelitic layer like those observed in the lower Ugab metaturbities favours limited vertical permeability. It is also known that sedimentary basins undergoing compaction and prograde metamorphism are areas of strong fluid release (Sibson, 2000). The fluids may be primary derived from the sediments, themselves released with compaction. Devolatilization reaction during prograde metamorphism may have also been a source for the fluids. The regional metamorphic peak in the biotite zone of the greenschist facies is contemporaneous to the D1 deformation. Since the veins form pre-to early D1, the reaction of destabilization of the phyllosilicates due to the prograde metamorphism may have generated substantial fluid overpressure (Connolly, 1997). Devolatilizations reactions in the pelite as a source of fluid imply a local origin of the fluid, which is in agreement with the isotopic results. The very early stage of the syenite intrusive event during late D1 and D2 deformation may have also generated devolatilization reaction by contact metamorphism. However the effect must have been minor for the formation of the veins since the recorded thermal front with the crystallization of the contact metamorphism porphyroblasts occur after the vein formation. On the other hand, a fluid pressure gradient travels faster than a thermal gradient.

Another hypothesis to explain the formation of the veins in the more pelitic layers rather than in the sandstone could be that they formed when the sandstones were still not completely lithified and less competent than the pelites, which implicates syn/late-diagenesis formation of veins. This hypothesis is unlikely since no trace of syndigenetic minerals are left in the veins and presence of fibrous chlorite and biotite in some veins suggest a formation at higher metamorphism conditions in the greenschist facies.



late- D1, early D2

Ugab Valley, map view



D2

Ugab Valley, map view

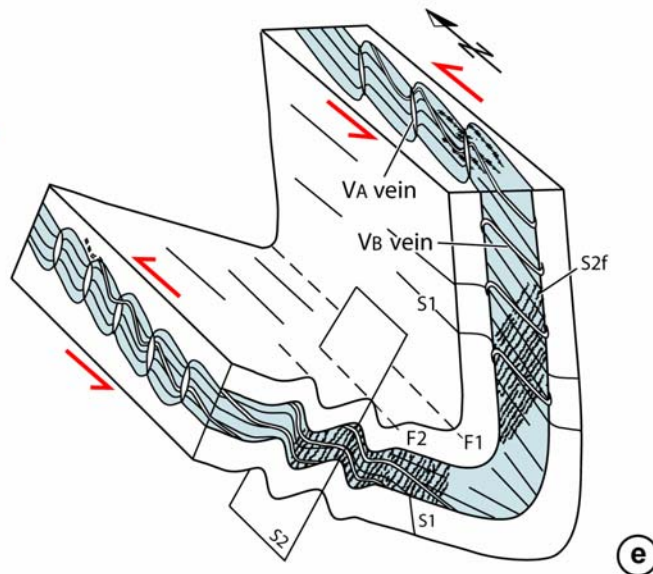
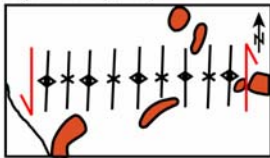


Fig. 3.36. (a) Initiation of the formation of two sets of veins of roughly orthogonal orientation, V_A and V_B veins, in the unfolded sediments, due to similar σ_2 and σ_3 . The veins preferentially form in the pelitic layers may have been helped by a high fluid pressure. (b) Initiation of the fold slightly oblique to the V_B veins in early D1 (c) progressive tightening of the folds during D1 deformation. A strong sinistral shearing component reoriented the D1 structure and caused reorientation of the veins and an asymmetric shape of the boudins. Flexural slip occurred due to the tightening of the folds. (d) Initiation of the intrusive event in the Lower Ugab Valley during late D1 to post D1 caused formation of the flame foliation S_{2f} in the pelite. Strong sinistral shearing continued the reorientation of the D1 structures and the veins. (e) D2 deformation caused open coaxial folds mostly in the flat limb of the D1 folds. S_2 crenulations cleavage overprinted S_{2f} .

3.6 Discussion on the deformation of the syntectonic veins of the Lower Ugab Domain

3.6.1 Effect of D1 deformation

Fig. 3.36 illustrates the inferred structural evolution of the two main types of syntectonic veins, V_A and V_B . D1 transpressional deformation caused the reorientation of both types of veins with a sinistral sense of rotation. Rotation of V_A veins causes the asymmetric shape of the boudins in pelite and marble layers by drag of the bedding. The rotation of the veins in non coaxial flow caused their boudinage in two directions, with boudin neck oriented at a high angle and subparallel to bedding planes. The reorientation of the veins caused the formation of abundant flanking folds of all types along their flanks, mainly marked by bedding and the main S1 foliation. Flexural slip during tightening of D1 folds caused the reorientation of the V_B veins in the limbs, so that they are now found with about the same orientation in the both limbs. Hook-shaped folds developed mainly in the steep limb of the D1 folds, where the tip of the veins penetrated the sandstone layers and testify to the rotation of the veins between bedding planes.

In some places near syntectonic intrusions of the region, granite-associated veins developed reaction rims with the host metasedimentary rocks, as for the veins near the Doros Pluton (Fig. 3.28). Those veins have been strongly reoriented during late D1 and D2 by east-west compression and north-south sinistral shearing and developed n-type flanking folds along their flanks due to the presence of alteration rim. S2f flame foliation formed late to post D1 and Pre D2 due to devolatilization reactions in the pelites caused by the emplacement of the syntectonic plutons in the regions. The flame foliation initiated frequently at the border of V_A and V_B veins.

3.6.2 Effect of D2 deformation

D2 coaxial deformation contributed to the tightening of the D1 folds and the reorientation of the veins in the two limbs of the folds (Fig. 3.30). V_B veins are folded by D2 open folds. S2f crenulations cleavage developed at a high angle to S1 by overprinting and reactivation of the S2f foliation.

3.6.3 Effect of D3 deformation

D3 north-south compression caused the folding of V_B veins and the narrowing of V_A veins by compression parallel to the layers, decreasing the aspect ratio of the boudins in the pelites and reinforcing the buckling of the bedding between the boudin necks. The resulting structure is comparable to the shortened boudins described by Vanbrabant and Dejonghe (2006) from the Ardennes also called “Mullion boudin” (Urai et al.,

2001; Kenis et al., 2002; 2004). In some places the entire boudins formed by V_A veins are strongly folded. The development of the regional scale D3 folds as the kilometric structures to the north of the Voetspoor granite caused the reorientation of the V_A veins by flexural slip, with opposite sense of shearing in the two limbs of the folds.

Chapter 4

Modelling of boudin neck rotation

4.1 Introduction

Flanking folds have been recently defined as the deflection of a passive planar marker in the rock, commonly named host element (HE) at the contact to a discontinuity such as a vein or a fault, named cutting element (CE). Both elements may rotate with respect to each other and external axes in progressive shear deformation (Passchier, 2001; Grasemann and Stüwe, 2001). Flanking folds have been previously described as fault drag, “hook folds”, or “fringe folds” (Hudleston, 1989; Grasemann et al., 1999). Much recent work based on analogue and numerical modelling has been carried out in order to understand the development of flanking folds (Grasemann et al., 2003; Wiesmayr and Grasemann 2005; Kocher and Mancktelow 2005; 2006; Exner et al. 2004; 2006). Grasemann et al. (2003) and Wiesmayr and Grasemann (2005) used the finite element program BASIL (Barr and Houseman, 1992; 1996) to investigate the development of the different type of flanking folds according to the vorticity conditions of the bulk flow and the initial orientation of the crosscutting element to the shear zone boundary. Exner et al. (2004; 2006) have shown the progressive development of s-type flanking folds and illustrated the development of flanking faults induced by multiple faults in simple shear. Kocher and Mancktelow (2005) used reverse modelling experiments of flanking folds to constrain the kinematic vorticity number of the bulk flow. They also investigated the effect of anisotropy in rocks on the development of flanking structures (Kocher and Mancktelow, 2006). The present study provides information about the development of asymmetric flanking folds at the tip of boudins necks when the boudins are deformed by coaxial and non-coaxial flow.

Comparison of numerical models with natural structures have been used to constrain different parameters of the bulk flow and the rheology of rocks (Kocher and Mancktelow 2005; Kenis et al. 2004; 2005). Kenis et al. (2004; 2005) performed a parameter-sensitive analysis on pure shear deformation of boudin structures to illustrate the effect of the total strain, the competency contrast between the vein and the rock, the stress exponent and the original geometry of the boudin on the resulting shape of the structure. The authors used the modelling results as a paleorheological gauge to constrain the relative viscosity of the sandstone in which the boudin developed and of the quartz in the veins (Kenis et al. 2005). A similar parameter-sensitive analysis was conducted on asymmetric boudins in the Lower Ugab Valley, Namibia. Details on these veins are given in the Chapter 3 of this thesis. The finite element program BASIL (Barr and Houseman, 1992; 1996; Houseman et al., in press) has been used to model boudin neck rotation in non coaxial flow and the formation of flanking folds leading to an asymmetric shape of the boudins. I investigated the effect of the total strain, the vorticity number of the bulk flow (W_k), the rheological contrast between the veins and the different layers and the initial geometry of the boudins.

The simulations were extended to the rotation of tension gashes in non coaxial flow, which can result in the formation of bone-shaped boudins, a common feature in the folded sediments of the Lower Ugab Domain. Such structures have been described by Malavieille and Lacassin (1988) and were interpreted to form in a transpression regime with extension parallel to the layers. The simulations show that those structures can also form in simple shear flow or a slightly transtensional regime.

4.2 Asymmetric boudins of the Lower Ugab Domain

Asymmetric boudins formed both in pelitic and marble layers of the metaturbites of the Lower Ugab Domain all over the area (Fig. 4.1; 4.2). Composite quartz-calcite veins form the boudin neck (V_A veins, Chapter 3). In the siliciclastic formation, the boudins developed in the pelitic layers surrounded by fine-grained sandstones. The boudin necks developed at a high angle to the D1 fold axes with a roughly east-west strike during the early stage of the regional deformation due to north-south extension. Asymmetric flanking folds marked by the bedding interface at the tips of the boudin neck are observed (Fig. 4.1; 4.2). They are interpreted to form due to sinistral rotation of the boudin neck. The originally symmetric boudins were deformed to an asymmetric shape by ongoing non-coaxial flow during mainly the transpressional D1 deformation (Chapter 3, Fig. 4.4). Non-sheared boudins show that the veins were originally oriented at a high angle to bedding before their rotation in non-coaxial flow (Figure 3.17). S_2 cuts the asymmetric flanking folds, indicating that the sinistral rotation of the veins mostly occurred during D1 (Fig. 3.12). Some indications show that a minor sinistral shearing component has also been active during D3. Evidence are en echelon veins along D3 fold axes and S_3 clockwise cleavage-transected folds (Passchier et al. 2002; Johnson, 1991). However, the minor D3 component of sinistral shearing developed locally and is restricted to the northwestern part of the area and D3 forms regionally mainly a north-south pure shear progressive phase of deformation (cf. Chapter 2). Boudinage of the boudin neck veins and an extreme convex bedding interface between the boudin necks indicates shortening parallel to the layers. In the pelites, S_3 is at a high angle to the bedding with a rough ENE-WSW orientation and is in general axial planar to the asymmetric boudin buckling folds. This testifies that the buckling of the bedding between the boudin necks partly results from D3 north-south compression parallel to the layers (Fig. 4.1). D3 therefore strengthened the buckling of S_0 between the boudin necks. In places where D3 is strong, the buckling folds between the boudin neck are clearly too tight to result only from the rotation of the vein or from the original boudinage of the layer; they develop as D3 folds where the hinge forms at the tip of the boudin neck, as shown in the example of Fig. 4.3. The observed asymmetric boudin structures are therefore polyphases reworked structures due to a transpressional sinistral shearing during D1, shortening perpendicular to the layer during D2 and a shortening parallel to the layers during D3 (Fig. 4.4). The estimation of the amount of strain resulting from D1-D2 and D3 phases of deformation is not easy in outcrop and in most cases impossible. The geometry of the asymmetric boudin varies with the lithologies. In the pelite, the buckling of S_0 is general stronger than in the limestone layers, probably due to a stronger rheological contrast between

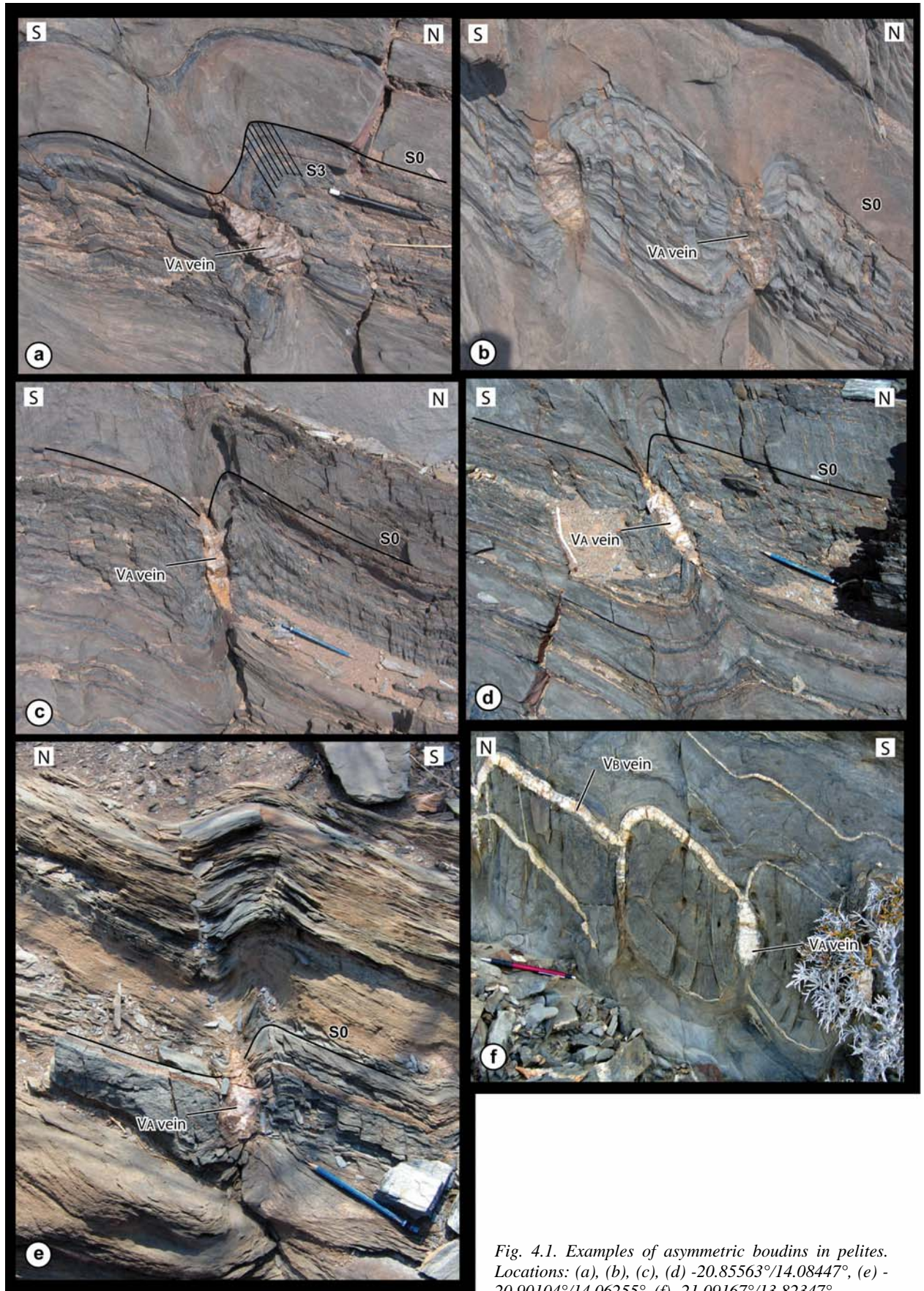


Fig. 4.1. Examples of asymmetric boudins in pelites. Locations: (a), (b), (c), (d) -20.85563°/14.08447°, (e) -20.90104°/14.06255°, (f) -21.09167°/13.82347°.

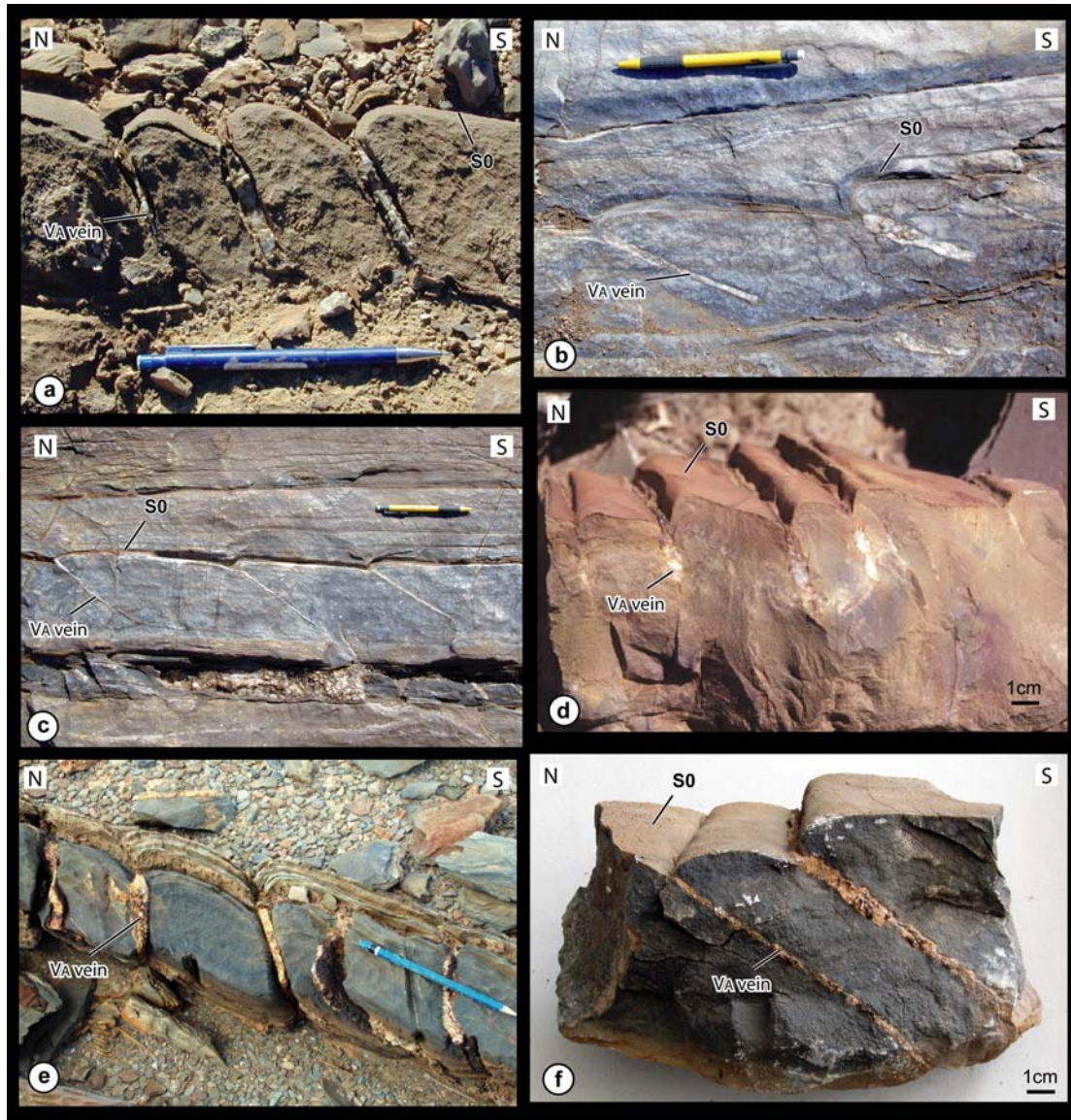


Fig. 4.2. Examples of asymmetric boudins in marble. Pictures (d) and (f) show that asymmetric flanking folds of the bedding surface at the tip of the veins are cylindrical structures. Locations: (a) - $20.86254^{\circ}/14.09392^{\circ}$ (b), (c), $-20.90588^{\circ}/14.30331^{\circ}$, (e) $-20.87298^{\circ}/14.14179^{\circ}$, (f) $-20.83929^{\circ}/14.13401^{\circ}$.



Fig. 4.3. Example of an extreme buckling of the bedding between the boudin necks. S3 is axial surface of the buckling which show that it developed as a D3 fold (location: $-20.94956^{\circ}/13.81637^{\circ}$).

Pre-syn D1

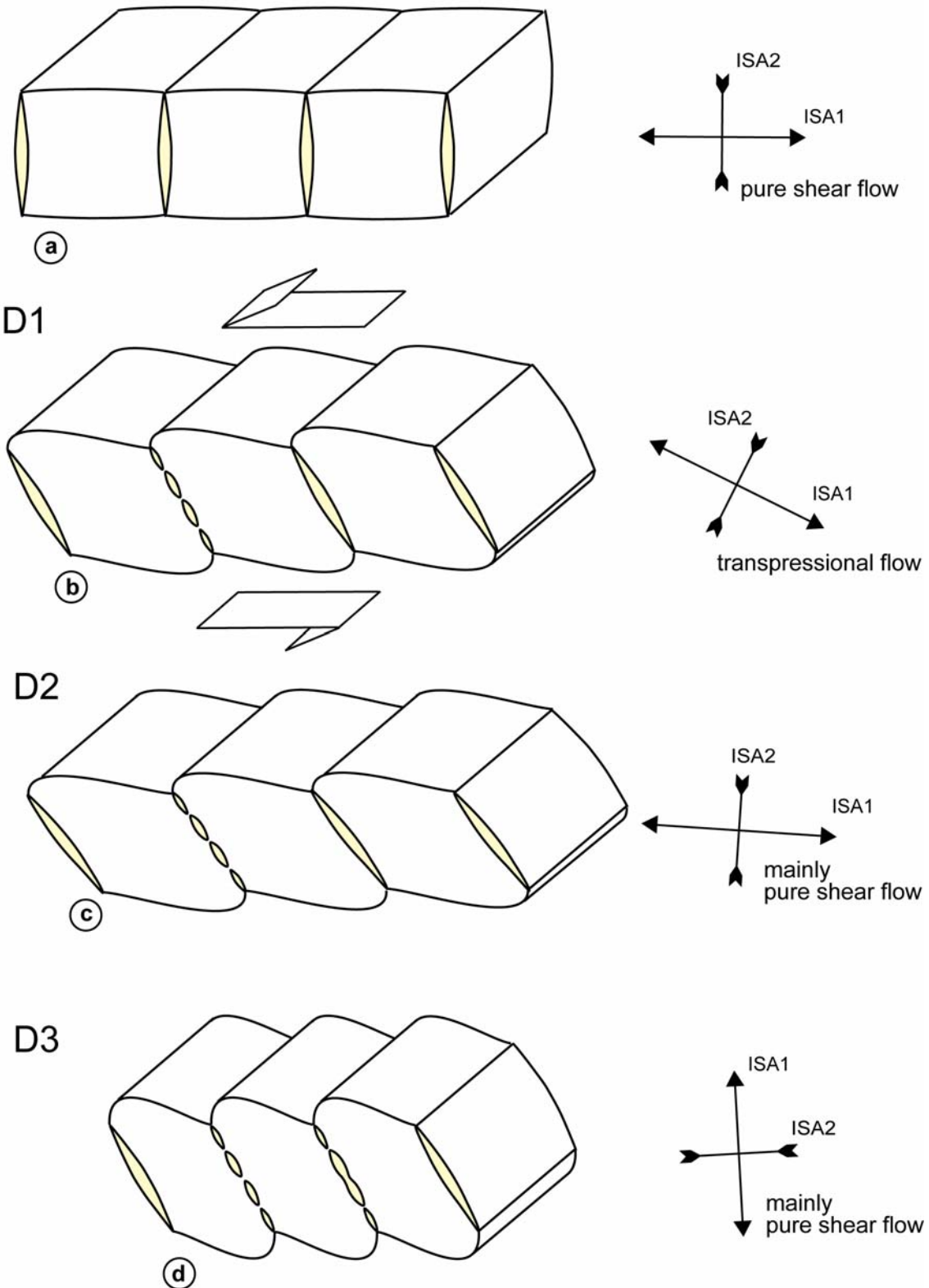


Fig. 4.4. Polyphase deformations of the boudins in the Lower Ugab Domain. (a) pre-D1 boudinage of the layer and formation of quartz and calcite boudin necks (b) D1 transpressional phase of deformation caused the rotation of the boudin neck and the formation of the asymmetric flanking folds at the tips of the veins, marked by the bedding interface. (c) D2 deformation caused mainly of a shortening perpendicular to the layer. (d) D3 caused a shortening parallel to the layer which led to the narrowing of the boudin necks.

the pelite and the surrounding sandstone layers. The hinges of the asymmetric folds are in general more angular in the pelite than in the limestone.

4.3 Bone shape boudins in the lower Ugab Domain

Bone-shaped boudins as described by Malavieille and Lacassin (1988) appear both in pelite and folded limestone layers of the Lower Ugab Domain, but are more common in the limestone. There are two generations of bone-shaped boudins. One is observed in section parallel to D1 fold axes with boudin necks at a high angle to the fold axes, with rough east-west strike. The other generation is observed in sections perpendicular to the D1 fold axes with boudin necks roughly parallel to the fold axes and a roughly north-south strike (Fig. 4.5). The two generations of bone-shaped boudins formed in both limbs of the D1 folds. In both cases the boudin necks are observed at a high angle to the bedding.

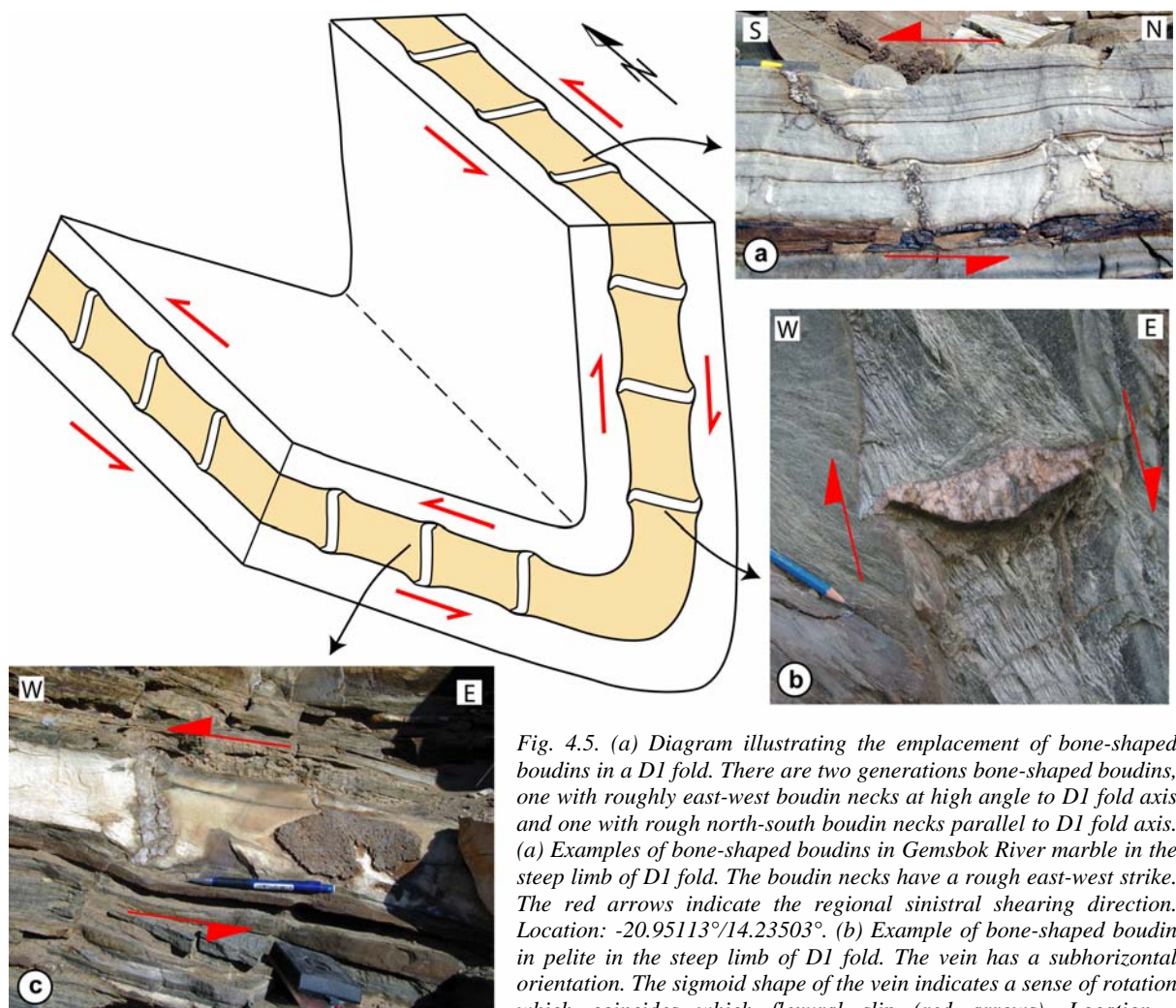


Fig. 4.5. (a) Diagram illustrating the emplacement of bone-shaped boudins in a D1 fold. There are two generations bone-shaped boudins, one with roughly east-west boudin necks at high angle to D1 fold axis and one with rough north-south boudin necks parallel to D1 fold axis. (a) Examples of bone-shaped boudins in Gemsbok River marble in the steep limb of D1 fold. The boudin necks have a rough east-west strike. The red arrows indicate the regional sinistral shearing direction. Location: $-20.95113^{\circ}/14.23503^{\circ}$. (b) Example of bone-shaped boudin in pelite in the steep limb of D1 fold. The vein has a subhorizontal orientation. The sigmoid shape of the vein indicates a sense of rotation which coincides with flexural slip (red arrows). Location $-20.98051^{\circ}/13.81146^{\circ}$. (c) Example of bone-shaped boudin in Gemsbok River marble the flat limb of D1 fold. The sigmoid shape of the boudin indicates a sense of shearing which coincides with flexural slip (red arrows) (location: $-21.006254^{\circ}/14.03498^{\circ}$).

Bone-shaped boudins in sections oriented parallel to the D1 fold axes with rough east-west boudin-neck strike have generally a sigmoid shape. The sigmoid shape is formed by the bending of the tips of the veins. This seems to result from the deformation of the veins rather than the original shape of the vein due to its opening, since the bedding bends also at the tip of the veins. The sigmoid shape and development of flanking folds along the veins indicate that they underwent sinistral rotation. They are therefore associated with V_A veins of roughly similar strike and which underwent the same sinistral shear. However, the original orientation of the bone-shaped boudin necks was probably originally oblique to the bedding, since the necks lie roughly perpendicular to the bedding after sinistral rotation. These veins may therefore have formed as tension gashes during the early D1 deformation due to the sinistral shearing component of the bulk flow. Some undeformed boudin necks may have formed originally at a high angle to the bedding like the V_A veins. The bone shape may then have resulted from further north-south ductile extension of the layer that contains the veins.

Bone-shaped boudins in sections perpendicular to the fold axes, with roughly north-south strike show generally the same sigmoid shape with development of flanking folds along their side, indicating a reorientation (Fig. 4.5). The sigmoid shape and the flanking folds indicate two opposite shearing directions in the two limbs. The shear senses coincide with flexural slip along the flanks of the D1 folds. The veins may have also initially formed as tension gashes along the flanks at the early stage of flexural slip or as boudin veins due to the extension along the limbs caused by east-west D1-D2 shortening during tightening of D1 folds.

4.4 Numerical technique

The program “BASIL” of Barr and Houseman (1992; 1996) has been used to model boudin neck rotation and the formation of flanking folds along the rotating veins. It is a two-dimensional finite element program which can be used to model non-coaxial bulk flow. In the natural examples, the veins and flanking fold structures are mostly cylindrical in three dimensions (Fig. 4.2d, f) and therefore BASIL is well-suited for the dynamic interpretation. This program has been already used to model flanking structure development (Grasemann and Stüwe, 2001; Grasemann et al., 2003; Wiesmayr and Grasemann, 2005).

Viscous medium behaviour can be described by the constitutive relationship (Jessell et al., 2005):

$$\tau_{ij} = 2\eta\varepsilon_{ij} = \eta \left[\frac{\partial u_i}{\partial x_j} + \frac{\partial u_j}{\partial x_i} \right] \quad (1)$$

Where τ_{ij} is the stress tensor, ε_{ij} is the strain rate tensor, u is the velocity and η is the viscosity, which is defined by:

$$\eta = \frac{1}{2} B E^{\frac{n-1}{n}} \quad (2)$$

E is the second invariant of the strain rate tensor, n is a power-law exponent describing the non-linearity of the proportionality between stress and strain rate, and B is a material dependent constituent. BASIL calculates incompressible plane strain deformation by solving the force balance equation in two dimensions:

$$\frac{\partial}{\partial x_j} \tau_{ij} + \frac{\partial}{\partial x_i} p = 0 \quad (3)$$

Where the summation is over the i and j indices and p is the pressure.

4.4.1 Mesh generation and boundary conditions

Three different meshes have been used, all composed of a square divided by three horizontal parallel layers, one internal and two externals (Fig. 4.6a). The internal layer is cut by one or two veins. The viscosity of the internal layer, the two external layers and the veins can vary. The internal layer represents the boudinaged layer in the natural examples. It therefore represents the pelitic layer in the siliciclastic formations, while the two external layers model the fine grained sandstone layers. In the carbonate formations, the internal layer is the boudinaged marble layer and the external layers are the two neighbouring non-boudinaged marble layers. We assumed in the model that the two external layers show the same viscosity. The first and second mesh represent respectively one or two veins that cut perpendicular the internal layer (Fig. 4.6b and c). The third mesh represents two veins at 135° to the shear zone, which is the orientation of the formation of tension gashes veins, oriented parallel to the shortening instantaneous stretching axis of isochoric plane strain in simple shear flow (Fig. 4.6d). The three meshes include horizontal passive markers named “A, B, C, D, E, F, G, H” (Fig. 4.6a). The markers are parallel to the shear zone boundaries, and consequently parallel to the fabric attractor of the flow (Passchier, 1997). “A” is at the centre of the internal layer and “C” is the contact surface between the layers (bedding interface). For reference, the length of the side of the square of the mesh is 1.

The grid in the meshes is generated with a self-meshing routine which creates rectangles subdivided by diagonals in alternating directions for the two first types of mesh and diagonal in one direction for the third type. The model includes a region of 25 by 25 elements for the mesh with a single vein and 30 by 30 elements for the meshes with two veins. The relatively simple geometry of the mesh allows high strain deformation. Finer meshing and a grid composed of Delauney triangles (Houseman et al., in press) with hexagonal symmetry have been tested and do not influence the general shape of the deformed boudins.

Boundary conditions were defined to approximate ideal simple shear and general shear. The displacement boundary conditions at the top and bottom of the grid are described by the velocity gradient tensor \mathbf{L} for homogeneous isochoric plane strain flow:

$$L = \begin{pmatrix} \frac{\partial u_i}{\partial x_i} & \frac{\partial u_i}{\partial x_j} \\ \frac{\partial u_j}{\partial x_i} & \frac{\partial u_j}{\partial x_j} \\ 0 & 0 \end{pmatrix} \quad (4)$$

Where:

$$\frac{\partial u_i}{\partial x_i} = \frac{\partial u_j}{\partial x_j}$$

Steady flow is assumed, so that the incremental strain matrix doesn't change during the deformation history, i.e. for an experiment the stretching rate factor S and the kinematic vorticity number W_k remain constant. W_k defines the boundary flow and corresponds to the cosine of the angle α between irrotational material lines (eigenvectors) (Passchier, 1987). $W_k = 0$ for pure shear and $W_k = 1$ for simple shear (Means et al., 1980). The flow type also defines the orientation of the stretching (ISA₁) and shortening axis (ISA₂), given respectively by the angles $\beta + 90^\circ$ and β . α and β are related by $\beta = (\alpha + 90^\circ)/2$. In order to translate the velocity gradient tensor into comparable finite deformation, the component of L can be calculated by (Grasemann et al., 2003; Wiesmayr and Grasemann, 2005; modified after Passchier, 1987):

$$L = \begin{pmatrix} \frac{S}{2}\sqrt{1-W_k^2} & W_k S \\ 0 & -\frac{S}{2}\sqrt{1-W_k^2} \end{pmatrix} \quad (5)$$

The corresponding deformation gradient tensor D given by Ramberg (1975) and combined with Eq. (5) is (Wiesmayr and Grasemann, 2005):

$$D = \begin{pmatrix} \exp\left(\frac{St}{2}\sqrt{1-W_k^2}\right) & \frac{2W_k \sinh\left(\frac{St}{2}\sqrt{1-W_k^2}\right)}{2W_k} \\ 0 & \exp\left(-\frac{St}{2}\sqrt{1-W_k^2}\right) \end{pmatrix} \quad (6)$$

Where t is the time.

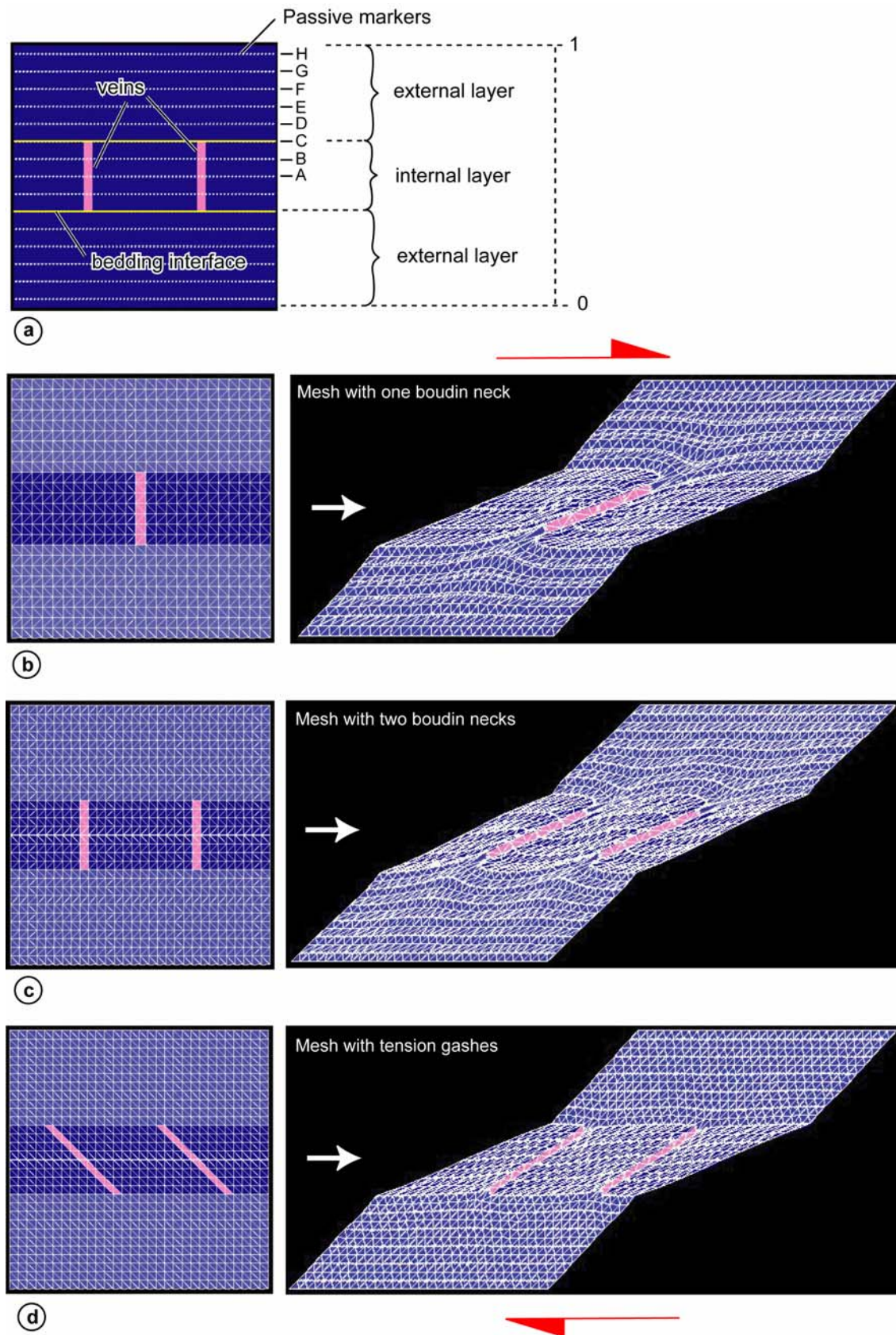


Fig. 4.6. Three different meshes used in the simulations. (a) All the three meshes are composed of a square divided by three horizontal layers. Veins cut the internal layer. The meshes have horizontal passive markers (A-H). (b) Mesh with one boudin neck cutting perpendicular the internal layer. (c) Mesh with two boudin necks cutting perpendicular the internal layer. (d) Mesh with two tension gashes cutting the internal layer at 45° . The relative viscosity of the layers and the veins can vary. The three meshes are deformed by coaxial and non-coaxial flow (here simple shear progressive deformation indicated by the red arrows).

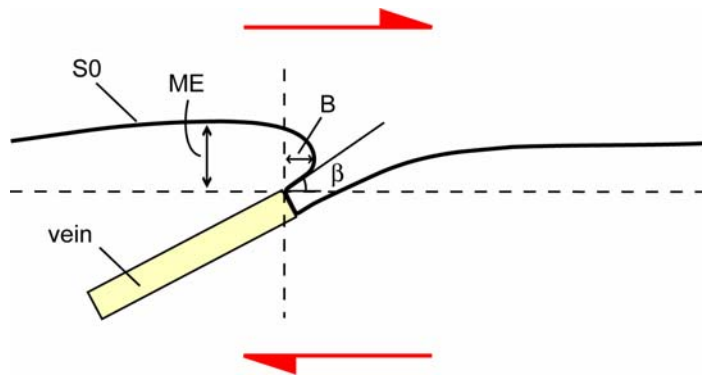


Fig. 4.7. Drawing of a flanking structure at the tip of a vein. We used the parameters Maximum Elevation (ME), bulge (B) and β , the angle between the tangent of the flanking folds at the border of the vein and the horizontal to describe the structure.

4.5 Parameter sensitivity analysis

The aim of the numerical approach is to see how the conditions of the flow, the competency contrast between the boudinaged layer, the external layers and the veins and the initial geometry of the boudins before deformation do influence the shape of the reworked boudin in coaxial and non-coaxial flow. A parameter sensitivity analysis was therefore performed. In each experiment only one parameter varies, the others being fixed to a certain value (value by default). The following parameters are investigated:

1. The total deformation
2. The boundary flow conditions (kinematic vorticity number)
3. The competence contrast between pelite, the psammite layers and the quartz veins.
4. The initial aspect ratio of the boudins
5. The thickness of the veins
6. The stress exponent

Kenis et al. (2005) have shown that in the middle crust, the psammite or polyphase quartz rich rocks seems to be significantly weaker than wet quartz and that rocks seems to behave in a Newtonian way during deformation. Since the veins of the boudin neck are mainly composed of quartz, they are therefore fixed in the different meshes at a viscosity value ten times stronger than the wall rock during the experiments where we vary the other parameters. By default, the n-exponent is also fixed to be 1 and therefore Newtonian deformation is considered. The three layers are fixed by default with the same viscosity for a better measure of the influence of the tested parameter.

Description of flanking folds geometry both by qualitative classification and quantitative description by Bézier curves are given by Coelho et al. (2005). The asymmetric flanking fold marked by the bedding at the tip of the boudin necks of the investigated deformed boudins present neither slip nor lift (Fig. 4.1; 4.2; 4.6, Coelho et al., 2005). The asymmetric shape of the structure is marked by an over- or neutral roll with bulge geometry on one side of the vein and a neutral-roll without bulge on the other side of the vein. In order to compare the different shape of flanking folds between different simulation results, we introduce three

parameters, i.e the maximum elevation of the flanking folds (ME), the bulge (B) and the angle β between the horizontal shear zone and the tangent of the folded layer interface (Coelho et al., 2005), which is also an expression of the bulge (Fig. 4.7).

4.5.1 Effect of the total finite strain in simple shear flow

The effect of the total strain in simple shear flow on the buckling geometry of the interface layer is illustrated in Fig. 4.8 with the mesh with one boudin neck. The viscosity of the internal layer is fixed at the same value as the viscosity of the two surrounded layers and the vein is ten times stronger than the wall rock. Fig. 4.8 shows simulations of simple shear deformation up to $\gamma = 3$. Simple shear experiments up to $\gamma = 4$ have been carried out and the results are presented in the appendix 4.8a, b.

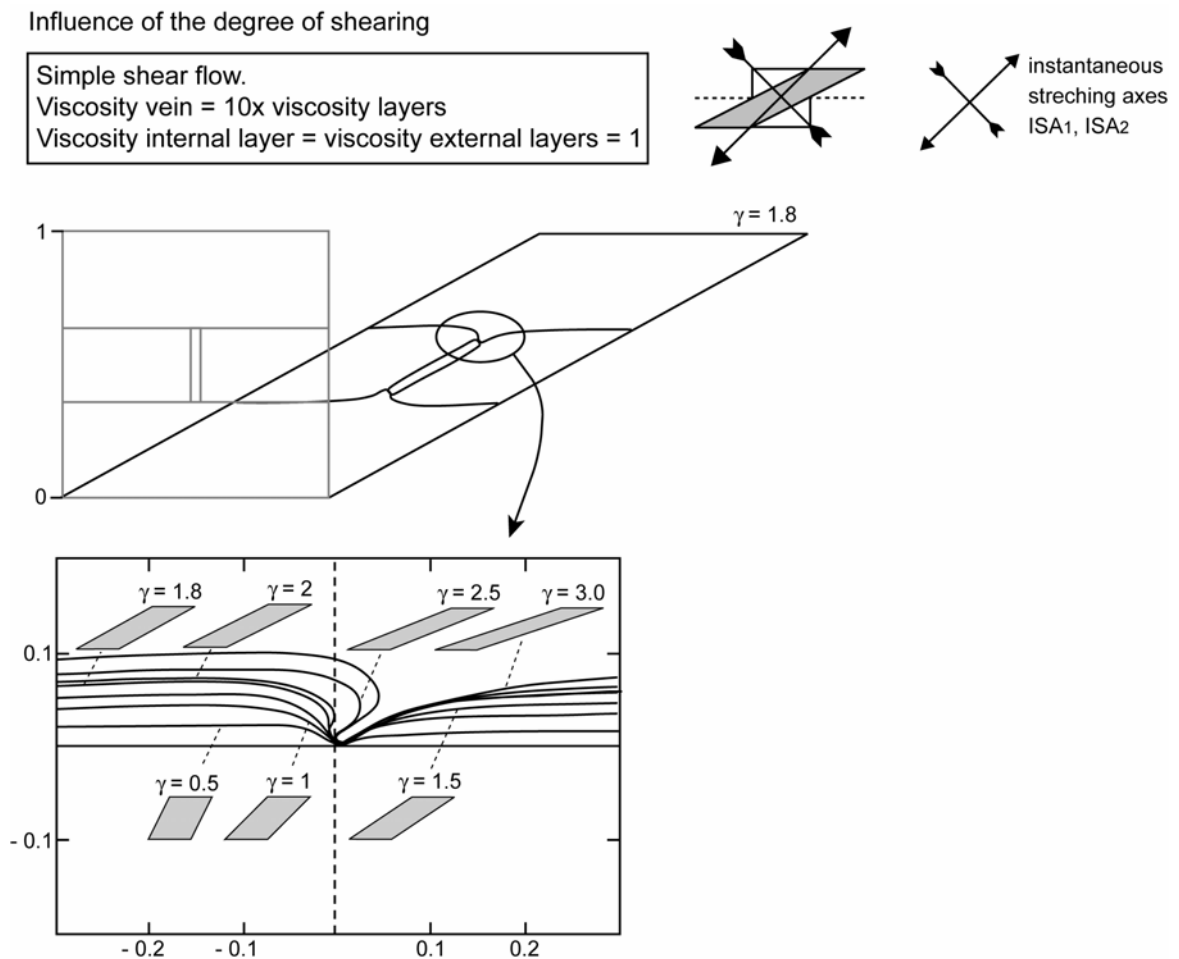


Fig. 4.8. Diagrams showing the influence of simple shear progressive deformation for the mesh with a single vein.

An evolution of the geometry of the asymmetric buckling of S0 at the tip of the vein can be observed with an increase of simple shear deformation. The resulting asymmetric shape of the bedding is similar to what is observed in nature (Fig. 4.1; 4.2). Elevation and bulge of the bedding interface increases and the angle α decreases with an increase in simple shear deformation (Fig. 4.8). The bulge begins to be positive from $\gamma = 2$ in the presented example. The results show therefore that the total strain and the amount of rotation of the vein are important parameters for the shape of the deformed boudins. Simple shear flow is enough to cause an asymmetric buckling of S0. The asymmetric geometry can also form without competence contrast between the layers, but with veins stronger than the host medium. Passive markers in the simulation results show the formation of n-type flanking folds along the rotating veins (appendix 4.8a, b). This is in agreement with the numerical simulations done by Grasemann and Stüwe (2001) on the rotation of strong cutting element in simple shear flow. Those experiments show the development of n-type flanking folds along a rotating crossing element stronger than the host medium.

4.5.2 Effect of the kinematic vorticity number

4.5.2.1 *Transtensional regime*

The effect of a progressive change of the kinematic vorticity number (W_k) in transtensional regime on the mesh with two boudin veins is illustrated in Fig. 4.9. W_k varies in the experiments by increasing progressively the pure shear component of the flow, with shortening parallel to the layers. W_k is 1 for simple shear flow and 0 for strictly pure shear flow (Means et al., 1980). The results show that an increase of pure shear component parallel to the layer increases significantly the maximum elevation of the buckling between the boudin necks. The bulge and the angle β vary only slightly by increasing the pure shear component. In strictly pure shear flow, we obtained typical shortened boudin geometry with extreme convex layer interface between the boudin necks. The structure is similar to the “mullion” boudin as described by Kenis et al. (2004) and Urai et al. (2001) with a symmetric buckling of the bedding between the boudin necks (Fig. 3.17). Appendix 4.9.1 a,b and 4.9.2 a,b show the simulation results of the meshes with one and two boudin necks. Both meshes show similar resulting geometries. The passive markers inside the internal layer (markers A, B) show the development of n-type flanking folds along the veins from $W_k = 1$ to $W_k = 0.89$. The flanking folds are slightly asymmetric near the bedding surface (see marker B). Increasing the pure shear component causes a change of geometry towards symmetric folding of the passive marker at both sides of the veins, following the geometry of the layer interface.

The effect of the kinematic vorticity number in transtension with a pure shear component of the flow perpendicular to the layers in a mesh with tension gashes is illustrated in Fig. 4.10. From $W_k = 1$ to $W_k = 0.89$, the rotation of the veins lead to bone-shaped boudins as described by Malavielle and Lacassin (1988). Those structures were interpreted to form in a transpressional regime, with the extensional eigenvector parallel to layering (Passchier, 1998; Malavielle and Lacassin, 1988). It is therefore interesting to note that such structures can also appear in a slightly transtensional regime, with the shortening eigenvector parallel

Influence of the kinematic vorticity number

General shear flow, transtensional regime
 Viscosity vein = 10x viscosity layers
 Viscosity internal layer = viscosity external layers = 1

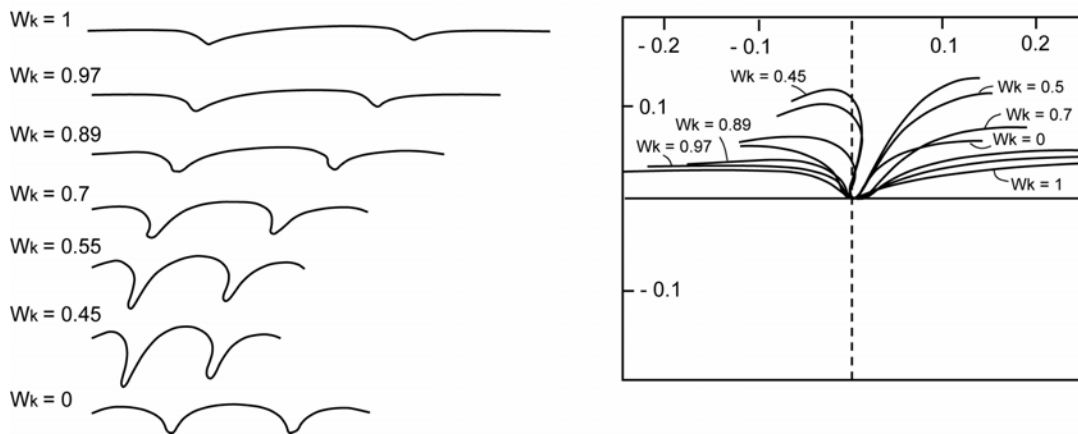
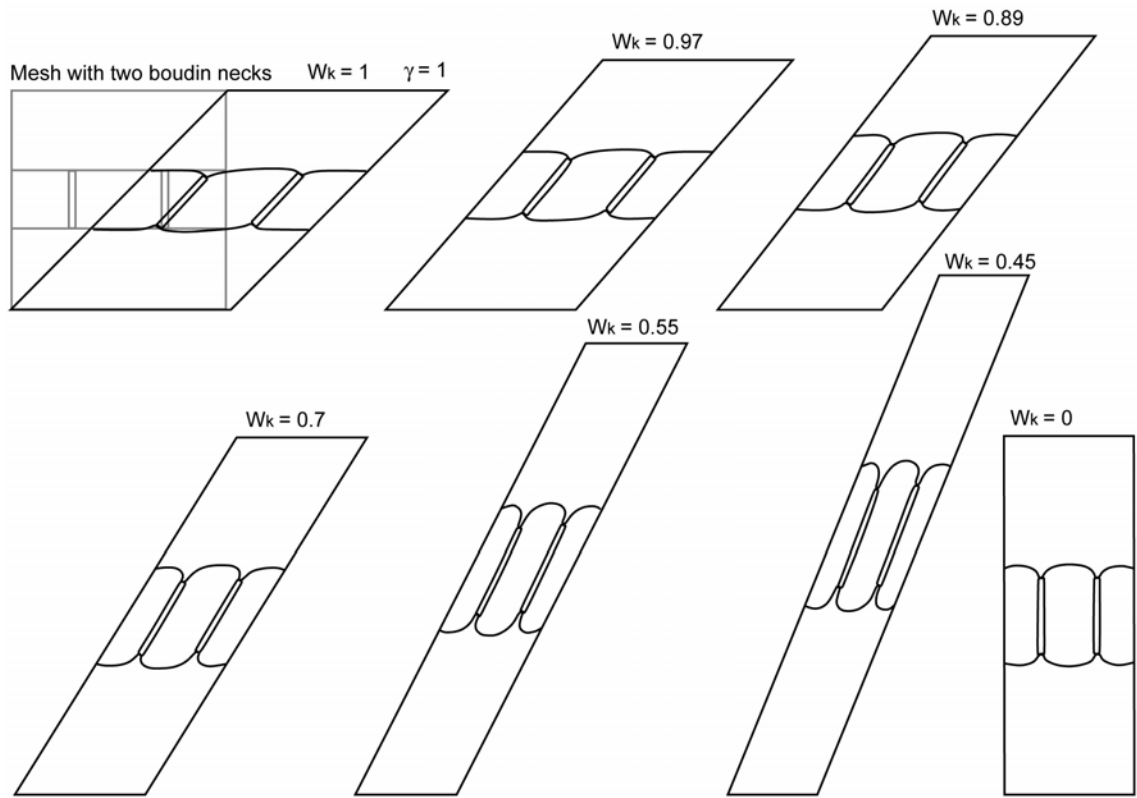
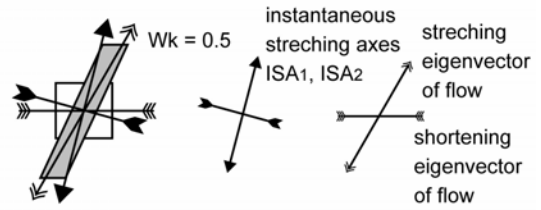


Fig. 4.9. Diagrams showing the influence of the kinematic vorticity number W_k of the bulk flow in transtensional regime for the mesh with two veins perpendicular to the layers. We vary the amount of pure shear component for a similar amount of simple shear progressive deformation.

Influence of the kinematic vorticity number

General shear flow, transtensional regime
 Viscosity vein = 10x viscosity layers
 Viscosity internal layer = viscosity external layers = 1

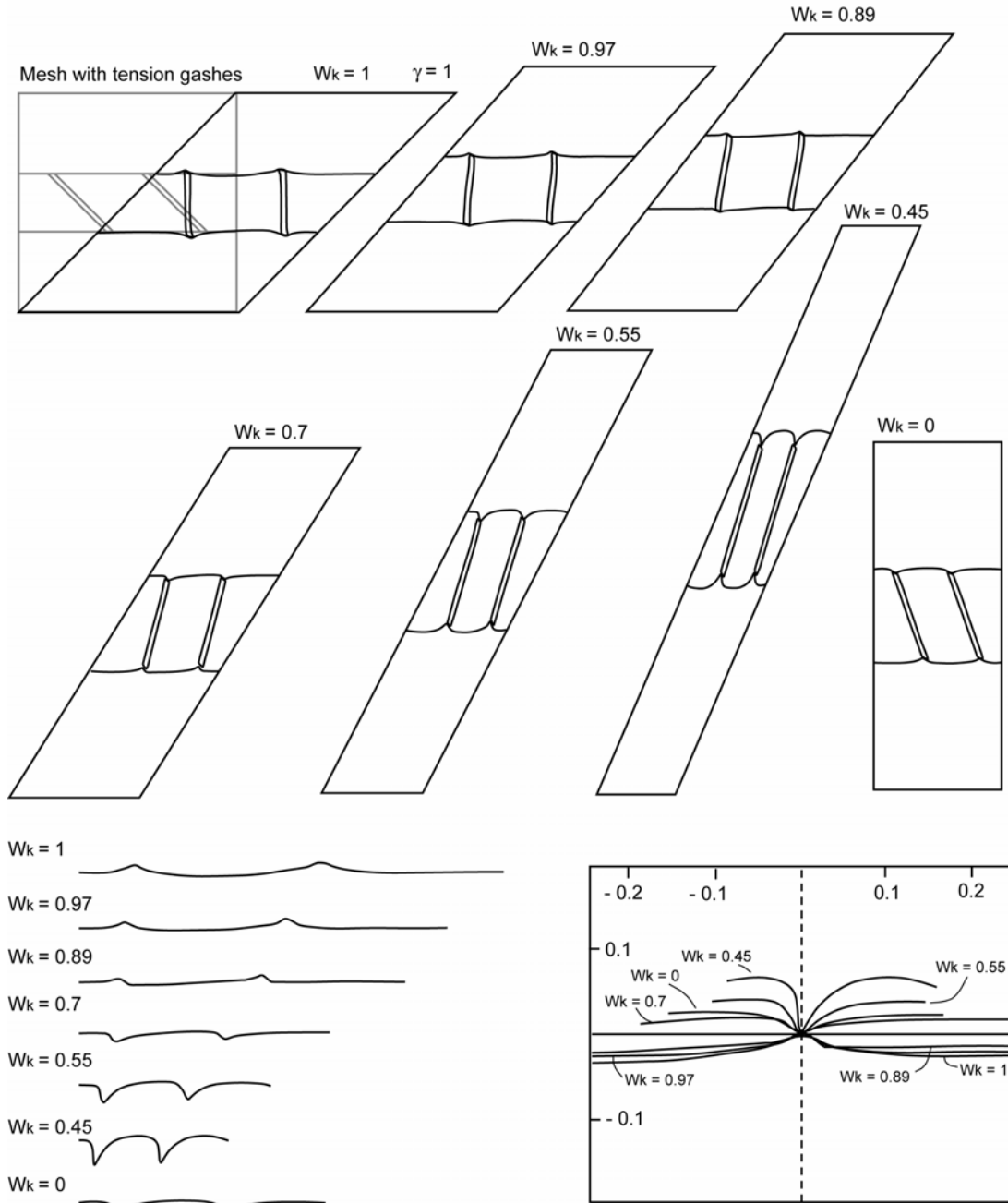
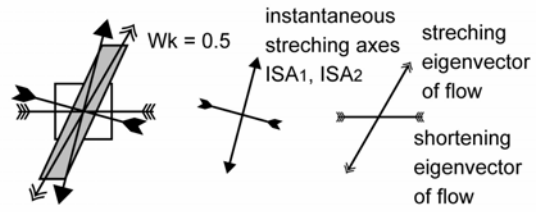


Fig. 4.10. Diagrams showing the influence of the kinematic vorticity number Wk of the bulk flow in a transtensional regime for the mesh with tension gashes.

to the layer (Passchier, 1998). Occurrence of “bone shape” boudins in the field should therefore not necessarily lead to the interpretation of an extension component parallel to the layer but may also appear in simple shear flow or in a slightly transtensional regime, associated with the rotation of originally oblique veins as tension gashes. With an increase of the amount of compression parallel to the layer, the geometry of the boudin tends towards a symmetric buckling of the bedding interface between the boudin necks similar to shortened boudin structures (see marker C, appendix 4.10 a, b). Passive markers A and B in the internal layer show s-type flanking fold geometries with a slight synthetic displacement of the marker along the rotating tension gashes in a transtensional regime (Passchier, 2001). When the deformation is not strong enough to rotate the veins to a position $\geq 90^\circ$ to the shear plane, the passive markers show shear band geometries along the veins, as illustrated by the simulation result of strictly pure shear deformation of appendix 4.10 b.

4.5.2.1 Transpressional regime

The effect of a progressive change of the kinematic vorticity number (W_k) in a transpressional regime on the mesh with two boudin veins is illustrated in Fig. 4.11 and appendixes 4.11 a and b. The pure shear component progressively increases with shortening perpendicular to the layer (extensional stretching eigenvector parallel to the layer; Passchier, 1998). The results show that an increase of the shortening perpendicular to the layer slightly decreases the maximum elevation of the flanking folds marked by the bedding interface at the tips of the veins. From $W_k=1$ until $W_k=0$, the flanking folds show always a slight asymmetry at the tip of the veins. The pure shear component perpendicular to the bedding in the non-coaxial flow induces passive rotation of the veins. In strictly pure shear flow, the internal layer stretches parallel to the layering between the boudins necks, creating a bone-shaped boudin geometry. The veins remain at their original orientation orthogonal to the bedding and act as rigid objects during the compression perpendicular to the layer (veins ten times stronger than the layers). The deformation therefore concentrates in the internal layer that stretches horizontally in the direction of the extensional eigenvector of the flow. The bone shape geometry therefore is due to the competency contrast between the veins and the layers. This confirms the observations of Kenis et al. (2004) who show the development of similar bone-shaped structure in their numerical simulations of deformed boudins in pure shear flow with extension parallel to the layers with a boudin neck stronger than the layers.

The effect of the kinematic vorticity number (W_k) in a transpressional regime on the mesh with two tension gashes is illustrated in Fig. 4.12 and appendixes 4.12 a and b. An increase of the shortening component perpendicular to the layers tends to flatten the bedding interface at the tips of the veins. From $W_k=1$ to $W_k=0.89$ the bedding interface forms a geometry of bone-shaped boudins. From $W_k=0.55$ to $W_k=0$ the bedding interface remains almost flat. The pure shear component perpendicular to the layer induces a passive rotation of the veins in a sense opposite to the rotation due to the simple shear flow component. This occurs because of the original oblique orientation of the veins of 45° relative to the layer. From $W_k=0.45$, the counter rotation due to the pure shear component of the progressive deformation is more important than the normal rotation due to the simple shear component and the veins are found in a new position with an angle to the bedding that is smaller than 45° . With an increase in the pure shear component

Influence of the kinematic vorticity number

General shear flow, transpressional regime
 Viscosity vein = 10x viscosity layers
 Viscosity internal layer = viscosity external layers = 1

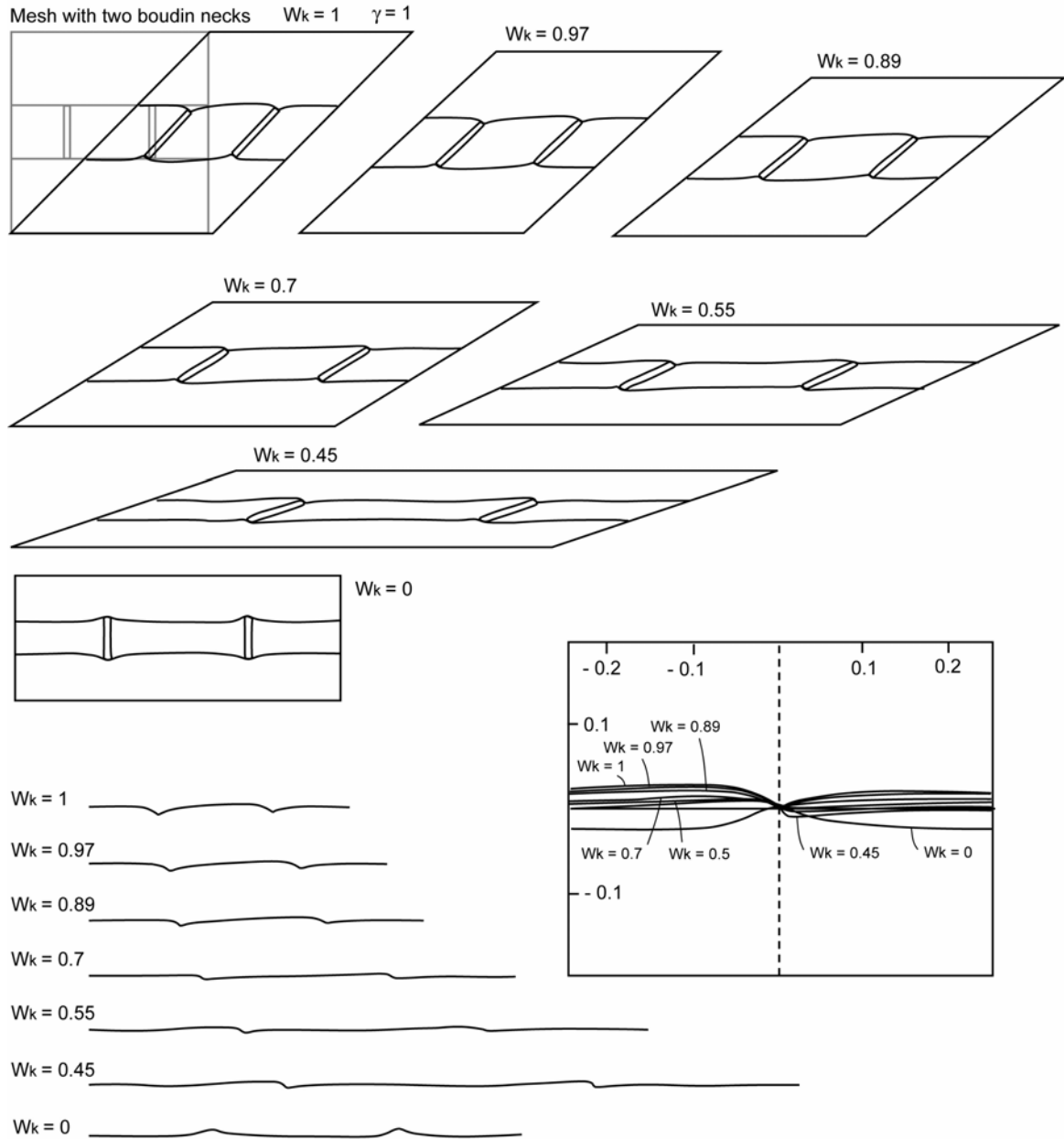
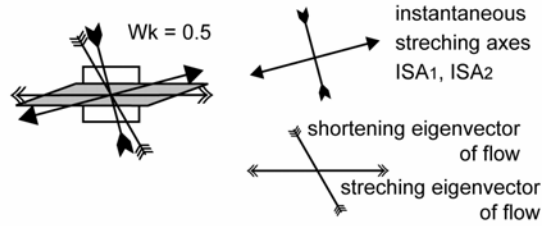


Fig. 4.11. Diagrams showing the influence of the kinematic vorticity number W_k of the bulk flow in transpressional regime for the mesh with a two boudin necks.

Influence of the kinematic vorticity number

General shear flow, transpressional regime
 Viscosity vein = 10x viscosity layers
 Viscosity internal layer = viscosity external layers = 1

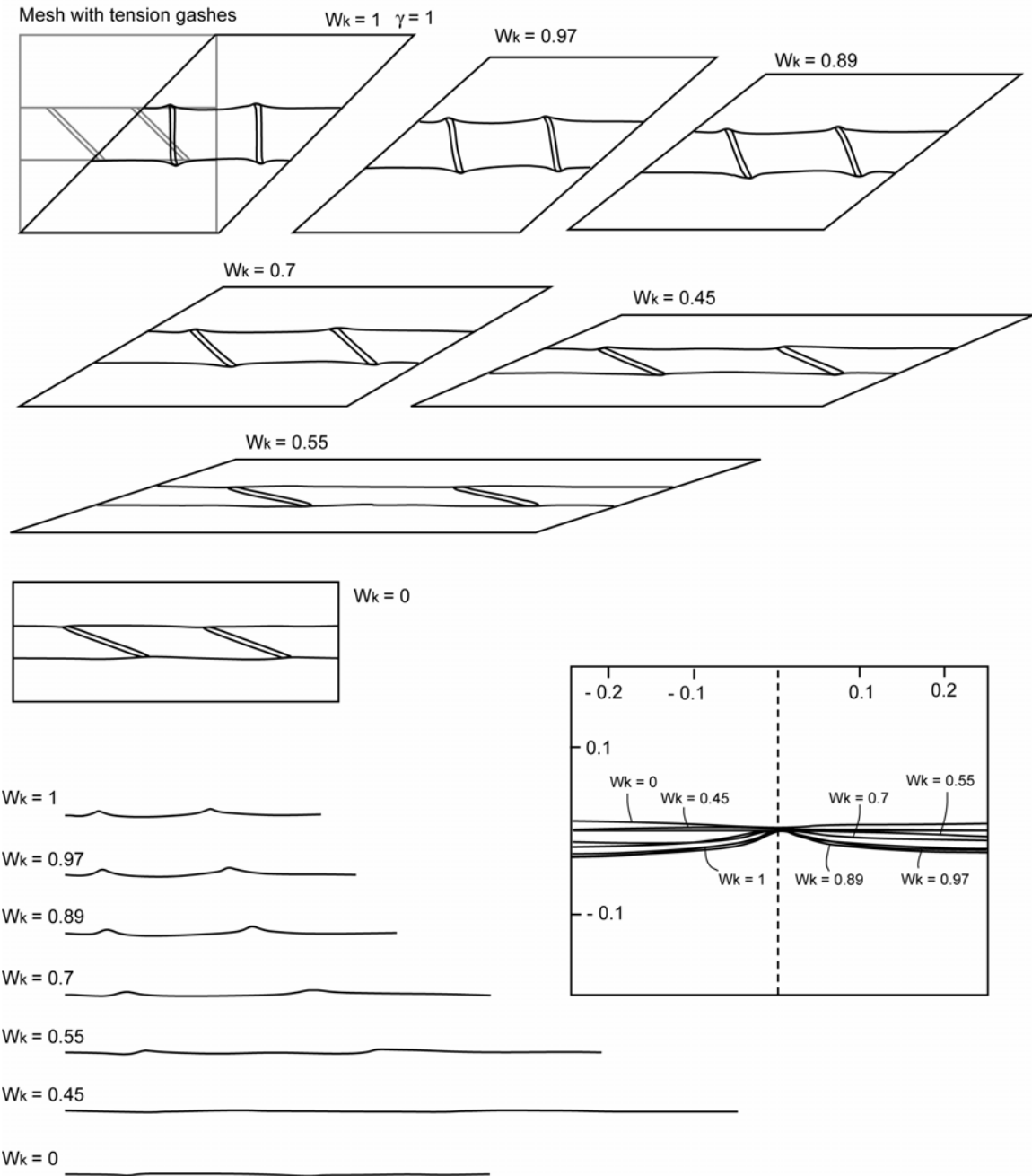
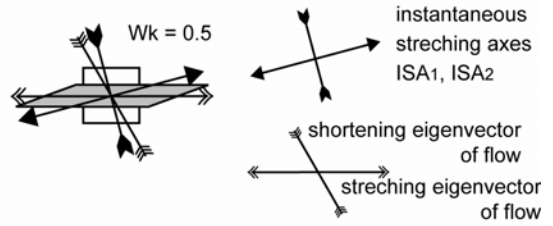


Fig. 4.12. Diagrams showing the influence of the kinematic vorticity number W_k of the bulk flow in a transpressional regime for the mesh with tension gashes.

perpendicular to the layer, the veins tend to parallelism to the bedding interface. The counter-intuitive rotation of the original oblique veins may lead to an erroneous shear sense interpretation in the field.

4.5.3 Effect of the competency contrast between the layers

Variation in viscosity of the internal layer has been implemented in the experiments with all three types of meshes (appendixes 4.13.1, 4.13.2 and 4.14). The viscosity of the vein is fixed to a value ten times stronger than the that of three layers and we applied a simple shear strain of $\gamma = 1.35$. Fig. 4.13 illustrates the different experiments with the mesh with two boudin necks. A weak internal layer implies a stronger rotation of the veins in the simulations because the deformation concentrates in the weakest layer. Both elevation and bulge of the asymmetric flanking folds at the tip of the veins increases with a decrease in the viscosity of the internal layer (Fig. 4.13). The bulge increases significantly between the two experiments with an internal layer that is 0.5 and 0.25 times weaker than the surrounding layers. Experiments with internal layers stronger than the surrounding layers show very small elevation and develop only weak or no asymmetric shape. The layer interface remains flat in the experiments with the internal layer 5 times stronger than the surrounding layers.

Experiments of simple shear deformation with $\gamma = 1.35$ for the meshes with tension gashes with variable viscosity of the internal layer are illustrated in Fig. 4.14. Only the experiment with an internal layer 4 times weaker than the surrounding layers leads to an asymmetric geometry of the layer interface with positive bulge and elevation. The other simulations show the development of bone-shaped geometries caused by the rotation of the veins in simple shear flow. In the examples where the viscosity of the internal layer is between 2 times weaker and equal to the viscosity of the surrounding layers, the tension gashes deform slightly into a sigmoid shape caused by their rotation in simple shear flow. Like the simulations with initially perpendicular veins, the results with an internal layer 5 times stronger than the surrounding layers show flat bedding interface with no vein rotation.

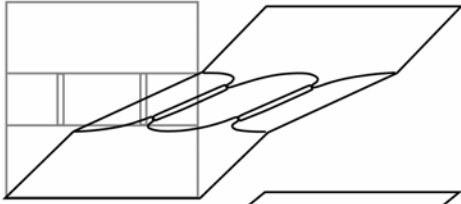
4.5.4 Effect of the competence of the veins

The viscosity of the internal layer is fixed at the same value as the two external layers and the total sinistral shear strain is maintained at $\gamma = 1.35$. The relative viscosity of the vein is varied in this series of experiments. Fig. 4.15 illustrates the simulation results for the mesh with two boudin necks. The results show that buckling of bedding increases with an increase of the viscosity of the boudin necks. However, the geometry of the buckling remains approximately the same for veins with viscosities 50 to 1000 times stronger than the layers. The bulge of the asymmetric buckling of the bedding remains approximately the same in all the simulations with veins stronger than the layers, only the elevation increases with an increase of the viscosity of the veins. Experiments with boudin necks weaker than the matrix show antithetic slip between the boudins as domino boudins structures (Passchier and Druguet, 2002; Goscombe and Passchier, 2003; Fig. 4.15). The weak discontinuities allow slip to occur. Appendixes 4.15.1 and 4.15.2 show the

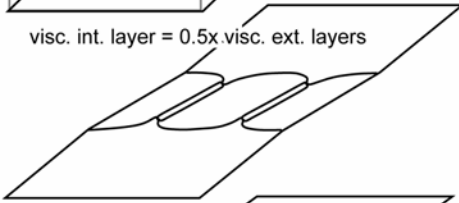
Influence of the relative viscosity of the internal layer

Mesh with two boudin necks

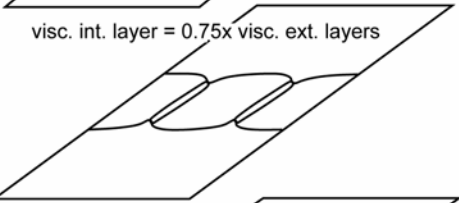
visc. int. layer = 0.25x visc. ext. layers



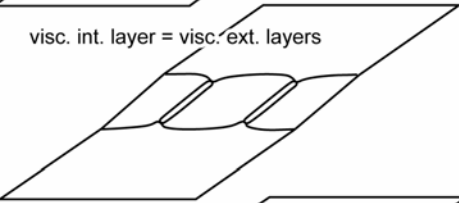
visc. int. layer = 0.5x visc. ext. layers



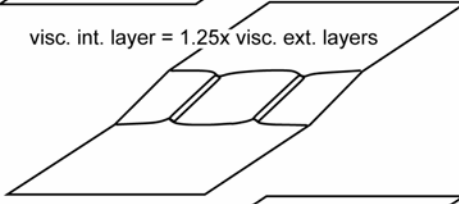
visc. int. layer = 0.75x visc. ext. layers



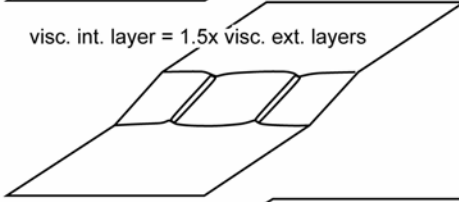
visc. int. layer = visc. ext. layers



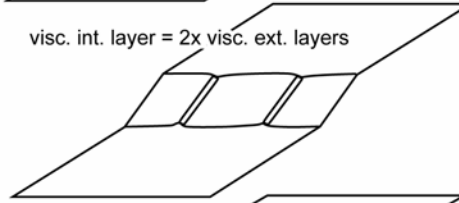
visc. int. layer = 1.25x visc. ext. layers



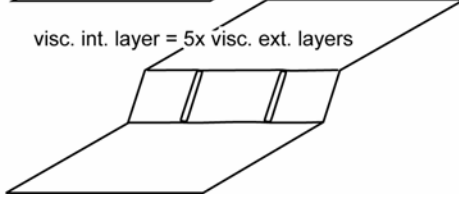
visc. int. layer = 1.5x visc. ext. layers



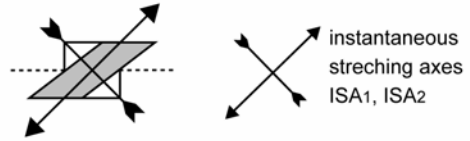
visc. int. layer = 2x visc. ext. layers



visc. int. layer = 5x visc. ext. layers



Simple shear flow, $\gamma = 1.35$
 Viscosity vein = 10x viscosity external layers
 Viscosity internal layer varies



visc. int. layer = 0.25x visc. ext. layers



visc. int. layer = 0.5x visc. ext. layers



visc. int. layer = 0.75x visc. ext. layers



visc. int. layer = visc. ext. layers



visc. int. layer = 1.25x visc. ext. layers



visc. int. layer = 1.5x visc. ext. layers



visc. int. layer = 2x visc. ext. layers



visc. int. layer = 5x visc. ext. layers

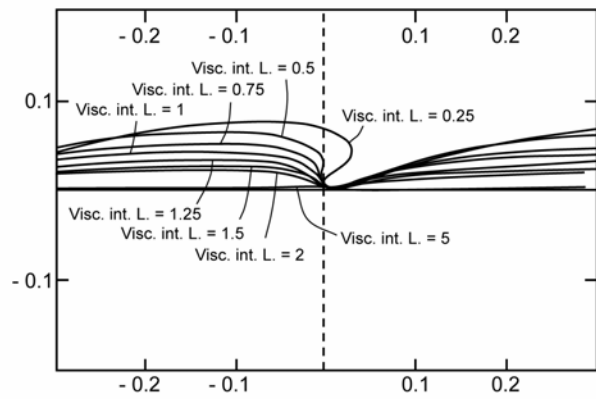
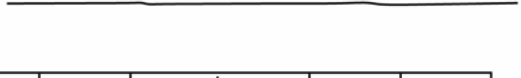


Fig. 4.13. Diagrams showing the influence of the viscosity of the internal layer for the mesh with two boudin necks.

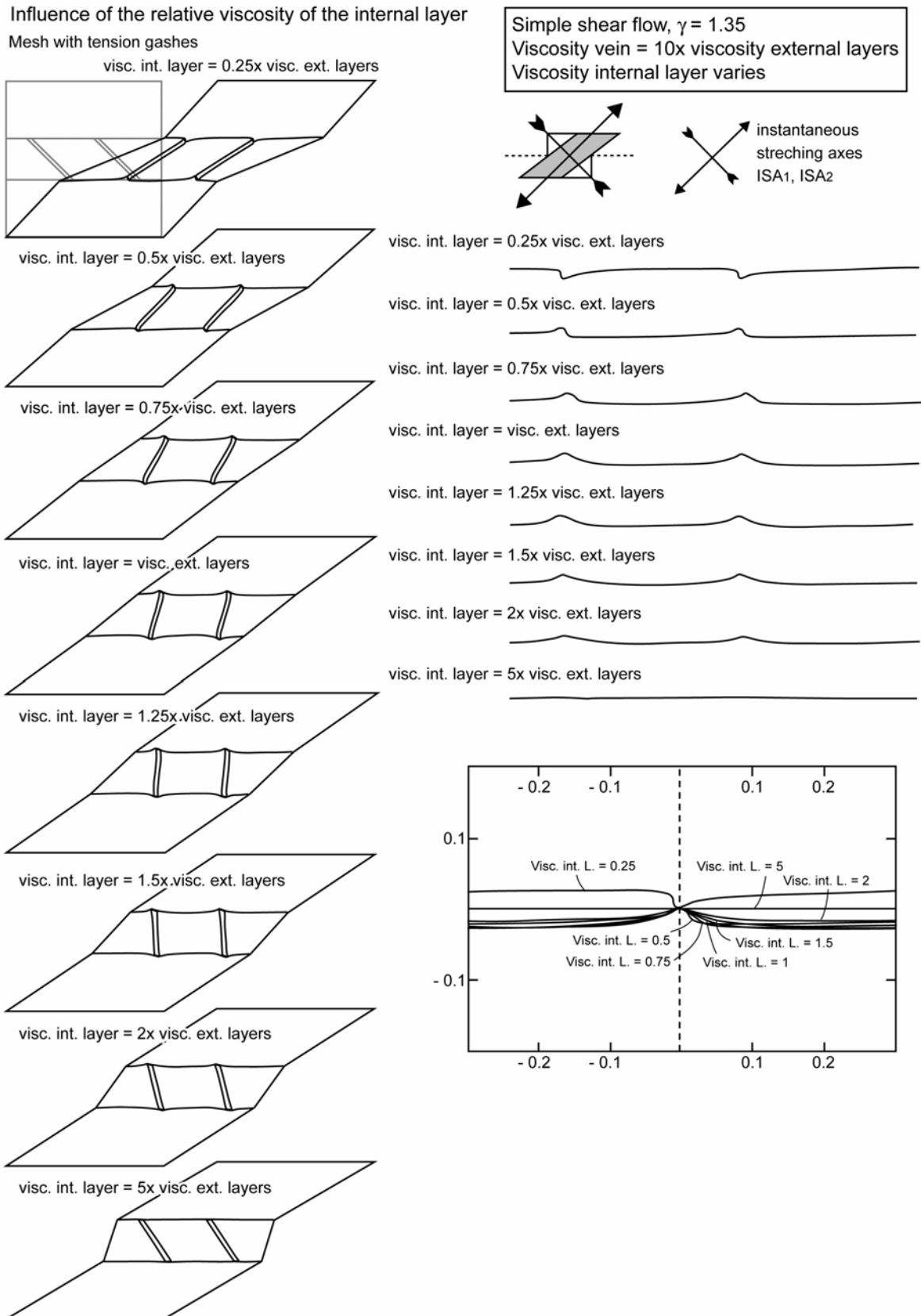
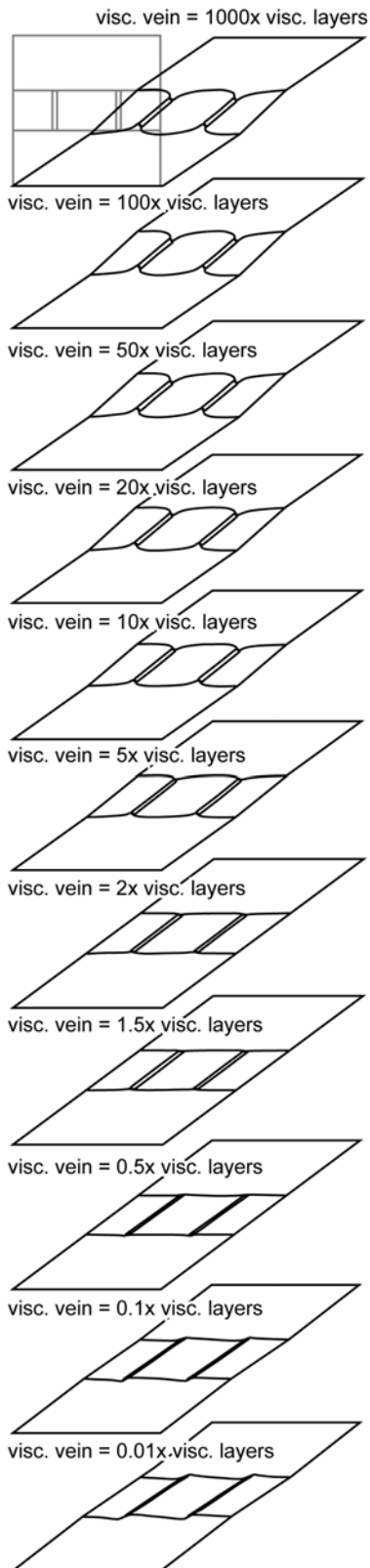


Fig. 4.14. Diagrams showing the influence of the viscosity of the internal layer for the mesh with tension gashes.

Influence of the relative viscosity of the veins
Mesh with two boudin necks



Simple shear flow, $\gamma = 1.35$
Viscosity vein varies
Viscosity internal layer = viscosity external layer

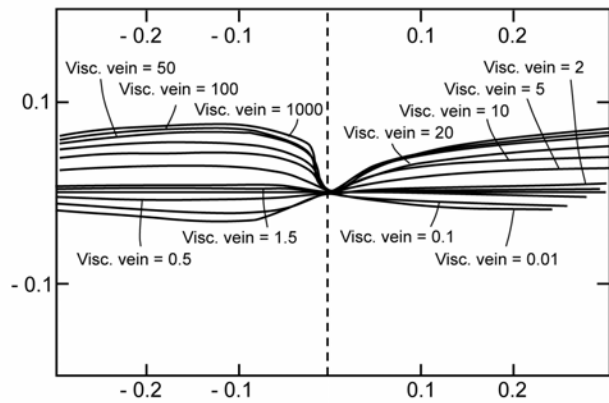
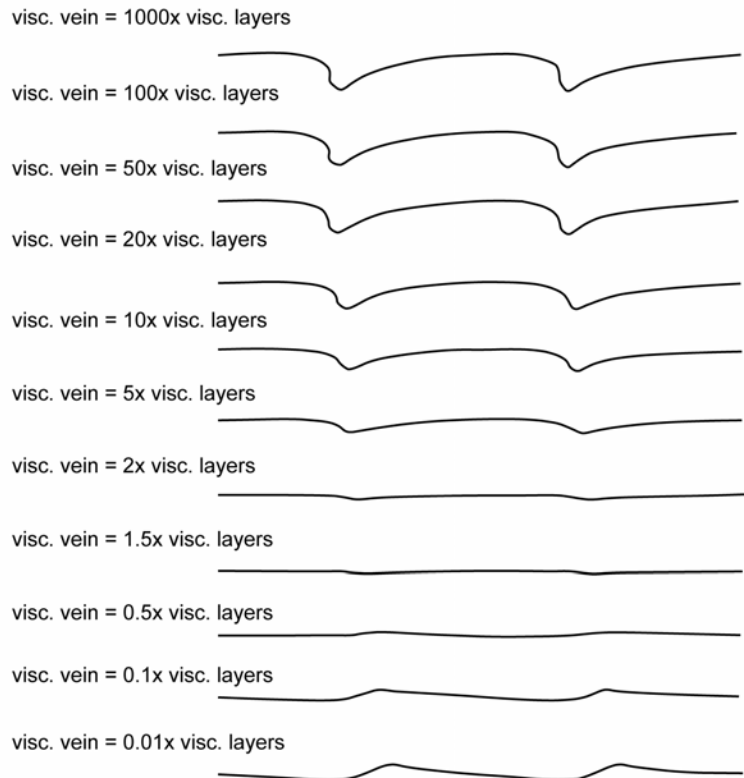
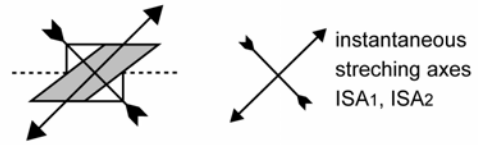


Fig. 4.15. Diagrams showing the influence of the viscosity of the vein for the mesh with two boudin necks.

simulation results of the meshes with one and two boudin necks. The passive markers A and B in the internal layer show n-type flanking folds when the veins are stronger than the layers and a-type flanking folds with reverse drag when the veins are weaker than the layers. This is in good agreement with the results of Grasemann et al. (2003) and Wiesmayr et al. (2005), which show the development of a-type flanking folds with reverse drag and extensional offset with simple shear deformation when the initial orientation of the fault is at 90° with the shear plane.

The effect of the relative viscosity of the tension gashes under simple shear deformation is illustrated in Fig. 4.16. Strong competency contrast between the veins and the layers strengthened the bone shape geometry of the bedding interface. The bedding interface remains almost flat in the range of veins with viscosities between 2 times stronger to 2 times weaker than the layers. It seems that a vein must be at least more than 2 times stronger than the wall rock for bone-shaped boudins to occur in simple shear flow. The tension gashes deform slightly into a sigmoid shape where their viscosity is in the range of 100 to 10 times stronger than the layers. The simulations with tension gashes weaker than bedding show antithetic slip along the veins, like the results with veins initially perpendicular to the layers. In those cases, tension gashes deform into a lozenge shape. Appendix 4.16 show the simulation results of simple shear progressive deformation of the tension gashes with different viscosities. The passive markers A and B in the internal layers show a-type flanking folds with reverse drag and extensional offset when the tension gashes are weaker than the layers, as in the simulations with the boudin necks. Where the veins are stronger than the layers, the passive markers show n-type flanking folds along the rotating tension gashes.

4.5.5 Effect of the initial aspect ratio of the boudins

Fig. 4.17 and appendix 4.17 a, b illustrate the simulation results with a mesh with two boudin necks with variable distance between the veins. A simple shear of $\gamma = 1.35$ is applied to the mesh and the viscosity of the internal layer is maintained the same as the external layers and ten times stronger than the veins. The results show that the geometry of the buckling does not change measurably with aspect ratio. Only when the veins are very narrow, the bedding interface between the veins develops a smaller buckling, which can be seen in the example with an aspect ratio of $\frac{1}{4}$.

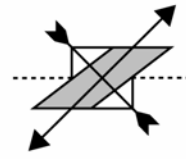
4.5.6 Effect of the thickness of the veins

The simulation results of the variation in thickness of boudin necks for the mesh with two boudin necks are shown in Fig. and appendix 4.18. The viscosities of the layers are similar and ten times stronger than the veins. A simple shear of $\gamma = 1.35$ is applied in all cases. The results show that layer interface asymmetric flanking folds at the tip of the veins do not significantly change with a variation in the thickness of the vein. The elevation of asymmetric flanking folds slightly diminishes in the cases of relatively thick veins. The thickness of the veins doesn't influence the bulge of the flanking fold.

Influence of the aspect ratio (spacing / thickness)

Mesh with two boudin necks

Simple shear flow, $\gamma = 1.35$
 Viscosity vein = 10x viscosity layers
 Viscosity internal layer = viscosity external layer



instantaneous
 stretching axes
 ISA1, ISA2

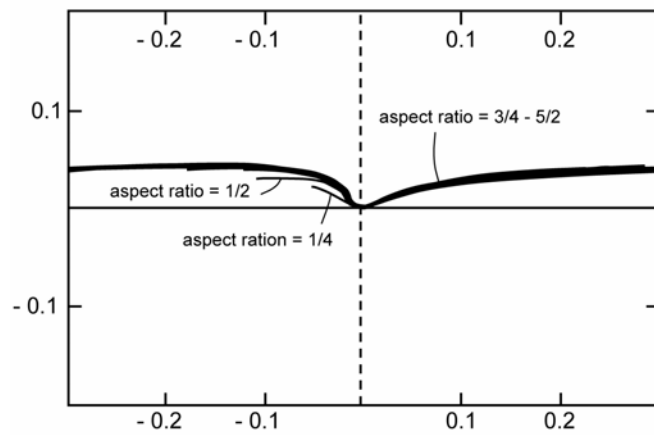
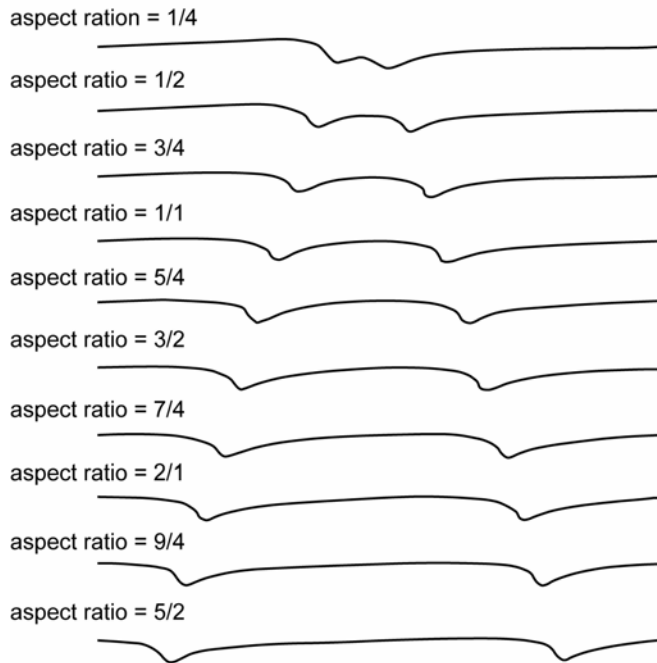


Fig. 4.17. Diagrams showing the influence of the aspect ratio of the boudins (spacing/thickness).

4.5.7 Effect of the stress exponent

The effect of the stress exponent of the Power Law equation of the flow is illustrated in Fig. and appendix 4.19. An increase of the stress exponent only very slightly changes the shape of the buckling of the bedding. The passage from a Newtonian flow to a non-Newtonian flow (from $n = 1$ to $n = 2$) mark the biggest change with a slight increase of the elevation of the asymmetric buckling of the bedding.

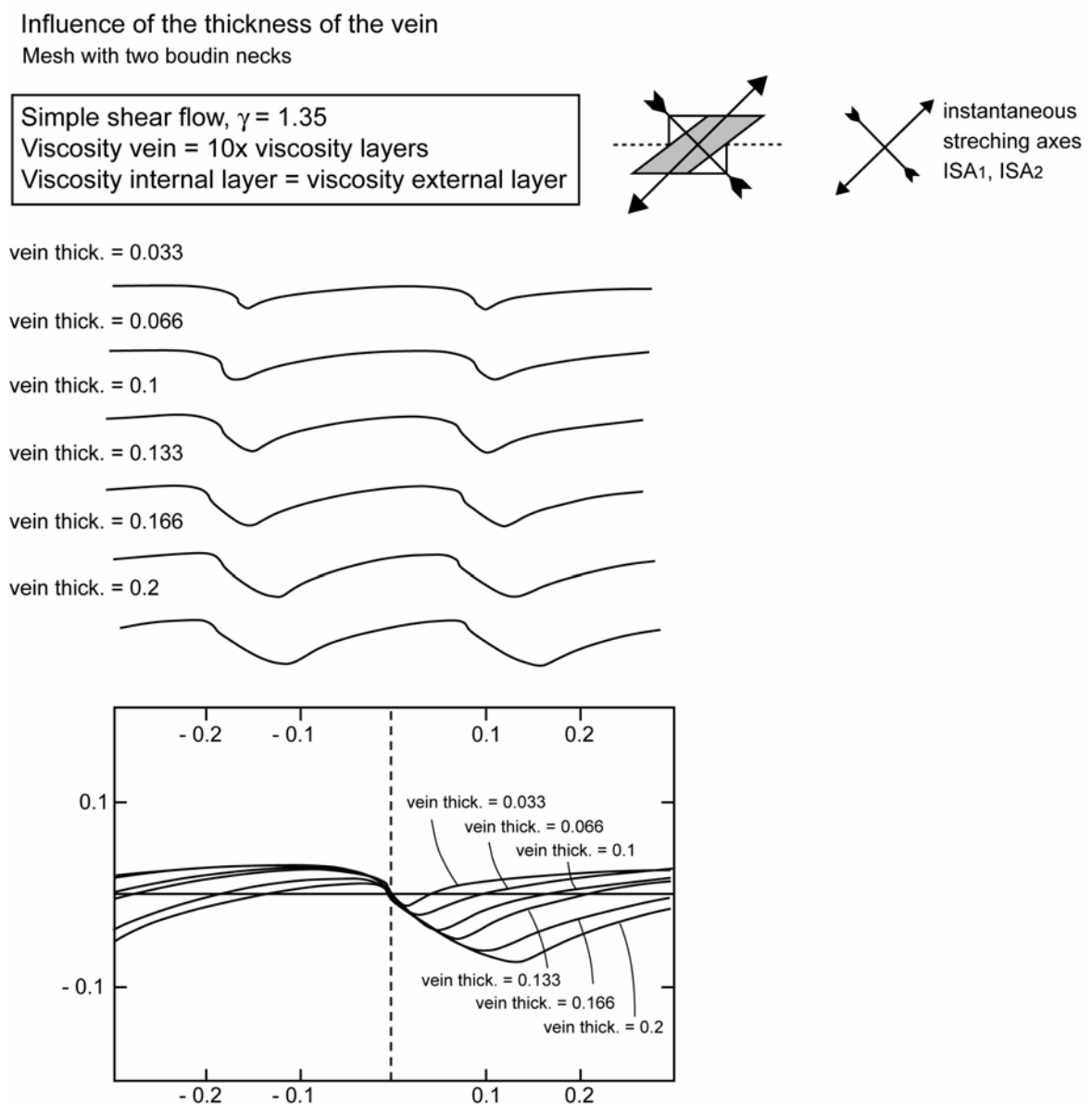


Fig. 4.18. Diagrams showing the influence of the vein thickness.

Influence of the stress exponent of
Power law equation

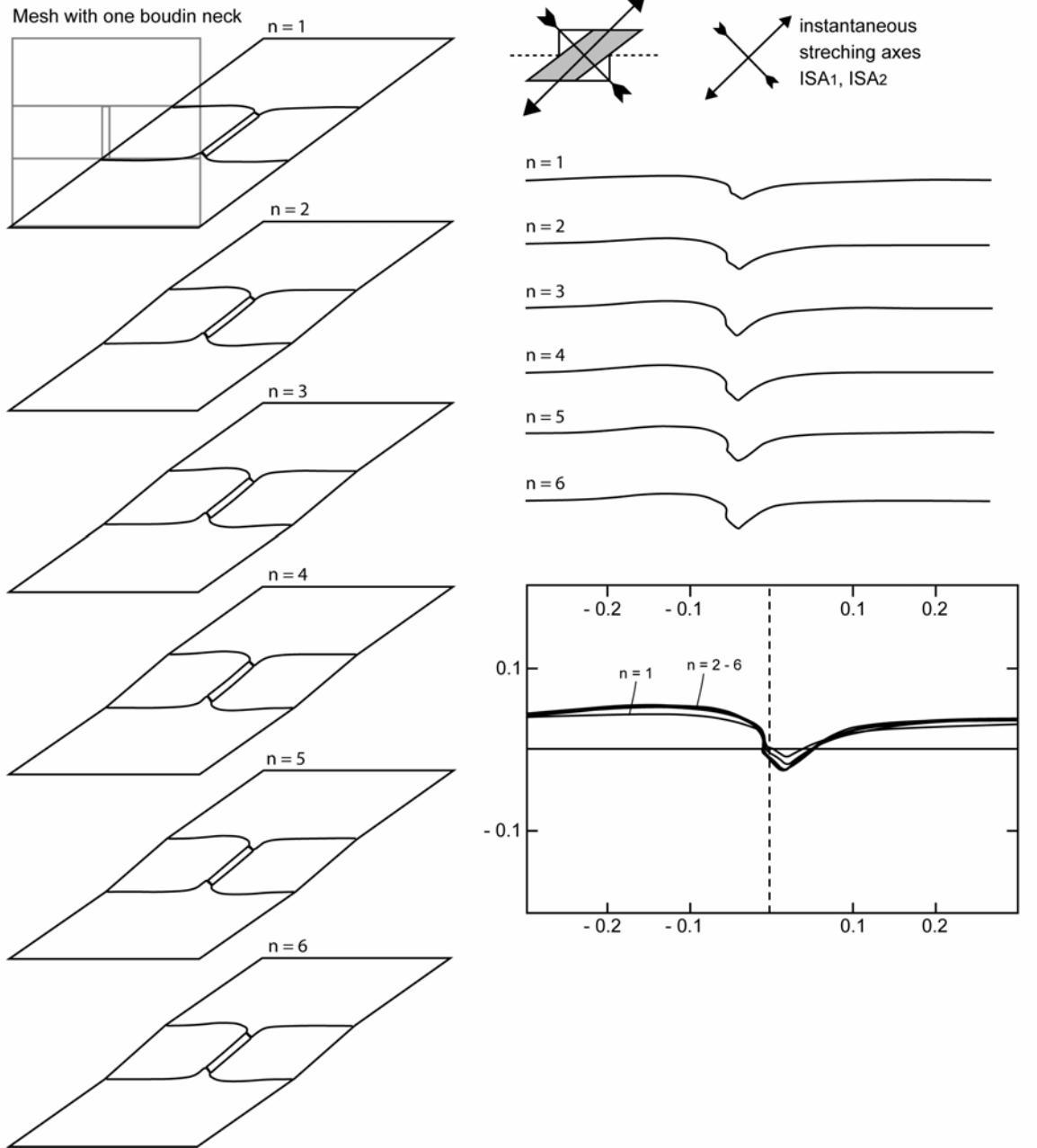


Fig. 4.19. Diagrams showing the influence of the stress exponent.

4.6 Discussion on the parameter sensitivity analyses

The parameter sensitivity analysis show that mainly four parameters determine the shape of the deformed boudins:

1. The total strain
2. The kinematic vorticity number of the flow
3. The competence contrast between the boudinaged layer and the surrounding layers
4. The competence contrast between the veins and the layers.

A summary of the influence of tested parameters on the meshes with two boudin necks is given in Fig. 4.20. The aspect ratio of the boudins, the thickness of the vein and the stress exponent of the Power Law equation do not influence significantly the layer interface geometry of the reworked boudins. A summary of the effect of the kinematic vorticity number of the resulting shape of the reworked meshes with boudin necks and tension gashes is given in Fig. 4.21. The results on the meshes with tension gashes show “counter” rotation of the veins where the shortening perpendicular to the layer is high. Because of the “counter” shearing of the tension gashes, no bone-shaped boudin forms in the experiment where the flow is only composed of pure shear perpendicular to the layer.

The numerical simulation results show that asymmetric flanking folds formed at the tips of rotated boudin necks, which usually coincide with a lithological boundary in nature. The geometry of the asymmetric flanking folds marked by the bedding interface of the reworked boudins in the simulations is comparable with the geometry of the natural examples in the Lower Ugab Domain, which seem to the interpretation that the asymmetric boudins in the studied area results from the rotation of the veins with respect to layering. The influence of the total shear strain, the kinematic vorticity number and the relative viscosity of the internal layer and the veins on the maximum elevation (ME) is given in Fig. 4.22. ME seems to increase linearly with the simple shear progressive deformation (γ) (Fig. 4.22a). In a transtensional regime, the slope of the curve is relatively shallow between $W_k=0$ (pure shear flow parallel to the layer) and $W_k=0.5$ (Fig. 4.22b). ME therefore increases more significantly between $W_k=0.5$ and $W_k=1$. In a transpressional regime with the shortening component perpendicular to the layer, ME is negative between $W_k=0$ and $W_k=0.35$ (Fig. 4.22c). This means that in that range of W_k with veins originally perpendicular to the bedding and stronger than the boudinaged layer, a bone-shaped boudin geometry should be found (Malavieille and Lacassin, 1988). ME seems to increase exponentially with a decrease of the relative viscosity of the internal layer (Fig. 4.22d). ME decreases exponentially with a decrease of the relative viscosity of the internal layer (Fig. 4.22e). Slip occurs along the boudin necks where they are weaker than the wall rocks and domino boudins form inducing a negative ME (Goscombe and Passchier, 2003; Fig. and appendix 4.15).

The influence of the different parameters on the β -angle (Fig. 4.7) is given in Fig. 4.23. A β -angle greater than 90° implies a negative bulge (B) and a β -angle smaller than 90° a positive bulge (Fig. 4.7). A β -angle greater than 180° implies a negative ME, i.e. the reworked boudin has a bone-shaped or domino boudin geometry (Malavieille and Lacassin, 1988; Goscombe and Passchier, 2003). The results show that the β -

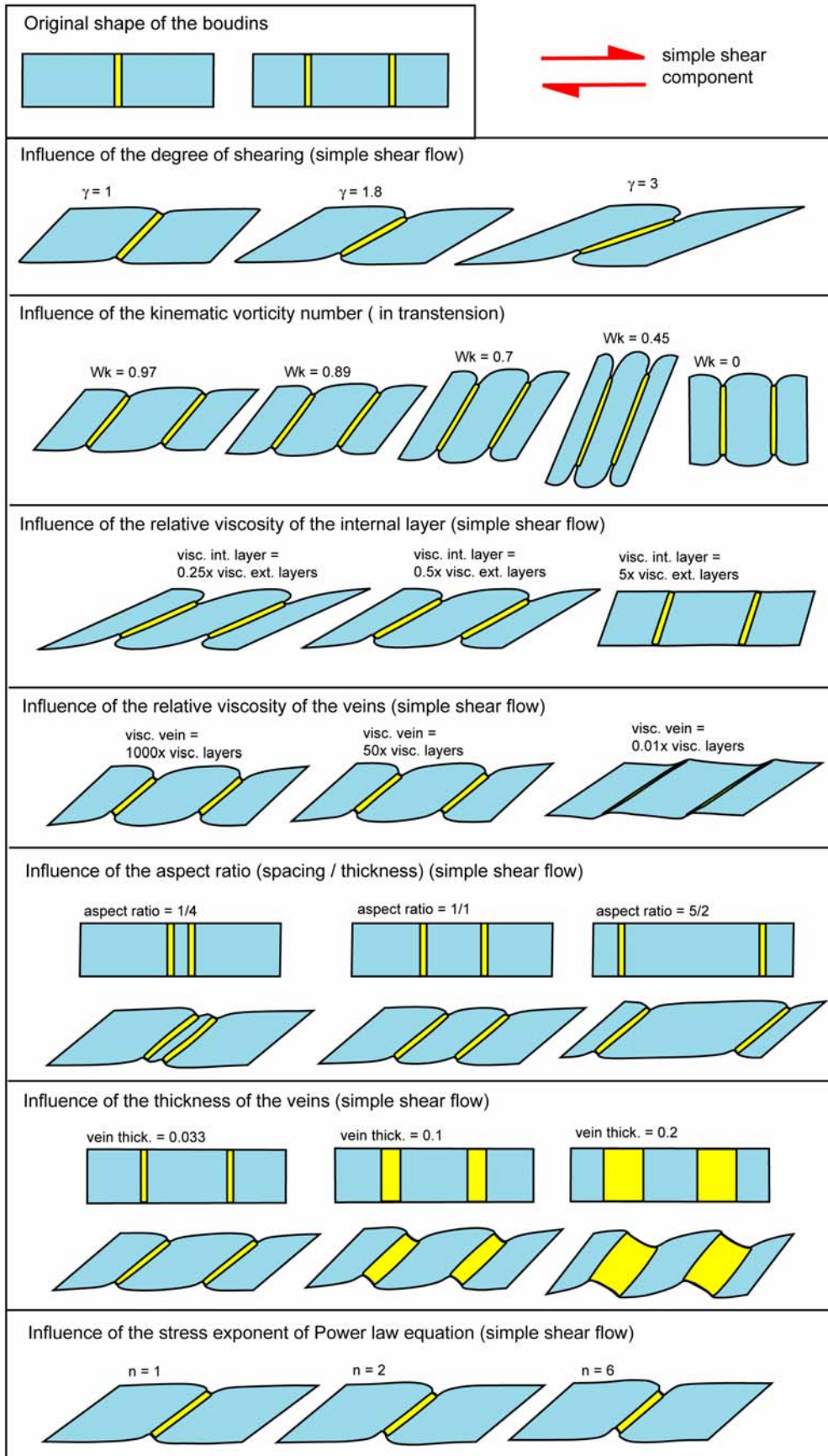


Fig. 4.20. Schematic drawing showing the influence of the different tested parameters on the shape of the reworked boudins.

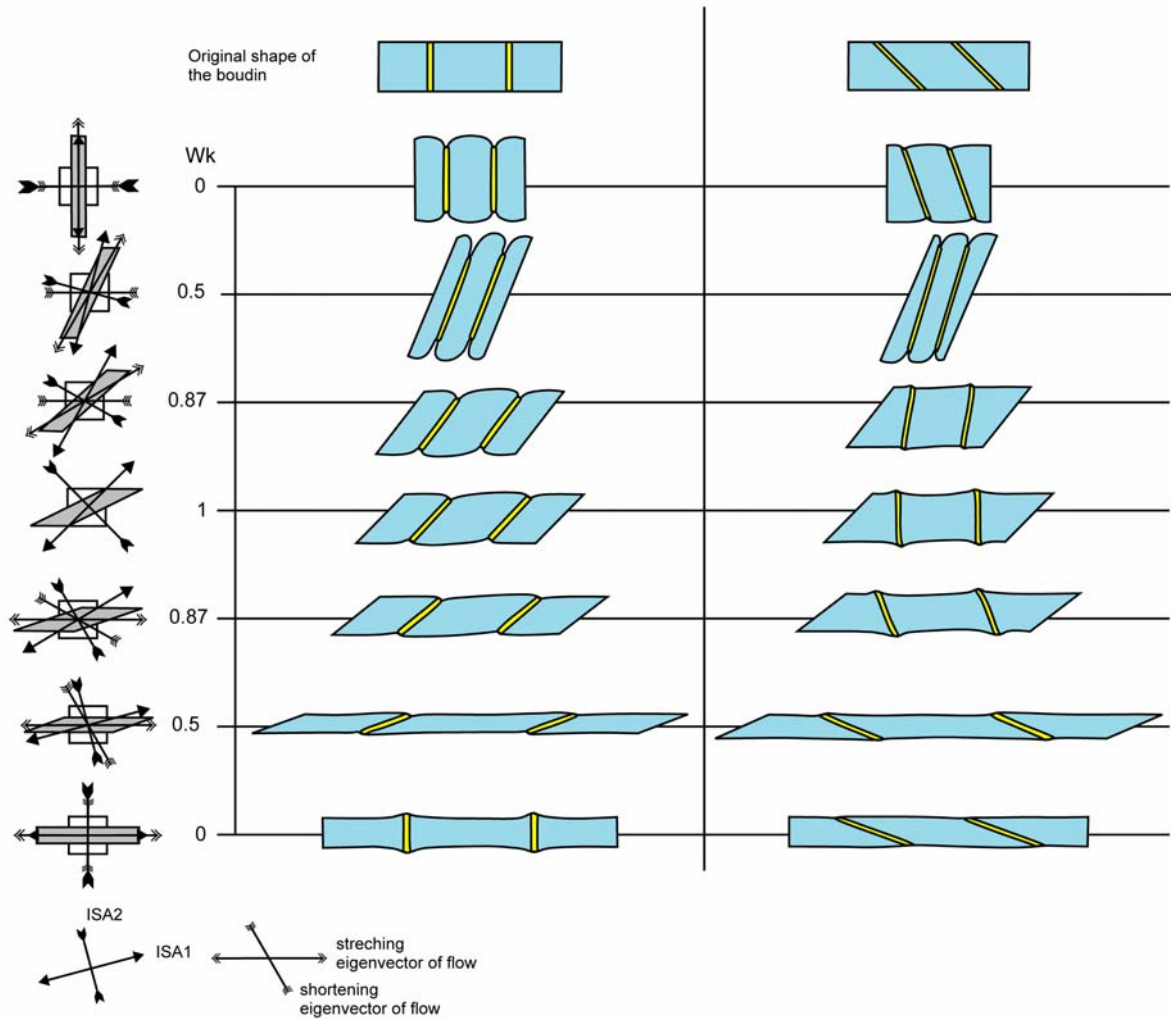


Fig. 4.21. Schematic drawing the influence of the kinematic vorticity number both in transpression and transtension for meshes with two boudin necks and tension gashes.

angle changes significantly between $\gamma=1.5$ and $\gamma=2$, passing from a negative into a positive bulge at about $\gamma=1.9$ (Fig. 4.23a). In a transtensional regime, the bulge increases between $Wk=0$ and $Wk=0.7$ to reach a maximum and then decreases linearly to $Wk=1$ (Fig. 4.23b). The bulge becomes negative from $Wk=0.8$. In transpression, the bulge decreases slowly with an increase of shortening perpendicular to the layers (Fig. 4.23c). It can be seen from the graph that negative ME and bone-shaped boudins should be expected between $Wk=0$ and $Wk=0.25$ (0.35 in the graphic of the influence of Wk in transpression on ME). The conditions for bone-shaped boudins to form should be therefore expected between these two Wk values. The most appropriate flow condition to have the maximal asymmetry and bulge in the flanking folds forming at the tip of rotating boudin necks seems therefore to occur in a transtensional regime, when the kinematic vorticity number is around 0.7. Both graphs of the influence of the relative viscosity of the internal layer and the veins on β -angle show an abrupt change of the slope of the curve (Fig. 4.23d and e). β increases significantly between a viscosity of the internal layer 0.25 and 1 times the external layers. For an internal layer stronger than the external layers, β increases slowly with an increase of the internal layer's

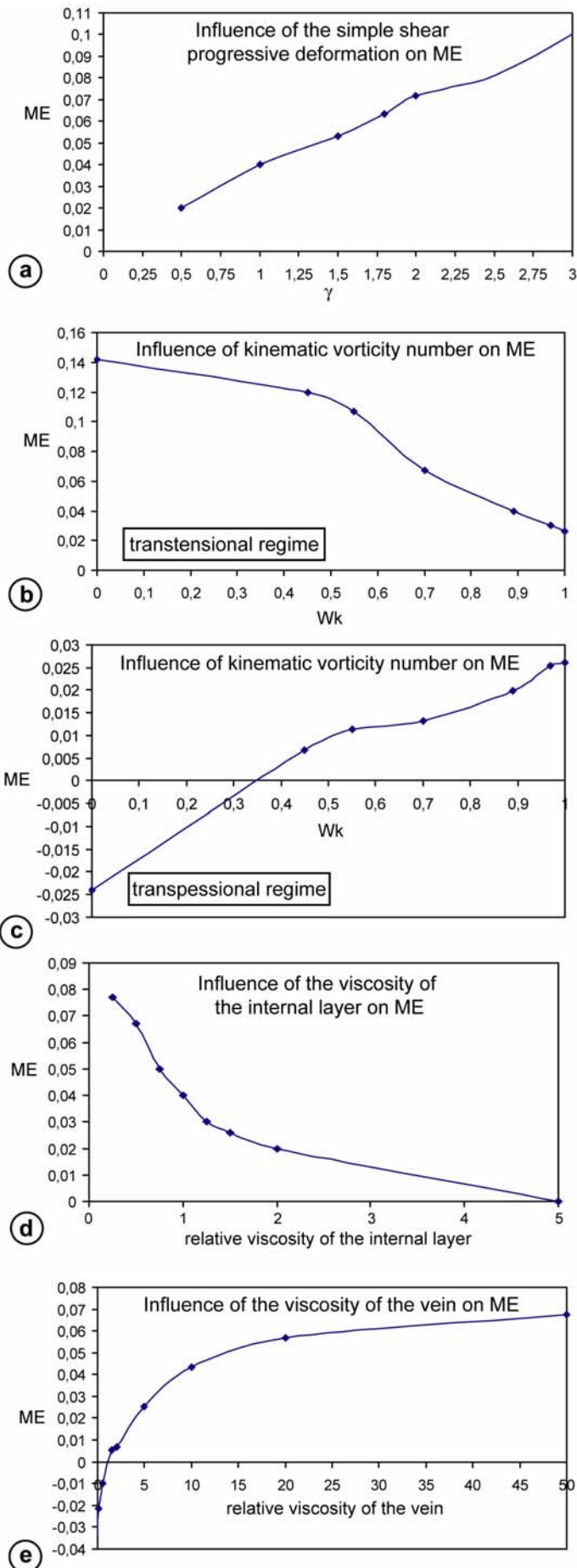


Fig. 4.22. (a) Relation between the simple shear progressive deformation and the Maximum Elevation (ME) of the flanking fold at the tip of the boudin necks. The veins are ten times stronger than the wall rock and the three layers have the same viscosity. (b) Relation between the kinematic vorticity number in transpression and ME. The veins are ten times stronger than the wall rock and the three layers have the same viscosity. (c) Relation between the kinematic vorticity number in transpression and ME. The veins are ten times stronger than the wall rock and the three layers have the same viscosity. (d) Relation between the relative viscosity of the internal layer and ME. The veins are ten times stronger than the external layers and the simple shear progressive deformation is fixed to $\gamma=1.35$. (e) Relation between the relative viscosity of the veins ME. The three layers of the mesh have the same viscosity and the simple shear progressive deformation is fixed to $\gamma=1.35$. A Newtonian regime of deformation is assumed for all the simulations.

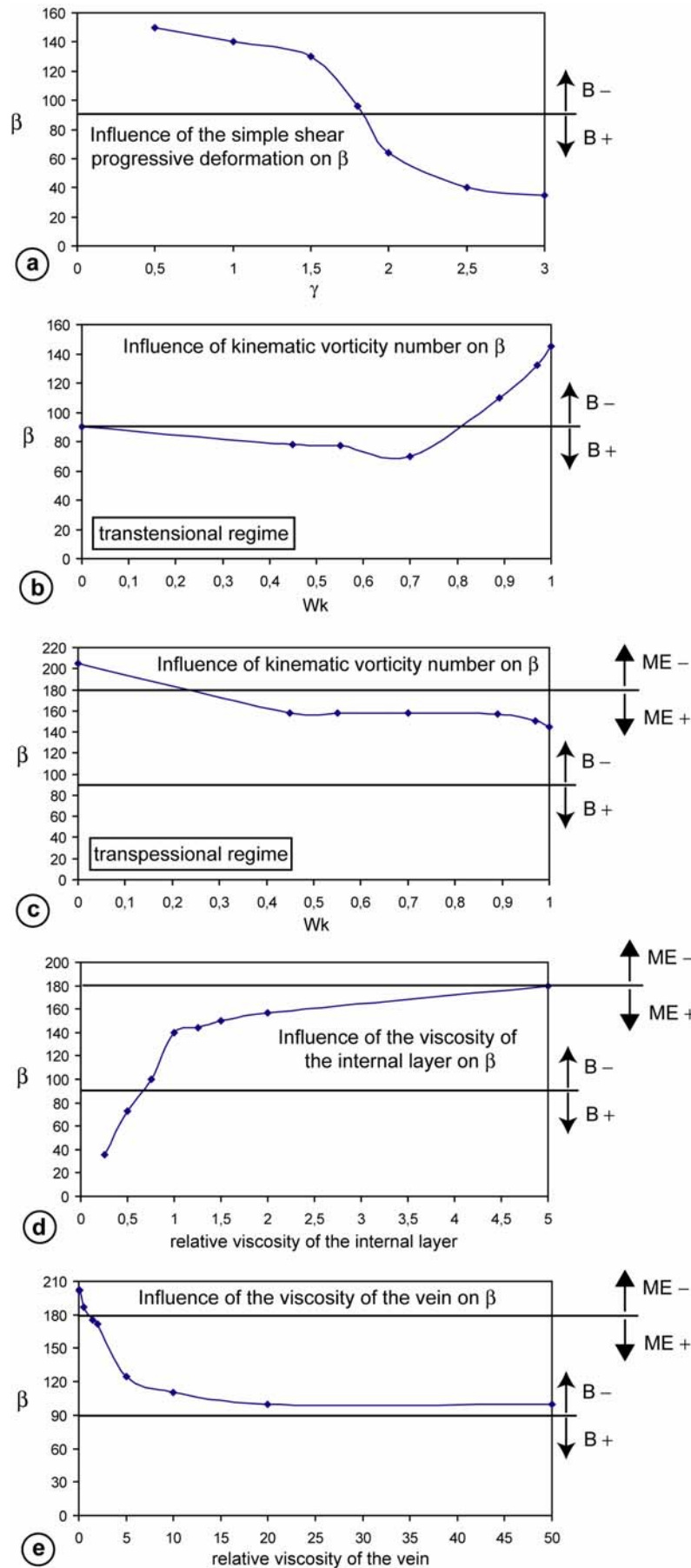


Fig. 4.23. (a) Relation between the simple shear progressive deformation and the tangent of the flanking folds at the border of the vein and the horizontal (β). The veins are ten times stronger than the wall rock and the three layers have the same viscosity. (b) Relation between the kinematic vorticity number in transpression and β . The veins are ten times stronger than the wall rock and the three layers have the same viscosity. (c) Relation between the kinematic vorticity number in transpension and β . The veins are ten times stronger than the wall rock and the three layers have the same viscosity. (d) Relation between the relative viscosity of the internal layer and β . The veins are ten times stronger than the external layers and the simple shear progressive deformation is fixed to $\gamma=1.35$. (e) Relation between the relative viscosity of the veins β . The three layers of the mesh have the same viscosity and the simple shear progressive deformation is fixed to $\gamma=1.35$. A Newtonian regime of deformation is assumed for all the simulations.

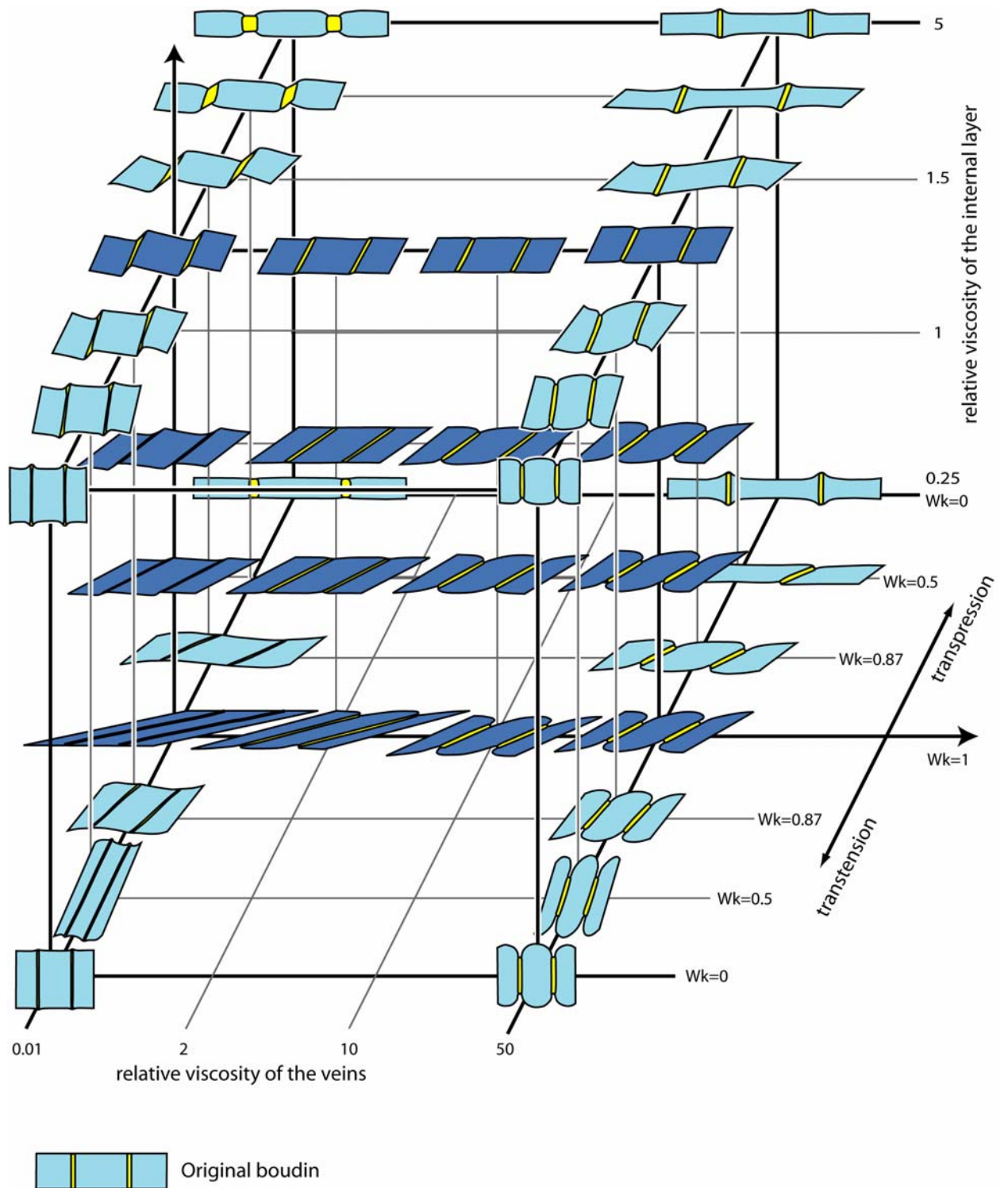


Fig. 4.24. 3D Diagram showing the different shapes of the reworked boudin according to the relative viscosity of the internal layer, the veins and the kinematic vorticity number in transpressional and transtensional regimes. In dark blue the reworked boudins in simple shear flow ($Wk=1$.)

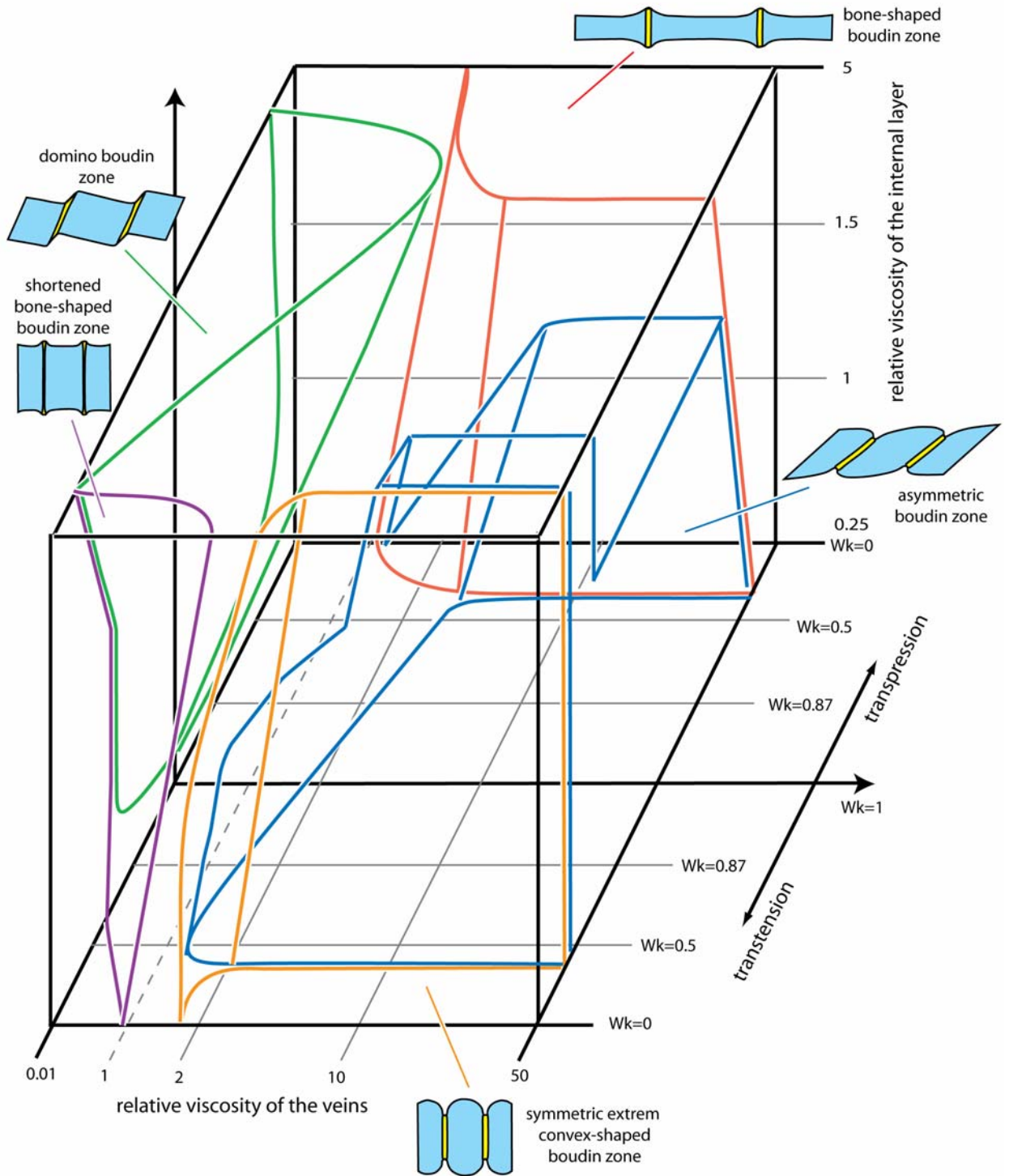


Fig. 4.25. Diagram showing the repartition of the zones where the reworked boudins have an asymmetric shape (blue), a symmetric extreme convex-shape (orange), a domino boudin geometry (green), a bone-shape (red) and a shortened bone-shape (purple), according to the three parameters of the relative viscosity of the internal layer, the veins and the kinematic vorticity number in transpression and transtension.

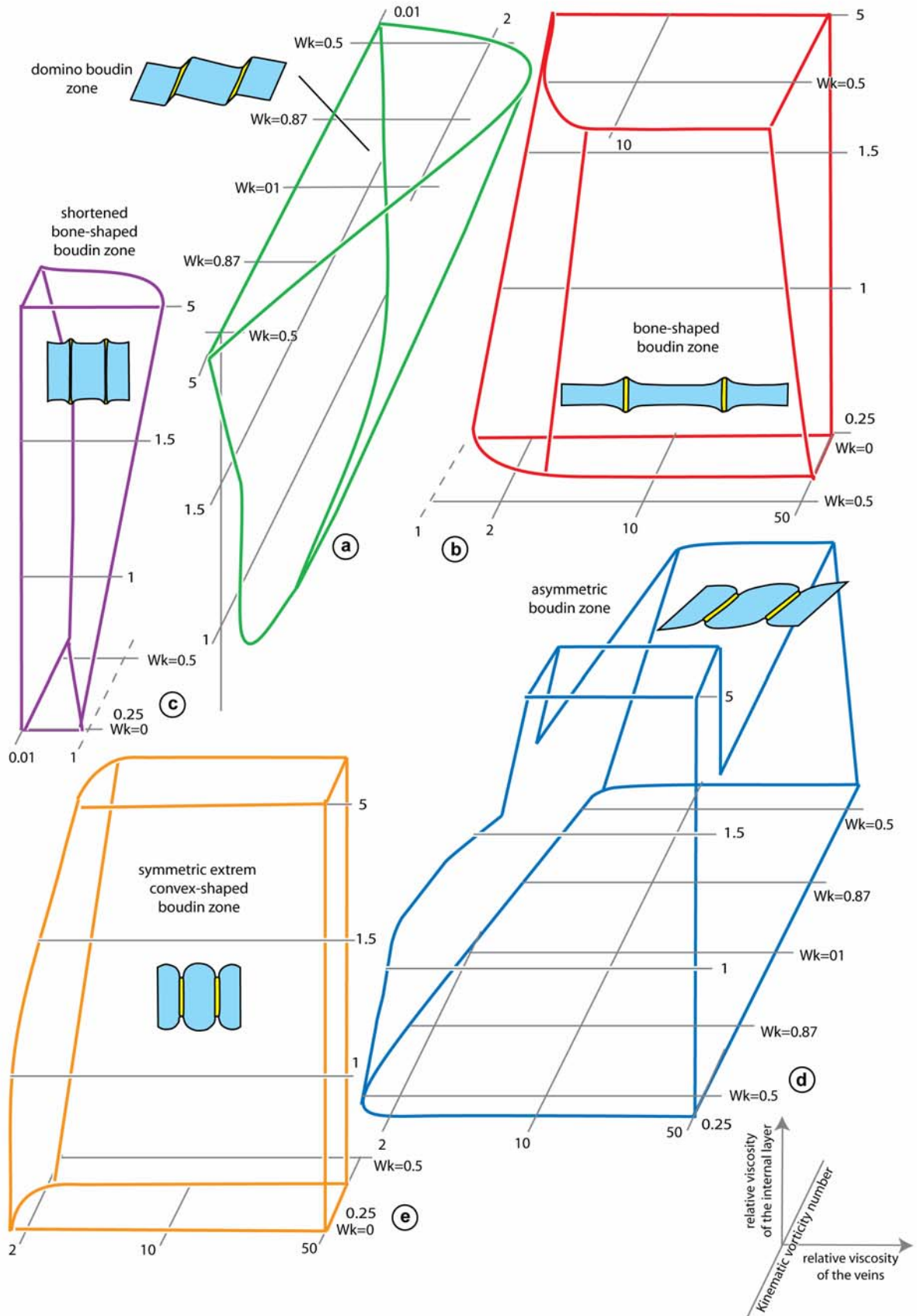


Fig. 4.26. Details on the zones of the different geometries of reworked boudins in transpressional and transtensional regimes.

viscosity. The veins must be stronger than the internal layer to have a positive ME. β decreases significantly between relative viscosities of the veins of 0.25 to 5 times the internal layer.

Fig. 4.24 shows the different shape of reworked boudins according to the relative viscosity of the veins, the internal layer and the kinematic vorticity number in transtension and transpression for a certain strain ($\gamma = 2$). Zones can be determined where the reworked boudin has respectively an asymmetric shape, a domino boudin geometry, a symmetric extreme convex-shape, a bone-shape or a “shortened bone-shape” (Fig. 4.25, 4.26). Asymmetric boudins occur both in transpression and transtension between W_k slightly under 0.5 (0.35-0.25), with veins stronger than the internal layers. The asymmetric effect is stronger in a transtensional regime around $W_k=0.5$ - $W_k=0.7$, where asymmetric boudins also form with an internal layer 5 times stronger than the external layers, with relative viscosity of veins ≥ 10 times the viscosity of the external layers. Domino boudinage also form in transpression and transtension if W_k is slightly under 0.5 and with veins weaker than the internal layer. Domino boudin geometry is favoured by a high contrast between the competence of the veins and the internal layer (Fig. 4.24). Where the internal layer has a relative viscosity of more than 2 times weaker than the external layers, the simulations show no slip between the boudin elements and the bedding interface remains flat. Bone-shaped boudins form where the flow is composed of pure shear perpendicular to the layer, or with a very small simple shear component ($W_k < 0.35$). The veins must be stronger than the internal layer for a bone-shape to form. The bone shape effect is also favoured with a high viscosity contrast between the veins and the internal layer. Symmetric extreme convex-shaped boudins occur where the flow is consisting of pure shear parallel to the layer, with veins of higher viscosity than the internal layer. Shortened bone-shaped boudins occur where the veins have very low relative viscosity and the flow is composed of shortening parallel to the layer or with a very weak simple shear component. The veins underwent more stretching perpendicular to the layer than the internal layer which marks a bone-shaped geometry of the bedding interface.

4.7 Comparison between the simulations and the natural structures

Although the rheology of real rocks is more complex than the model in our experiment, a comparison between real cases and the simulations can be made. Fig 4.27 shows an asymmetric boudin structure from a marble of the Brandberg West formation. Since non sheared boudin necks show an orthogonal position to the layer (Fig.3.13), the vein is supposed to be originally in a position perpendicular to the bedding before rotation. This means a rotation of $\sim 57^\circ$ with respect to the layering. When the same vein rotation is applied to simulations, it is possible to vary the different parameters to obtain a geometry which is comparable to the natural case. The results are presented in Fig. 4.28. The natural example shows two flanking folds with different maximum elevation at the top and the bottom of the bedding, but with similar β -angles near 90° and a bulge of near by zero. Solutions 1 or 2 of Fig. 4.28 seem to fit best, with almost neutral bulge. This can mean that the viscosities of the internal layer (boudinaged layer) could have been about the same than that of the two external layers. However it is difficult to constrain the exact competence contrast between

the veins and the layers, since in both simulations examples with veins that are respectively 10 to 100 times stronger than the layers could be comparable to the natural example. The observations of natural examples demonstrate that a qualitative comparison with the numerical result appears to be difficult. The geometry of the interface between the boudin necks varies too much between different veins of similar orientation in a given layer in the same locality to allow a good comparison. For example, Fig. 4.2f shows two adjacent veins of similar orientation and which most probably underwent the same amount of deformation, since there are very narrow and of equal deformation and displacement. The layer interfaces show two very different geometries of asymmetric flanking folds at the tip of the veins. The first from the left show clear negative bulge with small elevation and the second a positive bulge with a relatively strong maximum elevation. This means that the shape of the flanking folds can depend on other parameters than the viscosity of the internal-external layers and the veins, the kinematic vorticity of the flow and the total strain. Local heterogeneities in the layers, undetected elements or clasts in the layers, slight different quartz-calcite zonation in the veins can also influence the shape of the flanking folds at the tips of the vein. In the simulations, a flat bedding interface of the boudins is assumed before the progressive deformation. Classical formation of torn boudin can lead to barrel shape boudin geometry with slightly convex bedding interface (Goscombe et al., 2004). The original small-amplitude barrel shape of the original undeformed boudins can influence the shape of the reworked structure (Vanbrabant and Dejonghe, 2006). The exact orientation of the veins in an original orthogonal position to the layering may be also subject to controversy. It is possible that some veins opened during the progressive deformation and not during the initial stage of boudinage of the layers.

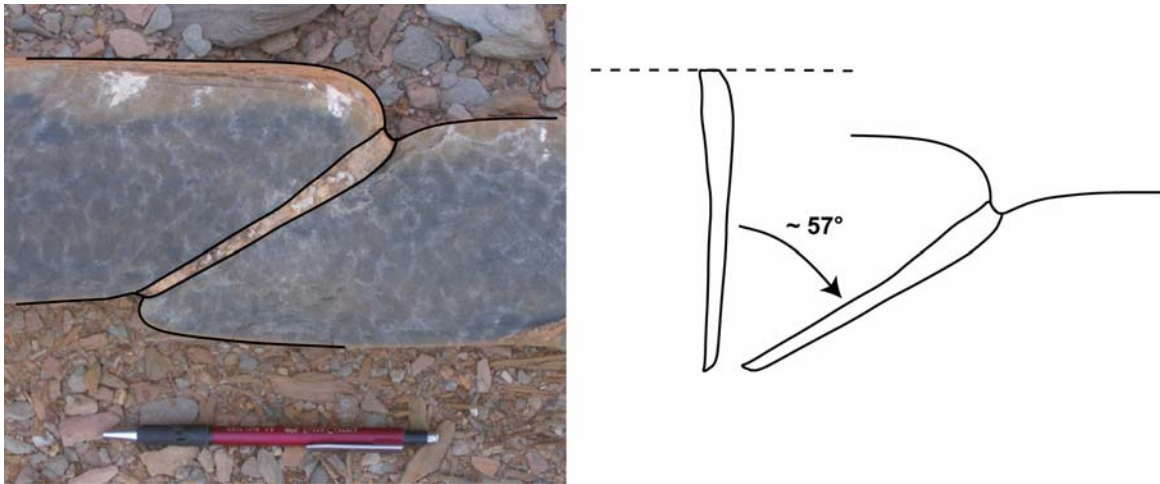
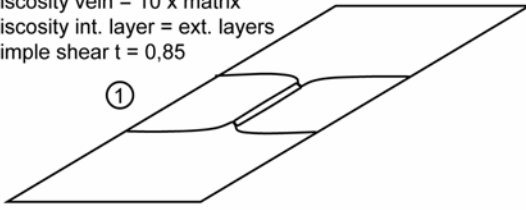


Fig. 4.27. Example of asymmetric flanking folds at the two tips of a vein in a marble layer of the Brandberg Formation (location: $-20.83982^{\circ}/14.13346^{\circ}$). The vein was probably at high angle to the bedding before its reorientation in the actual oblique position to the bedding. This means a rotation of the vein of about 57° .

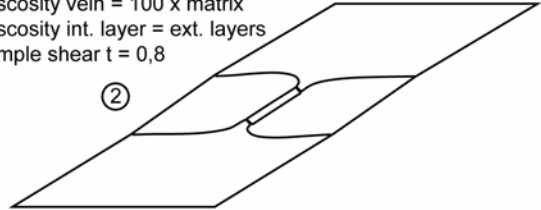
Test of the different parameters

viscosity vein = 10 x matrix
viscosity int. layer = ext. layers
simple shear $t = 0,85$



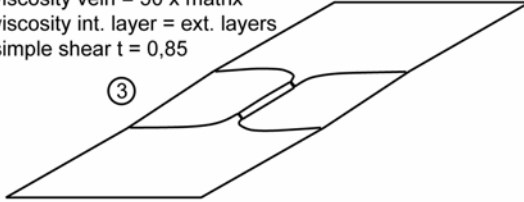
①

viscosity vein = 100 x matrix
viscosity int. layer = ext. layers
simple shear $t = 0,8$



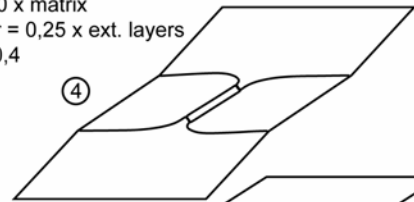
②

viscosity vein = 50 x matrix
viscosity int. layer = ext. layers
simple shear $t = 0,85$



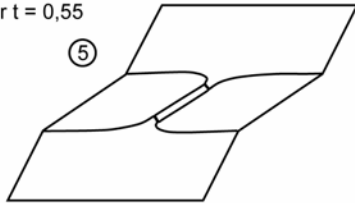
③

viscosity vein = 50 x matrix
viscosity int. layer = 0,25 x ext. layers
simple shear $t = 0,4$



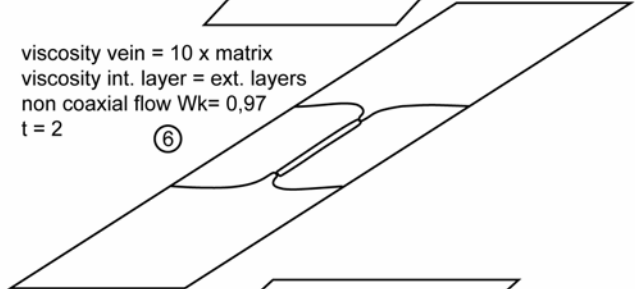
④

viscosity vein = 50 x matrix
viscosity int. layer = 0,5 x ext. layers
simple shear $t = 0,55$



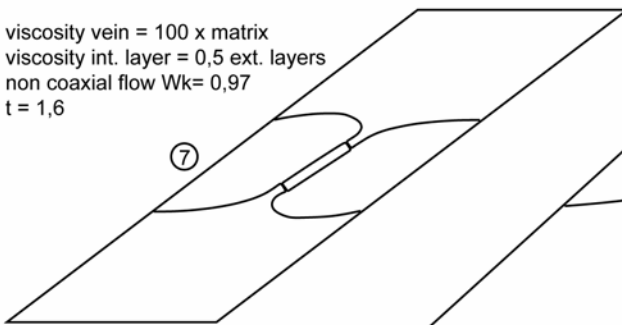
⑤

viscosity vein = 10 x matrix
viscosity int. layer = ext. layers
non coaxial flow $Wk = 0,97$
 $t = 2$



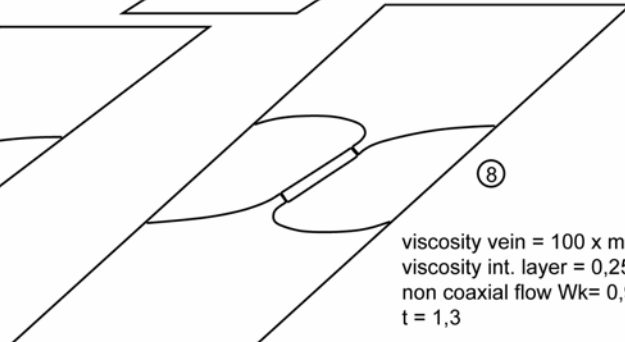
⑥

viscosity vein = 100 x matrix
viscosity int. layer = 0,5 ext. layers
non coaxial flow $Wk = 0,97$
 $t = 1,6$



⑦

viscosity vein = 100 x matrix
viscosity int. layer = 0,25 ext. layers
non coaxial flow $Wk = 0,97$
 $t = 1,3$



⑧

Comparison between the simulations result and the natural example

example Fig. 4.27:



simulations:

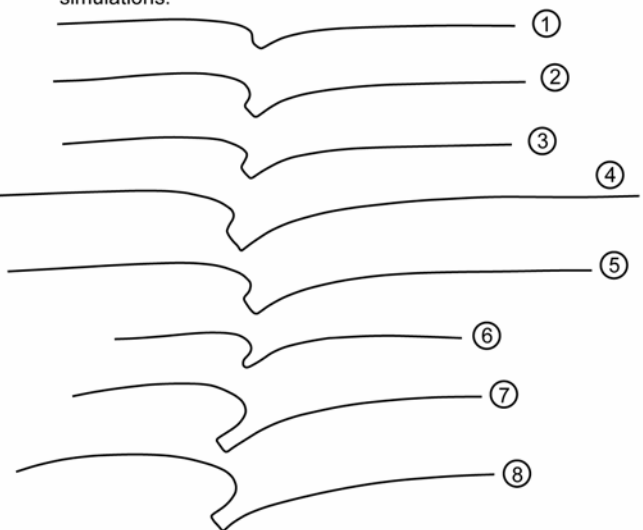


Fig. 4.28. The different parameters which influence the shape of the reworked boudin are varied in order to find the best fit solution for a comparison with the natural example of Fig. 4.27.

If quantitative estimations of the different parameters are difficult, we can however constrain some conditions for the formation of asymmetric flanking folds at the tip of boudin necks. For an asymmetric flanking fold with positive elevation to develop, the rotating vein must be at least stronger than the internal layer. The internal layers must also be of the same or weaker competence than the external layers. The internal layer can be also slightly stronger than the external layers (the order of 1.5 -2 times) than the external layer if the shear strain is high and the competency contrast between the vein and the internal layer is high. The results show therefore that the quartz rich veins are stronger than the pelite and the marble layer in the Lower Ugab Domain. This confirms that wet quartz is stronger in the middle crust, in the greenschist facies conditions where the deformation of the boudins occurs, than the quartz and mica rich wall rock, as show by the experiments of Kenis et al. (2005).

A better use of numerical simulations as a paleorheological gauge for internal and external layers and veins and as gauge for the conditions of the flow may be possible if the model is refined. It is necessary to have a precise idea of the amount of rotation of the vein. The deformation that the vein underwent and the host rock may be estimated by microstructural observations which may allow a better constraint of the competency contrast between the vein and the host rock (Kenis et al., 2004; 2005). Statistical work can be relevant since the shape of the flanking folds always slightly varies from one vein to the other in the same layer in nature.

Chapter 5

Flame Foliation

5.1 Introduction

Foliations are planar features that occur penetratively in deformed rocks. They can be defined by a preferred orientation of platy mineral grains or grain aggregates, grain shape fabric, compositional banding, planar discontinuities such as microfractures (e.g. in low-grade quartzite), or by a combination of these elements (Passchier and Trouw, 2005). Secondary foliations described in the literature can be subdivided into two types (Passchier and Trouw, 2005): foliations that track the XY-plane of finite strain, and those that remain oblique to XY. XY-tracking foliations form mainly by passive rotation or shape change of fabric elements (Fig. 5.1a and b), and by pressure solution. This includes primary, homogeneous foliation and secondary polyphased spaced disjunctive and crenulation foliations (Fig. 5.1c). XY-tracking foliations tend to parallelism with the XY-plane of finite strain in coaxial and non-coaxial flows. Non-tracking foliations are “active” foliations and form by a combination of the previously mentioned processes and mechanisms that destroy or alter foliation. As a result they are oblique to finite strain axes in non-coaxial flow. Examples of non-tracking foliation are shear band cleavage (Gapais and White, 1982) and oblique (steady state) foliation (Means, 1981), where recrystallisation constantly rejuvenates the fabric. Active foliations are common in mylonites. Both tracking and non-tracking foliations form at a high angle to the instantaneous shortening direction in the rock. We present here a third type foliation, which have been named “flame foliation” (Fig. 5.1), which differs from all known foliation types in that it forms at a high angle to the instantaneous extension direction and approximately parallel to the YZ plane of finite strain. Flame foliation has been found in the Lower Ugab Domain of NW Namibia (Fig. 5.2; Swart, 1992; Passchier et al., 2002), at the junction of the Neoproterozoic Kaoko and Damara mobile belts (Miller et al., 1983; Miller and Grote, 1988; Hoffman et al., 1994).

5.2 Geological setting

Flame foliation has been found in the Lower Ugab Domain of NW Namibia (Fig. 5.2; Swart, 1992; Passchier et al., 2002), at the junction of the Neoproterozoic Kaoko and Damara mobile belts (Miller et al., 1983; Miller and Grote, 1988; Hoffman et al., 1994). The Lower Ugab Domain consists of Neoproterozoic siliciclastic and carbonate metaturbidites (Fig. 5.2; Miller et al., 1983; Swart, 1992) affected by three phases

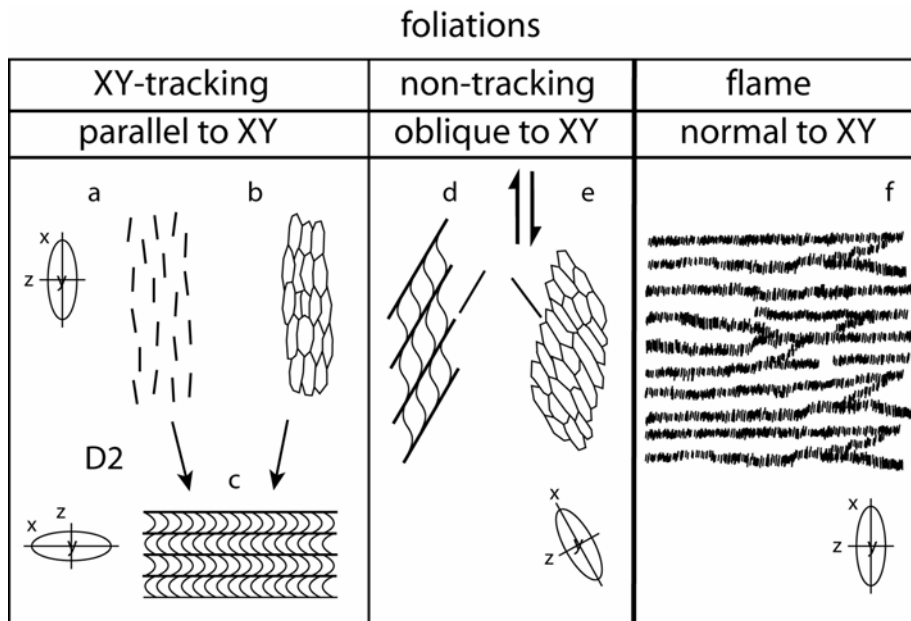


Fig. 5.1. Different types of secondary foliations. XY-tracking foliations tend to parallelism with the XY-plane of finite strain and include a) foliations formed by preferred orientation of platy minerals, b) grains or aggregates, and c) crenulation cleavage. Non-tracking foliations form in non-coaxial flow. They are oblique to the XY-plane of finite strain and include d) shear bands, and e) oblique foliations. f) Flame foliation with biotite oriented perpendicular to the foliation, which forms in extension normal to the XY-plane of finite strain.

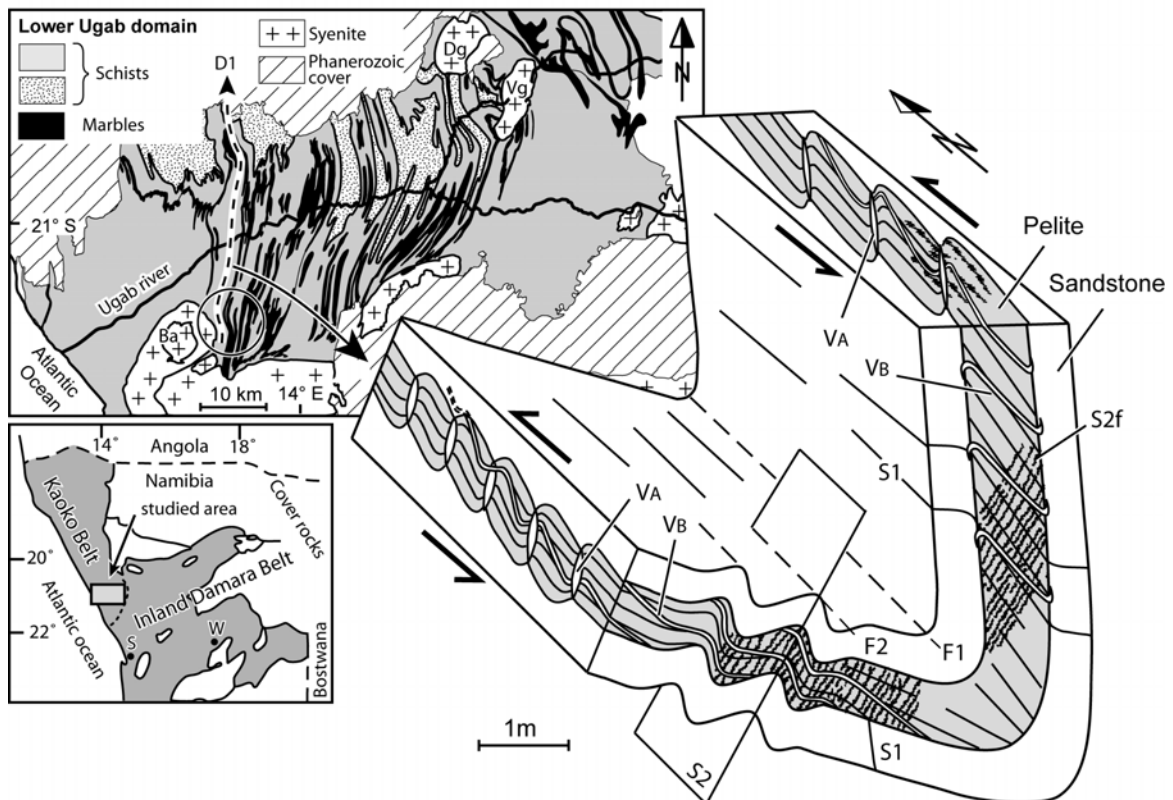


Fig. 5.2. Geological map of the lower Ugab domain in NW Namibia (modified from Miller and Grote, 1988) with the representation of a W vergent F1 fold in the siliciclastic metasedimentary rocks. Two types of syntectonic veins, V_A and V_B , developed respectively oblique to the D1 fold axis and at small angle to S1, respectively. V_A veins are affected by sinistral non-coaxial flow which formed flanking folds alongside the veins and an asymmetric shape of the boudins. Flame foliation S2f developed at a high angle to the S1 cleavage after the main phase of D1. The flames are parallel to the S2 crenulation cleavage and axial planar of F2 folds (see text for further explanation). The circle in the geological map indicates the origin area of the pictures of Fig. 3 and 4. S- Swakopmund; W- Windhoek; Ba- Bandombaai intrusive complex; Dg- Doros syenite intrusion; Vg- Voetspoor syenite intrusion.

of Cambrian or late Proterozoic deformation (Passchier et al. 2002). D1 formed upright kilometre scale N-S to NW-SE trending chevron folds with subhorizontal axes and an axial planar slaty cleavage S1. S1 is marked by a preferred orientation of muscovite, quartz and biotite in metapelites. Throughout the area, two sets of quartz veins formed during D1, V_A oblique to F1 fold axes in boudin necks in pelitic layers and V_B at a small angle to the bedding (Fig. 5.2). Both sets of veins are of the same age, since they crosscut mutually, and probably formed in response to high fluid pressure in the layering. F1 folds represent a main component of E-W shortening, but there evidence that they did not form in bulk coaxial EW shortening. Mantled porphyroclasts and asymmetric D1-boudin necks with flanking folds (Passchier, 2001) adjacent to the V_A veins in boudin necks (Fig. 5.2) in steep limbs of F1 folds indicate that bulk flow was probably by sinistral shear within an EW shortening component.

D2 is less prominent than D1 and caused open folds preferentially in the flat limbs of F1 folds (Fig. 5.2). S2 is locally developed as an axial planar crenulation cleavage of S1, preferentially in more pelitic layers (Fig. 5.2; Fig. 5.4c and d). The F2 fold axes are parallel to F1 axes, but S2 lies invariably at a high angle to S1; where S1 is vertical, S2 is horizontal and vice-versa (Passchier et al., 2002). D1 and D2 deformed the V_B veins in steep limbs of F1 folds, creating hook-shaped folds at the tips of the veins that we interpret as an effect of flexural flow during tightening of F1 folds (Fig. 5.2). Peak metamorphic conditions for the Ugab domain during D1-D2 is estimated at 540-570°C and 2.5-3.2 kbar (Goscombe et al., 2004). The high temperature and low pressure is associated with a tight anticlockwise P-T path for the Ugab Domain by according to Goscombe et al. (2004). These authors suggested that such a P-T path could indicate pervasive contact metamorphism in the area, attributed to extensive granite intrusions during D1-D2 (Fig. 5.2). S1, S2 and the early folds are overprinted by a late D3 phase of weak N-S shortening producing map scale to meter scale folds. D3 is not developed everywhere the effect described above can easily be separated from D3. Crenulation cleavages like S2 usually form by shortening and folding of a previous foliation with fold limbs developing into cleavage domains of the new cleavage (Cosgrove, 1976; Gray, 1979; Gray and Durney, 1979; Williams et al., 2001). Where D2 is weak, however it can be shown that the S2 crenulation cleavage is not simply formed by refolding of S1, but developed through an intermediary step: it grows over a previous foliation that overprints S1, and which we named “flame foliation” (Fig. 5.3 and 5.4).

5.3. Flame foliation

Flame foliation (S2f) is an anastomosing disjunctive mm-spaced biotite foliation composed of biotite-rich selvages of 1 cm to several dm long and 0.1 mm to 3 mm wide with an irregular flame-shape (Fig. 5.3a and b). It occurs penetratively in the more pelitic layers of siliciclastic sediments giving a striped appearance to the rock (Fig. 5.3a and b). The foliation everywhere transects S1 at a high angle and overprints the asymmetric flanking folds around V_A boudin neck veins associated with D1 sinistral shear (Fig. 5.2). This brackets the age of the flame foliation as late to post D1 and pre D2, which excludes any sedimentary origin for the flames. Flame foliation is unique because the constituting micas are not parallel, but perpendicular to the foliation (Fig. 5.3c-e; Fig. 5.4a and b).

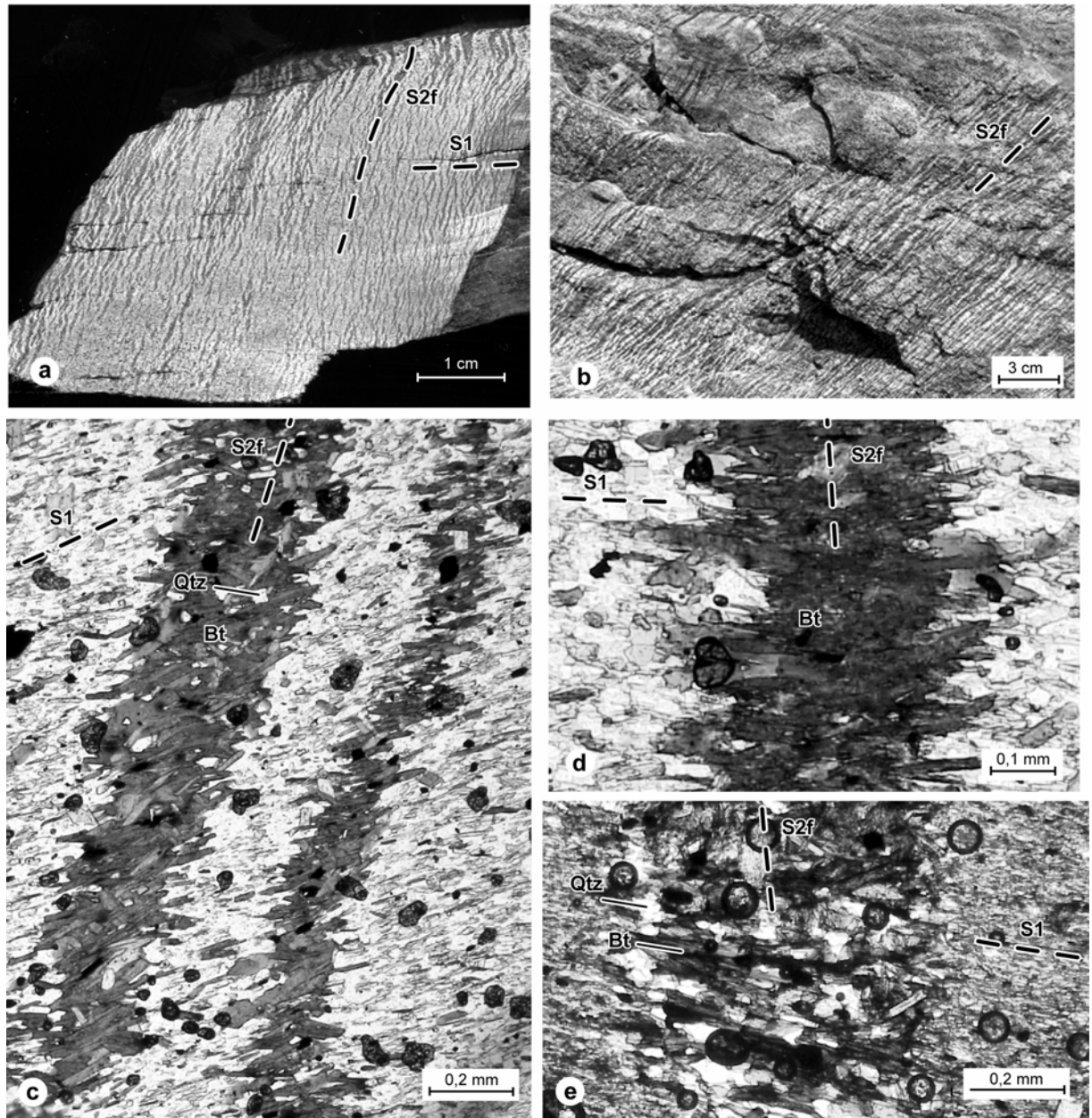


Fig. 5.3. a,b) S2f flame foliation in the rock and the outcrop respectively. c) S2f in thin section. S2f developed at high angle to S1 and is composed of biotite oriented parallel to S1. d) Detail of flame foliation in thin section. e) Detail of an S2f composed of a larger amount of quartz. Bt- biotite; Qtz- quartz.

Flame foliation is composed of biotite with a composition of X_{Mg} between 0,58 and 0,60 with Al_{total} around 44%. The size of the biotite in the flames exceeds that in the matrix forming the S1 slaty cleavage (40-200 μm in the flames and 30-60 μm in the host rock). Some flame foliations contain some quartz in equigranular grains at the border of the foliation or spread throughout the foliation (Fig. 5.3e). Quartz never exceeds 30% of the modal composition of the foliation and is usually present with only a few percent (1-2%). Some of the flames contain equigranular quartz also in the center (Fig. 5.4a). When quartz forms the center of the flames, the grains contain biotite inclusions oriented oblique to the foliation selvages. The grain size of quartz in the flame foliation exceeds that in the pelitic host rock (70-100 μm in the flames and 20-50 μm in the host rock). Ilmenite tends to concentrate in the centre of the flames as well.

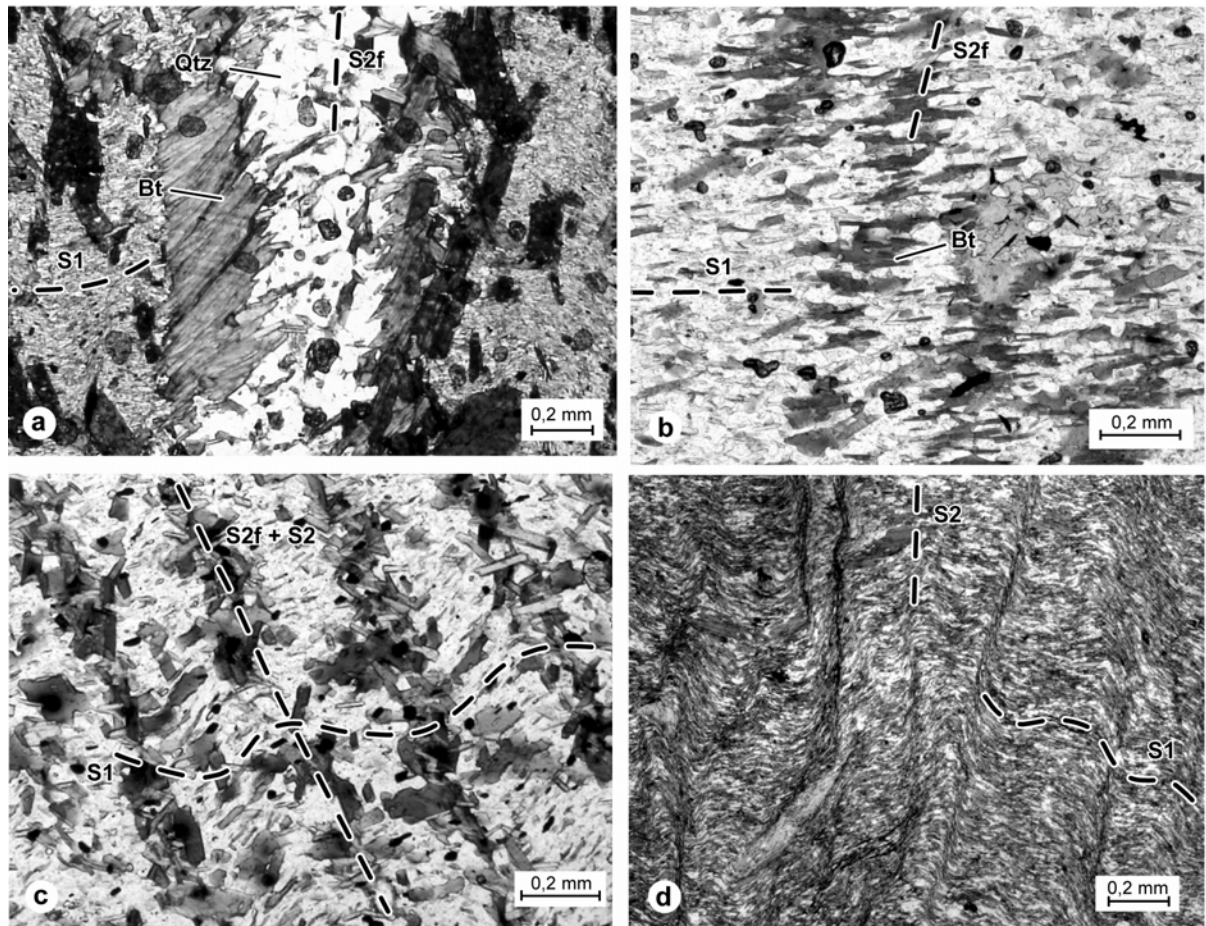


Fig. 5.4. a) S2f with quartz in the centre. b) S2f initiation, the foliation is composed of several single biotite grains oriented parallel to S1. c) Flame foliation overprinted by S2 crenulation cleavage. New growth of biotite occurs parallel to the crenulation. d) S2 crenulation cleavage. Bt- biotite; Qtz- quartz.

5.4. Occurrence of flame foliation

Flame foliation can be found throughout the Lower Ugab Domain, but is best developed in the proximity of syenite intrusions of late syn-D1 age (Fig. 5.2; Passchier et al., in revision). Flame foliation is especially abundant in metapelite of the Amis River Formation near the Bandombaai and Voetspoor intrusive complexes (Fig. 5.2, Ba, Vg; Passchier et al., 2002; van de Flierdt et al., 2003). The Bandombaai Complex is composed of metaluminous hornblende- and sphene-bearing quartz diorites with an age U-Pb zircon of 540 ± 3 Ma (van de Flierdt et al., 2003). It is intruded by younger allanite-bearing granodiorites and granites, and peraluminous garnet- and muscovite-bearing leucogranite. The Voetspoor Pluton is mainly composed of hornblende syenite with published ages of 530 ± 2 Ma by Pb-Pb single zircon evaporation (Seth et al., 2000) and 541 ± 6 Ma by conventional U-Pb dating of sphene (Jung et al., 2005). Contact metamorphism occurred in a typical 5 km wide margin around the intrusive bodies producing dark spots in the metapelites which contain biotite porphyroblasts and biotite-muscovite-chlorite aggregates pseudomorphing original cordierite and/or andalusite. The porphyroblasts overprint both the S1 cleavage and the flame foliation (Goscombe et al., 2004), which brackets the age of S2f as late to post S1 and

predating D2 and the heating front of the intrusions that led to porphyroblast growth related to contact metamorphism. In the central and eastern part of the Lower Ugab area, minor granitic veins show D1 deformation and the large scale intrusions cut the D1 folds when they are still relatively open, which constrains the age of the intrusions as syn to late D1. In the western part the allanite-bearing granodiorites of the Bandombaai complex cut the D1 structures, and some minor granitic veins show D2 deformation which brackets the age of the intrusion as post-late D1 and pre-syn D2. Since flame foliation formed late-post D1 and pre D2, it is of the same age of the intrusive events in the area.

5.5 Development mechanism of flame foliation

The internal structure and the penetrative character of the flame foliation excludes an origin as deformed objects or deformed retrograde biotite porphyroblasts or clasts. The fibrous geometry of biotite growth parallel to S1, the association with quartz veins and the occurrence of quartz suggest that flame foliations formed by opening of fractures that acted as channels for fluids that caused biotite growth parallel to preexisting S1. The orientation of the flames is normal to S1 but they formed late during the deformation phase that gave rise to this foliation, which means that they formed orthogonal to the direction of late D1-extension in both limbs of tightening D1 folds (Fig. 5.5). The flame foliation can therefore be considered to develop in a similar process as synmetamorphic veins. However, the penetrative character, the internal structure (Fig. 5.3a-c, 5.4a and b) and the very narrow spacing of the flames (0.1- 1mm) is not a classical feature of vein formation. Less developed flame foliations show columns of several single biotite grains oriented parallel to S1 (Fig. 5.4b). The observations presented here suggest an initiation by metamorphic reaction or metasomatic alteration. The late D1 syenite intrusions may have caused extensive devolatilization reactions in the schists, notably chlorite and muscovite decomposition which produces biotite (Connolly, 1997). These reactions occur in metapelite at a lower temperature than the reaction for the growth of cordierite. This explains the overgrowth of the contact metamorphism porphyroblasts on the flames and the occurrence of the flame foliation beyond the limit of crystallization of the porphyroblasts in the contact margin. Devolatilization reactions due to the syenite intrusions together with added magmatic fluids locally increased fluid pressure which may led to hydrofracturing in overlying metasedimentary rocks (Furlong et al., 1995; Hanson, 1995). Hydrofracturing occurs rapidly in the order of several tens of years (Nishiyama, 1989). It may have also predated the growth of the porphyroblasts as evidenced by the temporal relation between porphyroblasts and the flames, because the thermal front migrated more slowly through the metasedimentary rocks as the fluid pressure front. Electron microprobe analyses show that the biotite crystals in the flames have the same composition as those in the matrix and biotite porphyroblasts that postdate the flames. This indicates that all biotites have a metamorphic origin rather than a magmatic one. It is therefore unlikely that magmatic fluids reached the growth sites of the biotite flames: no trace of such fluids is left in the biotite composition and the flame foliation is restricted to the more pelitic layers of the siliciclastic metasedimentary rocks. The flame foliation is therefore interpreted as a kind of alteration rim along synmetamorphic microfractures formed by devolatilization reaction closer to the granite. They

developed along tension fractures, i.e. parallel to the σ_1 - σ_2 plane of the local stress field, or the YZ-plane of incremental strain. Since the flame foliation formed late during D1, they developed therefore normal to S1, which formed parallel to the XY-plane of finite strain.

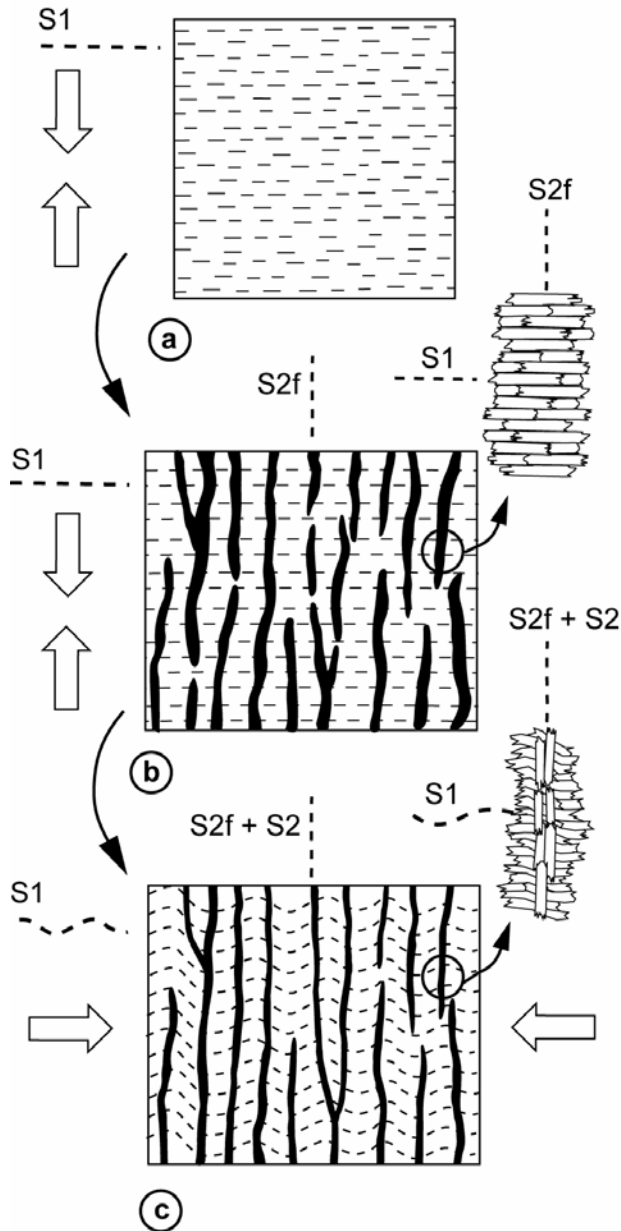


Fig. 5.5. a; b) In the last stage of the D1 deformation, biotite rich selvedges (S2f) form due to devolatilization reactions, with crystallisation of biotite nearly orthogonal to the selvedges. c) The selvedges are later overprinted by S2 crenulation which causes the thickening of the selvedges and new growth of biotite parallel to the crenulation

5.6. Significance of the flame foliation

Flame foliation could be regarded as an obscure, apparently rare foliation type but its significance is enhanced by its relationship with crenulation cleavage. Flame foliation is only visible in selected sites of low D2 strain. Elsewhere, a complete transition can be found from undeformed S2f flame foliation through slightly folded S1 between biotite flames to a typical S2 crenulation cleavage with biotite enrichment in the

cleavage lamellae (Passchier and Trouw 2005; Fig. 5.3g and 5.5). Locally, the S2 microfolds lie slightly oblique to the older flame foliation, showing that the formation of the biotite flames and the crenulation cleavage are two distinct events. The biotite flames are therefore apparently the preferential nucleation sites for the development of cleavage lamellae of an S2 crenulation cleavage, and their original nature becomes obscured. This explains the unusual orientation of S2 crenulation cleavage in the Ugab area, everywhere at high angles to S1 (Passchier et al., 2002). The fact that flame foliation in the Ugab area can be deformed into a typical crenulation cleavage with biotite enriched cleavage lamellae implies that crenulation cleavage in other areas may go through a similar, hitherto undetected flame foliation stage. Before we discovered flame foliation at sites of weak D2 deformation we noticed no special microstructural geometry of the S2 crenulation cleavage, since the flame stage of development can be completely obliterated. Crenulation cleavage formed this way is not necessarily parallel to the XY plane of finite strain, since it depends on the presence of an older fabric element. Biotite enrichment in cleavage domains can also therefore have another origin than enrichment by dissolution of quartz (Gray and Durney, 1979).

The previous pages of Chapter 5 are the text of the article:

Maeder, X., Passchier, C.W., Trouw, R.A.J., 2007. Flame foliation: Evidence for a schistosity formed normal to the extension direction, Journal of Structural Geology 29, 378-384.

Some new material about the flame foliation obtained after this publication is presented below.

A preliminary EBSD study have been performed on the sample X.04.81 (location: -21.0993°/13.8707°, in metapelite of the Amis River Formation near the Bandombaai granite) (Fig. 5.6a). “Band contrast maps” have been made on one of the flames and the wall rock. Band contrast maps show the degree of indexing that is possible; dark parts are areas where no indexing (Kikuchi patterns) can be obtained. This usually occurs at grain boundaries, and band contrast maps are therefore suitable to mark these boundaries. A preferential orientation of biotite can be seen in the flame (Fig. 5.6b). The biotite is oriented perpendicular to the flame foliation and parallel to S1. The band contrast map of the wall rock shows the grains oriented in S1 (Fig. 5.6c).

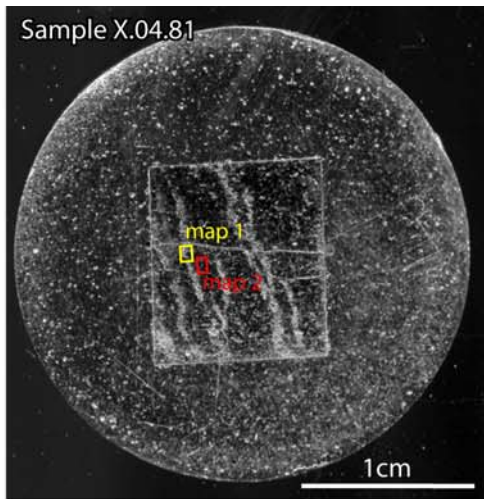
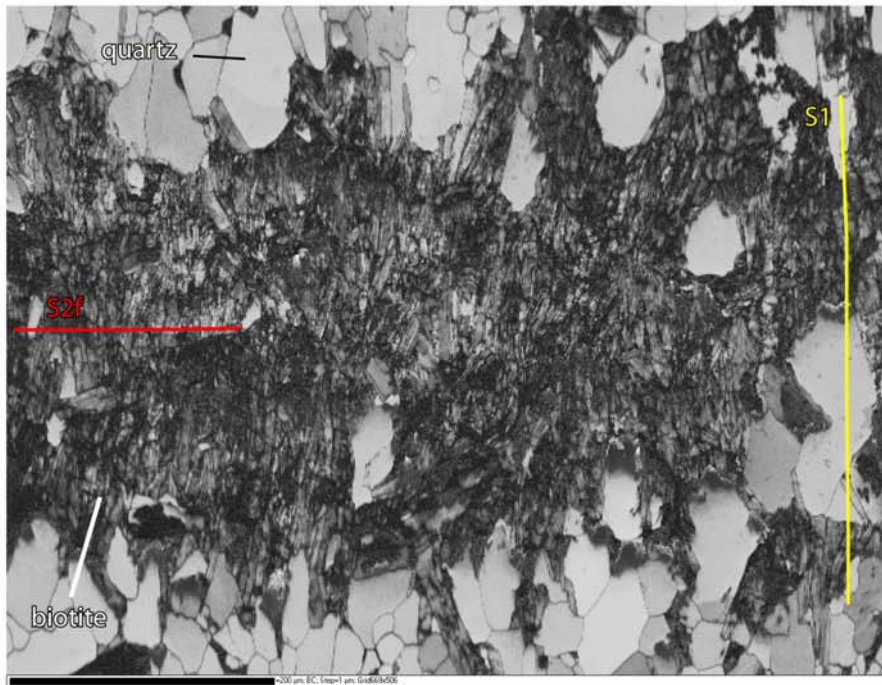


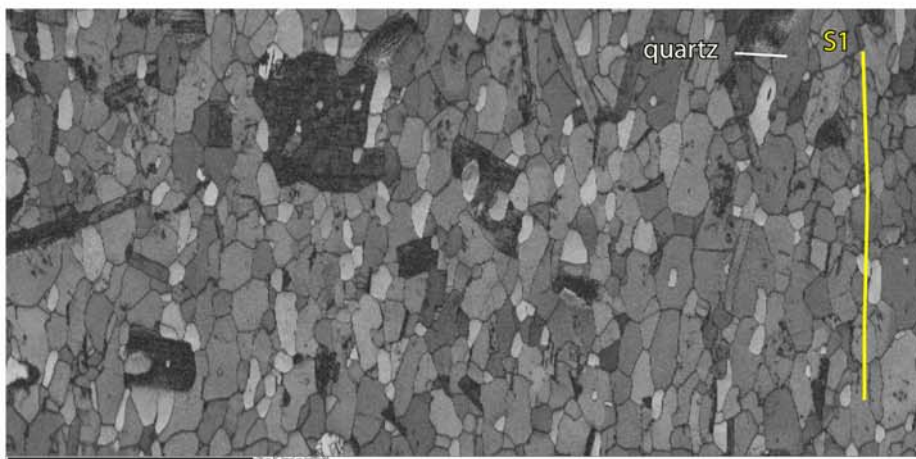
Fig. 5.6. (a) Sample X.04.81 analysed by EBSD. The flame foliation is subvertical. (b) Band contrast map of the flame foliation (c) Band contrast map of the wall rock

(a)



map 1, flame foliation band contrast

(b)



map 2, wall rock band contrast

(c)

Chapter 6

Conclusions

6.1 Structural evolution of the Lower Ugab Domain

The Lower Ugab Domain underwent three phases of deformation which define two main tectonics events: D1-D2 and D3. D1 formed the kilometre-scale upright to west vergent north-south trending en chevron folds that dominate the structure of the region and the main slaty cleavage in axial planar position. Asymmetric folds, delta and sigma structures, asymmetric boudins and flanking folds along displaced quartz veins indicate a strong component of sinistral shearing all over the area. S2 cut the asymmetric fold and flanking folds without being deformed, indicating that the sinistral shearing component mainly occurred during D1. D1 is therefore associated with a transpressional phase of deformation with east-west shortening and steep north-south oriented sinistral shearing components. During late D1 S2f flame foliation formed due to devolatilization reaction in the contact margin of the contemporaneous syenite intrusions at a high angle to S1 during tightening of D1 folds. D2 is less conspicuous than D1 and formed open folds with parallel axes to D1 folds. D1 and D2 present therefore a similar component of east-west shortening. D1 and D2 formed at the same metamorphic conditions in greenschist facies associated with crystallisation of biotite and seem therefore to belong to the same continuous tectonic event. S2f is the preferential nucleation site for the development of S2 crenulation cleavage in the region which explains the formation of S2 always at a high angle to S1. D1 and D2 are part of large cleavage fans which occur at the west of the Voetspoor and De Rust granites. The fanning is interpreted to be due to east-west compression of the metasediment towards the planar late D1-syn D2 intrusions during D2. The relative downward motion of the Voetspoor pluton during the intrusion may have favoured the rotation of D1 structures towards an east-vergence to the west of the pluton.

Asymmetric folds with NW gently plunging axes and north-east vergence form in the flat limbs of D1 folds at the west of the Voetspoor granite. They are oblique to D1 and D2 structures and belong to a distinctive deformation episode. The asymmetric folds may be linked to movements in the flat limbs of D1 folds during the reorientation of the structure during the sinistral shearing or the effect of the rigid pluton on the deformation of the wall rock.

Structural field relationships show that the Bondambaai, Doros, Voetspoor and Brandberg West syenites all intruded during late D1-syn D2 and belong to the same intrusive event. The dykes associated with the De Rust granite are strongly deformed by D1 attesting that the granite intruded early-syn D1. Since the De Rust granite presents the same rock facies, it seems to be related to the same intrusive event as the other syenites intrusion of the area. D1 may have therefore developed slightly later in the eastern part of the area.

D1 and D2 are linked to the major tectonic event of oblique convergence and collision of the Rio de la Plata craton and the Coastal Terranes towards the Congo craton which caused the dominant structures of the

Kaoko belt that started at 580 Ma in the north of the Belt (Gray et al, submitted). The maximum age for D2 is given by a granitic veins from the Doros Pluton which is dated at 533 ± 6 Ma by shrimp U-Pb (Passchier, unpublished report).

D3 is entirely distinct from D1-D2 since it caused ENE-WSW trending open folds, indicating a major component of north-south shortening. A small component of sinistral flow may have prevailed during D3 in the north-eastern part of the area where D3 fold trains are asymmetric and northeast-southwest trending. D3 is associated with north-south convergence and collision of the Congo and Kalahari cratons (Miller, 1983). The age of D3 is constrained by the pre-syn D3 biotite granite of the Doros and Voetspoor intrusion estimated at 530 ± 5 Ma by shrimp U-Pb (Passchier, unpublished report). D2 and D3 seem therefore to be relatively close in age.

6.2 Syntectonic veins in the Lower Ugab Domain

Three main sets of syntectonic veins formed in metapelite of the Lower Ugab Domain, labelled V_{bed} , V_A and V_B veins. V_{bed} are quartz stripped bedding veins which show top to the west Pre D1 bedding-parallel slip. V_A veins are composite quartz-calcite veins which formed at a high angle to the bedding and the D1 folds axes pre to syn-D1. They formed as boudin necks in the pelitic and marble layers due to north-south extension parallel to the layers. The displacement of the veins relative to the bedding, the boudinage of the veins, the formation of flanking folds along side the veins and the asymmetric buckling of the bedding interface at the tip of the veins indicate a sinistral rotation of the veins relative to the bedding mainly caused by D1 non-coaxial flow. D3 caused the narrowing of V_A boudin neck veins due to north-south compression parallel to the layer, leading to an extreme convex shape of boudins.

V_B veins are composite quartz-calcite veins which lie slightly oblique to D1 folds axes and roughly perpendicular to V_A veins. Hook-shaped folds developed in the steep limb of D1 folds at the limit of the pelitic layer where the tip of the vein penetrates the adjacent sandstone layers. They attest to reorientation of the veins due to flexural slip during tightening of the folds. The formation of V_A and V_B veins in the more pelitic layers rather than the sandstone is not classical for boudinage and may be explained by high fluid pressure. Contradictory cross-cutting relationships show that V_A and V_B are contemporaneous. The contemporaneous formation of two sets of veins roughly perpendicular can be explained by local inversion of σ_2 and σ_3 between high fluid pressure pulses. Isotopic compositions indicate a local origin of the material that forms the veins.

6.3 Modelling of boudin neck rotation

Finite element numerical simulation of boudin neck rotation in coaxial and non-coaxial flow show that asymmetric flanking folds similar to those observed in the Lower Ugab Domain can form at the tips of the rotating boudin necks. This confirms the interpretation that the asymmetric boudins in the Lower Ugab Domain formed due to the rotation of the boudin necks with respect to the layering. The parameter sensitivity analysis shows that the controlling parameters for the shape of the reworked boudins are the total strain, the kinematic vorticity number of the bulk flow, the relative viscosity of the veins and the internal layer and external layers. The effect of the stress exponent of the Power law equation is very small on the simulations. It is therefore impossible to estimate the stress exponent value of the natural deformation conditions with the numerical experiments. The simple shear component of bulk flow mainly contributes to asymmetric flanking folds with positive bulge at the tip of the boudin necks. An increase of the simple shear component of progressive deformation increases the bulge and the elevation of flanking fold at the tip of the boudin necks. An increase in pure shear strain component of progressive deformation parallel to the layers increases the elevation of the bedding interface between the boudin necks. In a transpressional regime with shortening perpendicular to the layering, an increase of the pure shear component of the progressive deformation decreases the maximal elevation of the bedding interface and can lead to the formation of bone-shaped boudins (Malavielle and Lacassin, 1988) where Wk approaches zero. Bulge and elevation increase with an internal layer weaker than the surrounding layers and with stronger boudin necks. Boudin necks weaker than the internal layer cause slip of the boudins along the boudin necks during the progressive deformation. This results in a domino boudin structures (Goscombe and Passchier, 2003). Zones have been determined for the conditions of the relative viscosity of the vein, the layers and the kinematic vorticity number of the flow in transtensional and transpressional regime for a certain strain where the reworked boudins have an asymmetric shape, a bone-shape, a symmetric extreme convex-shape, a domino boudin geometry or a shortened bone shape. The necessary conditions to form asymmetric reworked boudin as observed in the Lower Ugab metasediments are boudin necks stronger than the internal layer, an internal layer weaker, with the same or only slightly higher competence than the external layers and a significant simple shear component of the bulk flow. The quartz veins are therefore stronger than the quartz rich wall rock in the greenschist facies where the progressive deformation occurred, which confirms the conclusions of Kenis et al. (2005) on boudins in the Ardennes. The flow condition for greater bulge of the asymmetric flanking folds at the tip of the boudin necks seems to be for a transtensional regime with shortening parallel to the layer with a kinematic vorticity number around 0.7.

Numerical simulations show that rotation of tension gashes in simple or slightly transtensional shear flow can result in bone-shaped boudins with boudin necks stronger than the layers. The bone shape geometry is strengthened in the case of weak boudinaged layers. Bone shaped-boudins are usually interpreted to result from transpressional progressive deformation (Malavielle and Lacassin, 1988). The simulation results show therefore that such structure can also form by rotation of veins originally oblique to the layering as tension gashes in simple shear flow or slight transtensional flow.

6.4 Flame foliation

Flame foliation (S2f) developed as penetrative anastomosing biotite rich selvages at a high angle to S1 in the metapelite of the Lower Ugab Domain during late-post D1. The biotite grains in the selvages are oriented perpendicular to the foliation and parallel to the previous S1 cleavage. The flame foliation is therefore interpreted to form in extension rather than in compression like classical foliation. The localisation of the flame foliation preferentially close to the contemporaneous syntectonic syenite intrusions suggest that they form by devolatilization reactions in the metapelites and high fluid pressure as a kind of alteration rim along synmetamorphic microfractures. S2f seems to be the preferentially nucleation site for the development of S2 crenulation cleavage which overprint the flame foliation. This can explain the orientation of S2 always at a high angle to S1 in the area.

6.5 Further perspectives

An area such as the Ugab Domain presents exceptional outcrop conditions over surface area of more than 3000 km² which is well suitable to study large and small scales structures. The present study investigated the main structures that can be found in the area, but some aspects can be investigated in more detail. For instance, the overprint between S1, S2f and S2 crenulation cleavage presents a puzzling scenario that deserves to be further studied. It would be helpful to find flame foliation in other localities which present comparable or different tectonic settings for comparison and to understand the relation of S2f with a previous and an eventual later cleavage. The Lower Ugab Domain presents the first case study of the formation of flame foliation and it would be therefore interesting to study this structure in other areas for a better understanding of the process of its formation.

The coaxial D1 and D2 deformations present an interesting case study of the evolution of two continuous but distinct phases of deformation. The transition between D1 and D2 can be also more investigated in more detail.

The Brandberg West and De Rust intrusions have not yet been investigated in detail. The detailed study of the Voetspoor and Doros granites in the north-west of the area have been successful to constrain the intrusive mechanism and the structural evolution around the plutons (Passchier et al., 2007). A detailed study of the Brandberg West granite and The De Rust granite can reveal some more detailed informations about their intrusive mechanism and their relation with the regional deformation. It may also bring informations about the possible diachrony of D1 and D2 from the central to the eastern part of the area.

Finite element modelling of boudin neck rotation may be use as a better paleogauge to constrain the rheology of the veins and the wall rock during deformation if the flow can be more constrained. By focussing on a specific area where D1, D2 and D3 strain can be well estimated it may be possible to constrain better the simulation and the parameters of the viscosity of the veins relative to the wall rock. Statistical analysis of the shape of the natural asymmetric boudins in a same outcrop can be made to solve the problem of slight variations in geometry of the reworked bedding interface from one boudin to the other.

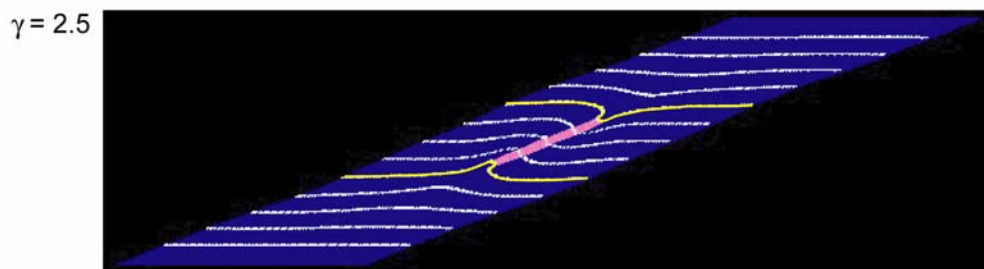
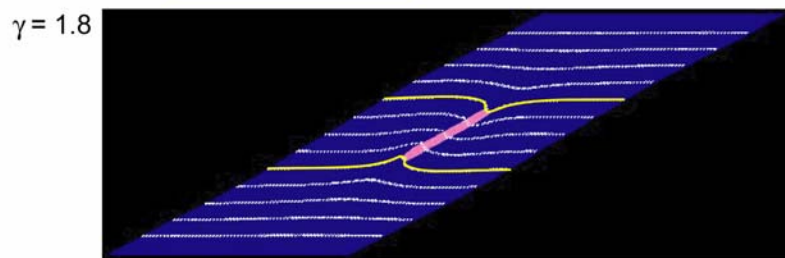
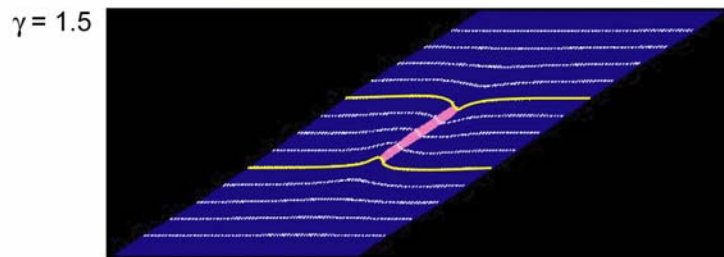
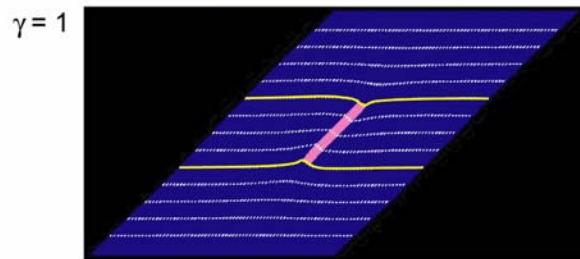
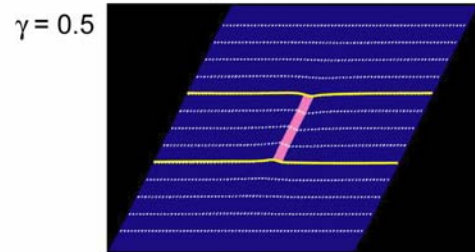
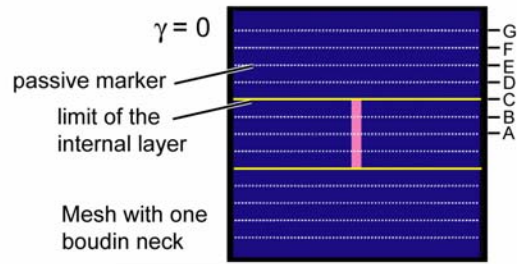
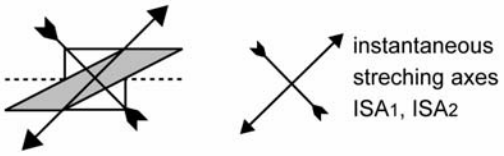
Appendices

The Appendix numbers are made to fit the Figure numbers of Chapter 4

Appendix 4.8 a

Influence of the degree of shearing

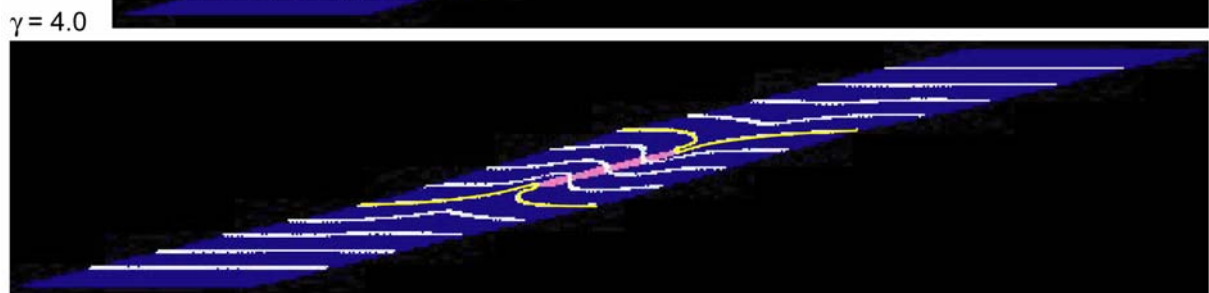
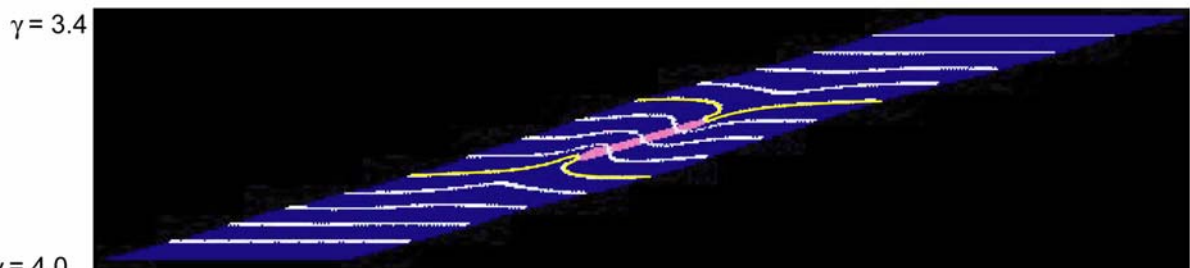
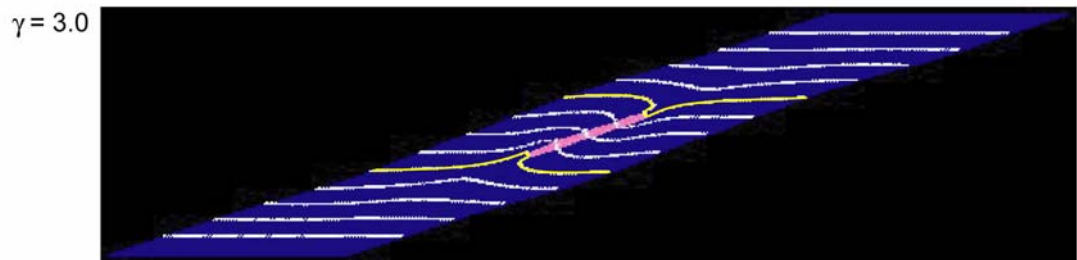
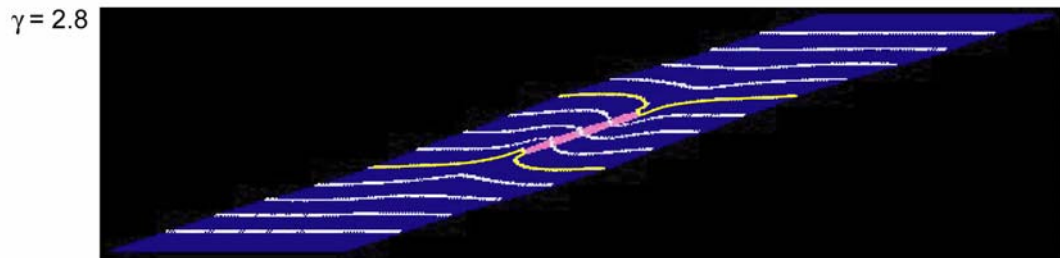
Simple shear flow.
 Viscosity vein = 10x viscosity layers
 Viscosity internal layer = viscosity external layers = 1



Appendix 4.8 b

Influence of the degree of shearing (continuation)

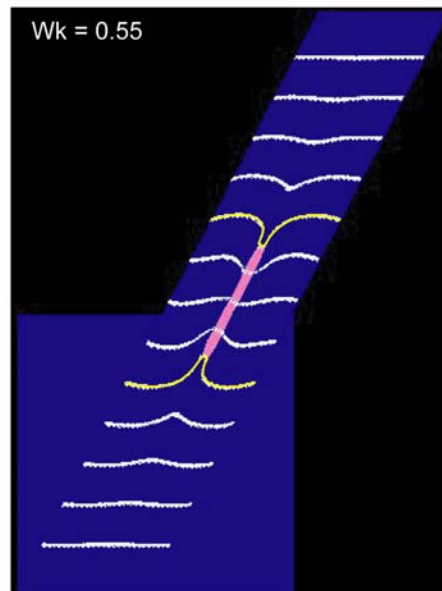
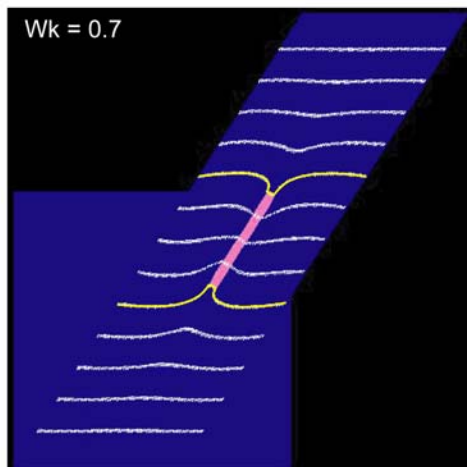
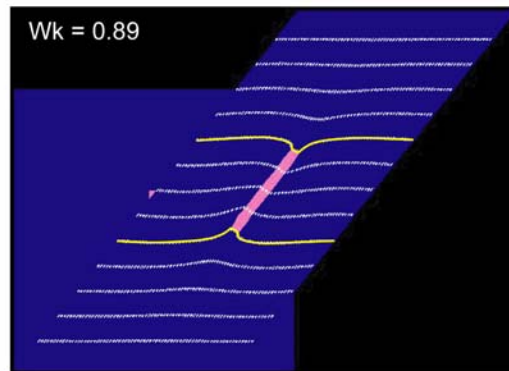
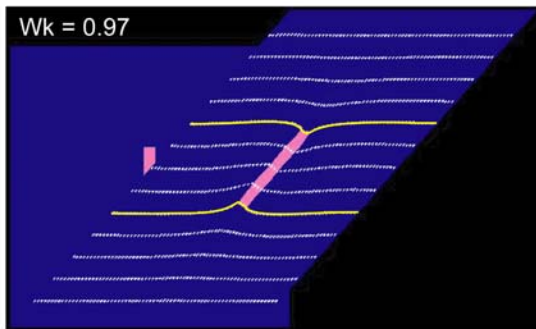
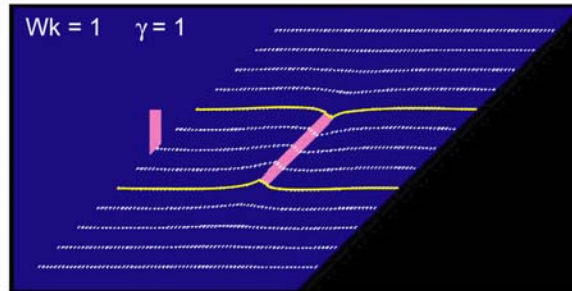
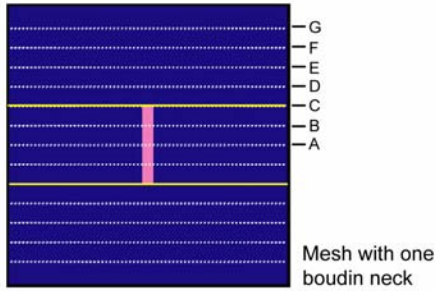
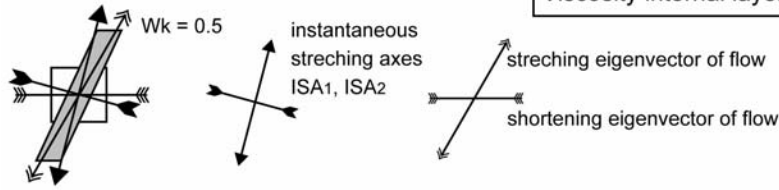
Simple shear flow.
 Viscosity vein = 10x viscosity layers
 Viscosity internal layer = viscosity external layers = 1



Appendix 4.9.1 a

Influence of the kinematic vorticity number

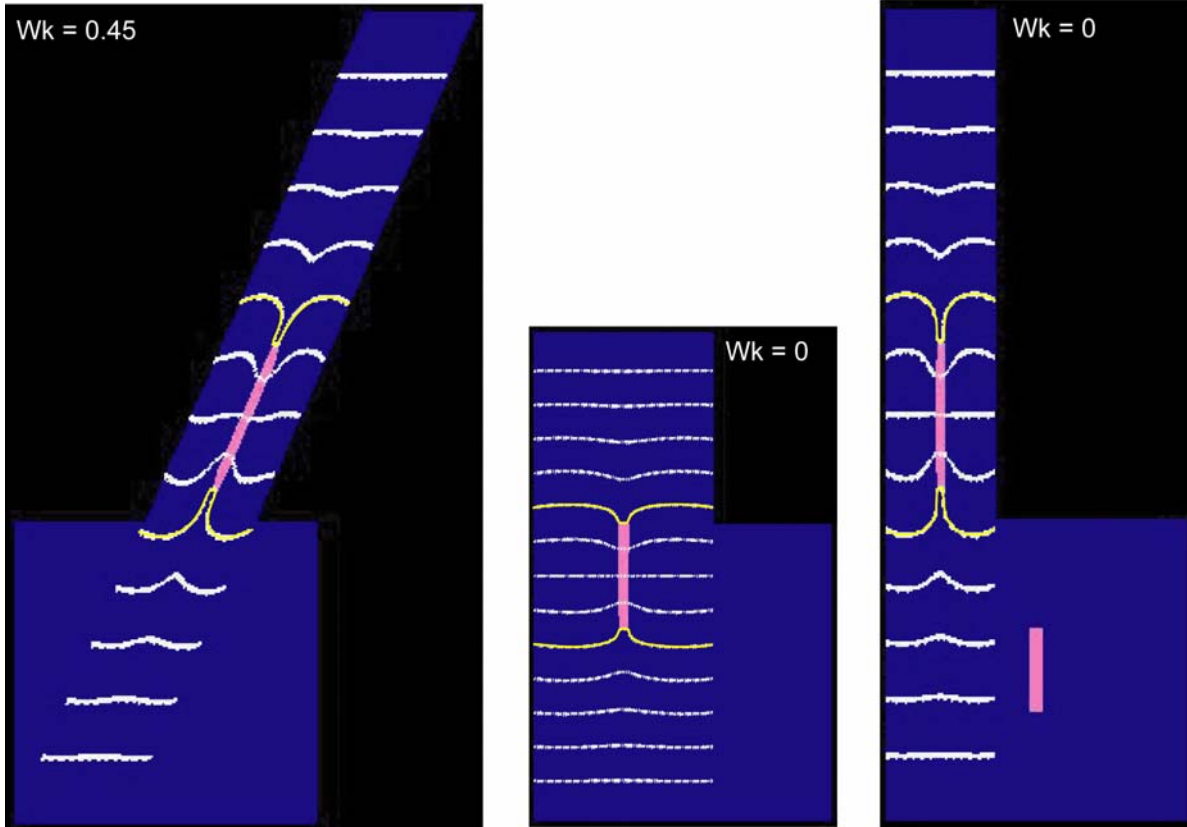
General shear flow, transtensional regime
 Viscosity vein = 10x viscosity layers
 Viscosity internal layer = viscosity external layers = 1



Appendix 4.9.1 b

Influence of the kinematic vorticity number
 Mesh with one boudin neck (continuation)

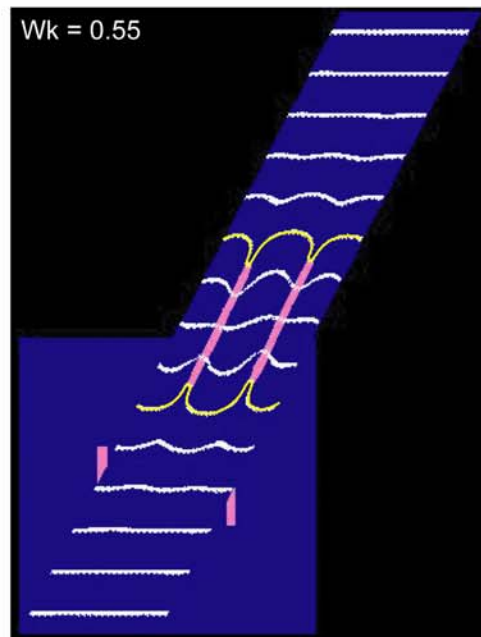
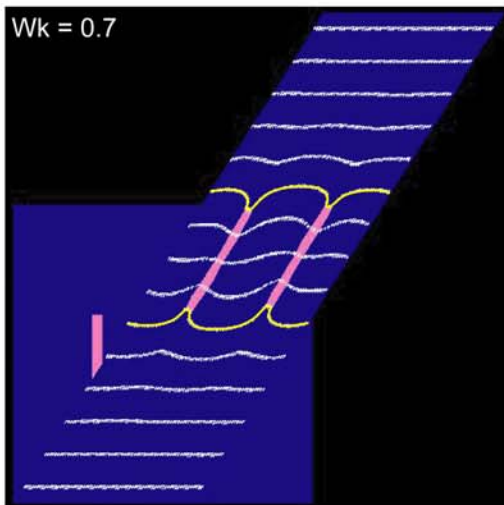
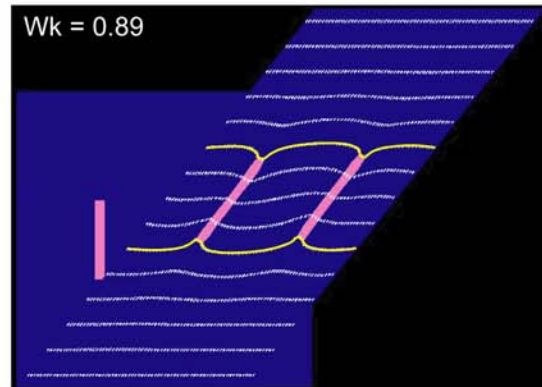
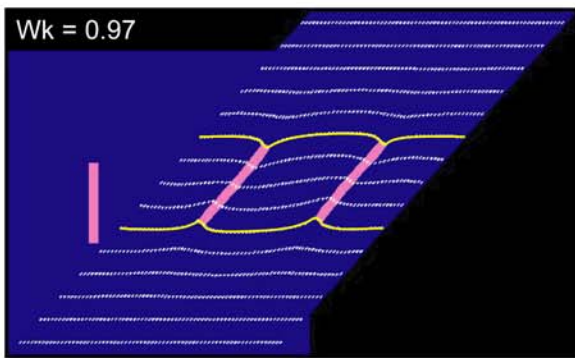
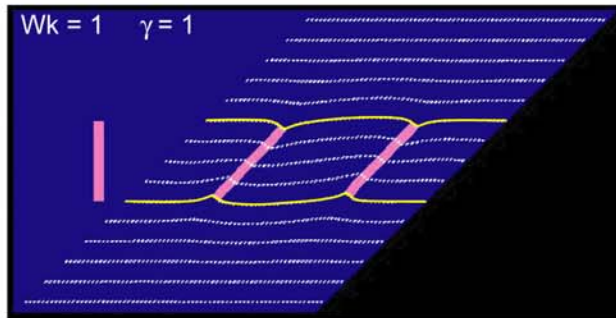
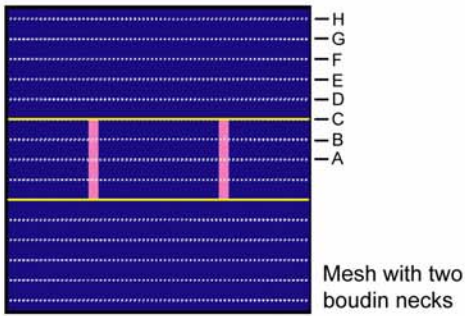
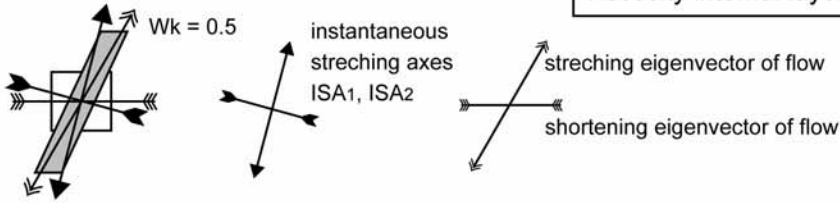
General shear flow, transtensional regime
 Viscosity vein = 10x viscosity layers
 Viscosity internal layer = viscosity external layers = 1



Appendix 4.9.2 a

Influence of the kinematic vorticity number

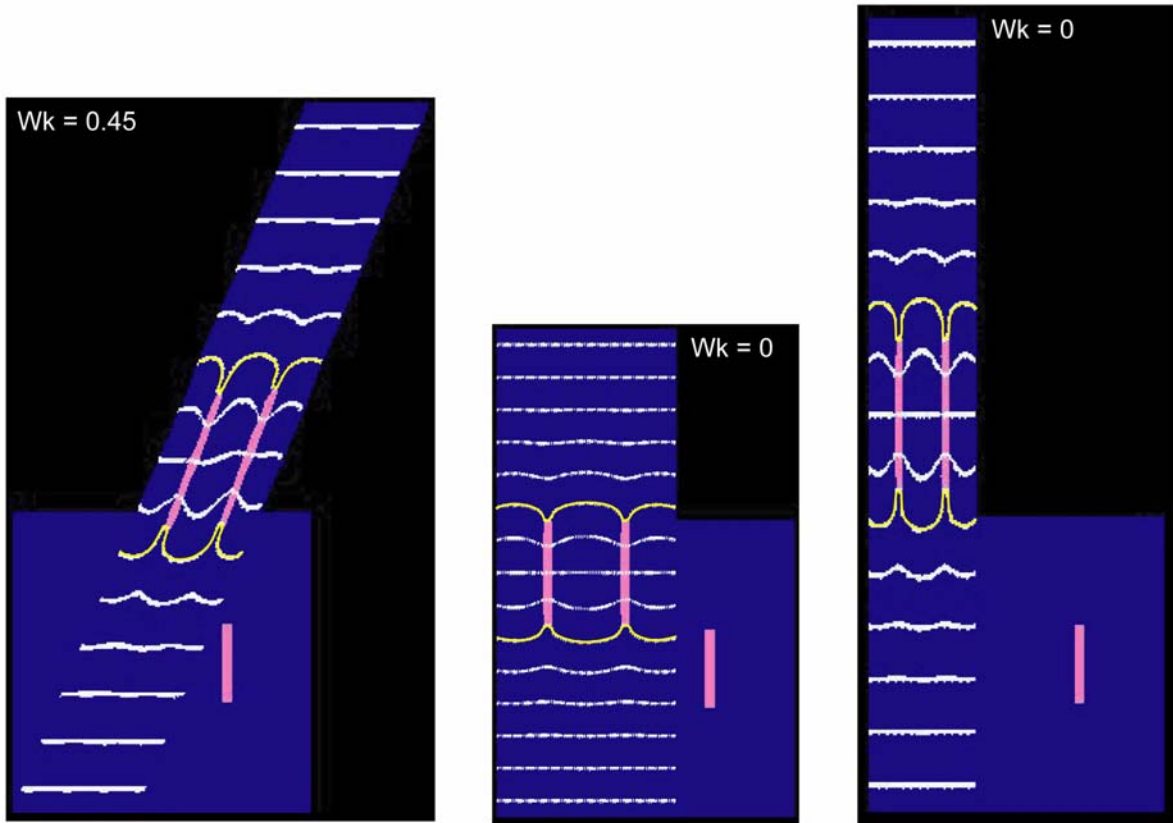
General shear flow, transtensional regime
 Viscosity vein = 10x viscosity layers
 Viscosity internal layer = viscosity external layers = 1



Appendix 4.9.2 b

Influence of the kinematic vorticity number
 Mesh with two boudin necks (continuation)

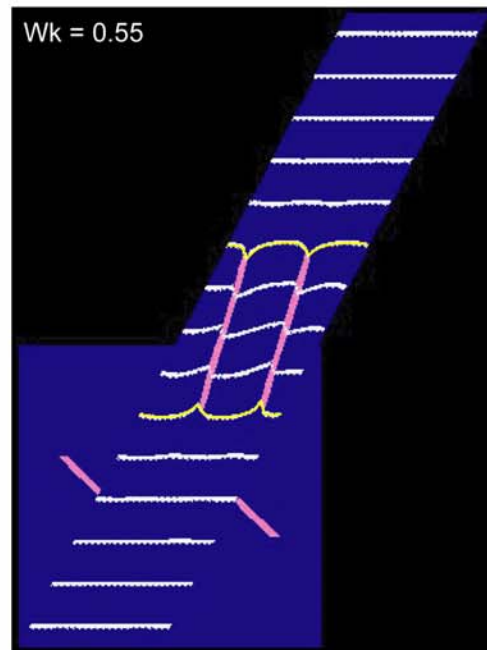
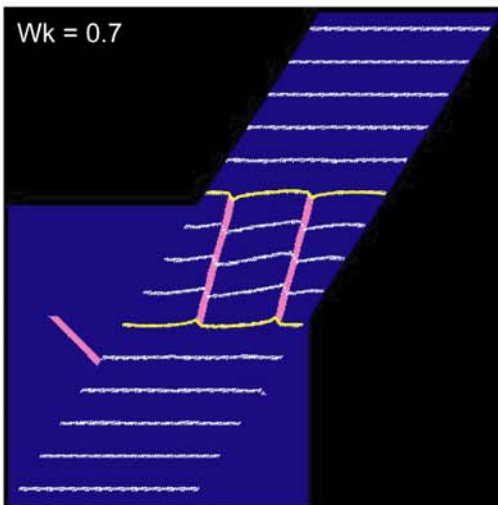
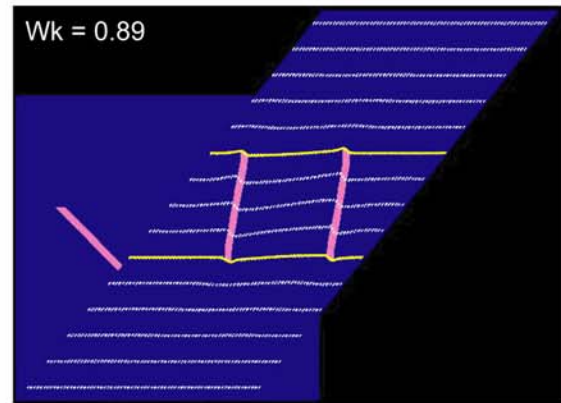
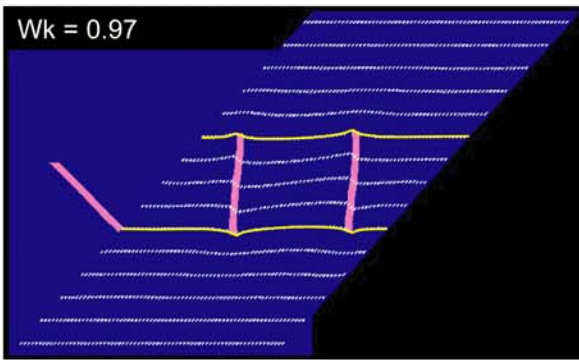
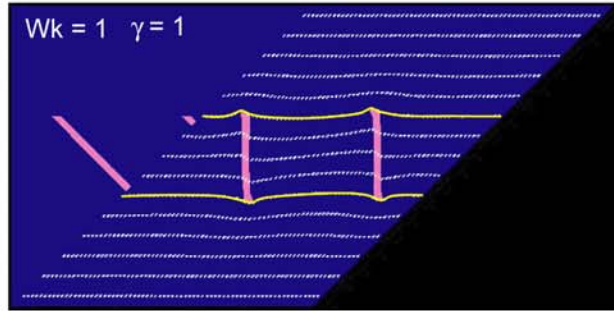
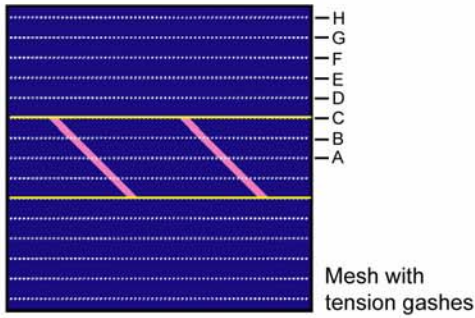
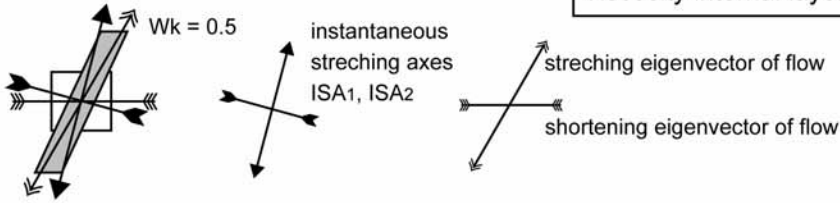
General shear flow, transtensional regime
 Viscosity vein = 10x viscosity layers
 Viscosity internal layer = viscosity external layers = 1



Appendix 4.10a

Influence of the kinematic vorticity number

General shear flow.
 Viscosity vein = 10x viscosity layers
 Viscosity internal layer = viscosity external layers = 1



Appendix 4.10b

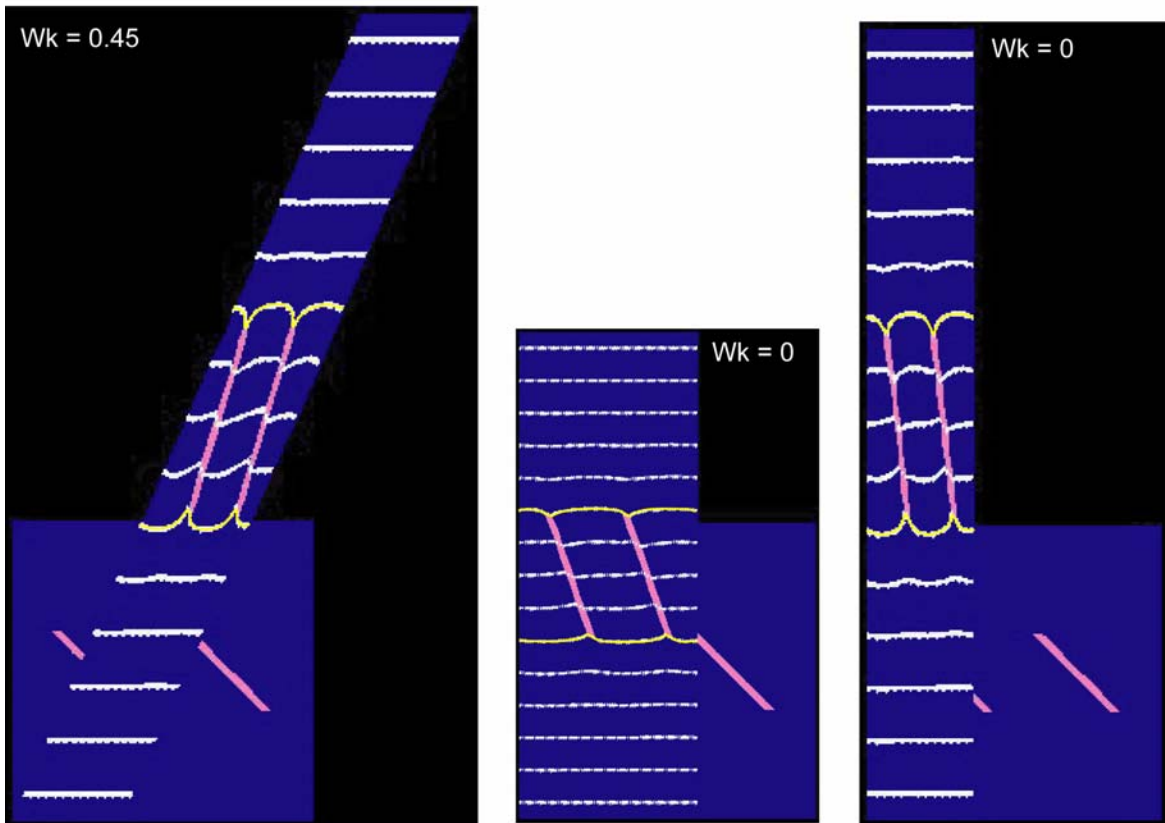
Influence of the kinematic vorticity number

Mesh with tension gashes (continuation)

General shear flow.

Viscosity vein = 10x viscosity layers

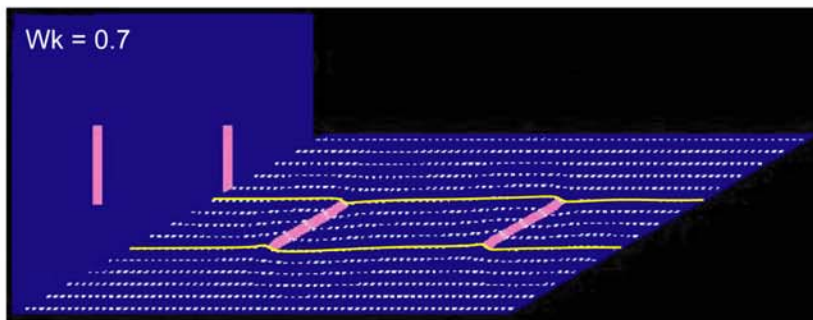
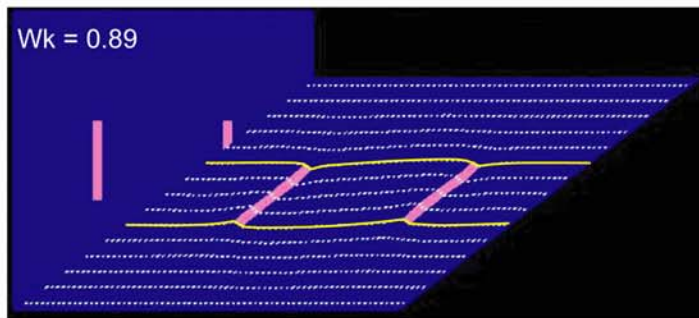
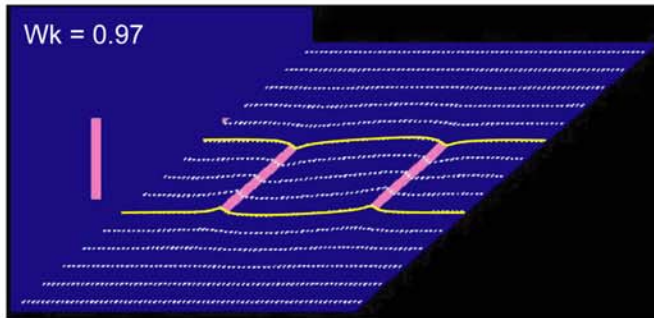
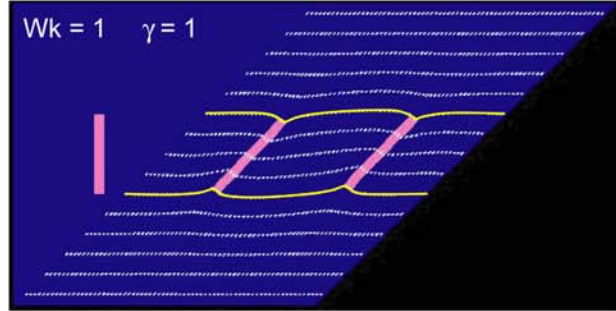
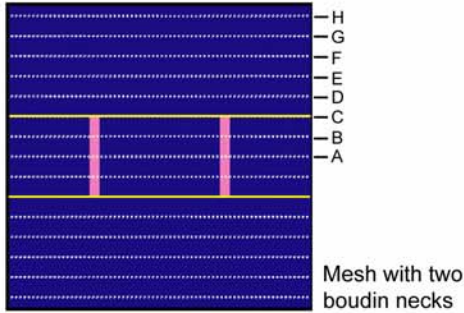
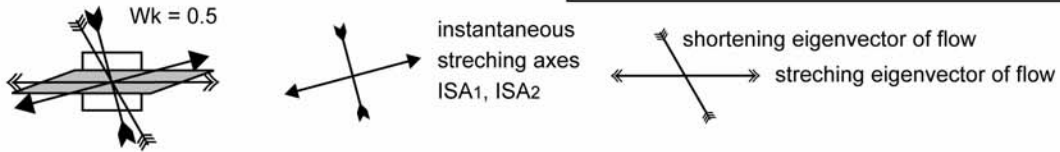
Viscosity internal layer = viscosity external layers = 1



Appendix 4.11 a

Influence of the kinematic vorticity number

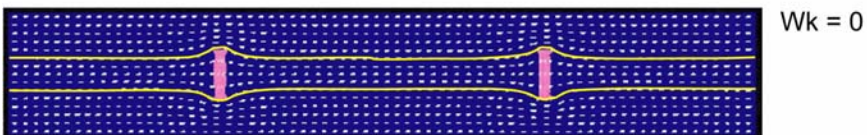
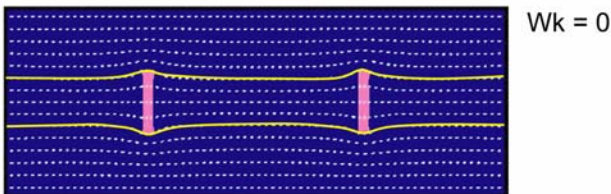
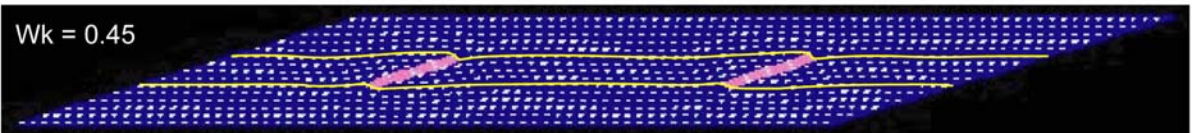
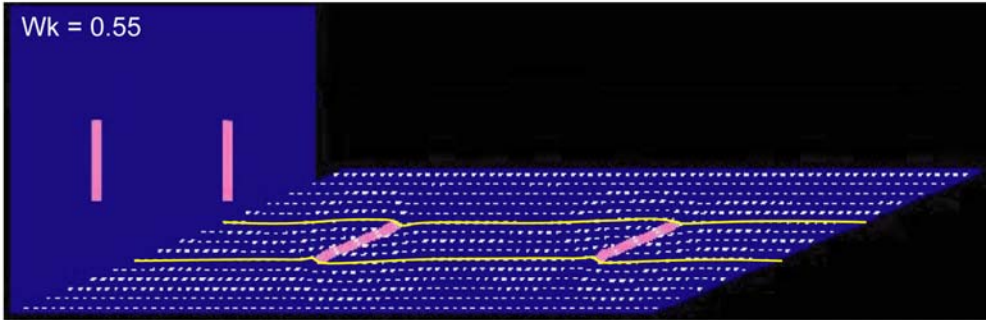
General shear flow, transpressional regime
 Viscosity vein = 10x viscosity layers
 Viscosity internal layer = viscosity external layers = 1



Appendix 4.11 b

Influence of the kinematic vorticity number

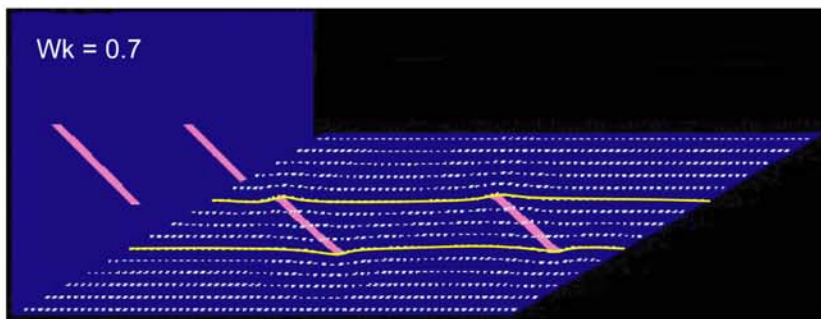
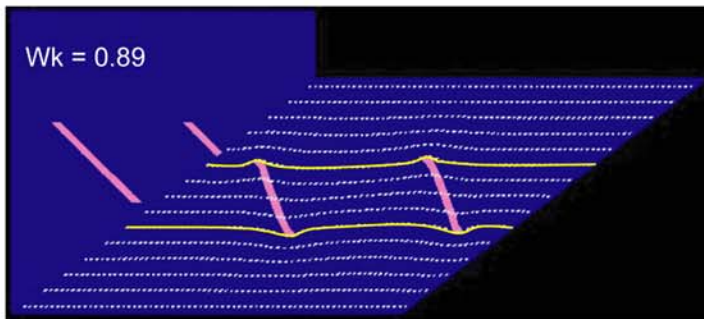
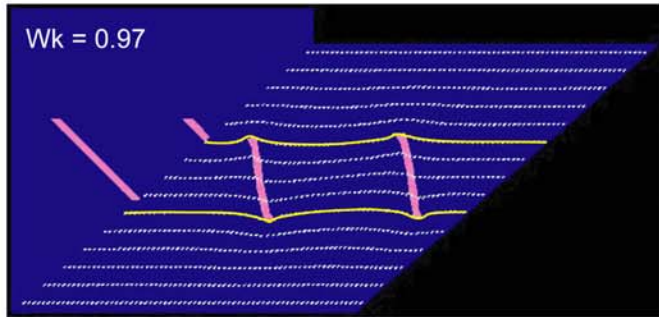
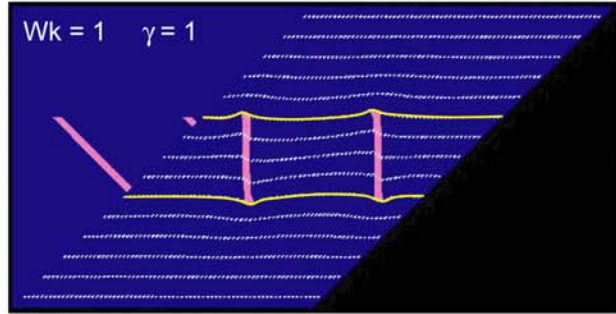
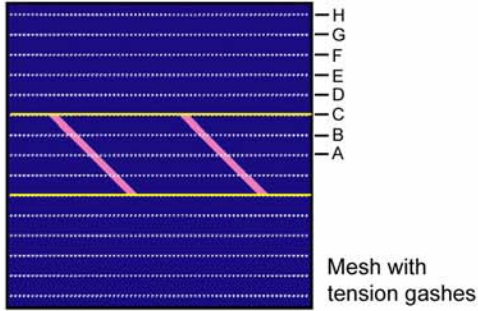
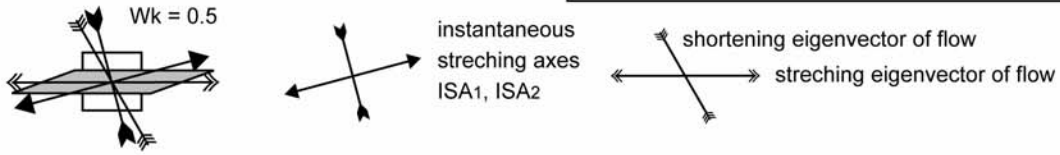
General shear flow, transpressional regime
 Viscosity vein = 10x viscosity layers
 Viscosity internal layer = viscosity external layers = 1



Appendix 4.12 a

Influence of the kinematic vorticity number

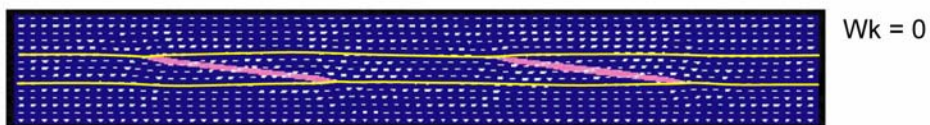
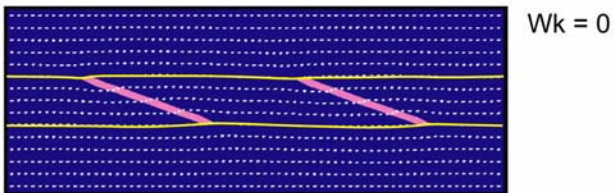
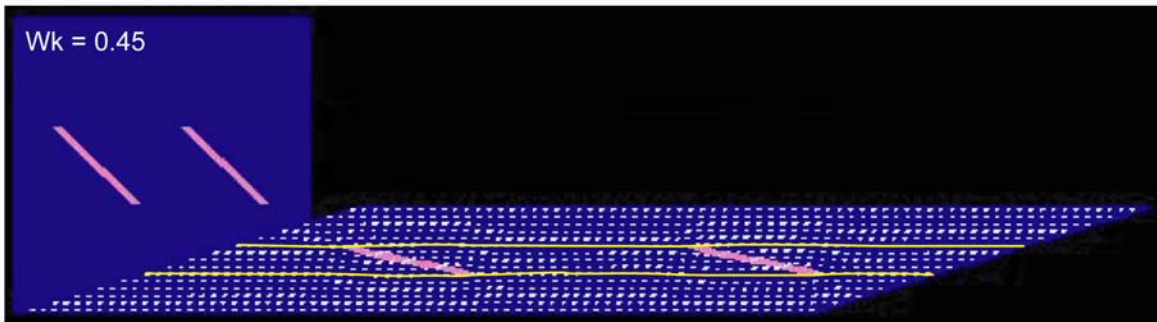
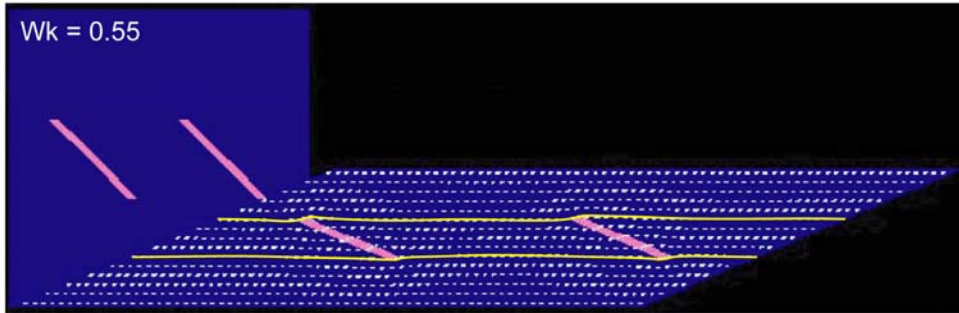
General shear flow, transpressional regime
 Viscosity vein = 10x viscosity layers
 Viscosity internal layer = viscosity external layers = 1



Appendix 4.12 b

Influence of the kinematic vorticity number

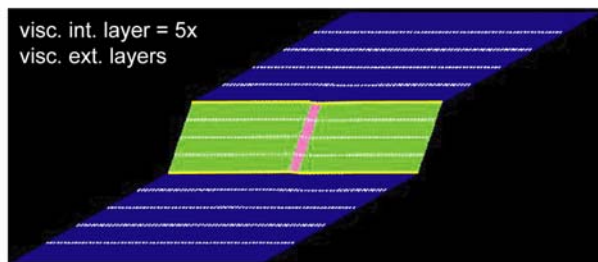
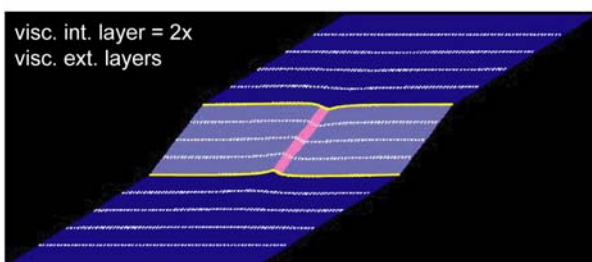
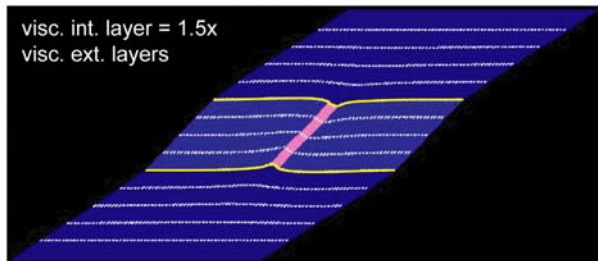
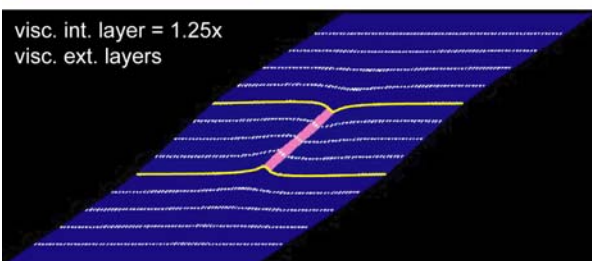
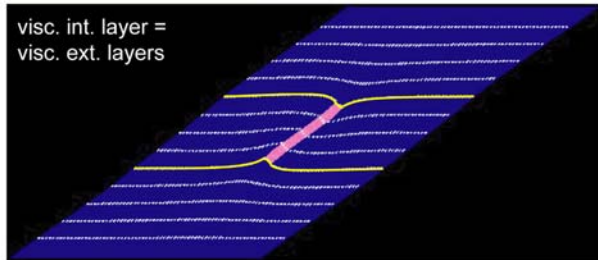
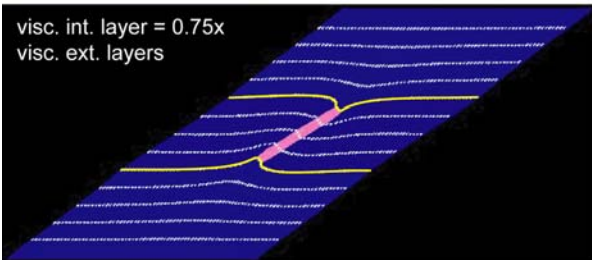
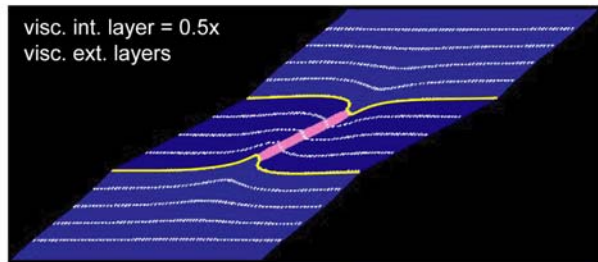
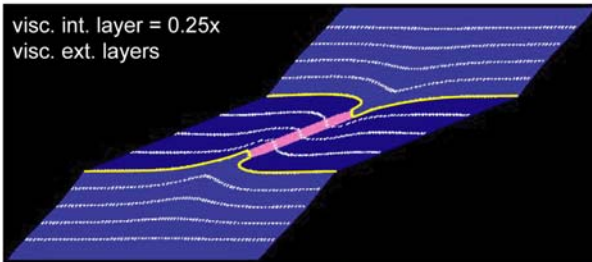
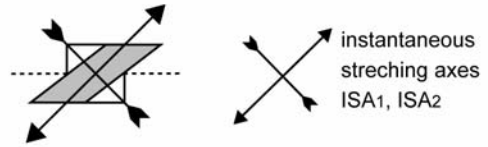
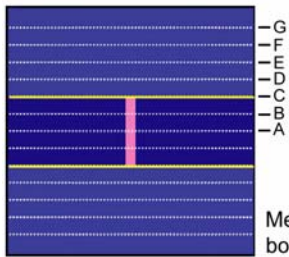
General shear flow, transpressional regime
 Viscosity vein = 10x viscosity layers
 Viscosity internal layer = viscosity external layers = 1



Appendix 4.13.1

Influence of the relative viscosity of the internal layer

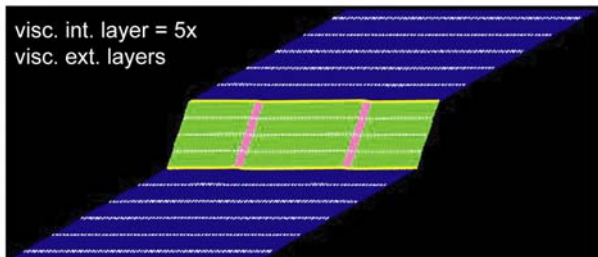
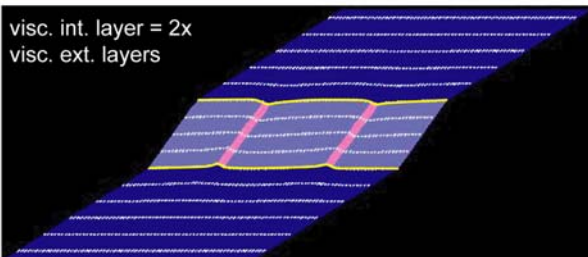
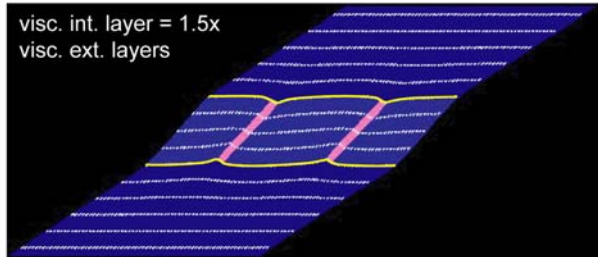
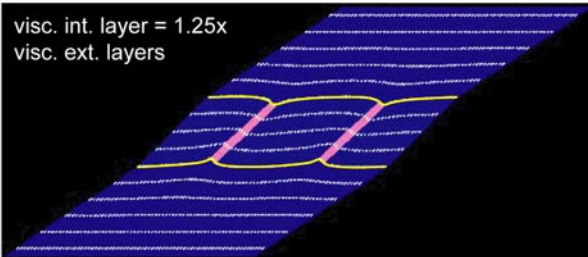
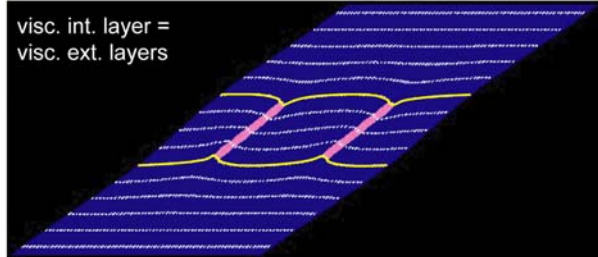
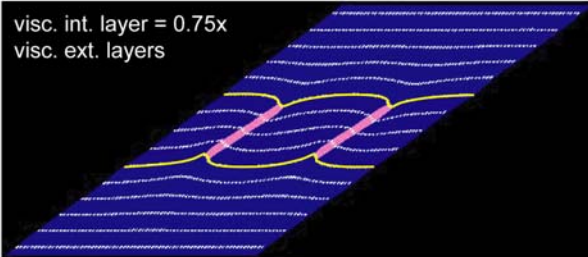
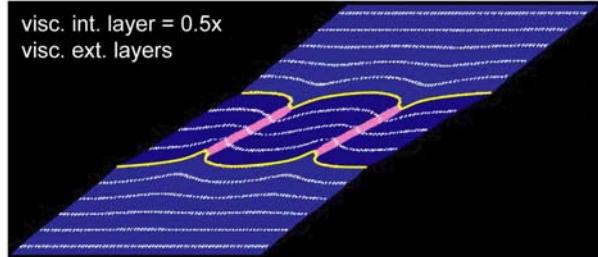
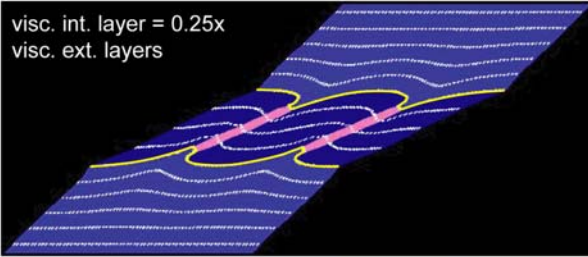
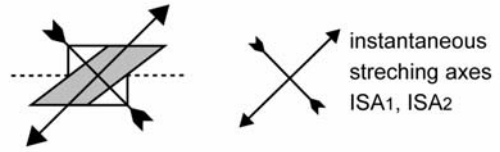
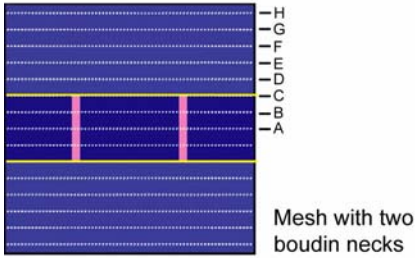
Simple shear flow, $\gamma = 1.35$
 Viscosity vein = 10x viscosity external layers
 Viscosity internal layer varies



Appendix 4.13.2

Influence of the relative viscosity of the internal layer

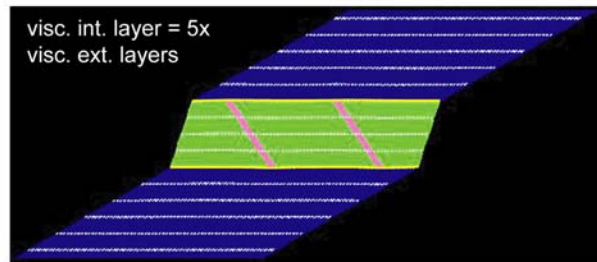
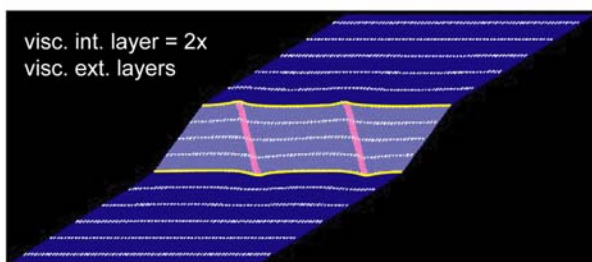
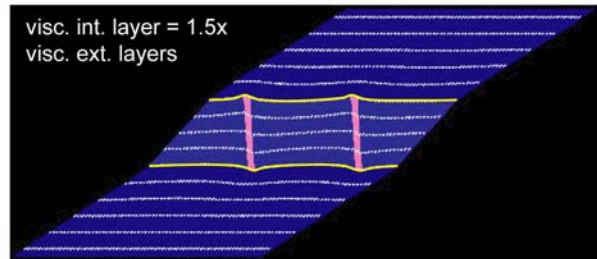
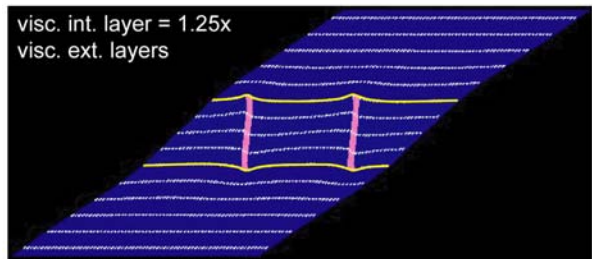
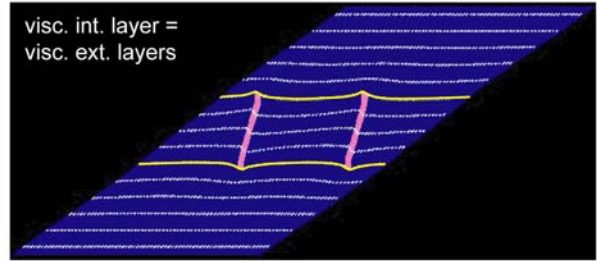
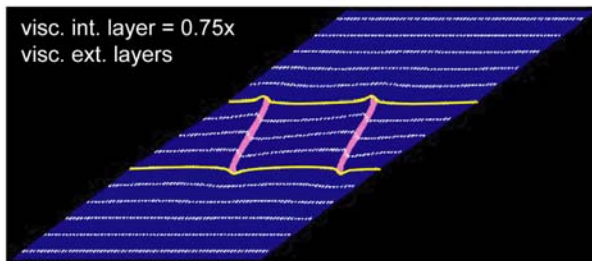
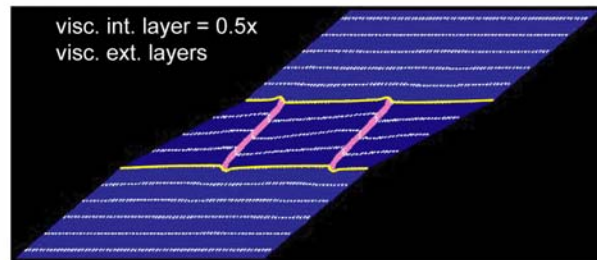
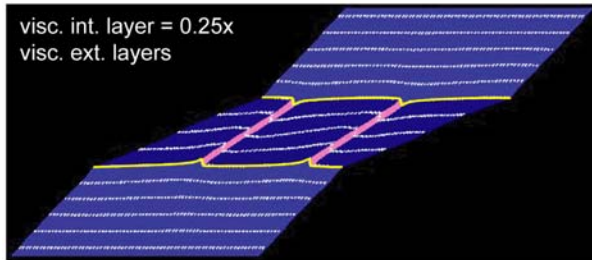
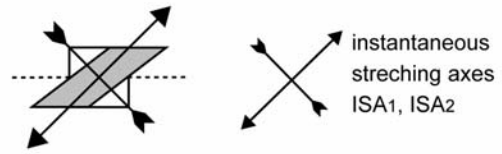
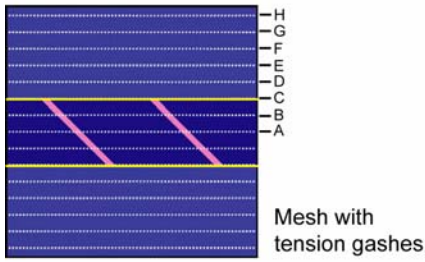
Simple shear flow, $\gamma = 1.35$
 Viscosity vein = 10x viscosity external layers
 Viscosity internal layer varies



Appendix 4.14

Influence of the relative viscosity of the internal layer

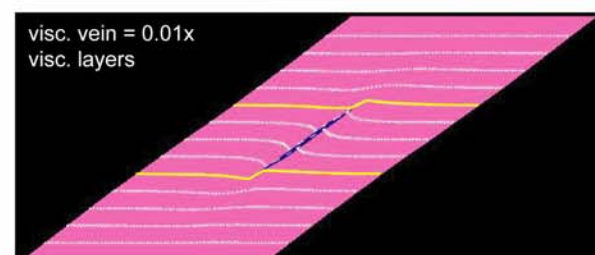
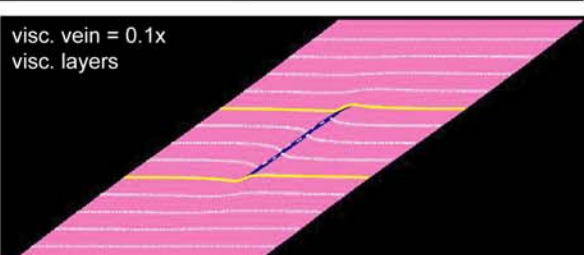
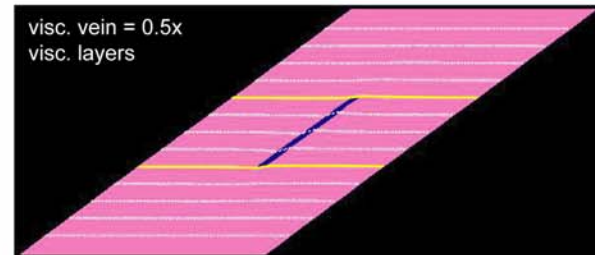
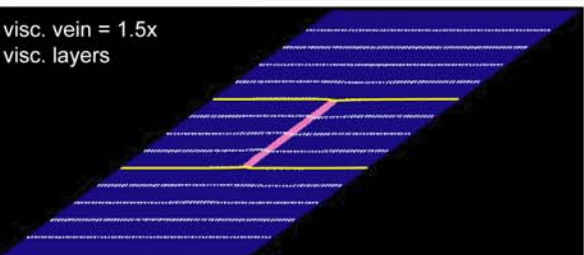
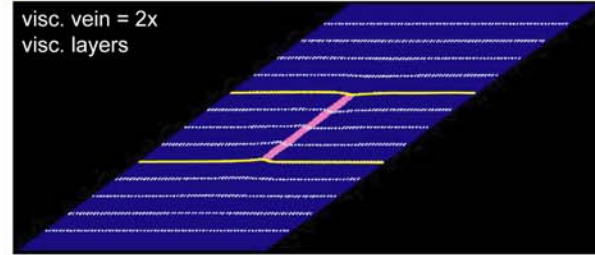
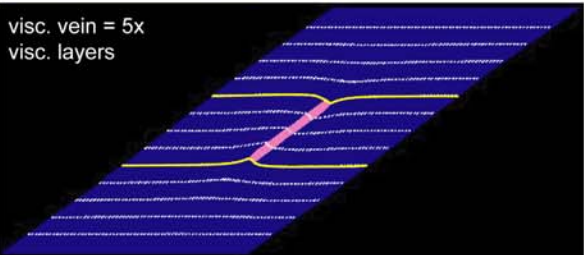
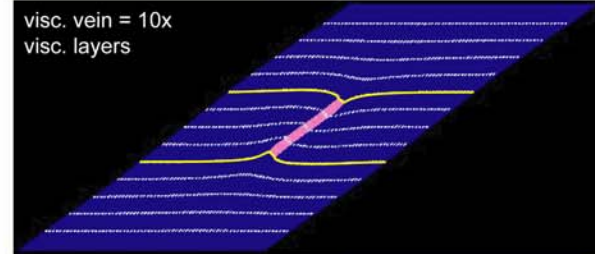
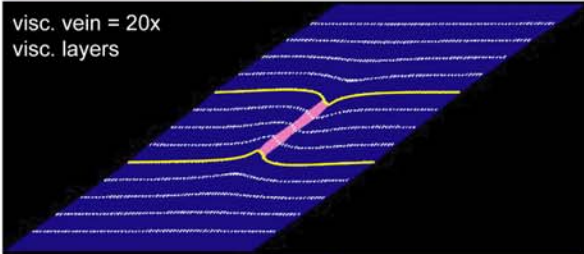
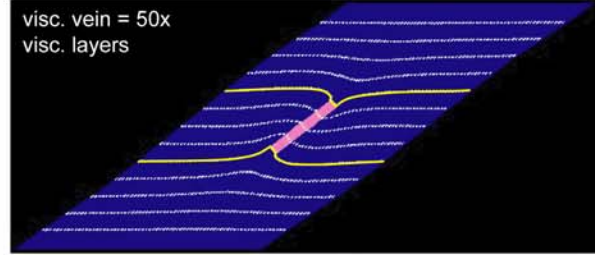
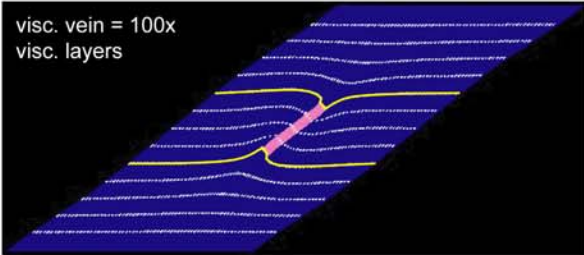
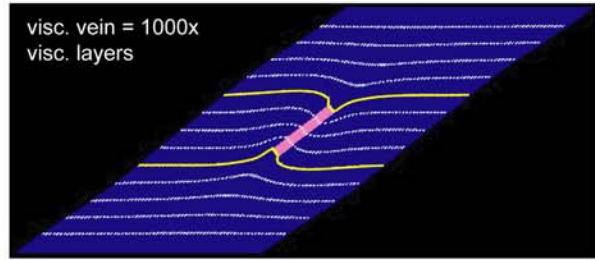
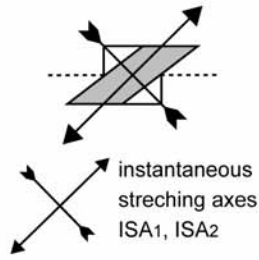
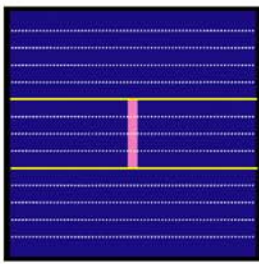
Simple shear flow, $\gamma = 1.35$
 Viscosity vein = 10x viscosity external layers
 Viscosity internal layer varies



Appendix 4.15.1

Influence of the relative viscosity of the vein

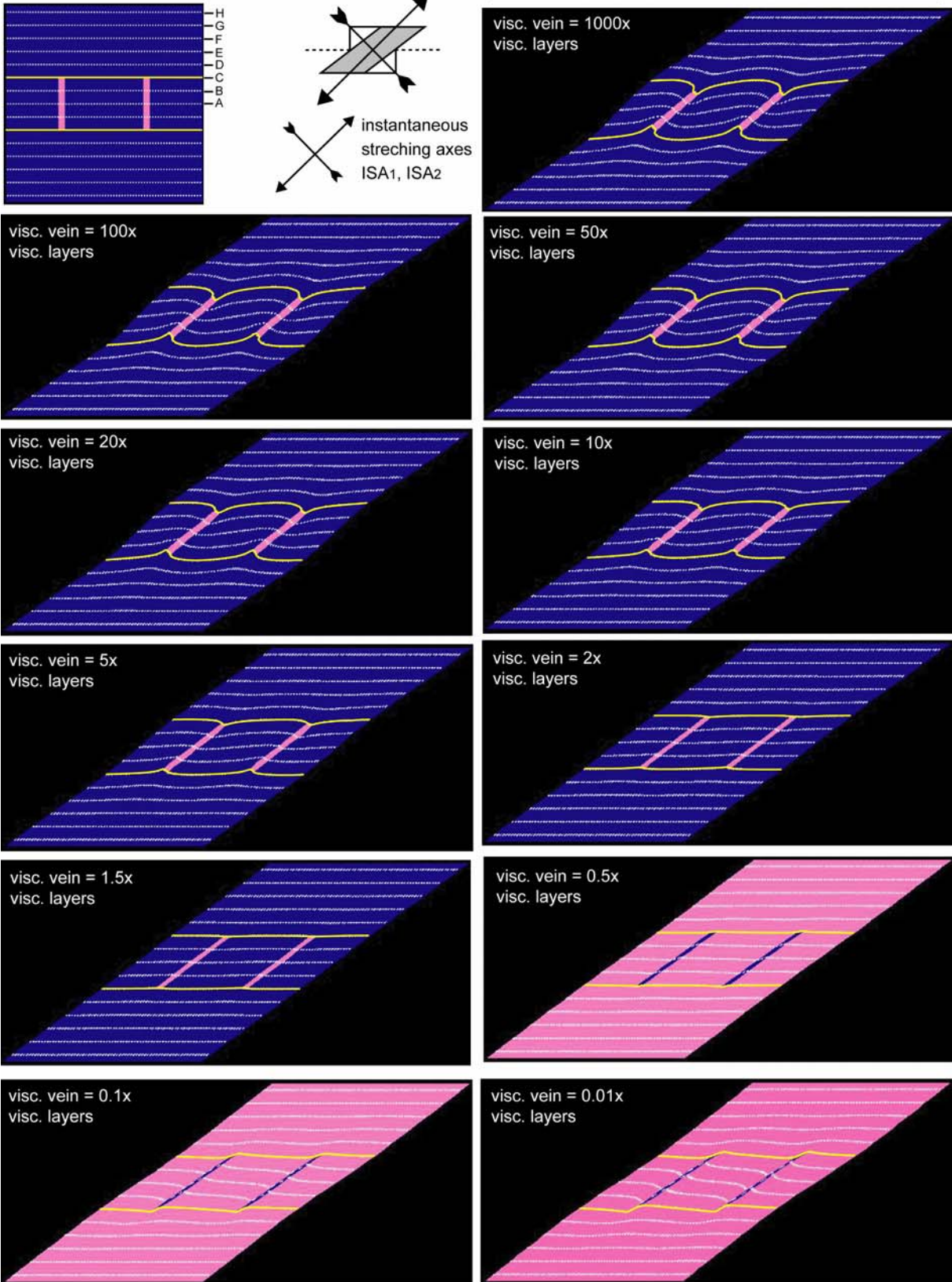
Simple shear flow, $\gamma = 1.35$
 Viscosity vein varies
 Viscosity internal layer = viscosity external layer



Appendix 4.15.2

Influence of the relative viscosity of the veins

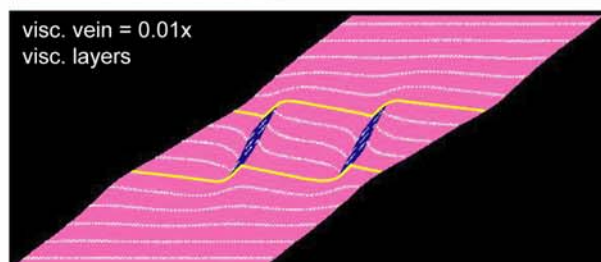
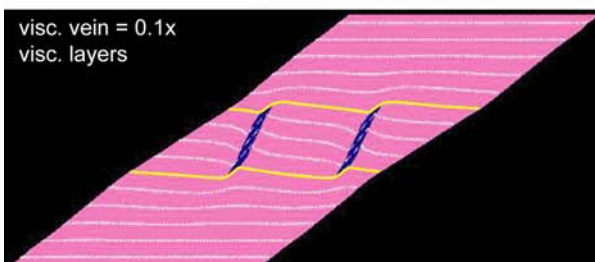
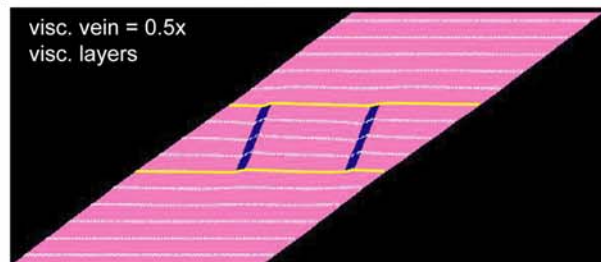
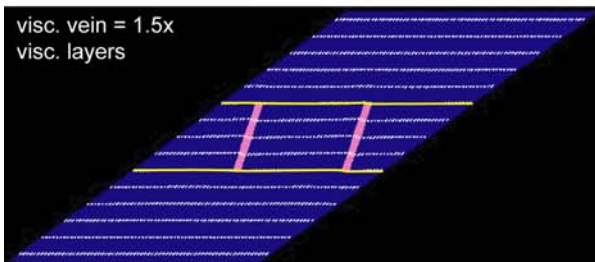
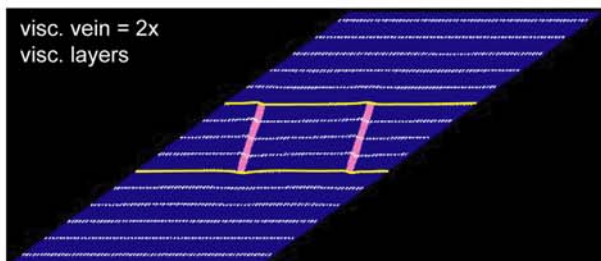
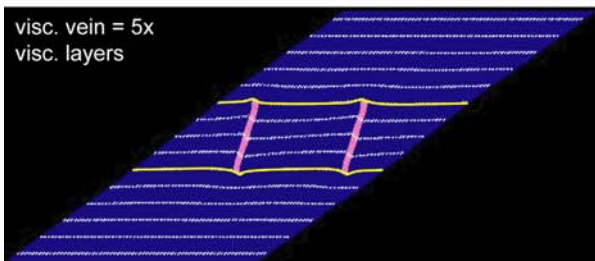
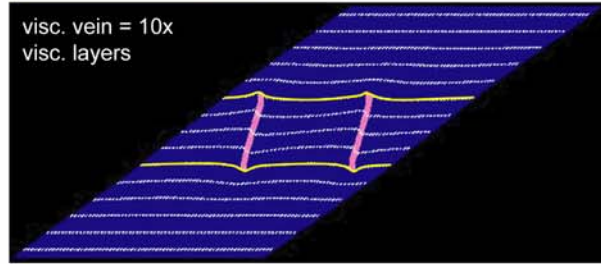
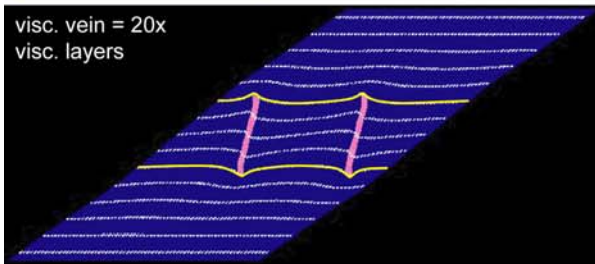
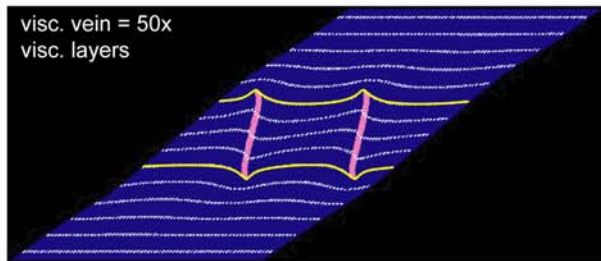
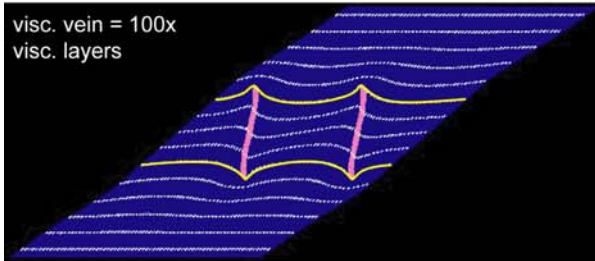
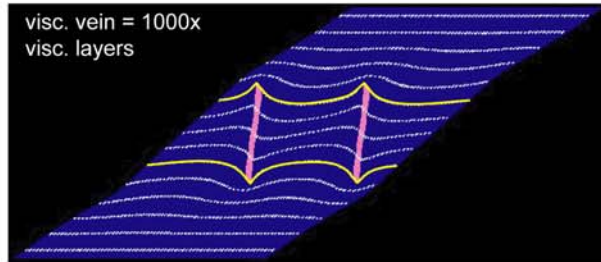
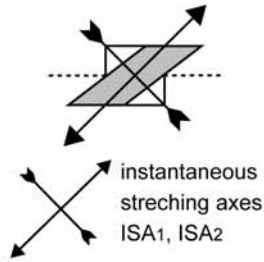
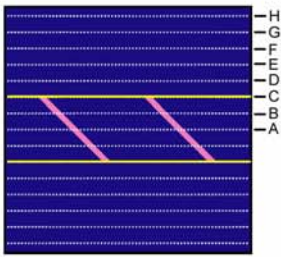
Simple shear flow, $\gamma = 1.35$
 Viscosity vein varies
 Viscosity internal layer = viscosity external layer



Appendix 4.16

Influence of the relative viscosity of the vein

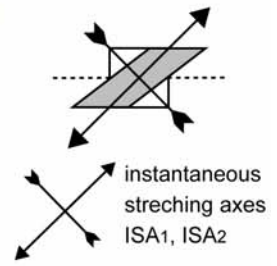
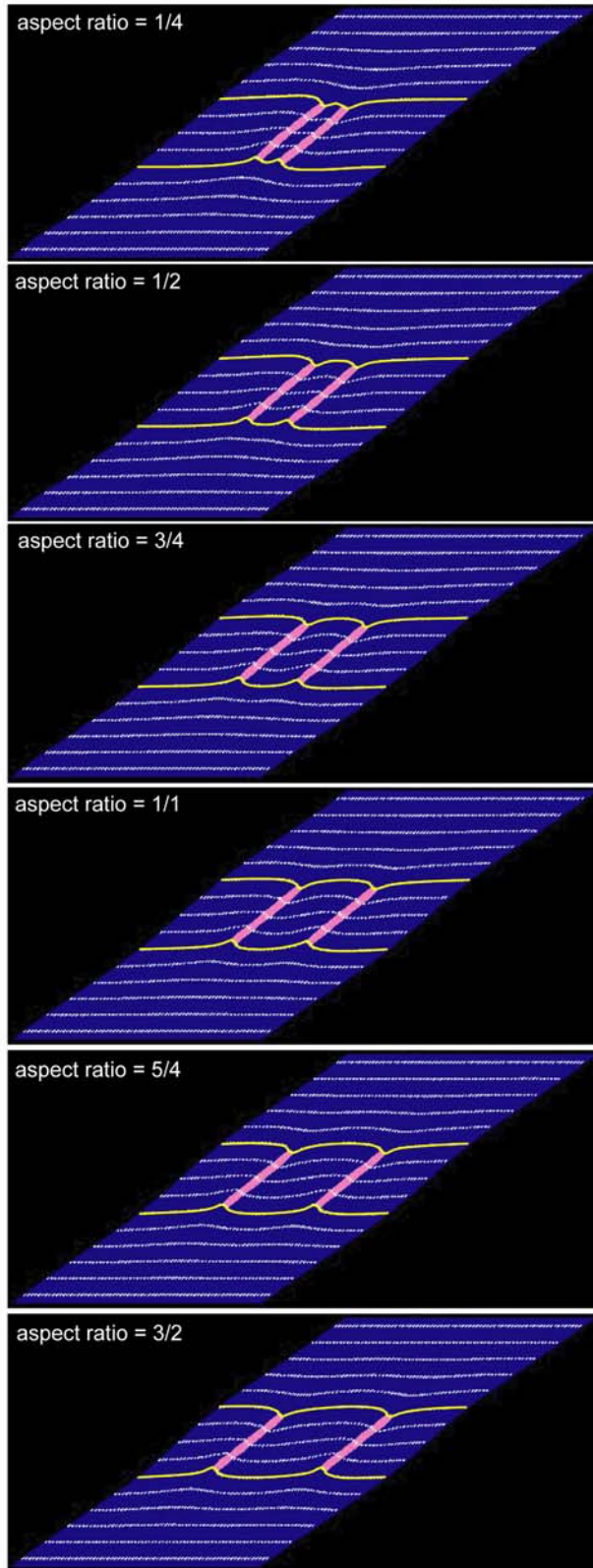
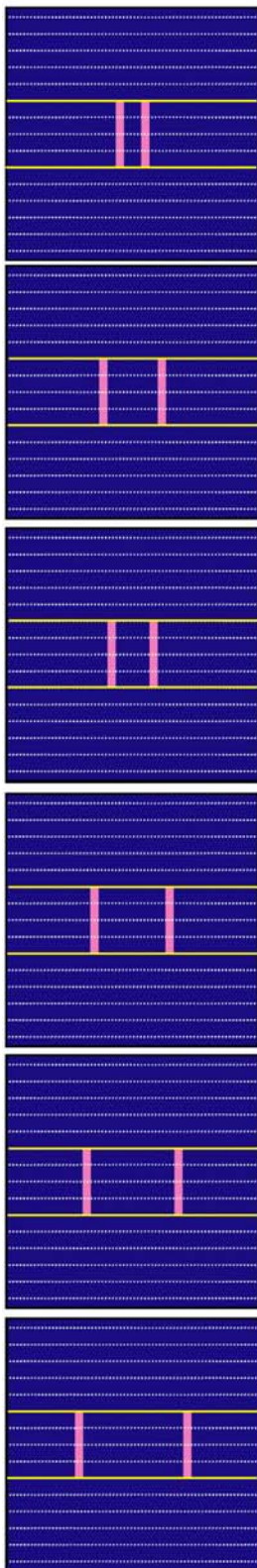
Simple shear flow, $\gamma = 1.35$
 Viscosity vein varies
 Viscosity internal layer = viscosity external layer



Appendix 4.17 a

Influence of the aspect ratio (spacing / thickness)
 Mesh with two boudin necks

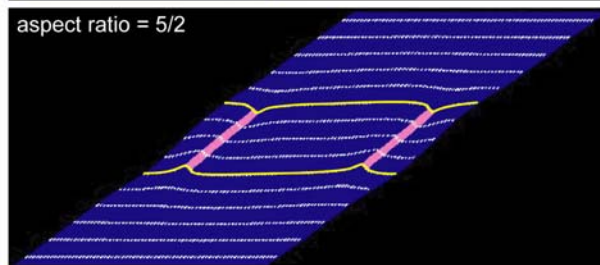
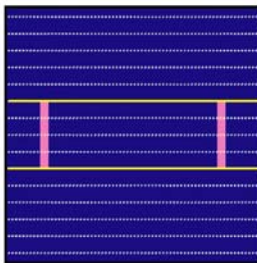
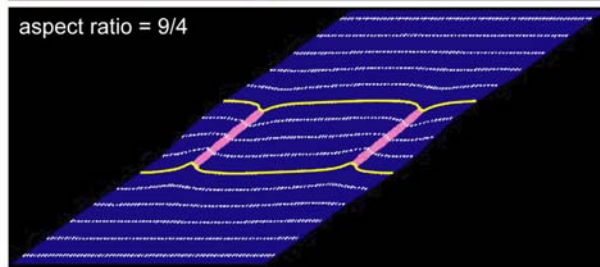
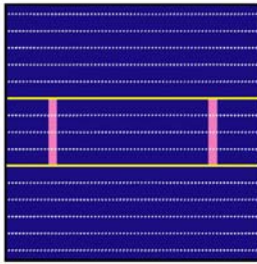
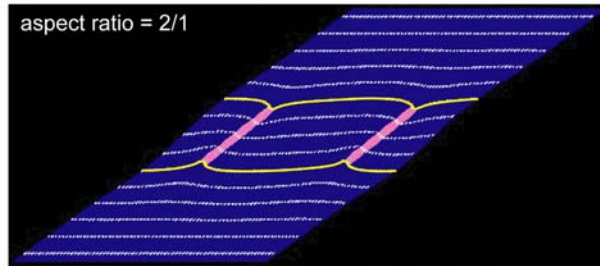
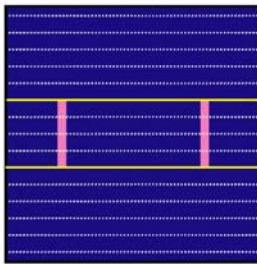
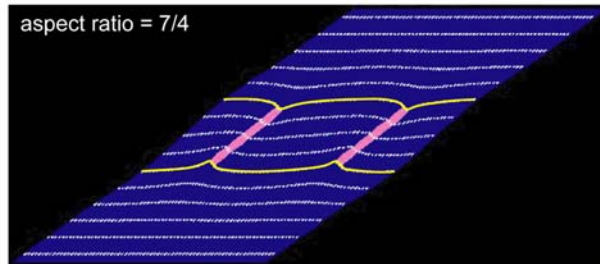
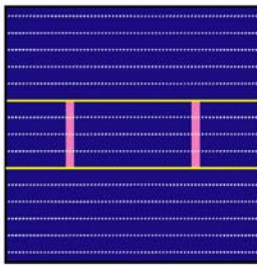
Simple shear flow, $\gamma = 1.35$
 Viscosity vein = 10x viscosity layers
 Viscosity internal layer = viscosity external layer = 1



Appendix 4.17 b

Influence of the aspect ratio (spacing / thickness)

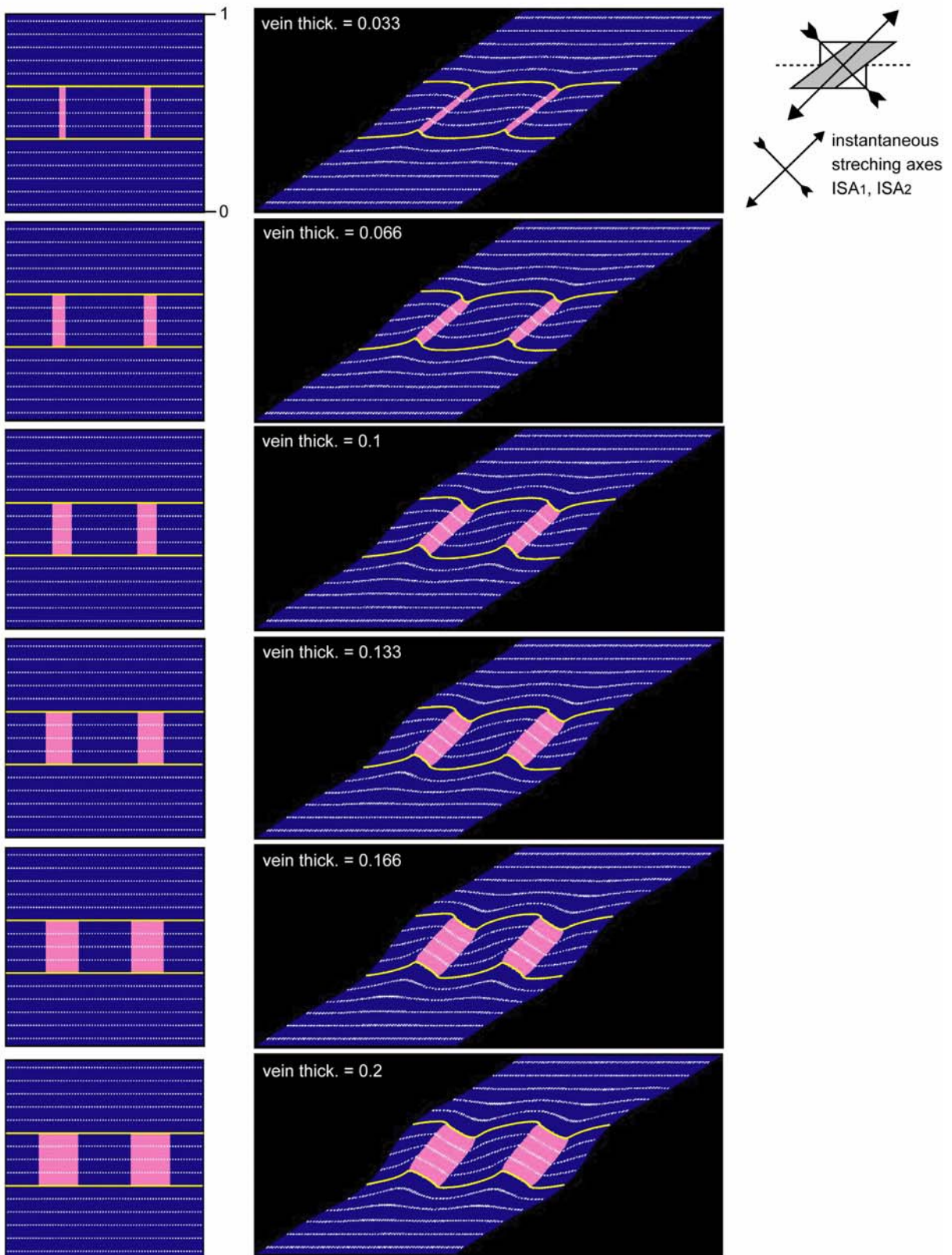
Simple shear flow, $\gamma = 1.35$
 Viscosity vein = 10x viscosity layers
 Viscosity internal layer = viscosity external layer = 1



Appendix 4.18

Influence of the thickness of the vein

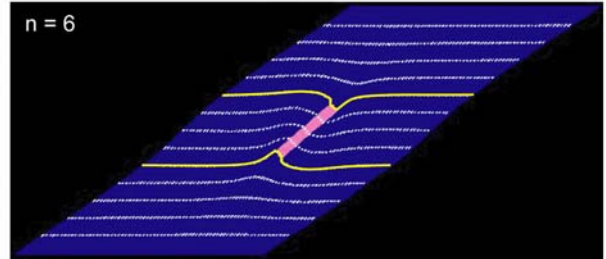
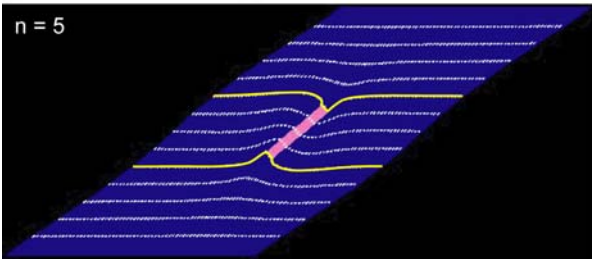
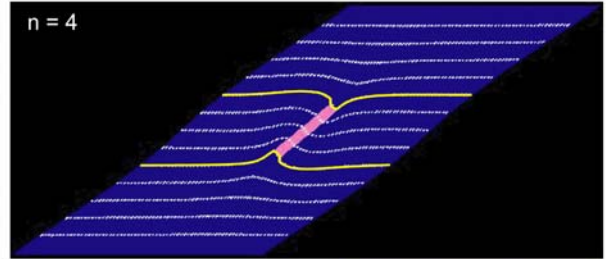
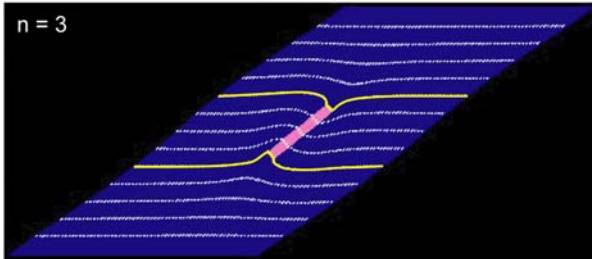
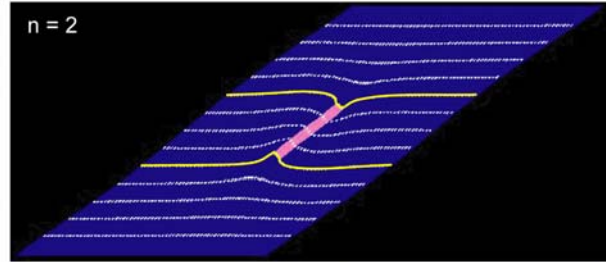
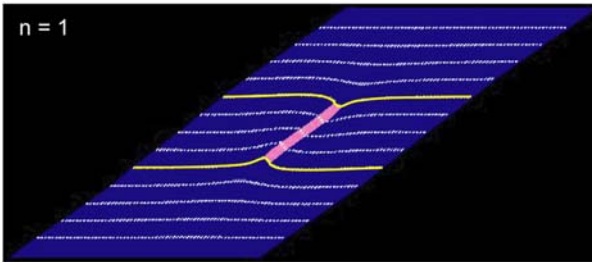
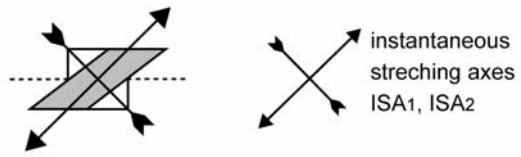
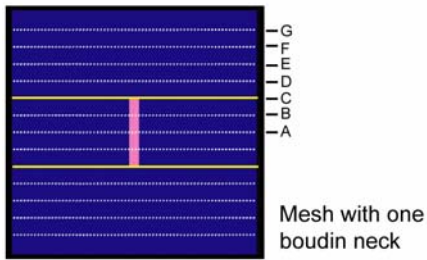
Simple shear flow, $\gamma = 1.35$
 Viscosity vein = 10x viscosity layers
 Viscosity internal layer = viscosity external layer = 1



Appendix 4.19

Influence of the stress exponent of Power law equation

Simple shear flow, $\gamma = 1.35$
 Viscosity vein = 10x viscosity layers
 Viscosity internal layer = viscosity external layers = 1



References

- Allaz, J., Maeder, X., Vannay, J.C., Steck, A., 2005. Formation of aluminosilicate-bearing quartz veins in the Simano Nappe (Central Alps): structural, thermobarometric and oxygen isotope constraints. *Schweizerische Mineralogische und Petrographische Mitteilungen* 85, 191–214.
- Bai, T., Pollard, D.D., 2000a. Fracture spacing in layered rocks: a new explanation based on the stress transition. *Journal of Structural Geology* 22, 43–47.
- Bai, T., Pollard, D.D., 2000b. Closely spaced fractures in layered rocks: initiation mechanism and propagation kinematics. *Journal of Structural Geology* 22, 1409–1425.
- Barr, T.D., Houseman, G.A., 1992. Distribution of deformation around a fault in a non-linear ductile medium. *Geophysical Research Letters* 19, 1145–1148.
- Barr, T.D., Houseman, G.A., 1996. Deformation fields around a fault embedded in a non-linear ductile medium. *Geophysical Journal International* 125, 473–490.
- Basei, M.A.S., Siga, O., Masquelin, H., Harara, O.M., Reis Neto, J.M., Preciozzi, F., 2000. Dom Feliciano Belt of Brazil and Uruguay and its foreland domain. In Cordani, U. (Ed), *Tectonic evolution of South America*. 31st International Geological Congress, Rio de Janeiro, Brazil, pp. 311–334.
- Bellahsen, N., Fiore, P., Pollard, D.D., 2006. The role of fractures in the structural interpretation of Sheep Mountain Anticline, Wyoming. *Journal of Structural Geology* 28, 850–867.
- Bergbauer, S., Pollard, D.D., 2004. A new conceptual fold-fracture model including prefolding joints, based on the Emigrant Gap anticline, Wyoming. *Geological Society of America Bulletin* 116 (3/4), 294–307.
- Biermann, C., 1987. Basement topography and thrust fault ramping, a model to explain cleavage fans in the Mosel area (Rheinisches Schiefergebirge). *Geology en Mijnbouw* 66, 333–341.
- Burkhard, M., 1993. Calcite twins, their geometry appearance and significance as stress-strain markers and indicators of tectonic regime: a review. *Journal of Structural Geology* 15, 351–368.
- Burkhard, M., Kerrich, R., 1988. Fluids regimes in the deformation of the Helvetic nappes, Switzerland, as inferred from stable isotope data. *Contribution to Mineralogy and Petrology* 99, 416–429.
- Brunt, R., 2003. Geometry of quartz boudins in marble. Diploma thesis, Utrecht University, 59pp.
- Coelho, S., Passchier, C.W., Grasemann B., 2005. Geometric description of flanking structures. *Journal of Structural Geology* 27, 597–606.
- Connolly, J.A.D., 1997. Devolatilization-generated fluid pressure and deformation-propagated fluid flow during prograde regional metamorphism. *Journal of Geophysical Research* 102, 18149–18173.
- Cosgrove, J.W., 1976. The formation of crenulation cleavage. *Journal of the Geological Society of London* 132, 155–178.
- Coward, M.P., 1981. The junction between the Pan-African mobile belts in Namibia, its structural history. *Tectonophysics* 76, 59–73.
- Coward, M.P., 1983. The tectonic history of the Damaran belt. *Special Publication of the Geological Society of South Africa* 11, 409–421.
- Dietrich, D., McKenzie, J.A., Song, H., 1983. Origin of calcite in syntectonic veins as determined from carbon-isotope ratios. *Geology* 11, 547–551.
- Druguet, E., Passchier, C.W., Carreras, J., Victor, P., den Brock, S., 1997. Analysis of a complex high-strain zone at Cap de Creus, Spain. *Tektonophysics* 280, 31–45.
- Dunne, W.M., North, C.P., 1990. Orthogonal fracture systems at the limits of thrusting: an example from southwestern Wales. *Journal of Structural Geology* 12, 207–215.
- Exner, U., Mancktelow, N., Grasemann, B., 2004. Progressive development of s-type flanking folds in simple shear. *Journal of Structural Geology* 26, 2191–2201.

- Exner, U., Grasemann, B., Mancktelow, N., 2006. Multiple faults in ductile simple shear: analogue models of flanking structure systems. Geological Society, London, Special Publications 253, 381-395.
- Frimmel, H.E., Frank, W., 1998. Neoproterozoic tectono-thermal evolution of the Gariep Belt and its basement, Namibia and South Africa. *Precambrian Research* 90, 1-28.
- Furlong, K.P., Hanson, R.B., and Bowers, J.R., 1991. Modeling thermal regimes. In: Kerrick, D.M. (Ed.), *Contact Metamorphism. Review in Mineralogy* 26, pp. 437-506.
- Gapais, D., and White S.H., 1982. Ductile shear bands in a naturally deformed quartzite. *Textures and Microstructures* 5, 1-17.
- Goscombe, B.D., Hand, M., Gray, D., 2003a. Structure of the Kaoko Belt, Namibia: progressive evolution of a classic transpressional orogen. *Journal of Structural Geology* 25, 1049-1081.
- Goscombe, B.D., Hand, M., Gray, D., Mawby, J., 2003b. The metamorphic architecture of a transpressional orogen: the Kaoko Belt, Namibia. *Journal of Petrology* 44, 679-711
- Goscombe, B.D., Passchier, C.W., 2003. Asymmetric boudins as shear sense indicators – an assessment from field data. *Journal of Structural Geology* 25, 575-589.
- Goscombe, B.D., Passchier, C.W., Hand, M., 2004a. Boudinage classification: end-member boudin types and modified boudin structures. *Journal of Structural Geology* 26, 739-763.
- Goscombe, B.D., Gray, D., and Hand, M., 2004b. Variation in metamorphic style along the Northern margin of the Damara Orogen, Namibia. *Journal of Petrology* 45, 1261-1295.
- Goscombe, B.D., Gray, D., Hand, M., 2005a. Extrusional Tectonics in the Core of a Transpressional Orogen; the Kaoko Belt, Namibia. *Journal of Petrology* 46, 1203-1241.
- Goscombe, B.D., Gray, D., Armstrong, R., Foster, D.A., Vogl J., 2005b. Event geochronology of the Pan-African Kaoko Belt, Namibia. *Precambrian Research* 140, 103.e1–103.e41.
- Goscombe, B.D., Gray, D., 2007. The Coastal Terrane of the Kaoko Belt, Namibia: outboard arc-terranes and tectonic significance. *Precambrian Research* 155, 139-158.
- Gray, D.R., 1979. Microstructure of crenulation cleavages: an indication of cleavage origin. *American journal of science* 279, 97-128.
- Gray, D.R., Durney, D.W., 1979. crenulation cleavage differentiation: implication of solution-deposition processes. *Journal of Structural Geology* 1, 73-80.
- Gray, D.R., Willman, C.E., 1991. Thrust-related strain gradients and thrusting mechanisms in a chevron-folded sequence, southeastern Australia. *Journal of Structural geology* 13, 691-710.
- Gray, D.R., Foster, D.A., Goscombe, B., Passchier, C.W., Trouw, R.A.J., 2006. $^{40}\text{Ar}/^{39}\text{Ar}$ thermochronology of the Pan-African Damara Orogen, Namibia, with implications for tectonothermal and geodynamic evolution. *Precambrian research* 150, 49-72.
- Gray, D.R., Foster, D.A., Goscombe, B., Armstrong, R., Trouw, R.A.J., Passchier, C.W., 2007. A Damara Orogen perspective on the assembly of southwestern Gondwana, submitted.
- Grasemann, B., Stüwe, K., 2001. The development of flanking folds during simple shear and their use as kinematic indicators. *Journal of Structural Geology* 23, 715-724.
- Grasemann, B., Fritz, H., Vannay, J-C., 1999. Quantitative kinematic flow analysis from the Main Central Thrust Zone (NW-Himalaya, India): implication for a decelerating strain path and the extrusion of orogenic wedges. *Journal of Structural Geology* 21, 837-853.
- Grasemann, B., Stüwe, K., Vannay, J-C., 2003. Sense and non-sense of shear in flanking structures. *Journal of Structural Geology* 25, 19-34.
- Guiton, M., Sassi, W., Leroy, Y., Gauthier, B., 2003. Mechanical constraints on the chronology of fracture activation in the folded Devonian sandstone of the western Moroccan Anti-Atlas. *Journal of Structural Geology* 25, 1317–1330.
- Hanson, R.B., 1995. The hydrodynamics of contact metamorphism. *Geological Society of America Bulletin* 107 (5), 595-611.
- Heilbron, M., Pedrosa-Soares, A., Neto, M., Da Silva, L., Trouw, R., Janasi, V., 2004. Brasiliano Orogens in Southeast and South Brazil. In: Weinberg, R., Trouw, R.A.J., Fuck, R., Hackspcher, P. (Eds.) *The 750-550 Ma Brasiliano E 675 vent of South America*, *Journal of the Virtual Explorer* 17, 1441-8142.

- Houseman, G.A., Barr, T., Evans, L., 2007. Basil: stress and deformation in a viscous material. In Bons, P., Koehn, D., Jessell, M. (Eds.), *Microdynamics Simulation*. Springer Verlag, Berlin, in press.
- Heesakkers, V.M.J., 2003. Flanking structures of the Ugab and Goantagab valley, Namibia: Natural observations and comparison with new analogue experiments. Diploma thesis, Utrecht University, 61pp.
- Henry, C., Burkhard, M., Goffé, B., 1996. Evolution of synmetamorphic veins and their wallrocks through a Western Alps transect: no evidence for large-scale fluid flow. Stable isotope, major- and trace-elements systematics. *Chemical Geology* 127, 81-109.
- Hoffman, P.F., Swart, R., Freyer, E.E., and Guowei, H., 1994. Damara Orogen of Northwest Namibia. In Niall, M., McManus, C. (Eds.), *Geological Excursion Guide of the international conference Proterozoic crustal and metallogenic evolution*. Geological Society and the Geological Survey of Namibia, 55pp.
- Hudleston, P.J., 1989. The association of folds and veins in shear zones. *Journal of Structural Geology* 11, 949-957.
- Jessell, M.W., Willman, C.E., Gray, D.R., 1994. Bedding parallel veins and their relationship to folding. *Journal of Structural Geology* 16, 753-767.
- Jessell, M.W., Siebert, E., Bons, P.D., Evans L., Piazzolo, S., 2005. A new type of numerical experiment on the special and temporal patterns of localization of deformation in a material with a coupling grain-size and rheology. *Earth and Planetary Science Letters* 239, 309-326.
- Ji, S., Saruwatari, K., 1998. A revised model for the relationship between joint spacing and layer thickness. *Journal of Structural Geology* 20, 1495-1508.
- John, T., Schenk, V., Hasse, K., Scherer, E., Tembo, F., 2003. Evidence for a Neoproterozoic ocean in south-central Africa from mid-oceanic-ridge-type geochemical signatures and pressure-temperature estimates of Zambian eclogites. *Geology* 31, 243-246.
- John, T., Schenk, V., Mezger, K., Tembo, F., 2004. Timing and PT evolution of whiteschist metamorphism in the Lufilian Arc-Zambezi Belt Orogen (Zambia): implications for the assembly of Gondwana. *The Journal of Geology* 112, 71-90.
- Johnson, T.E., 1991. Nomenclature and geometric classification of cleavage-transected folds. *Journal of Structural Geology* 13, 261-274.
- Jung, S., Hoffer, E., Hoernes, S., 2007. Neo-Proterozoic rift-related syenites (Northern Damara Belt, Namibia): Geochemical and Nd-Sr-Pb-O isotope constraints for mantle sources and petrogenesis. *Lithos*, in press.
- Jung, S., Mezger, K., 2003. U-Pb garnet chronometry in high-grade rocks; case studies from the central Damara Orogen (Namibia) and implications for the interpretation of Sm-Nd garnet ages and the role of high U-Th inclusions. *Contributions to Mineralogy Petrology* 146, 382-396.
- Jung, S., Hoernes, S., and Hoffer, E., 2005. Petrogenesis of cogenetic nepheline and quartz syenites and granites (northern Damara Orogen, Namibia) – enriched mantle vs. contamination. *Journal of Geology* 113, 651-672.
- Kendall, B.S., Creaser, R.A., Ross, G.M., Selby, D., 2004. Constraints on the timing of Marinoan ‘‘Snowball Earth’’ glaciation by $^{187}\text{Re}/^{187}\text{Os}$ dating of a neoproterozoic, post-glacial black shale in Western Canada. *Earth and Planetary Science Letters* 222, 29e740.
- Kenis, I., Muechez, Ph., Sintubin, M., Mansy, J.-L., Lacquement, F., 2000. The use of a combined structural, stable isotope and fluid inclusion study to constrain the kinematic history at the northern Variscan front zone (Bettrechies, northern France). *Journal of Structural Geology* 22, 589– 602.
- Kenis, I., Sintubin, M., Muechez, Ph., Burke E.A.J., 2002. The ‘‘boudinage’’ question in the High-Ardenne Slate Belt (Belgium): a combined structural and fluid-inclusion approach. *Tectonophysics* 348, 93-110.
- Kenis, I., Urai, J.L., van der Zee, W., Sintubin, M., 2004. Mullions in the High-Ardenne Slate Belt (Belgium): numerical model and parameter sensitivity analysis. *Journal of Structural Geology* 26, 1677-1692.
- Kenis, I., Urai, J.L., van der Zee, W., Hilgers, C., Sintubin, M., 2005. Rheology of fine-grained siliciclastic rocks in the middle crust- evidence from structural and numerical analysis. *Earth and Planetary Science Letters* 233, 351-360.

- Kocher, T., Mancktelow, N.S., 2006. Flanking structure development in anisotropic viscous rocks. *Journal of Structural Geology* 28, 1139-1145.
- Kocher, T., Mancktelow, N.S., 2005. Dynamic reverse modelling of flanking structures: a source of quantitative kinematic information. *Journal of Structural Geology* 27, 1346-1354.
- Koehn, D., Passchier, C.W., 2000. Shear sense indicators in striped bedding veins. *Journal of Structural Geology* 22, 1141-1151.
- Konopásek, J., Kröner, S., Kitt, S.L., Passchier, C.W., Kröner, A., 2005. Oblique collision and evolution of large-scale transcurrent shear zones in the Kaoko belt, NW Namibia. *Precambrian Research* 136, 139-157.
- Kröner, A., 1977. Precambrian mobile belts in southern and eastern Africa—ancient sutures or sites of ensialic mobility. A case for crustal evolution towards plate tectonics. *Tectonophysics* 40, 101-135.
- Kröner, A., 1982. Rb-Sr geochronology and tectonic evolution of the Pan-African Damara Belt of Namibia, Southwestern Africa. *American Journal of Science* 282, 1471-1507.
- Kukla, P., Stanistreet, I., 1991. Record of the Damaran Khomas Hochland accretionary prism in central Namibia: refutation of an “ensialic” origin of a late Proterozoic orogenic belt. *Geology* 19, 473-476.
- Maeder, X., Passchier, C.W., Trouw, R.A.J., 2007. Flame foliation: Evidence for a schistosity formed normal to the extension direction. *Journal of Structural Geology* 29, 378-384.
- Malavieille, J., Lacassin, R., 1988. “Bone-shaped” boudins in progressive shearing. *Journal of Structural Geology* 10, 335-345.
- Martin, H., Porada, H., 1977a. The intracratonic branch of the Damara Orogen in South West Africa. I. Discussion of geodynamic models. *Precambrian research* 5, 311-338.
- Martin, H., Porada, H., 1977b. The intracratonic branch of the Damara Orogen in South West Africa. II. Discussion of relationships with the Pan-African Mobile Belt system. *Precambrian research* 5, 339-357.
- Means, W.D., 1981. The concept of steady-state foliation. *Tectonophysics* 78, 179-199.
- Means, W.D., Hobbs, B.E., Lister, G.S. and Williams, P.F., 1980. Vorticity and non-coaxiality in progressive deformations. *Journal of Structural Geology* 2, 371-378.
- Miller, R.McG., 1983. The Pan-African Damara Orogen of Southwest Africa/Namibia. In: Miller, R.McG. (Ed.), *Evolution of the Damara Orogen*. Special Publication of the Geological Society of South Africa, vol. 11, pp. 431-515.
- Miller, R.McG., Freyer, E.E., and Hälbig, I.W., 1983. A turbidite succession equivalent to the entire Swakop Group. In Miller, R.McG., (Ed.), *Evolution of the Damara Orogen*. Special Publication of the Geological Society of South Africa 11, pp. 65-71.
- Miller, R.McG., and Grote, W., 1988. Geological map of the Damara Orogen of South West Africa/Namibia. Geological Survey of Namibia, scale 1:500.000.
- Narr, N., Suppe, J., 1991. Joint spacing in sedimentary rocks. *Journal of Structural Geology* 13, 1037-1048.
- Nishiyama, T., 1989. Kinetics of hydrofracturing and metamorphic veining. *Geology* 17, 1068-1071.
- Passchier, C.W., 1987. Efficient use of the velocity gradients tensor in flow modelling. *Tectonophysics* 136, 159-163.
- Passchier, C.W., 1991. Deformation in the Revenue granite pluton, Mount Isa Inlier, Australia. *Geologie en Mijnbouw* 70, 275-285.
- Passchier, C.W., 1997. The fabric attractor. *Journal of Structural Geology* 19, 113-127.
- Passchier, C.W., 1998. Monoclinic model shear zones. *Journal of Structural Geology* 20, 1121-1137.
- Passchier, C.W., 2001. Flanking structures. *Journal of Structural Geology* 23, 951-962.
- Passchier, C.W., 2007. Photograph of the month (Editorial). *Journal of Structural Geology* 29, 377.
- Passchier, C.W., Druguet, E., 2002. Numerical modelling of asymmetric boudinage. *Journal of Structural Geology* 24, 1789-1803.
- Passchier, C.W., Trouw, R.A.J., Ribeiro, A., and Paciullo, F.V.P., 2002. Tectonic evolution of the southern Kaoko belt, Namibia. *Journal of African Earth Sciences* 35, 61-75.

- Passchier, C.W., and Trouw, R.A.J., 2005. *Microtectonics*, 2nd edition. Springer Verlag, Berlin, 366pp.
- Passchier, C.W., Trouw, R.A.J., Goscombe, B., Gray, D., 2007. Intrusion mechanisms in a turbidite sequence: The Voetspoor and Doros Plutons in NW Namibia. *Journal of Structural Geology* 29, 481-496.
- Porada, H., 1989. Pan-African Rifting and Orogenesis in Southern to Equatorial Africa and Eastern Brazil. *Precambrian Research* 44, 103-136.
- Prave, A.R., 1996. Tale of three cratons: Tectonostratigraphic anatomy of the Damara orogen in northwestern Namibia and the assembly of Gondwana. *Geology* 24, 1115-1118.
- Price, N.J., Cosgrove, J.W., 1990. *Analysis of geological structures*. Cambridge University Press, Cambridge, 501pp.
- Ramberg, H., 1975. Particle paths, displacement and progressive strain applicable to rocks. *Tectonophysics* 28, 1-37.
- Ramsay, J.G., 1967. *Folding and fracturing of rocks*. McGraw-Hill, New York, 568 pp.
- Ramsay, J.G., Huber, M.I., 1983. *Modern Structural Geology, Volume 1 Strain Analyses*, Academic Press, San Diego, 307 pp.
- Ranalli, G., 2003. Discussion: how soft is the crust? *Tectonophysics* 361, 319-320.
- Rives, T., Rawnsley, T.D., Petit, J.-P., 1994. Analogue simulation of natural orthogonal joint set formation in brittle varnish. *Journal of Structural Geology* 16, 419-429.
- Roedder, E., 1984. *Fluid inclusions*. Reviews in Mineralogy 12, Mineralogical Society of America, Washington, 644pp.
- Seth, B., Okrush, M., Wilde, M., Hoffmann, K.H., 2000. The Voetspoor intrusion, Southern Kaoko Zone, Namibia: mineralogical, geochemical and isotopic constraints for the origin of a syenitic magma. In Miller, R.McG. (Ed.), *Henno Martin commemorative volume*. Communications of the Geological Survey of South West Africa/Namibia 12, pp. 125-137.
- Sharp, Z.D., 1992. In situ laser microprobe techniques for stable isotope analysis, *Chemical Geology: Isotope Geoscience Section* 101, 3-19.
- Sharp, Z.D., Kirschner, D.L., 1994. Quartz-calcite oxygen isotope thermometry: A calibration based on natural isotopic variations. *Geochimica et Cosmochimica Acta* 58, No. 21, 4491-4501.
- Sibson, R.H., 2000. Tectonic controls on maximum sustainable overpressure: fluid redistribution from stress transitions. *J. Geochem. Explor.* 69-70, 471-475.
- Singletary, S.J., Hanson, R.E., Martin, M.W., Crowley, J.L., Bowring, S.A., Key, R.M., Ramokatw, L.V., Direng, B.B., Krol, M.A., 2003. Geochronology of basement rocks in the Kalahari Desert, Botswana, and implications for regional; Proterozoic tectonics. *Precambrian Research* 121, 47-71.
- Sintubin, M., Kenis, I., Schroyen, K., Muchez, P., Burke, E., 2000. "Boudinage" in the High-Ardenne slate belt (Belgium), reconsidered from the perspective of the "interboudin" veins. *Journal of Geochemical Exploration* 69-70, 511-516.
- Stanistreet, I.G., Charlesworth, G., 2001. Damaran basement-cored fold nappes incorporating pre-collisional basins Kaoko Belt Namibia and controls on Mesozoic supercontinental break-up. *South African Journal of Geology* 104, 1-12.
- Swart, R., 1992. The sedimentology of the Zerrissene turbidite system, Damara Orogen, Namibia. *Memoir of the Geological Survey of Namibia* 13, 54pp.
- Swart, R., 1994. Late Precambrian outer-fan turbidites from Namibia – vertical and lateral characteristics. *Journal of African Earth Sciences* 18, 3-13.
- Touret, J.L.R., 2001. Fluids in metamorphic rocks. *Lithos* 55, 1-25.
- Tricart, P., Coron, J.-M., Gay, M., Vialon, P., 1977. Relais de schistosités, structures en éventail et discontinuités majeures sur la transversale du Pelvoux (Alpes occidentales). *Bull. Soc. Géol. France* 4, 873-881.
- Twiss, R.J., Moores, E.M., 1992. *Structural Geology*. Freeman, New York, 532 pp.
- Urai, J.L., Spaeth, G., Van der Zee, W., Hilgers, C., 2001. Evolution of mullion (formerly boudin) structures in the Variscan of the Ardennes and Eifel. *Journal of the Virtual Explorer* 3, 1-15. [url: http://virtualexplorer.com.au/2001/Volume3review/Urai2/index.html](http://virtualexplorer.com.au/2001/Volume3review/Urai2/index.html).

- Vanbrabant, Y., Dejonghe, L., 2006. Structural analysis of narrow reworked boudins and influence of sedimentary successions during a two-stage deformation sequence (Ardenne-Eifel region, Belgium-Germany). *Memoirs of the Geological Survey of Belgium* 53, 43 pp.
- Van de Fliedert, T., Hoernes, S., Jung, S., Masberg, P., Hoffer, E., Schaltegger, U., and Friedrichsen, H., 2003. Lower crustal melting and the role of open-system processes in the genesis of syn-orogenic quartz diorite-granite-leucogranite associations: constraints from Sr-Nd-O isotopes from the Bandombaai Complex, Namibia. *Lithos* 67, 205-226.
- Van der Pluijm, B.A., Marschak, S., 2004. *Earth Structure*, 2nd edition. W. W. Norton & Compagny Ltd, New York, 656 pp.
- Wiesmayr, G., Grasemann, B., 2005. Sense and non-sense of shear in flanking structures with layer-parallel shortening: implications for fault-related folds. *Journal of Structural Geology* 27, 249-264.
- Williams, M.L., Scheltema, K.E., Jercinovic, M.J., 2001. High-resolution compositional mapping of matrix phases: implications for mass transfer during crenulation cleavage development in the Moretown Formation, western Massachusetts. *Journal of Structural Geology* 23, 923-939.
- Wu, H., Pollard, D.D., 1995. An experimental study of the relationship between joint spacing and layer thickness. *Journal of Structural Geology* 17, 887-905.

Lebenslauf

- June 12th 1979 - Born in Pompaples, Switzerland
- 1987- 1992 - Primary school at Penthalaz (Switzerland)
- 1992- 1995 - Pregymnasium in mathematic and sciences at Cossonay (Switzerland)
- 1995- 1998 - Gymnasium in mathematic and sciences at the Gymnase de la Cité (Lausanne, Switzerland)
- 1998- 2003 - Study of Geology at the University of Lausanne, Switzerland
- June 2003 - « Diplôme de Géologue » (MSc equivalent), University of Lausanne, Switzerland
- 2003- 2007 - Ph.D. student at the Institut für Geowissenschaften, Johannes-Gutenberg-Universität, Mainz